ORNL/RSIC-44

CONF-800471--

ornl

OAK RIDGE NATIONAL LABORATORY

UNION CARBIDE

OPERATED BY
UNION CARBIDE CORPORATION
FOR THE UNITED STATES
DEPARTMENT OF ENERGY

A Review of the Theory and Application of Monte Carlo Methods Proceedings of a Seminar-Workshop, Oak Ridge, Tennessee April 21—23, 1980

Edited and Compiled by
D. K. Trubey and B. L. McGill

ORNL/RSIC-44

Contract No. W-7405-eng-26

Radiation Shielding Information Center (RSIC)
Engineering Physics Division

A Review of the Theory and Application of Monte Carlo Methods Proceedings of a Seminar-Workshop, Oak Ridge, Tennessee April 21–23, 1980

Date Published: August 1980

Edited and Compiled by
D. K. Trubey and B. L. McGill

Note:
This work is partially supported by
DEFENSE NUCLEAR AGENCY
under IACRO-DNA80-819
and
U.S. NUCLEAR REGULATORY COMMISSION
NRC No. 48 20 25 60 8

OAK RIDGE NATIONAL LABORATORY
Oak Ridge, Tennessee 37830
operated by
UNION CARBIDE CORPORATION
for the
DEPARTMENT OF ENERGY

TABLE OF CONTENTS

Papers not presented orally

ABSTRACT

This report consists of 24 papers which were presented at the seminar on Theory and Application of Monte Carlo Methods, held in Oak Ridge on April 21–23, plus a summary of the three-man panel discussion which concluded the seminar and two papers which were not given orally. These papers constitute a current statement of the state of the art of the theory and application of Monte Carlo methods for radiation transport problems in shielding and reactor physics.

Blank

FOREWORD and ACKNOWLEDGMENTS

The seminar-workshop on Monte Carlo Theory and Application, held in Oak Ridge on April 21–23, was the first of its kind in which RSIC collaborated on an international basis. The Monte Carlo methods development of the CEA/CEN/Saclay SERMA Shielding Laboratory was featured in the workshop and OECD Nuclear Energy Agency (NEA) Data Bank personnel assisted in advance preparations. The meeting was attended by 110 people and provided a well-rounded review of the state of the art. A total number of 53 institutions were represented from eleven nations: Brazil, Canada, France, West Germany, Hungary, Israel, Italy, Japan, Sweden, United Kingdom, and the USA.

The presentations included surveys of applications at various laboratories, discussions of new techniques, and descriptions of particular code systems. Both shielding and reactor core applications were discussed.

The survey papers summarized applications at Argonne National Laboratory (principally the use of VIM), Hanford Engineering Development Laboratory (KENO and MCNP), Los Alamos Scientific Laboratory (MCNP), and Oak Ridge National Laboratory (MORSE, KENO, and TRIPOLI II). Extensive presentations were made on SAM-CE (MAGI) and MCNP (LASL) Additional overviews were given on KENO V (ORNL), TRIMARAN and TRIPOLI II (CEA/CEN/Saclay), KIM (CNEN), and new MORSE modules (ORNL). Reports were given on perturbation theory to obtain sensitivities, on recursive Monte Carlo to develop importance functions, and applications of TRIPOLI II to sodium duct and integral experiment analysis. Other papers were given on analysis of LWR lattices, thermal reactor benchmarks, ex-core water level detectors, and biological organ dose estimates.

Two contributions of the Japanese Ship Research Institute, not presented orally, appear in these proceedings.

A summary panel of "three wise men" concluded the seminar and gave extemporaneous comments and some forecasts for the years ahead. The three panelists were Ely M. Gelbard (ANL), Malvin H. Kalos (Courant Institute), and Edward D. Cashwell (LASL).

The workshop on TRIPOLI II was led by J. C. Nimal, J. R. Gonnord, and T. Vergnaud of the CEA/CEN/Saclay SERMA Shielding Laboratory. TRIPOLI II is a very complex, but powerful general purpose particle transport code which treats neutrons and gamma rays for both core physics and shielding problems. The geometry treatment is quite general and cross sections, in a very fine multigroup form, can be taken from ENDF, UKNDL, and other sources. The importance sampling is based on a highly-developed system using equal-weight surfaces which, when properly used, minimizes splitting and Russian Roulette. A particularly important recent development with this system is the interfacing of the code to ENDF/B formatted data and/or multigroup data in AMPX format.

We are grateful to our French colleagues, Nimal, Gonnord, and Vergnaud, for their very significant and successful efforts on behalf of making the TRIPOLI system available for use in other countries. We are also grateful to the CEA for its support in making the workshop possible. We also wish to express our appreciation to Enrico Sartori, IAEA representative to the OECD NEA Data Bank, for his assistance in testing and packaging TRIPOLI II and KIM, and to Noel Cramer of ORNL/EPD for special assistance in preparation for the seminar-workshop.

We are grateful to: authors of the papers for submitting their manuscripts in camera-ready form; Eddie Bryant, Nancy Hatmaker, Mildred Landay, and Marie Anthony for their services in program preparation, proceedings preparation and publication, and registration of attendees; banquet speaker, Johnny Rosen; Betty Maskewitz for general management; and to R. W. Roussin, R. M. Westfall, and others who chaired sessions of the meeting.

D. K. Trubey and Betty McGill
Radiation Shielding Information Center (RSIC)

MONTE CARLO IN THE 1980s

Summary of a Panel Discussion

Panel Members:
E. D. Cashwell
Los Alamos Scientific Laboratory
E. M. Gelbard
Argonne National Laboratory
M. H. Kalos
New York University

E. M. Gelbard: The title of the panel suggests that we're supposed to tell you what will happen to Monte Carlo in the next decade, and I think we would be very rash to try to tell you what will happen to *anything* in the next decade, particularly anything in nuclear energy. I think that the most we can do is to say what we would like to happen. I think that no one can help being impressed by the power of the Monte Carlo codes that have been described here. Codes seem to be available now to solve the most complicated problems and they seem to be getting more and more user-oriented, and to that extent it seems that really a great deal of progress has been made, so it seems a reasonable time to ask: "What more could be done?" "Where do we go from here?" "Is there anything that hasn't been done that ought to be done?" Everybody surely has a personal opinion here, depending on his own prejudices and experience. My feeling is that there are a number of things I would like to see, a number of changes I'd like to see--and improvements of both Monte Carlo usage and Monte Carlo methods. They are really two different subjects.

First of all, I have the feeling that Monte Carlo hasn't been used in some respects as well as it could be. There are some uses of Monte Carlo that have fallen by the wayside. Monte Carlo could be used to benchmark computational methods much more than it has been. Yet to some extent it has done that. I think we've seen that in the talks. But for one thing Monte Carlo could be used to benchmark the *whole* computational method. That is, we do slowing down calculations. We get group constants. We compute fluxes in cells. We group averaged, and in the group averaging we have to compute resonance escape probabilities and Dancoff factors, and when we're all finished we end up with a very complicated problem. Let's say we have a lattice that's facing a water channel, and we've got to make assumptions about Dancoff factors. Every stage of that calculation could be benchmarked by Monte Carlo techniques.

I think that it would be interesting also to develop specialized Monte Carlo techniques that are simplified and specially designed for benchmarking--very accurate and very fast. This could be done, but in the drive to get production-oriented codes, this kind of use of Monte Carlo has fallen away. I think that part of the reason that this has happened is that first of all there are two different kinds of people--they don't have enough contact with each other. I should think that

that's something that ought to change. People who work on Monte Carlo and people who work on deterministic methods ought to communicate more. Calculations by deterministic methods ought to be checked more by Monte Carlo to find errors and to understand approximations.

My second point is that I think that it's unfortunate that when most critical experiments were done, Monte Carlo codes were not available to do detailed analysis. So people fell into the habit of analyzing criticals by approximate techniques, and corrections were piled on top of corrections until when you finally get to compare the calculation with the experiment, you don't really know what you're comparing. We've reached the stage now where we can set up great detailed simulation of a critical and make essentially no approximations except those in the cross sections. That has not been done very much. There are very few cases. The TRX lattices we saw here are an example, and the safety-related criticals which were mentioned in the talk on VIM were another example. I don't know whether the information is even available anymore. If it's not, I think it's unfortunate; if it is, I think that a lot of old criticals should be reanalyzed in detail. If anybody wants to measure criticals in the future, I think they should be set up so that the description of the construction of the critical goes directly on cards so it can be put directly on cards so it can be put directly into a Monte Carlo code. If you don't do this, you have an enormous amount of difficulty just putting together a picture of the drawers and coming up with Monte Carlo input.

As far as the development of methods is concerned, the one thing that bothers me a lot has to do with safety calculations; it is that the perturbation method cannot handle a very important safety problem in which voids close or collapse. That can either be a sodium voiding problem, which is the most common type, or another class of problems in which in a fast reactor you have a molten pool or you have had a melt-down--you have a molten pool with bubbles in the pool, and something happens; the bubbles close. This is a kind of accident. You'd like to calculate the reactivity insertion. There is no analytic technique that anybody can use that is reliable. Monte Carlo seems to be an ideal way to benchmark that kind of calculation, but we can't do that kind of calculation by Monte Carlo. This is a kind of calculation that, as far as I know, you cannot do by Monte Carlo. People have tried and they failed. That is true for the sodium void calculation and the bubble calculation.

Another subject I come to is probably much more important than the others. I would like to see some sort of return to the study of basics. There are some holes in the theory, particularly in eigenvalue calculations. It is a known fact that the eigenvalue method used to calculate eigenvalues in the reactor is biased. It is known that the bias depends on the number of discrete histories per generation.. There's been very little study of the amount of that bias. The question becomes more and more important if you are more and more interested in accuracy. By the time you reach the stage where you finally calculate eigenvalues to a

quarter of a percent, you may well ask whether or not the bias is that large. People, when deciding how many histories to run per generation, pretty much do this on the basis of their own habits. No one really knows what should be done. I think, again, as requirements get more and more demanding on Monte Carlo, this question gets more and more important. More and more in the reactor business safety problems are becoming crucial. In analyzing an accident, you've got to know whether or not the reactivity difference is small compared to a dollar. A dollar is only 0.3 of a percent. So, if you're going to use Monte Carlo at all to try to analyze safety calculations, you've got the problem that you really won't calculate differences to within this very small amount, and small biases become important and perturbation methods become important.

A related question has to do with a confidence statement--statements of accuracy. There are various problems in confidence statements. First of all, in calculating confidence intervals for eigenvalues, you have again a well-known problem. Different generation eigenvalues are correlated, so when you get means over generations, you have no way of knowing what the accuracy of your answer is. There isn't any very simple relation between a printed out standard deviation and the real accuracy, and it becomes particularly bad if you're dealing with a very large reactor in which convergence is slow.

But even leaving aside this question, there are other questions. How accurate is the standard deviation? In a study of criticality safety of casks, standard deviations of this type were taken very seriously. How accurate is the standard deviation? That depends a great deal on the kind of distributions you have. Very little is known about those distributions. They may get very strange. For example, a track length distribution may be very strange inside of a single pin, that is, if you're interested in what happens in a pin. Maybe for an eigenvalue, that's not very serious. If you're interested in using Monte Carlo to compute what happens in individual pins, if you're trying to get a ratio between power in one pin and power in another, you're almost forced to use something like a track length estimator. Maybe there are improved ones. I guess Mal (Kalos) has suggested that to me, and if there are, they may make a difference. If you don't know anything about the distributions you're dealing with, and if those distributions are distorted by your biasing schemes or by peculiar features of the estimator itself, you really can't tell what the accuracy of the Monte Carlo answer is, and one of the main advantages of Monte Carlo goes right down the drain. Monte Carlo is unique in the respect it tells you its error. But unless you know the distributions, it's really an illusion,

So, I want to point out, this is a question that Maienschein raised just at the beginning of this meeting-what do biasing methods do to standard deviations--and I would add, how reliable are standard deviations when you're using peculiar estimators? I would like to see, then, a shift to some study of these basic problems now that we have so

many powerful computing tools, some more study of theory I think would be very appropriate.

M. H. Kalos: First, I would like to start by expressing my thanks to Bob Coveyou, from whom I learned a lot over many years and for whose good health I wish everything. Second of all, I'd like to express my dismay at this imperceptible transformation that has occurred in me from "wise guy" to "wise man." And, I would like to echo Ely's call for a return to, or at least never losing sight of, basics in Monte Carlo.

There are a lot of basics that are being forgotten in the rush to implement new and better codes--more user-oriented codes. Let me point to one that I think is very important. I think that in almost every implementation of the exponential transformation, it's been done wrong, in such a way that it introduces a totally spurious singularity in the neighborhood of the transformed attenuation coefficient equal to the total attenuation coefficient. That can be dispensed with entirely by a simple change in the way the code carries out the sampling.

A related thing is that in spite of the very elaborate ways of treating importance sampling, I want to remind you all that if you have an importance function which is expressed as a function of position, energy, and direction, and then you multiply the *a priori* flight probability by the importance function as a function of position, that product does *not* correctly represent the marginal distribution of the function you want to sample. If you really want to implement the ideas of importance sampling correctly, you should calculate that marginal distribution. The effect will be, I would think, if you can do it, an enormous improvement in running time--perhaps as much as a factor of 10 in deep penetration calculations.

I would like to say a good thing: I think the future of recursive Monte Carlo is very bright. This is something that Herb Steinberg, John Brooks, and I demonstrated the feasibility of about 10 years go, and I'm very pleased that Goldstein and Greenspan have brought it to an apparently practical point. I think this is a very valuable thing because all of us find that the use of Monte Carlo is spreading and the necessity of teaching the basic ideas becomes more and more onerous, and anything that automates this is to be welcomed.

With respect to criticality calculations, I would hope that somebody in the 80s will pay attention to the desirability of doing importance sampling in criticality studies of large reactors. This is a point that is often neglected. It is possible to make an importance sampling transformation, which in principle permits you to calculate the eigenvalue with zero variance and zero bias. Most people misunderstand this because they say, "But a reactor is set up so that fission is not an unlikely event." That's missing the point. The point of this kind of importance sampling is to accelerate the outer convergence, to minimize the sequential correlation of fission sites from generation to generation, and thereby reduce the variance and reduce the bias. I think that's really worth thinking about.

Finally, I think in the 80s, Monte Carlo is going to be very strongly influenced by progress in computers. All of you know that computers have become a lot faster. Most of that has been through the implementation of vector or pipeline processors, and the payoff for the kind of Monte Carlo we do is extremely small and very difficult to come about. Computer architecture can be made more general in a way which is much more profitable for this kind of Monte Carlo. At NYU we have a project now for considering the architecture of large arrays--we hope eventually for thousands of processors which are strongly coupled together. And if I might have my first transparency, I will. . .Well, that's my last transparency, but no matter. Everything goes forwards and backwards in the same way. We see here a switching network which is designed to connect, in this case, 16 processors on the left with 16 memory modules on the right. This kind of strong coupling of processors and memory is what we have in mind, and it would permit 16 processors, each with its own instruction stream, to carry out Monte Carlo calculations more or less independently, accessing large cross section sets, large geometry descriptions, and large arrays of answers in memory without serious contention problems.

We are now building a software simulator, and starting to design a hardware emulator, which will be capable of treating parallel arrays of 128, or possibly up to 256, processors. I would like to try out some more or less stripped down standard Monte Carlo to see how well they work. I would encourage you to keep in touch with this and use it when it becomes available.

E. D. Cashwell: When I was asked yesterday if I would sit in for Bob Coveyou, disregarding the fact that I didn't know what I would say, I was very honored to appear on the platform with these distinguished individuals. But then last night I found out why they really asked me. It's a conspiracy to keep me from giving the same lousy paper over and over again. That's quite a price to pay. I've got to find a new paper!

What I'd like to say as we talk about what will happen in the 80s--let me start out by making a few comments on this meeting. Ten years ago I attended a similar meeting, and this time I'm quite impressed by certain things. I'm quite impressed by the applications. They're very interesting and showed very careful analysis by very knowledgeable practitioners with many difficult problems being quite cleverly and successfully solved. As Ely pointed out, in terms of the codes, they've gotten very much more sophisticated. With many importance sampling techniques implemented, geometry very carefully treated, cross sections very carefully treated, the user has an easier time of it. So, that's very good. So I think in that sense we don't have to worry about particle transport going away in the 80s. It'll just get more and more important.

Furthermore, I think I see--and we all see--more and more applications outside the area of particle transport, even though particle transport may be used to help solve these problems, and we look at what happened when Monte Carlo first started. We look back at the history. The first thing people did was rush out and solve many new and different problems,

and most of the methods, due to the state of computers and so on, were dismissed as being quite interesting but impractical. Now, due to better techniques and better machines and more available machines, both large and small, some of these methods, some of these problems, are becoming very fruitful areas for research, as I'm sure Mal would agree from some of his research.

So, I think that we have nothing to worry about. I think that many applications will come from outside the area--there are plenty of them now--in different fields, and we just hope that we can keep up with them and use our knowledge and experience from what we've done in particle transport and try to apply that to some of these problems.

MONTE CARLO APPLICATIONS AT HANFORD ENGINEERING DEVELOPMENT LABORATORY

L. L. Carter, R. J. Morford, A. D. Wilcox and C. A. Rogers
Hanford Engineering Development Laboratory
Richland, Washington, USA

ABSTRACT

Twenty applications are summarized utilizing the Monte Carlo method to solve neutron and photon transport problems. The majority of the applications are for either the Fusion Materials Irradiation Test (FMIT) Facility or the Fast Flux Test Facility (FFTF). The degree of success in solving each problem is described quantitatively by a satisfaction factor. The satisfaction factor is based upon the adequacy of the nuclear data, the geometry model, and the numerical data for the expenditure of labor and computer time.

INTRODUCTION

The current use of Monte Carlo at Hanford Engineering Development Laboratory (HEDL) is dominated by neutron and photon transport problems relevant to the Fast Flux Test Facility (FFTF) and the Fusion Materials Irradiation Test (FMIT) Facility. The Monte Carlo effort is oriented towards engineering applications and does not encompass code development. This paper will summarize our applications during the last three years.

We utilize the KENO[1] code for criticality problems and the general purpose code, MCNP,[2,3] for all other applications. The KENO code has been adapted to run on either the CYBER or UNIVAC computer systems at Hanford. The MCNP code with its associated cross section library is maintained on the MFE computer system at Livermore, California by Los Alamos Scientific Laboratory (LASL) and we utilize this computer system for our calculations for the FMIT facility. We have adapted an older version of MCNP to the CDC-7600 at Berkeley for solving FFTF problems.

The majority of the current applications of Monte Carlo involve design problems for the FMIT facility. This accelerator based facility,[4] now in the early stages of construction on the Hanford site, will provide a fusion-like radiation environment for testing potential fusion reactor materials. The neutron source, produced by a 0.1 Amp beam of 35 MeV deuterons incident upon a flowing lithium target, is highly anisotropic and features a rapid spectral variation with angle. The spectrum in the forward direction is characterized by a broad peak at $\sim$14 MeV with a high energy tail extending to $\sim$50 MeV. While the broad peak provides the

major portion of the source for material damage studies, other neutron energies are important in the overall design of the facility. Because of the importance of the very high energy neutrons between 20 and 50 MeV for shield design, neutron cross sections between 20 and 60 MeV were appended to existing (ENDF/B and ENDL based) MCNP library for the most important isotopes.[5]

Monte Carlo is a particularly useful tool for FMIT applications because of the two- and three-dimensional configurations, the anisotropic sources, the anisotropic neutron scattering at higher energies (especially above 20 MeV), many penetrations through shields with the resulting need to evaluate neutron streaming, and steep neutron flux gradients within the prime test region near the (d,Li) source. Its utilization as a tool to solve FFTF related problems is typically more difficult primarily because of the large expected number of collisions that a neutron experiences from birth to absorption in fast reactor materials. This disadvantage is alleviated somewhat in criticality safety calculations since the primary functional to be determined is the multiplication factor involving an integration over all of phase space.

Neutron transport through thick iron-dominated materials is important in both FMIT and FFTF applications. A calculational benchmark[6,7] for monoenergetic sources of 2, 14 and 40 MeV has recently been completed using cross sections tested against integral experiments. This calculational benchmark is used to validate multigroup cross section libraries and transport codes.

In the next three sections we summarize Monte Carlo applications encompassing the last three years. Our manpower allocation for Monte Carlo is small with four engineers contributing an equivalent of ∿ one full-time man. Approximately three-fourths of the effort is on FMIT and one-fourth on FFTF problems.

APPLICATIONS FOR FMIT FACILITY

The (d,Li) neutron source has been characterized by thick target measurements for ten different angles using time-of-flight techniques and the cyclotron at the University of California at Davis. The spectra at the four angles depicted in Figure 1 (measured data[8] without smoothing) are shown to illustrate neutron energy regimes that are important at various directions. Of particular importance from a shielding point of view is the flattening of the spectrum between 30 to 45 MeV at the angle of 8°. This flattening is significant for angles from about 6° to 20°. These source neutrons are the primary neutrons that penetrate thick shields in the forward direction.

A cut-out view of the test cell is shown in Figure 2 with the deuteron beam impinging upon the flowing lithium from the left. The corresponding plan view of the test cell shown in Figure 3 at the elevation of the neutron source does not show pipes and equipment

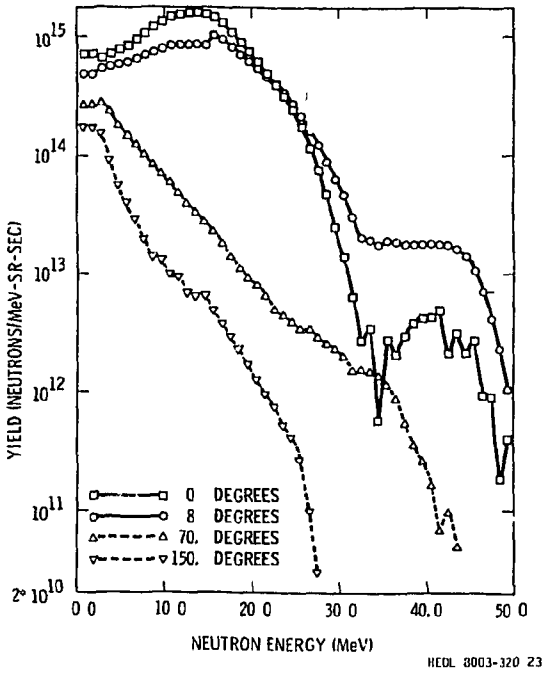

Fig. 1. Neutron spectra from a 0.1 Amp current of 35 MeV deuterons incident upon lithium.

within the test cell. Basic neutronic problems in and around the test cell include: (a) a determination of bulk shield thicknesses; (b) nuclear heat deposition within the test cell, thermal shield, and adjacent bulk shield; (c) neutron streaming through various penetrations; (d) neutron activation within the test cell and beyond the experimenters side wall; (e) confirmation of adequacy of collimator design; and (f) the generation of detailed neutron flux maps within the prime test volume. In addition, neutronics calculations are required for shield design, including neutron activation, for the Linear Accelerator (LINAC) and various service areas.

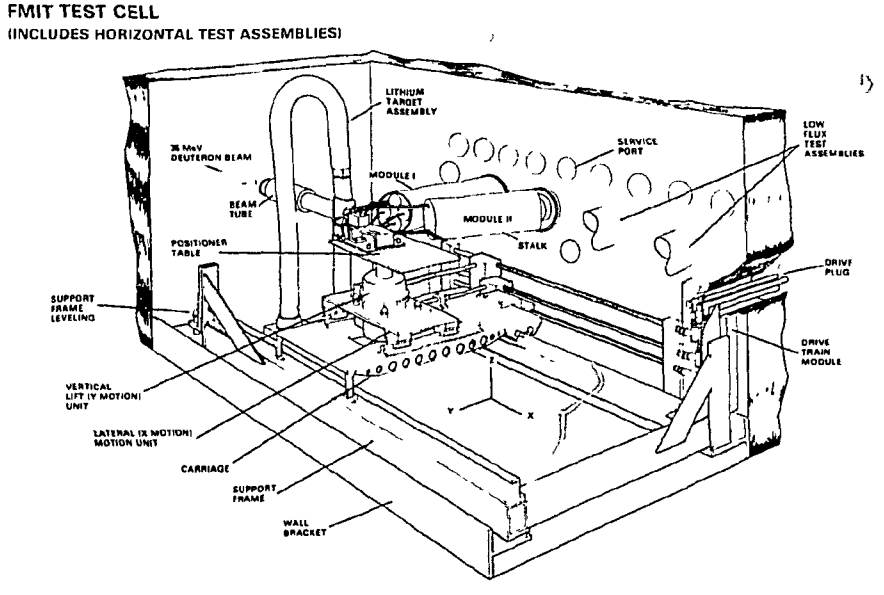

Fig. 2. Conceptual arrangement of 4 horizontal test assemblies and a vertical test assembly in the FMIT test cell.

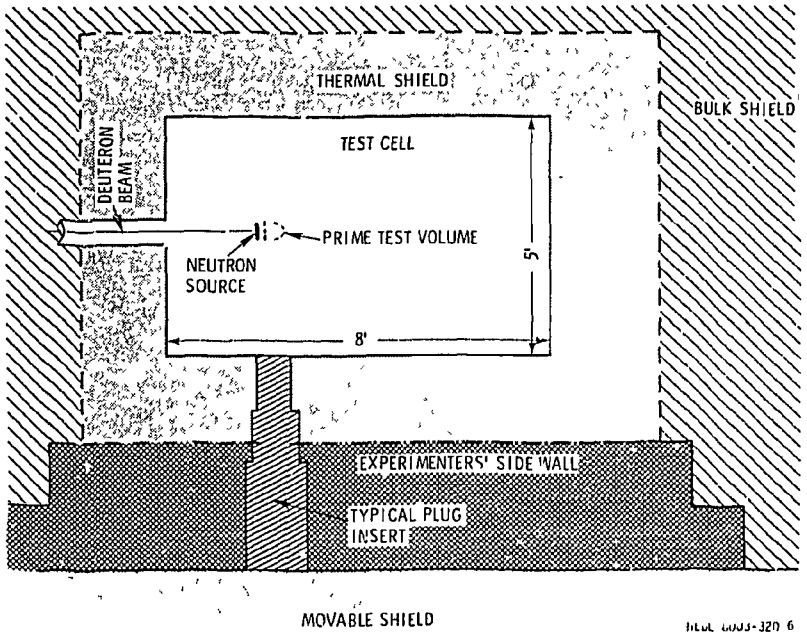

Fig. 3. Plan view of FMIT test cell.

The Monte Carlo calculations we have made for FMIT are listed in Figure 4. Many of these problems required the variation of one or more parameters in a number of separate calculations. In such cases, the "Minutes of CDC-7600 Execution Time" in the right hand column of Figure 4 represents a typical time for an individual run rather than for the series.

The "Satisfaction Factor" given in Figure 4 is an attempt to quantitatively assign an overall return from the investment in machine time and expenditure of manpower. The satisfaction factor is defined as

$$S = 10^{-2} \sqrt{g\ p\ m\ r}\ ,$$

where g, p, m, and r are assigned values between 0 (failure or far below expectations) and 100 (excellent or far above expectations) under the definitions:

g = adequacy of the geometric model in relation to the real-world situation,

p = adequacy of the physics models compared to state-of-the-art and/or desired accuracy (including cross section data and source data),

m = reasonableness of manpower effort required, and

r = return obtained from calculation, relative to need, for the expenditure in machine time (this also includes the adequacy of statistical errors).

	PROBLEM DESCRIPTION	PERTINENT FIGURE NUMBER	SATISFACTION FACTOR	MINUTES OF CDC-7600 EXECUTION TIME
1.	DOSE RATES THROUGH SLAB SHIELDS FOR MONOENERGETIC SOURCE NEUTRONS OF 15, 25 AND 50 MeV (NEUTRON AND GAMMA DOSE)	*	85 (100 90 100 80) g p m r	15
2.	DOSE RATES THROUGH BACK AND SIDE WALLS OF TEST CELL (NEUTRON AND GAMMA)	3	80 (90 90 100 80)	15
3	NEUTRON ACTIVATION THROUGH EXPERIMENTERS' SIDE WALL (VERIFICATION OF ANISN CROSS SECTION LIBRARY)	*	89 (100 100 100 80)	15
4.	NEUTRON STREAMING THROUGH GAP OF PLUG IN EXPERIMENTERS' SIDE WALL	3	63 (70 100 80 70)	60
5.	NEUTRON STREAMING THROUGH LITHIUM OUTLET PIPE IN FLOOR OF TEST CELL	*	57 (70 100 90 60)	15
6.	NUCLEAR HEAT DEPOSITION WITHIN THERMAL SHIELD AND ADJACENT BULK SHIELD	3	63 (80 70 100 70)	60
7.	TRANSMISSION OF (d, Li) NEUTRONS THROUGH IRON BLOCK (INCLUDING SOME GAMMA CALCULATIONS)	*	95 (100 100 100 90)	5
8	NEUTRON FLUX FOR ACTIVATION WITHIN TEST CELL	3	71 (70 100 90 80)	30
9.	NEUTRON FLUX FOR ACTIVATION WITHIN LINAC	5a, 5b	85 (90 100 90 90)	20
10	IMAGE ON TRACK LENGTH RECORDER FOR COLLIMATOR DESIGN	6	89 (100 100 100 80)	5
11.	ENERGY AND SPACE DEPENDENT NEUTRON FLUX MAPS NEAR SOURCE	*	72 (90 90 80 80)	30
12.	NEUTRON STREAMING THROUGH RF LINES INTO RF EQUIPMENT ROOM	7	67 (70 100 80 80)	20

*GEOMETRY NOT SHOWN

HEDL 8003-320 12

Fig. 4. Monte Carlo calculations for the Fusion Materials Irradiation Test Facility.

The satisfaction factor has the range $0 \leq S \leq 100$ depending upon the values assigned to the four parameters. In this paper the satisfaction factors were normalized so that values of ∿50 indicate marginal satisfaction with the calculation, values less than ∿50 are indicative of dissatisfaction with the calculation (the output data is of only limited usefulness), and a value greater than ∿70 is indicative of overall satisfaction with and usefulness of the data in the engineering application. Of course, problems with a satisfaction factor less than ∿50 will, in many cases, be difficult to solve with deterministic methods as well.

Problems 1 to 7 of Figure 4 are relevant to the design of the shields around the test cell. Some initial studies[5,9] (problem 1) addressed dose rates through slab shields for normally incident monoenergetic neutron sources with energies between 15 and 50 MeV. Comparisons were made between these calculations and pertinent discrete ordinates

calculations summarized in the literature.[10] The monoenergetic calculations subsequently provided useful benchmarks for comparisons with discrete ordinates calculations based upon an upgraded multigroup library.[11] They also provided initial assessments of material worths for shielding high energy neutron sources.

Careful biasing of the monoenergetic calculations enabled us to obtain satisfactory statistical precision for shield thicknesses corresponding to a reduction in the dose rate through the shield by about ten orders of magnitude. This was accomplished by adjusting cell importances[3] to obtain a roughly constant sample population throughout the shield in conjunction with the use of Russian roulette[3] as the neutron energy decreased. Russian roulette was used to discriminate against the lower energy neutrons ($<\sim$1 MeV) near the source side of the shield. Without the use of energy dependent biasing, we observed that a large fraction of the computer time was expended on those neutrons near the source face of the shield. These neutrons have a small probability of eventually penetrating the shield.

Using the information obtained and techniques learned from the monoenergetic source calculations, it was fairly straightforward to make the pertinent bulk shield calculations[5,9] of problem 2 for the back and side walls of the test cell (see Figure 3). The important source energy regime was determined to be $\sim$30 to 50 MeV for the back wall and $\sim$20 to 40 MeV for the side walls. The important energy regime for the side walls is increased upwards by very high energy neutrons (>30 MeV) that suffer elastic collisions within test assemblies and then scatter toward a side wall. Even though the probability of such events is low, the importance of these neutrons is large enough so that they are not negligible.

Activation is an important consideration for the experimenters' side wall (see Figure 3) since access to this wall is required for maintenance and removal of test assemblies. The wall material and thicknesses were optimized using one-dimensional ANISN calculations subsequent to a benchmark comparison (problem 3) with MCNP. The one-dimensional benchmark comparison, using the pointwise library of MCNP, verified that the multigroup library for ANISN would require the utilization of appropriate self-shielding factors.

Streaming calculations (problems 4 and 5) typically require an overspecification of the geometry in order to adequately assign spatial importances and focus the calculational effort in the vicinity of the streaming paths. This introduces additional complexity to already complicated models so the geometry factor, g, for problems 4 and 5 has only been rated at 70%. Version 1B of MCNP was used in these calculations. Version 2, with its improved geometry package, may help alleviate these types of difficulties in future problems.

The heat removal system for the test cell utilizes gas cooling. The gas cooling is economically sensitive to the total amount of heat (and its spatial distribution) deposited from nuclear interactions within the walls of the test cell. Monte Carlo is attractive to use for this

calculation since three-dimensional heat deposition information is needed for the wall configuration shown in Figure 3 with the highly anisotropic source distribution. Although calculational limitations exist, and hence problem 6 was rated with an r value of 70, it would have been at least as difficult to obtain satisfactory results with deterministic codes.

Shortcomings in the nuclear data base impacted the determination of heat deposition. Data sensitivities included the gamma production cross sections, neutron KERMA factors, and cross sections for the neutron transport. Unfortunately, energy balances in ENDF/B continue to have shortcomings for the generation of cross section libraries and for the calculation of neutron KERMA factors.[12] Hand corrections of the cross section data were made over various energy regimes for some of the elements. Improvements for iron are anticipated in the future with a new evaluation[13] by LASL using improved gamma production data and energy balances.

The heat deposition within the concrete beyond the thermal shield is sensitive to the proper transport of the higher energy (∿14 MeV) neutrons within the thermal shield. An integral measurement of the transmission of (d,Li) neutrons through an iron block as recently been completed. Comparisons between the calculated (problem 7 of Figure 4) and measured transmitted currents will provide an overall check on the data base.

Monte Carlo tends to be efficient for the calculation of neutron fluxes averaged over sufficiently large volumes. Hence, problems 8 and 9 of Figure 4 (see Figures 5a and 5b for geometry of problem 9) received reasonably good satisfaction factor ratings.

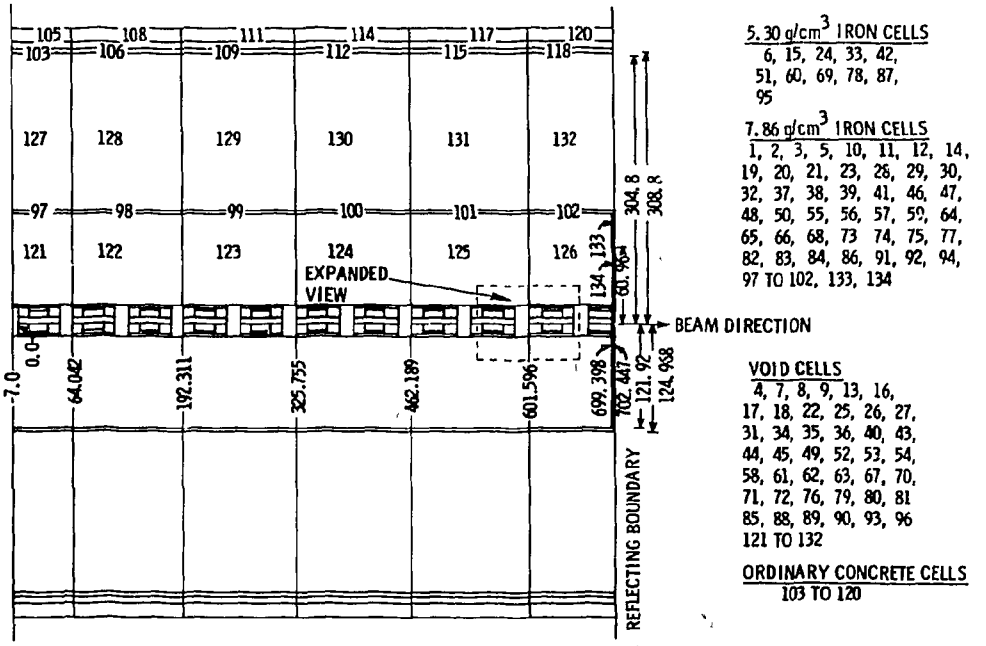

Fig. 5a. Cylindrical geometry model of LINAC for flux calculations. (Dimensions in cm) HEDL 8003-320 20

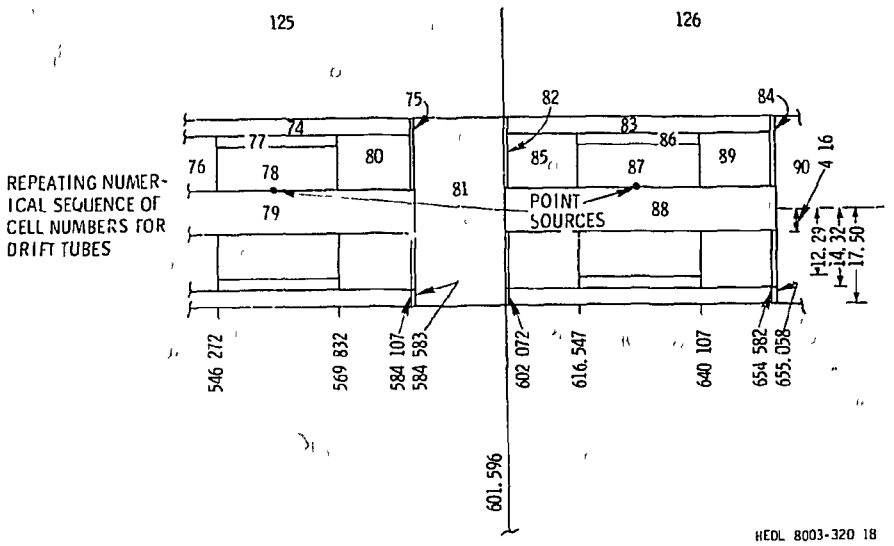

Fig. 5b. Cylindrical geometry model of drift tubes. (Dimensions in cm)

The evaluation of the collimator design for the track length recorder[14] (problem 10 and Figure 6) required a comparison of the source image from neutrons passing through the throat of the collimator to the background provided by neutron attenuation and scattering within the collimator material. This problem received a high satisfaction factor since ray tracing from the source and collision points near the throat of the collimator is a standard feature of MCNP using the point detector estimator.

An accurate method for the calculation of neutron flux maps within the material test assemblies is essential for the proper interpretation of experiments. In the current FMIT design the deuteron beam impinges upon the lithium target with a time-averaged distribution perpendicular to the beam that is roughly bivariate normal. The full-width-half-maxima are $\sim$3 cm and $\sim$1 cm along the horizontal and vertical directions, respectively, with a correlation coefficient of $\sim$0. Superimposed upon the spatial distribution of the deuteron density is the highly anisotropic distribution of the emerging neutrons which changes as the deuterons penetrate into the lithium. The resulting phase space density of the neutron source makes it difficult to apply discrete ordinates calculations in one, or even two, dimensions. Hence, we resort to Monte Carlo techniques for the generation of neutron flux maps. This is not straightforward since a rapid retrieval of energy dependent fluxes in a region of steep gradients is required.

Three-dimensional flux maps are generated in two steps. A Monte Carlo calculation is first made to determine fluxes averaged over small surface segments. The grid for the surface flux tallies is defined as follows: Small parallelepipeds are described within the test assembly by slicing the assembly with a number of planes normal to the x, y, and

z axes, respectively. Each rectangular side of a parallelepiped is a tally surface for a surface flux estimator.

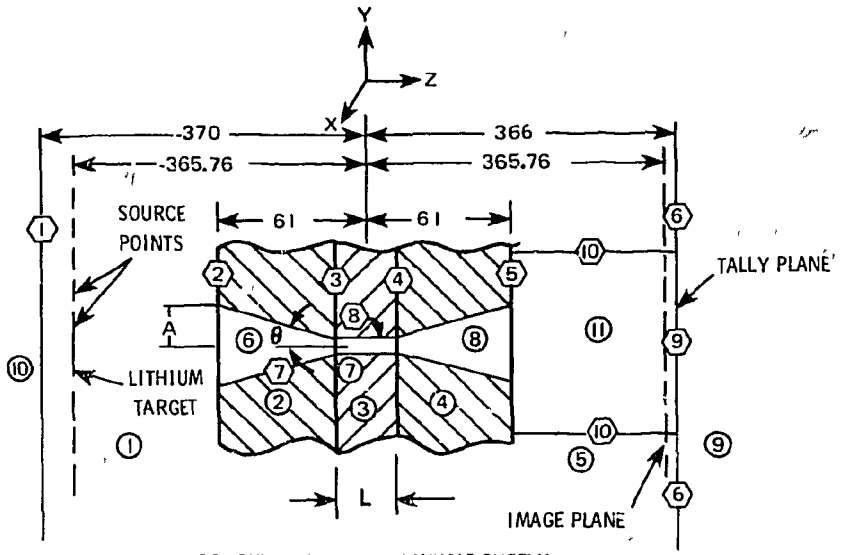

COMPUTER MODEL FOR PINHOLE SYSTEM

- ⬡ SURFACE NUMBERS
- ○ CELL NUMBERS
- ALL CROSS SECTIONS OF COLLIMATOR GIVE CIRCULAR HOLES

DIM	CASES 1-3	CASES 4-21
A	0.29	0.50
R(RAD)	0.025	0.025
L	10.46	6.096
θ	0.2741	0.4699

ALL DIMENSIONS ARE IN cm

HEDL 8003-320.10

Fig. 6. Collimator geometry.

The second step utilizes the surface fluxes from the Monte Carlo calculation to rapidly generate energy dependent neutron fluxes at positions of interest by using an accurate interpolation method within an auxiliary computer program. In a test problem,[15] 1,200,000 neutron histories were sampled on a CDC-7600 computer in 28 minutes. The auxiliary program calculated the energy dependent flux at ∿1700 spatial points per minute for positions within the test assembly where the total flux changes by an order of magnitude within a few centimeters. This calculation (problem 11 of Figure 4) utilized more than 2,000 surfaces for the tabulation of the neutron flux during the Monte Carlo calculation.

The geometry model shown in Figure 7 formed the basis for a calculation of neutron streaming through a chaseway between the LINAC accelerator and an adjacent RF Equipment Room. A finer mesh of cells than that shown in Figure 7 was actually required in order to obtain appropriate biasing with cell importances. The optimized calculation performed

reasonably well and received an overall satisfaction factor of 67 (problem 12 of Figure 4) in spite of a rather low geometry factor rating of 70.

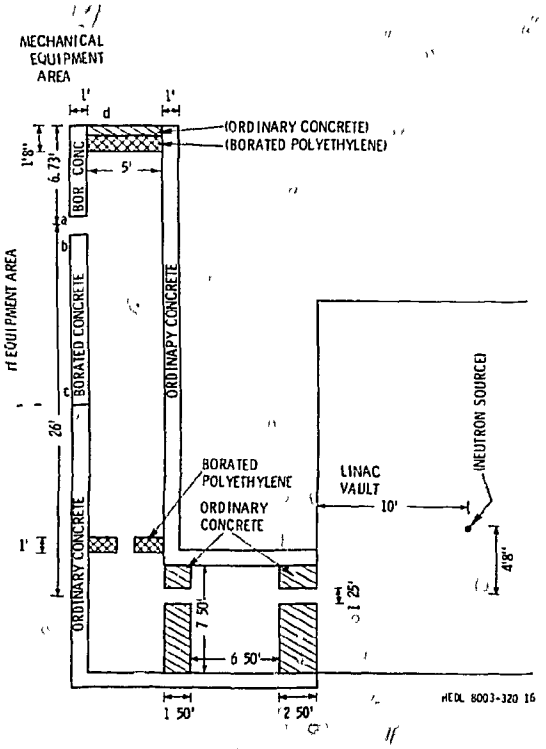

Fig. 7. Vertical view of RF chaseway along LINAC. (1.25' in diameter cylindrical penetrations; mirror boundary conditions in the third dimension)

APPLICATIONS FOR FFTF

Use of Monte Carlo Codes for Criticality Safety Calculations

Introduction

Monte Carlo codes in the field of Nuclear Criticality Safety are primarily used to calculate the neutron multiplication factor k_{eff} for arrays of fissionable materials. Storage of fissionable materials in a relatively small volume under conditions of complete safety is mandatory during the fuel fabrication process. The complexity of the array configurations and an economic reluctance to accept overly conservative limits necessitate use of Monte Carlo methods. At HEDL the KENO Monte Carlo code is presently used for all array calculations.

Storage Array Configurations

Each storage array has unique features. One of the simpler configurations consists of a cabinet with shelves which are spaced one foot apart, one above the other. Limits are placed upon the quantity of fuel each shelf can contain. The KENO code is used to calculate k_{eff} for

various postulated conditions of internal moderation, interspersed moderation, fuel overbatching, and interaction with other fuel nearby. K_{eff} is restricted to a value of less than 0.95 at a 95% confidence level for all normal or credible abnormal conditions.

A more complex configuration consists of a two-dimensional array of cubicles occupying an entire wall of a room. In this array both the areal density and the total quantity of fuel will be greater than for the individual cabinets. In one such array four different fuel limits are used. Moderated fuel is stored at one end, followed by partially moderated fuel, unmoderated fuel, and unmoderated fuel in specified small containers located in fixed positions to permit higher fuel concentrations. Examination of such an array under flooding conditions introduces additional geometric complexity because complete flooding is not necessarily the most reactive configuration. This necessitates a number of calculations to determine the most reactive configuration.

Another configuration consists of completed fuel pins and fuel bundles stored in a below grade array of stainless steel cylinders set in concrete. The concrete provides partial neutron isolation of the various rows and columns within the array. K_{eff} is found to depend on many parameters necessitating numerous calculations. These parameters include: (1) wall thickness of the stainless steel cylinders; (2) composition of concrete; (3) water content of concrete; (4) type of fuel stored; (5) separation of rows and columns in the array; (6) quantity of fuel stored; (7) quantity of moderators used in storage; and (8) the postulated degree of accidental water flooding possible. An interesting aspect of these calculations is the functional dependence of reactivity upon water content of the concrete and the degree of water flooding. Since the water content of the concrete influences the effect of flooding on reactivity, it is necessary to examine the effect of flooding on reactivity when the concrete is dry and when wet. As time passes the water content of the concrete will decrease and thereby change the value of k_{eff} under "worst case" conditions.

Another good example of a configuration requiring use of Monte Carlo calculations is an array of shipping containers. Here the problem is one of calculating the minimum critical number under worst case conditions. This can become highly complex since the arrangement of containers is also a variable.

Placement of Criticality Alarms

The GEM code, an earlier version of MONK, has been used in the past to calculate the relative neutron flux levels at various locations around a storage array. Heavy concrete shielding and complex array geometries made it difficult to determine whether or not sufficient neutrons would reach the criticality detectors during a small hypothetical excursion. Each detector location was represented in the computer model by a box so that neutrons reaching the box were counted and compared with the number leaving the fuel.

User Pitfalls

Although Monte Carlo techniques are the most powerful available for criticality calculations, the user must continually exercise caution. It is easy to develop an unwarranted degree of confidence and to overlook pitfalls.

The input required to describe an array configuration can be very complex and errors can be overlooked. For this reason, use of the picture drawing routine SCAN in the KENO code is imperative. Some errors can be spotted immediately, but others are more subtle. For example, a negative sign was once inadvertently omitted for a reflector boundary designation. This had the effect of completely removing the reflector from the calculation and leaving a bare core. Although pictures were printed, the reflector was not included since only the core could be drawn at that time because of limitations in the picture routine. Consequently, calculations were made for an unreflected array, although a full water reflection was intended. Since each calculation of the series left off the reflector, all computer results were self-consistent. However, the reactivity was unknowingly far too low; and since similar calculations or experimental results were unavailable for comparison, this error went undetected for a while. The input error would have been detected early if KENO-II had printed a diagnostic message telling the user that boundaries overlapped or if the picture routine had included the capability to show the reflector.

In a typical calculational study experimentally determined critical assemblies of similar design are unavailable. Therefore, it is difficult to determine if cross section sets and geometry approximations are giving satisfactory results. The user selects cross section sets for a KENO calculation according to the degree of moderation in the system. This requires a determination of the total scattering cross section per absorber atom and a selection of cross sections accordingly. If the degree of moderation is changed, a new set of cross sections must be selected. It would be highly desirable from the user point of view if KENO were modified to optionally select the cross section sets to be used.

Monte Carlo techniques have an inherent statistical uncertainty. This makes it difficult to plot curves for a determination of nominal or maximum k_{eff} values. It is necessary to track sufficient neutrons to have confidence that the error values given by KENO are themselves valid. A feature of KENO-IV which plots the accumulated average k_{eff} at each neutron generation may improve this limitation.

Improvement of the Geometry Routines

KENO, until recently, has contained a more restricted geometry package than MONK. A severe limitation has been the lack of ability to specify an array within an array. In addition, MONK has included the use of "hole" routines which expands the range of geometries available. At HEDL fuel bundles usually have a hexagonal lattice arrangement of fuel pins. MONK is able to treat this geometry, whereas KENO will not.

Fortunately, a new version of KENO-IV is now available which greatly expands the geometry package. Now KENO and MONK geometry capabilities are more nearly comparable. The usefulness of a Monte Carlo code depends very much upon the ease of inputing complex geometries.

Criticality Safety Application With KENO

Problem number 13 of Figure 8 is a pertinent example[16] of a criticality safety calculation. The geometry model for KENO, shown in Figures 9a and 9b, is for the Fuel Storage Facility of the FFTF. The model of the geometry utilizes a rectangular array to approximate annular storage rings of fuel assemblies. Since the reactivities of individual fuel assemblies vary, a check was made to determine the "worst case" configuration giving the greatest k_{eff}. The most reactive arrangement occurs when the outer driver assemblies are clustered together as shown in Figure 9a. To simplify input data requirements, the half-space model of Figure 9a incorporates a perfect mirror reflecting boundary condition at the lower surface.

	PROBLEM DESCRIPTION	PERTINENT FIGURE NUMBER	SATISFACTION FACTOR	MINUTES OF CDC-7600 EXECUTION TIME
13.	CRITICALITY SAFETY CALCULATIONS FOR FUEL STORAGE FACILITY	9a,9b	72 (80 90 90 80)	10
14.	CALCULATION OF STREAMING WITHIN IN-REACTOR THIMBLE	10a,10b	20 (70 60 70 30)	30
15.	CALCULATION OF NEUTRON FLUX AT LOW LEVEL FLUX MONITORS	11a,11b	37 (70 70 70 40)	60
16.	RESPONSE OF EX-VESSEL FLUX MONITORS	12a,12b	85 (100 90 90 90)	15
17.	GAMMA STREAMING THROUGH GAP AT WINDOW OF IEM CELL	13	50 (70 80 90 50)	10
18.	GAMMA STREAMING THROUGH DUCT BETWEEN IEM AND TACS CELLS	14	72 (80 90 90 80)	10

HEDL 8003-320.11

Fig. 8. Monte Carlo calculations for the Fast Flux Test Facility.

13	13	13	13	13	13	13	13	13	12	12	12	12	12	12	12	12	13	13	13	13	13	13	13	13	13
13	13	13	13	13	13	12	12	12	3	3	3	3	2	2	2	2	12	12	12	13	13	13	13	13	13
13	13	13	13	12	12	3	3	3	3	3	3	2	2	2	2	2	2	2	2	12	12	13	13	13	13
13	13	13	12	3	3	3	3	3	3	3	2	2	2	2	2	2	2	2	2	2	2	12	13	13	13
13	13	12	1	3	3	3	3	3	3	3	2	2	2	4	4	4	4	4	4	4	4	4	12	13	13
13	13	12	1	3	3	3	3	3	3	2	2	2	4	4	4	4	4	4	4	4	4	4	12	13	13
13	12	1	1	3	3	3	3	3	3	2	2	2	4	4	4	4	4	4	4	4	4	4	4	12	13
13	12	1	1	3	3	3	3	3	2	2	2	2	4	4	4	4	4	4	4	4	4	4	4	12	13
13	12	1	1	3	3	3	3	3	2	2	2	2	4	4	4	4	4	4	4	4	4	4	4	12	13
12	1	1	1	1	3	3	3	3	2	2	2	2	4	4	4	4	4	4	4	4	4	4	4	4	12
12	1	1	1	1	1	3	3	3	2	2	2	2	4	4	4	4	4	4	4	4	4	4	4	4	12
12	1	1	1	1	1	1	3	3	3	3	7	8	9	10	4	4	4	4	4	4	4	4	4	4	12
12	1	1	1	1	1	1	1	3	3	3	6	5	5	11	4	4	4	4	4	4	4	4	4	4	12

Numbering Legend

1. Core 1/2 Inner Driver Fuel Assembly
2. Core 1/2 Outer Driver Fuel Assembly
3 Core 3/4 Inner Driver Fuel Assembly
4. Core 3/4 Outer Driver Fuel Assembly
5. Na
6. B_4C/Na
7 B_4C/Na
8. B_4C/Na
9. B_4C/Na
10. B_4C/Na
11. B_4C/Na
12. C-Steel/Na
13. Nitrogen

Fig. 9a. Model of array for Fuel Storage Facility of FFTF.

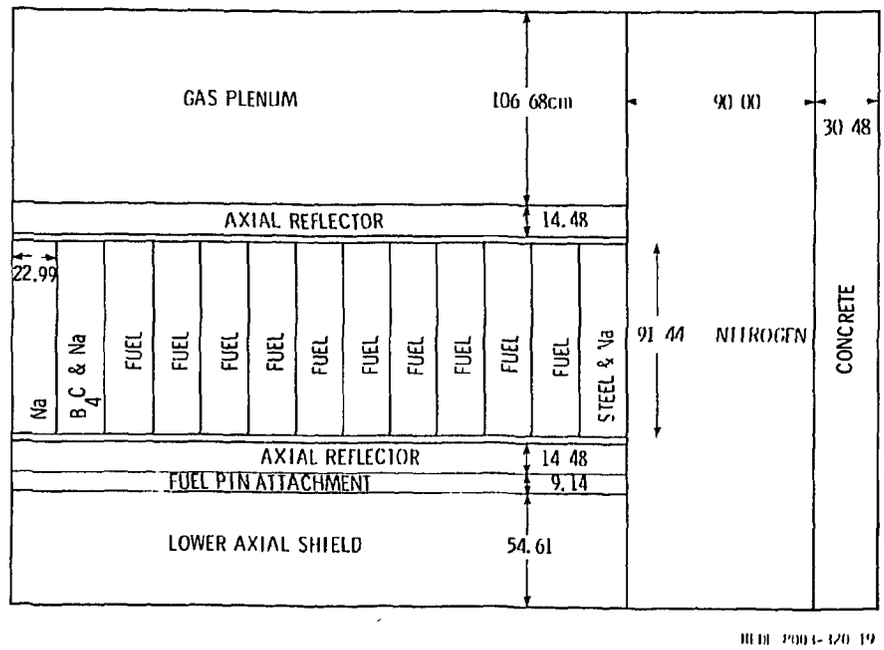

Fig. 9b. Axial distribution of materials for Fuel Storage Facility of FFTF.

General Purpose Applications With MCNP

Measurements within the In-Reactor Thimble Assembly, located near the center of the FFTF core, are being made to characterize the neutron and gamma-ray spectrum within the clean core during initial startup of the reactor. Basically the In-Reactor Thimble Assembly consists of several concentric tubes to circulate cooling gas (nitrogen) and provide insulation for the inner zone where the measurements are made. Instruments are placed inside the inner tube with streaming plugs above and below the detectors.

Monte Carlo calculations (problem number 14 of Figure 8 with geometry shown in Figures 10a and 10b) of neutron and photon fluxes within the In-Reactor Thimble Assembly are summarized in Reference 17. The concern is that neutron streaming within the In-Reactor Thimble Assembly may

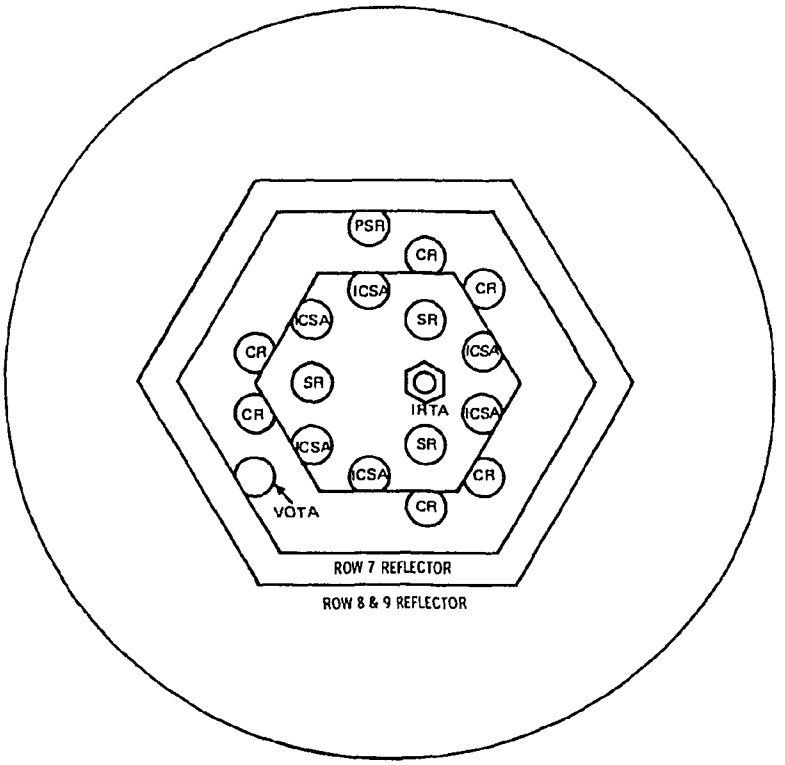

HEDL 8003-320.1

Fig. 10a. Radial view of geometry model for Monte Carlo calculations of flux within In-Reactor Thimble Assembly (IRTA) of FFTF. (See Figure 11b for general configuration axially.)

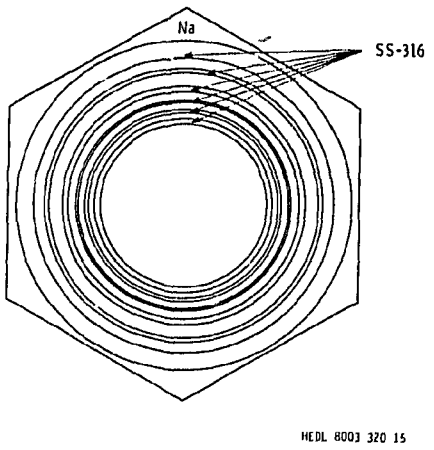

Fig. 10b. Radial view of In-Reactor Thimble Assembly.

require corrections to reaction rates calculated with diffusion theory. This Monte Carlo calculation is pushing the state-of-the-art for the following reasons:

- A typical neutron suffers a large number (>50) collisions before absorption so that the computation time required to analyze a source neutron is large compared to more ideal material configurations with the property of few collisions per source neutron.
- Even with considerable homogenization, the geometry is still complex.
- The flux within a small volume is needed. This led us to use a point detector estimator in spite of the associated costs involved in computing mean free paths from collision points to detector.
- The eigen function at steady-state should be determined in the Monte Carlo calculation. This was deemed impractical so the fission source distribution from a diffusion theory calculation was used.

Because of the above difficulties, the satisfaction factor shown in Figure 8 is only 20. Some useful information was obtained by using a lower energy cutoff of 0.5 MeV to obtain the responses of the higher energy threshold reactions of interest. These results indicate that streaming is important for locations within the In-Reactor Thimble above and below the core, but that the measurements at mid-core should be only slightly perturbed by streaming within the In-Reactor Thimble.

Similar calculational difficulties were experienced in the determination of the neutron flux at the Low Level Flux Monitors (LLFM)[18] (see Figures 11a and 11b). Some of the difficulties in problem number 15 of Figure 8 were due to an inadequate specification of the geometry, for

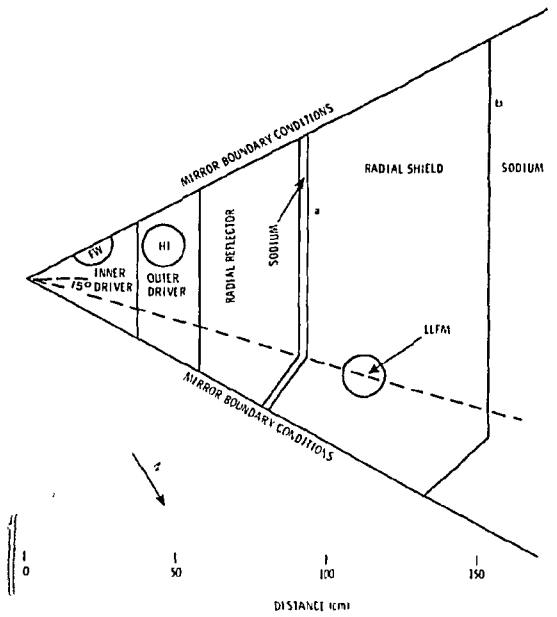

Fig. 11a. Radial view of geometry model at core midplane for Low Level Flux Monitor calculation.

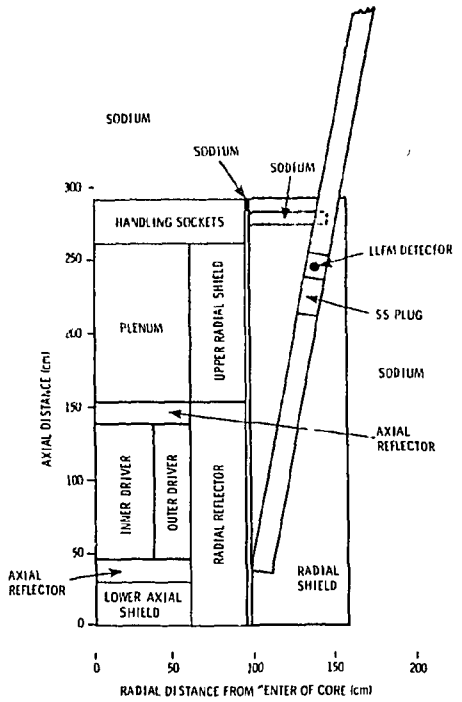

Fig. 11b. Axial view of geometry through Low Level Flux Monitor.

the optimization of importance biasing, because of manpower time constraints. The geometry package in the current version of MCNP (version 1B was used for the calculations) would help alleviate the difficulties.

In contrast to problems 14 and 15, we give the calculation of the response of the ex-vessel flux monitors (problem 16 of Figure 8) a high satisfaction factor. Neutrons were transported from a specified source incident upon a graphite block to detectors located within the block as shown in Figures 12a and 12b. The calculations increased our understanding of the detector responses and will provide input for future improvements in the design of the detectors. The capability to automatically include the three-dimensional aspects of the geometry was a definite advantage over a one- or two-dimensional treatment.

Gamma streaming problems (problems 17 and 18 of Figure 8) are shown in Figures 13 and 14. These are typical streaming problems in the sense that one is interested in the rare particles that penetrate through the shield while spending some of their time within the gaps. Such calculations usually require extensive source biasing along with an overspecification of the geometry for the near-optimal use of cell importances. A useful calculation typically requires familiarity with biasing schemes

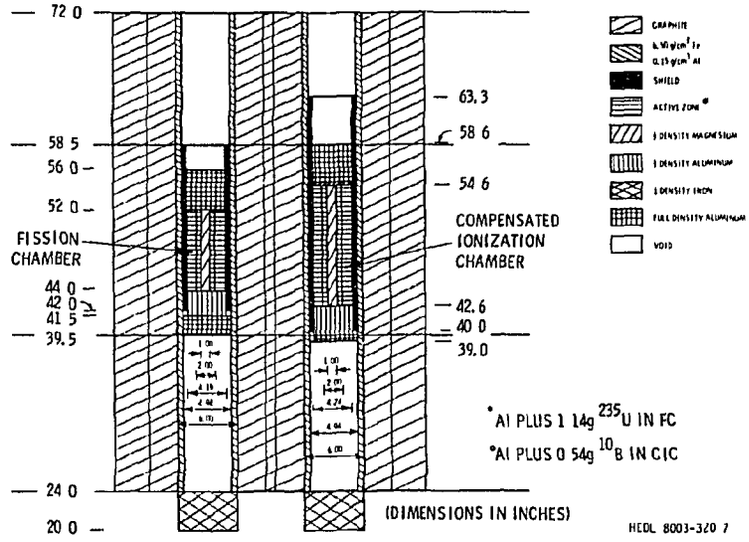

Fig. 12a. Vertical view through Ex-Vessel Flux Monitor Detectors in FFTF.

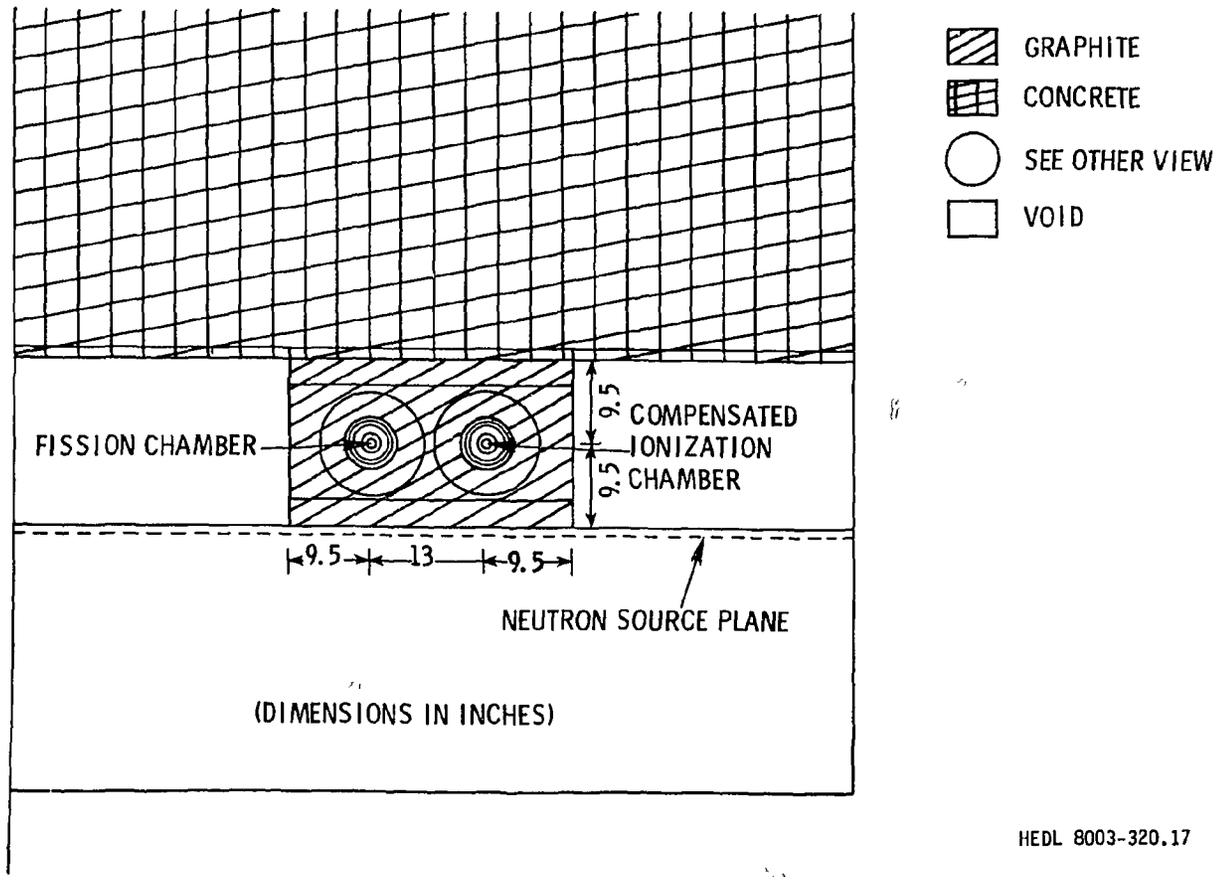

Fig. 12b. Plan view through Ex-Vessel Flux Monitor Detectors of FFTF.

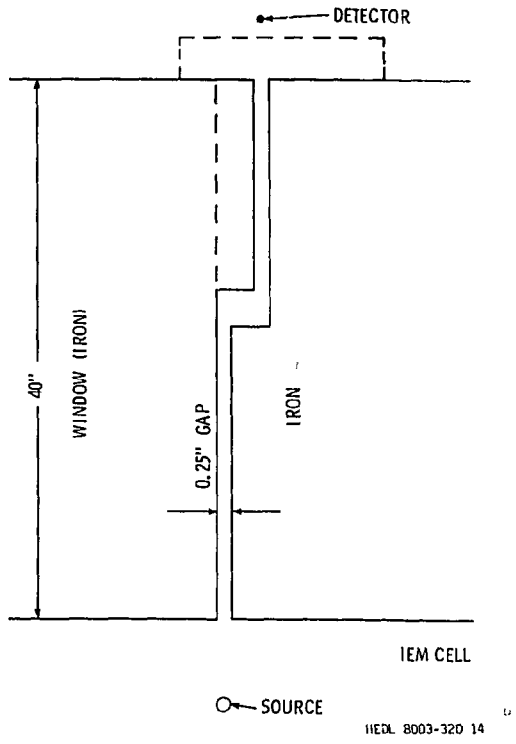

Fig. 13. Calculation of gamma streaming through gap between window and support wall adjacent to Interim Examination and Maintenance (IEM) cell of FFTF.

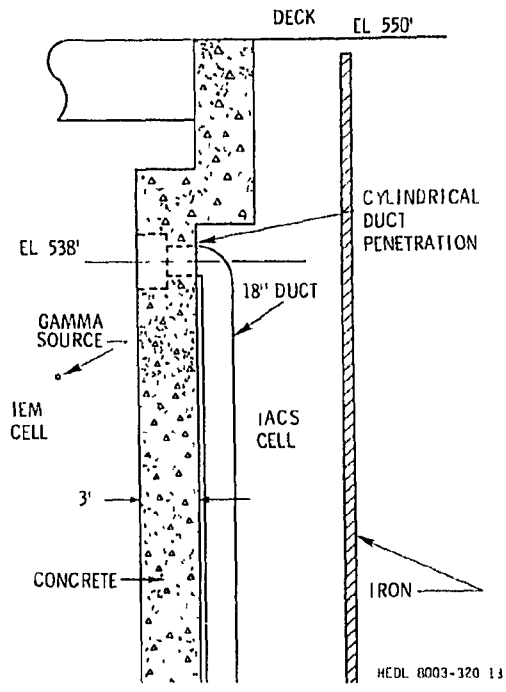

Fig. 14. Elevation view of Test Assembly Conditioning Station (TACS) and Interim Examination and Maintenance (IEM) cells of FFTF.

and good intuition about the transport process. The satisfaction factor for such problems tends to be low, but other calculational approaches are even less attractive to use than Monte Carlo.

MISCELLANEOUS APPLICATIONS

Problem 19 of Figure 15 is representative of those frequent problems the engineer encounters requiring quick answers to a rather difficult three-dimensional transport problem with minimal budget allocation. This problem arose because of a decision to build a new Patrol Headquarters building in the 300 Area at Hanford. The basement of this building was to meet specified dose criteria for guideline criticality accidents in adjacent buildings. The air-over-ground problem was modeled as two-dimensional with cylindrical symmetry about the source as shown in Figure 16. Neutron and gamma dose rates in the basement were determined in a timely manner for various concrete thicknesses of the main floor so that the appropriate thickness could be specified for construction of the building.

	PROBLEM DESCRIPTION	PERTINENT FIGURE NUMBER	SATISFACTION FACTOR	MINUTES OF CDC-7600 EXECUTION TIME
19.	DOSE WITHIN BASEMENT OF PATROL HEADQUARTERS DUE TO ABOVE-GROUND CRITICALITY ACCIDENT (NEUTRON AND GAMMA)	16	76 (80 100 90 80)	10
20.	BENCHMARK OF NEUTRON TRANSPORT THROUGH IRON	17	85 (100 100 90 80)	120

Fig. 15. Miscellaneous Monte Carlo calculations.

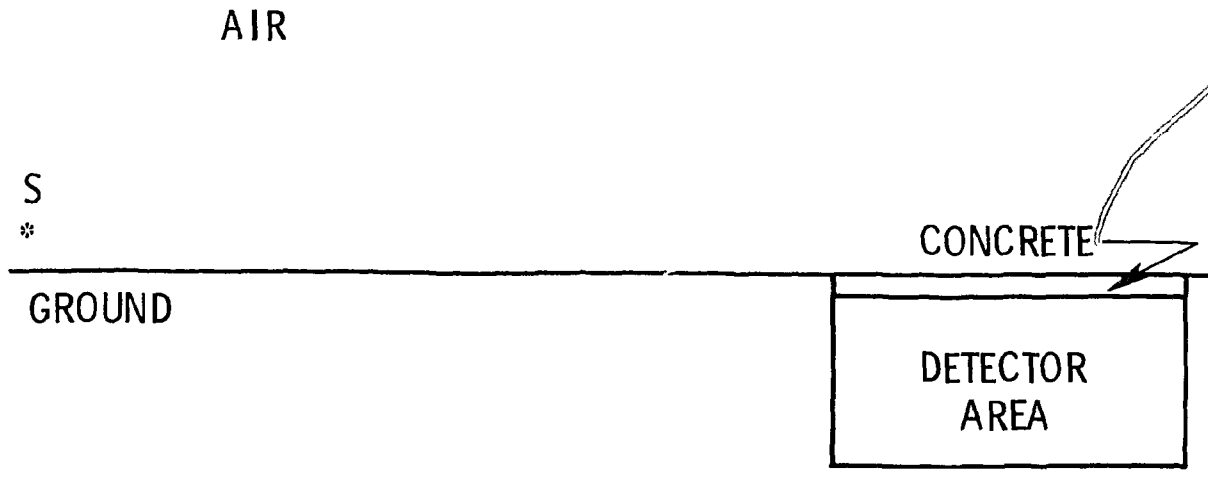

Fig. 16. Dose rate in basement of Patrol Headquarters building due to above-ground criticality accident.

Neutron transport through shield materials containing iron has been important since the early days of reactor physics. Applications in recent years have included fast reactors, fusion reactor concepts, and accelerators for fusion reactor material studies[4] and cancer therapy. Considerable complexity is introduced into transport calculations by the resonance structure of iron between 20 keV and ∿2 MeV. Multigroup constants, generated with an infinite media spectra as a weighting function, tend to overpredict the leakage through shields in discrete ordinates calculations. Improvements in accuracy are obtained by

correcting the weighting function in the vicinity of cross-section minima to account for preferential leakage.[19] These complex energy and space-dependent self-shielding problems inherent in thick iron shields dictate the need for a shielding benchmark problem to serve as a standard reference.

Unfortunately, experimental benchmark measurements are often difficult to model because of complicated neutron source and detector characteristics. We have defined a calculational benchmark which is simple to model with most standard transport codes. This benchmark features a simple geometry, a choice of monoenergetic sources, and a straightforward tabulation of fluxes and radiation doses at various iron thicknesses. The Monte Carlo calculation accurately models the fine energy structure of the ENDF/B data base and has been validated by comparisons with two experimental benchmark measurements: the ORNL iron benchmark[20] and the LLL pulsed sphere.[21]

Calculations were made with both ENDF/B-IV- and ENDF/B-V-based cross sections. The principal advantage of MCNP for this type of problem is that no gross approximations (such as the multigroup approximation) are required for the cross-section treatment. All the reactions described in ENDF/B are accounted for in MCNP. In fact, the only significant difference between the cross-section data in the MCNP library and the ENDF/B library from which it is derived (via the NJOY[22] code processing system) is that resonance data are represented in MCNP as linearly interpolated pointwise data, Doppler broadened to a specific temperature. The energy grid for this pointwise data is chosen so that the relative error between the MCNP and ENDF/B representations is less than a user-specified error criterion, usually <3%.

The calculational benchmark[6,7] shown in Figure 17 is simply a pure iron 7.86 g/cm^3 slab 3m thick and infinite in the other two dimensions.

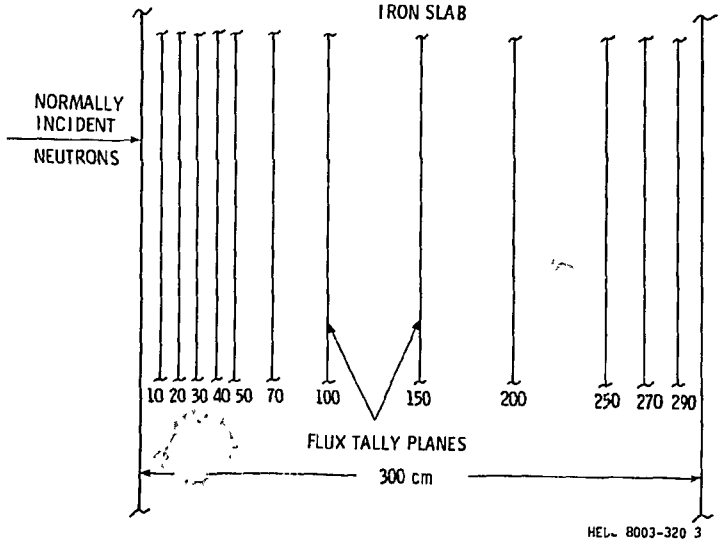

Fig. 17. Geometry for benchmark calculation.

Monoenergetic neutrons are normally incident (1 neutron/cm^2) upon the slab; and the energy-dependent neutron flux, current, and radiation dose are computed at various distances through the slab. These output quantities[7] are tabulated in a standard group structure[11] consisting of 47 energy groups between 0 and 60 MeV. The 35 groups below 17 MeV are a subset of a standard 171-group fusion library.[23] Benchmark calculations were made with source energies of 2, 14, and 40 MeV. These energies were chosen for applicability to fission systems, fusion systems, and accelerators with a neutron energy regime somewhat above 14 MeV.

SUMMARY

Twenty applications of neutron and photon transport with Monte Carlo have been described to give an overview of the current effort at HEDL. A satisfaction factor was defined which quantitatively assigns an overall return for each calculation relative to the investment in machine time and expenditure of manpower. We frequently encounter low satisfaction factors in day-to-day calculations. Usually this is due to limitations in execution rates of present day computers, but sometimes a low satisfaction factor is due to computer code limitations, calendar time constraints, or inadequacy of the nuclear data base.

Present day computer codes have taken some of the burden off of the user. Nevertheless, it is highly desirable for the engineer using the computer code to have an understanding of particle transport including some intuition for the problems being solved, to understand the construction of sources for the random walk, to understand the interpretation of tallies made by the code, and to have a basic understanding of elementary biasing techniques.

REFERENCES

1. L. M. Petrie and N. F. Cross, KENO-IV, An Improved Monte Carlo Criticality Program, ORNL-4938, Oak Ridge National Laboratory, Oak Ridge, TN (1975).

2. LASL Group X-6, MCNP - A General Monte Carlo Code for Neutron and Photon Transport, LA-7396-M, Los Alamos Scientific Laboratory, Los Alamos, NM (revised November 1979).

3. L. L. Carter and E. D. Cashwell, "Particle Transport Simulation With The Monte Carlo Method", TID-26607, ERDA Critical Review Series, U. S. Energy Research and Development Administration, Technical Information Center, Oak Ridge, TN (1975).

4. E. W. Pottmeyer, Jr., "The Fusion Materials Irradiation Test Facility at Hanford", Journal of Nuclear Materials, 85 & 86, 463-465 (1979).

5. L. L. Carter and R. J. Morford, "Nuclear Data Relevant to Shield Design of FMIT Facility", (HEDL-SA-2146), to be published in Proceedings for the Symposium on Neutron Cross Sections from 10-50 MeV, Brookhaven National Laboratory, May 12-14, 1980.

6. L. L. Carter and J. S. Hendricks, "Computational Benchmark for Deep Penetration in Iron", Trans. Am. Nucl. Soc., 33, 663 (1979).

7. J. S. Hendricks and L. L. Carter, Computational Benchmark Problem for Deep Penetration in Iron, LA-8193-MS, Los Alamos Scientific Laboratory, Los Alamos, NM (1980). (Manuscript also submitted to Nuclear Science and Engineering for publication.)

8. D. L. Johnson, F. M. Mann, J. W. Watson, J. Ullman, and W. G. Wyckoff, "Measurements and Calculations of Neutron Spectra from 35 MeV Deuterons on Thick Lithium for the FMIT Facility", Journal of Nuclear Materials, 85 & 86 (1979).

9. L. L. Carter and R. J. Morford, "Shielding Calculations for the Fusion Materials Irradiation Test Facility", Trans. Am. Nucl. Soc., 30, 618 (1978).

10. R. W. Roussin, R. G. Alsmiller, Jr., and J. Barish, "Calculations of the Transport of Neutrons and Secondary Gamma Rays Through Concrete for Incident Neutrons in the Energy Range 15 to 75 MeV", Nuclear Engineering and Design, 25, 250 (1973).

11. R. G. Alsmiller, Jr. and J. Barish, "Neutron-Photon Multigroup Cross Sections for Neutron Energies <60 MeV", Nuclear Science and Engineering, 69, 378-388 (1979).

12. R. E. MacFarlane, "Energy Balances of ENDF/B-V", Trans. Am. Nucl. Soc., 33, 681 (1979).

13. E. D. Arthur and P. G. Young, "Evaluation of Neutron Cross Sections to 40 MeV for ^{54,56}Fe", to be published in Proceedings for the Symposium on Neutron Cross Sections from 10-50 MeV, Brookhaven National Laboratory, May 12-14, 1980.

14. R. J. Morford, Neutron Pinhole Radiography for the Fusion Materials Irradiation Test Facility, HEDL-SA-1758, Third International Dosimetry Conference in Ispra, Italy (October 1979).

15. L. L. Carter, Neutron Environment in the Fusion Materials Irradiation Test Facility, HEDL-SA-1757, Third International Dosimetry Conference in Ispra, Italy (October 1979).

16. R. J. Morford, "Fuel Storage Facility Criticality Analysis", Core Engineering Technical Progress Report - October, November, December 1977, HEDL-TME 77-49, Hanford Engineering Development Laboratory, Richland, WA (1978).

17. L. L. Carter, "Calculations of Nuclear Environment Within the IRT", Core Engineering Technical Progress Report - January, February, March 1979, HEDL-TME 79-44, Hanford Engineering Development Laboratory, Richland, WA (January 1980).

18. L. L. Carter, W. R. Sloan, and R. A. Harris, "Monte Carlo Calculations of the Response of the Low Level Flux Monitors in the Inserted and Fully-Withdrawn Positions", Core Engineering Technical Progress Report - October, November, December 1977, HEDL-TME 77-49, Hanford Engineering Development Laboratory, Richland, WA (1978).

19. R. E. MacFarlane and M. Becker, "Self-Shielding Cross Sections for Neutron Transport in Iron", Trans. Am. Nucl. Soc., 22, 668 (1975).

20. R. E. Maerker and F. J. Muckenthaler, Final Report on a Benchmark Experiment for Neutron Transport Through Iron and Stainless Steel, ORNL-4892, Oak Ridge National Laboratory, Oak Ridge, TN (April 1974).

21. C. Wong et al., Livermore Pulsed Sphere Program: Program Summary Through July 1971, UCRL-51144, Rev. 1 (February 10, 1972).

22. R. E. MacFarlane, R. J. Barrett, D. W. Muir, and R. M. Boicourt, The NJOY Nuclear Data Processing System: User's Manual, LA-7584-M, Los Alamos Scientific Laboratory, Los Alamos, NM (December 1978).

23. "VITAMIN-C, 171 Neutron, 36 Gamma-Ray Group Cross Sections in AMPX and CCCC Interface Formats for Fusion and LMFBR Neutronics", DLC-41, Radiation Shielding Information Center, Oak Ridge National Laboratory, Oak Ridge, TN (1977).

VIM - A CONTINUOUS ENERGY MONTE CARLO CODE AT ANL

R. N. Blomquist, R. M. Lell and E. M. Gelbard
Argonne National Laboratory
Argonne, Illinois, USA

ABSTRACT

The continuous energy Monte Carlo neutron transport code, VIM, and its auxiliaries, are briefly described. The ENDF/B cross section data processing procedure is summarized and its benchmarking agains MC^2-2 is reviewed. Several representative applications at ANL are described, including fast critical assembly benchmark calculations and STF and TREAT Upgrade benchmark calculations.

INTRODUCTION

The VIM code is a continuous energy Monte Carlo code designed primarily for fast reactor calculations, but also containing a thermal neutron scattering capability. The development of VIM and the associated fast reactor cross section processing codes was initiated at Atomics International[1] and has been continued at Argonne National Laboratory. VIM, now available through the National Energy Software Center, features a flexible geometrical capability, a neutron physics data base closely representing the ENDF/B data from which it has been derived, and a calculational output directed to the needs of the fast reactor analyst.

DESCRIPTION

The original VIM geometry package was designed to permit a simple description of plate-lattice critical experiments. All cells of identical characteristics, with plates, clad, and void defined by combination of rectangular parallelepipeds, need be specified only once; the full assembly is then described as a rectangular lattice constructed from the basic cells. The combinatorial geometry package developed for the code SAM-CE[2] has been implemented in VIM and extended to specific geometrical descriptions of particular interest in reactor analysis. The above two techniques have been combined in VIM to provide options for the description of repeating hexagonal and rectangular lattices with the in-cell geometrical definition employing the full combinatorial geometry capability. In addition, an infinite, homogeneous medium option is available to provide an efficient capability for data testing and cross section methods evaluation.

VIM produces three distinct estimates of the reactor eigenvalue. The analog, or last-event estimator scores $W(\nu\Sigma_f)^{isotope}/\Sigma_a^{total}$ whenever absorption by a fissile isotope occurs. Here, W is the neutron weight, and Σ is the macroscopic cross section. The collision estimator scores the fission production rate, $W(\nu\Sigma_f)^{total}/\Sigma_{tot}^{total}$, at each collision event. The track (or path) length estimator scores $W(\nu\Sigma_f^{tot})/\Sigma_a^{total}$ times

the track length for all tracks within each zone, including uncolliding tracks. The estimates of standard deviation in the eigenvalue estimates are obtained using the assumption (never strictly correct in an eigenvalue computation) that the contributions from all the history batches are statistically independent.[3]

VIM produces a statistical edit of various quantities after a user-specified number of batches. Both collision and track length estimation provide groupwise reaction rate estimates by region and by isotope, while track length estimation generates region-wise integrated group fluxes. Optionally, infinite dilution region-averaged microscopic reaction rate ratios may be obtained in a designated central region. Track length estimates of reaction rates and fluxes are used to provide estimates of broad-group microscopic and macroscopic cross sections over edit regions. All quantities are provided with standard deviation estimates which are based on the statistical independence of the batch data.

VIM may be used with a combination of several variance reduction techniques. Neutrons can be tracked by a combination of absorption and analog weighting which can be assigned by zone or by cell. For example one might use analog weighting in the core region for an eigenvalue calculation and absorption weighting in a blanket region to improve the statistics of low-energy effects. The user can select a cutoff energy below which all weighting is analog to reduce the effort spent on unimportant neutrons. Splitting and Russian roulette can be used to spatially modify the sample distribution, improving local statistics. Combined estimators[4] produce averages of the eigenvalue estimates in linear combinations determined by the statistical characteristics of the data, using the assumption of normality of the batch results. This is most effective as a variance reduction technique when two estimators are strongly negatively correlated. Simple averages of the estimates are also provided, with the estimated standard deviations including the effects of correlation between the estimates.

In addition to a startup source guess and a restart capability a number of initialization options are available. The user may provide a set of source sites from a similar previous calculation to avoid wasting the first several batches converging on a source shape. One can specify a fixed source of arbitrary spatial, angular and energy distributions by supplying a fixed source subroutine within the framework provided by VIM.

The physics data base for the VIM code consists of a library of binary files, with each file providing the physics data for one material. Each such "VIM material file" is the end product of a moderately complex computational path beginning with ENDF/B tape files. At each intermediate step, a code is used to process one or more intermediate data libraries and produce an output library of data available to a succeeding step. A flowchart of the generation system is shown in Fig. 1.

The initial step of cross section processing is the program VIMB, which reformats and reorders ENDF/B data and generates the energy grid. VIMB calculates the potential scattering cross section, threshold energies

for inelastic levels, and normalized cumulative secondary energy distributions for (n,2n), fission, and inelastic continuum scattering. A grid of energies for unresolved resonance parameters is generated if they are energy-dependent in ENDF/B, and the elastic scattering cross section energy grid is tightened to permit linear-linear interpolation meeting a user input accuracy criterion. A common energy grid is then constructed by merging the energy points for all reactions and inserting a background grid of 20 points per decade. VIMB also interpolates File 3 cross sections to the expanded energy grid and processes the anisotropic angular distribution data for elastic, (n,2n), and inelastic levels by (a) calculating a 200 point angular table at each energy from Legendre coefficients, (b) calculating a 200 point angular distribution from a tabulation by a cubic spline fit to the logarithm of the differential cross section vs. cosine of the angle, (c) calculating normalized cumulative distributions from the 200 point tables and collapsing to 20 equal-cosine intervals.

The UNIDOP code produces point cross section data in the resolved resonance region from S-wave and P-wave resonance parameters from VIMB output. For each isotope, an energy mesh is obtained by merging a 99-point distribution around each resonance energy with a background grid at equal lethargy intervals of at least 40 points per decade. Zero degree Kelvin resonance calculations are performed using either single-level or multi-level Breit-Wigner representations over the energy grid, and the point data are Doppler broadened to the first specified temperature (presumably 300 degrees K). Any File 3 background are added in, and the resulting data are then Doppler broadened to as many as four other user-specified temperatures. The cross section arrays are then thinned according to user specified accuracy of either interpolation accuracy on total cross section alone, absorption cross section alone, or total and absorption cross sections simultaneously. Resonance integrals are calculated before and after Doppler broadening, after any File 3 background are added in, and before and after thinning.

The AUROX code generates unresolved resonance data for single isotopes obtained from a VIMB output file into cross section probability tables using Monte Carlo methods. For each spin series of resonances, the Wigner distribution for resonance spacings is sampled independently to obtain a ladder of resonances, and the appropriate chi-square distributions are sampled for resonance width parameters. Pointwise cross sections for scattering, capture, and fission are then constructed on an arbitrary energy scale using energy dependent factors evaluated at the ENDF/B specified energy point with Doppler broadening to the desired temperatures. The average values of the cross sections between any two energy points on the grid are then binned by total cross section value with weight equal to the energy interval. Additional ladders are generated and the cross sections binned until either a user-specified number of ladders has been processed or until the standard deviation in the observed infinitely dilute average cross sections satisfies a user input criterion. The average cross section value in each bin is then calculated, the cumulative probability for sampling from a bin is obtained from the binned weights, and the resulting tables are normalized to the known infinite dilute average cross sections by applying an addi-

tive constant to each bin of a given reaction type, preserving the observed higher moments. The process is repeated for all the ENDF/B energy points on the VIMB output data set or for as many as have been specified by card input.

The REDUCE code processes cross section probability tables with a large number of probability bands into a library of tables with a small number of bands. Conventionally, an AUROX output data set with 99 point tables is processed to an output data set with 20 point tables. At user option, the probability bands are combined either by minimizing the absolute difference between input and output total cross sections for high atom densities or the mean square difference for very dilute concentrations. In addition, REDUCE calculates average self-shielded cross sections for an array of user-supplied values for additional equivalent potential scattering in barns/atom (the potential scattering for the material being processed is included in the probability table scattering cross section). REDUCE may be used solely to calculate effective cross sections from the original tables to be compared with reduced tables to examine the effect of the reducing algorithms and to compare with analytical calculations.

Since AUROX cannot process unresolved resonance data for a natural material which is a mix of isotopes, the probability tables must be generated for each isotope separately. MERGER is then used to prepare a single set of "material" tables from the isotopic tables and the corresponding isotopic abundances. In Fig. 1, MERGER would replace, precede, and/or follow REDUCE.

MERGER uses the principle that the unresolved resonances from different isotopes are uncorrelated. Consequently, the joint probability distribution for the cross sections of two isotopes is the product of the two individual distributions. In forming the joint distribution from tables of length N1 and N2, a distribution of length N1*N2 is formed. For each such probability interval, the combined cross section values are obtained from the weighted sums of the corresponding individual values, the weighting factors being the isotopic abundances. The resulting arrays are sorted in order of increasing combined total cross section and the cumulative probability distribution obtained. The algorithms of the REDUCE code are then used to reduce the N1*N2 band tables to the desired output table length. MERGER will not process multitemperature correlated tables, but tables at different temperatures may be processed independently.[5]

The code VIMTAP produces a VIM material file for free atoms by combining the output data sets of the VIMB, UNIDOP, and AUROX (or REDUCE or MERGER) codes. VIMTAP replaces the VIMB data in the resonance range with the UNIDOP and AUROX data, and finds threshold energies and indices for total inelastic scatter and fission cross sections. The angular data may be thinned, and the elastic scattering cross section is corrected at very low energies to account for thermal motion by using a free gas model. Angular distributions for (n,2n) and the inelastic continuum are not retained, and only one interpolation code is allowed per reaction type.

Only two subsections are allowed in the secondary energy distributions; if more are present, only the first two are retained. In addition, the number of probability tables for any one material is limited to 140.

For those materials with thermal scattering law data specified in File 7 of an ENDF/B thermal tape, the procedure becomes more complex. The File 7 data are processed by the FLANGEX code into a library of discrete-energy double-P1 $S(\alpha,\beta)$ scattering kernels and thermal inelastic scattering cross sections. The KERINTX code subsequently processes these into a library of thermal scattering probability tables and thermal inelastic cross sections. If the thermal scatterer is a solid, VIMB extracts the elastic scattering cross section and angular distributions in the thermal energy range from the ENDF/B thermal tape. For each such thermal scatterer, the corresponding free atom VIM material file is input to THTAPE, along with the KERINTX output library and, if required, the VIMB thermal data, to produce a VIM material file incorporating a full thermal treatment.

VIM itself employs several models to treat scattering phenomena relevant to thermal problems. For incident energies above 10eV, a full kinematic treatment of non-thermal free atom inelastic or elastic scattering is applied which ignores thermal motion of target atoms heavier than $^{1}_{1}H$. Below 10eV but above a user-supplied maximum thermal energy cutoff, scattering is treated as either scattering by a free gas or as isotropic center-of-mass non-moderating scattering, depending on the target mass. For solid materials, both thermal elastic and inelastic scattering is modeled, while for liquids, only thermal inelastic scattering is incorporated.

One present limitation of the VIM library generation system, and consequently of VIM itself, is the inability to treat all the possible inelastic processes described in the ENDF/B data. At the present time, elastic scattering (MT=2), (n, 2n) reaction (MT=16 only, or MT=24 in the absence of MT=16), fission (MT=18), discrete level inelastic scattering (MT=51 through MT=90), inelastic continuum scattering (MT=91), and "capture" (the sum of MT=102 through MT=114) are incorporated. The total cross section is then defined to be the sum of the cross sections for these reaction types.

The VIMB, UNIDOP, and VIMTAP codes in use at ANL are modifications of similarly-named codes developed by Atomics International.[6] The code AUROX was derived from the AI code U3R[7] after extensive development and modification. The bulk of the development and testing of cross section preparation methods for VIM which has been done at ANL has been directed toward the treatment of resolved and unresolved resonance data. The FLANGEX and KERINTX codes were developed from the FLANGE and KERINT codes of Honeck and Finch at Savannah River.[8]

Figure 2 illustrates the data flow for codes which access the library of VIM material files. The codes FILEONE, XSEDIT, and BANDIT are not really a part of the library generation system, but rather are

utility codes for VIM and are part of the VIM export package. The code XSEDIT provides a binary-to-BCD and BCD-to-binary conversion capability for the VIM data base to permit export of the VIM code to non-IBM installations without the library processing capability. It may also be used to produce an edited listing of library contents. The code FILEONE is used to scan the library of material files and prepare a data file containing variable dimensioning information. The code BANDIT partitions the data from up to 20 VIM material files into as many as 16 energy bands and produces corresponding cross section data subsets requiring about equal and minimum amounts of computer storage to be used during VIM calculations.

Two auxiliary codes provide the user with the capability to modify the structure of the output data and to reanalyze it. KEFCODE permits the user to obtain a statistical edit of the VIM eigenvalue estimators for a subset of neutron batches completed by VIM. For example, one might wish to ignore the first several batches representing the unconverged source, or to lump the batches into larger ones. Using RETALLY, the user can perform group collapse, region homogenization, skip early batches and process only some of the records, and produce a new modified edit of the VIM batch data.

QUALIFICATION OF VIM

VIM was brought to Argonne primarily as a tool for fast critical assembly experimental analysis and for analytical methods benchmarking, so the code has been thoroughly benchmarked on fast reactor problems. Since the criticals program has included the assessment of nuclear cross section data and processing methods, much of the validation of VIM has focused on this area.

Prael and Henryson[9,10] tested VIM's cross section data preparation and its solution of the slowing-down problem by comparison with the MC^2-2 code, which was tested at the same time. MC^2-2 solves the fundamental mode neutron slowing-down equations with high accuracy using multigroup, continuous slowing-down, and integral transport theory algorithms. Since both MC^2-2 and VIM were designed to model the slowing-down process in great detail, and since the methods of each are distinct, such comparison provides confidence in the accuracy of both codes. In MC^2-2, the resonance calculations used an ultrafine group structure ($\Delta u = 0.008$), except below 4 keV where a hyperfine structure ($\Delta u \sim 0.001$) was applied to the resolved resonance region.

To test the cross section preparation algorithms, several infinitely dilute, zero-dimensional slowing down problems were solved[9] using ENDF/B-III data. Comparison of the resolved resonance broad-group cross sections revealed several large, local discrepancies. The first resulted from insufficient energy point densities away from resonance peaks due to the application of a linear-linear interpolation scheme to data spaced for log-linear interpolation. The second discrepancy arose from incomplete summing of resonance contributions. The third difficulty was due to distortion of absorption cross sections between well-separated resonances because the thinning criterion was applied only to the total cross section. This was solved by thinning out only those points at which both the absorption and total cross sections meet the thinning criterion.

After correcting these discrepancies, two test problems with 10 MeV source were run to produce broad-group edits for 27 groups of lethargy width 0.5. The problems solved were an infinite homogeneous medium of ^{23}Na with an infinitely dilute admixture of heavy isotopes, and an infinite homogeneous medium of ^{12}C with an infinitely dilute admixture of structural material. The capture and fission cross sections for ^{238}U and ^{239}Pu generally agreed to within a few tenths of a percent. However, resolved resonance capture in ^{238}U was still in error by almost 5% in certain groups due to the linear interpolation method; unresolved resonance cross sections required improved numerical normalization of the resonance probability tables; and ^{238}U and ^{239}Pu unresolved resonance cross sections were in error by as much as 2% because VIM uses a linear energy interpolation of probability tables. In addition, errors in capture in structural materials necessitated extending the energy grid farther from resonances, and the fluctuation of structural material cross sections required a denser energy grid in the keV range to overcome use of linear probability tables. These difficulties were also eliminated by adjusting the energy grid algorithms where appropriate.

Once agreement in cross section processing between VIM and MC^2-2 was achieved, both codes were tested on a typical homogeneous zero-dimensional fast reactor slowing down problem with a composition representative of the benchmark critical ZPR 6 Assembly 7. ENDF/B-III data were used, and 24 group edits of flux, fission spectrum, isotopic reaction rates, and isotopic microscopic cross sections, were produced for comparison. Extremely close eigenvalue agreement was obtained, and group fluxes agreed to within 1% down to the resonance range where differences of several percent were observed. Isotopic capture and fission rates and broad group cross sections were within 1% except for capture in ^{238}U and fission in ^{239}Pu, which was traced to VIM's use of linear interpolation between probability tables for unresolved resonance cross sections. Other broad-group cross sections agreed to within a few tenths of 1%, and within 1% in the resonance ranges.

As a result of these comparisons, there is confidence that the VIM cross section data are accurately represented in the material libraries, and that the physical slowing-down process is properly treated. VIM has subsequently been applied in the analysis of a number of fast reactor critical experiments, providing the most stringent tests of VIM's ability to analyze actual reactor cores. Both basic integral parameters e.g., multiplication eigenvalue, and detailed information specifically relevant to the critical assemblies under study[11] have been used to compare VIM with physical systems.

REPRESENTATIVE APPLICATIONS

At ANL, VIM is applied to diverse sets of problems. Although it is not possible to include here detailed discussions of each such set, in this section we will briefly describe some of the more common applications.

The level of agreement attained in the comparisons of VIM with fast reactor cross section processing codes and the experience gained in using VIM for the analysis of criticals has led to a widespread use of VIM as the benchmark for fast reactor cross section processing methods and as an analysis tool for numerous aspects of critical experiments. The continuous energy cross section treatment and the essentially exact geometrical modelling used in VIM permit the analyst to focus on the source of errors in deterministic calculations, e.g., deterministic eigenvalue calculations for critical systems which are typically in error by approximately 1.5% with the ENDF-B/IV data base. Eigenvalue and integral reaction rate comparisons with experiment and with other calculations have improved the quality of experiment analysis. Specifically, most of the eigenvalue errors have been traced to the ENDF data, and the effects of multigroup cross section processing on experiment analysis have been quantified, within limits.

For the analysis of most criticals, the need for VIM extends considerably beyond testing the effects of cross section treatment. The representation of fine structural details is often very important in the analysis. For example, if one has a detector or foil located in the core, the structure near this detector or foil can affect the number of counts obtained. An accurate calculation for such a treatment requires a flexible geometry package beyond the scope of most deterministic codes. The breeding ratio measurement of ZPPR-4 is an example of the need for such detailed analysis.

Certain classes of criticals have geometries that are so complex or irregular that analysis by deterministic codes requires extensive geometric approximations. A recent series of safety-related criticals involved the study of damaged cores, including mockups with slumped fuel, large cavities, and other severe geometric distortions. Such abnormal configurations severely strain the usual xy, xyz, rθ, rθz, and triangular geometric representations in most diffusion and S_N codes. These models must therefore verified by accurate reference calculations using the exact geometric representation available in VIM. Even when core geometries are regular in other respects, certain aspects of the experiment may require the VIM capabilities, at least for benchmark calculations. Some criticals, e.g., those related to GCFR studies, are notable for large neutron leakage and streaming effects. Diffusion codes require special treatments, e.g., anisotropic diffusion coefficients[12] to account for such effects, and special treatment of unit cell streaming paths, while S_N codes may require high angular resolution for accurate modelling of axial leakage. VIM provides a reliable treatment of neutron streaming and leakage, whether in small regular channels or in large irregular cavities.

Because of the relatively recent incorporation of a thermal scattering law treatment in VIM[13], benchmarking of the thermal cross section library in VIM is much less extensive than that for the fast energy range. Nevertheless, such benchmarking has been done for materials of particular interest to individual programs and users, e.g., graphite for the SAREF program and light water reactor materials for various thermal reactor programs at Argonne. As in the case of fast reactor cross section

studies, the agreement found between VIM, other thermal reactor codes, and experiments, is such that VIM has come to be accepted by many users as a standard for comparison with other thermal reactor cross section preparation codes.

Several groups in the Applied Physics Division at ANL use VIM to benchmark cross section methods used in thermal reactor analysis. For most of these applications, corresponding unit cells are calculated with VIM and with the thermal reactor code of interest, e.g., EPRI-CELL. The analyst then compares integral parameters such as k and regional reaction rates, and microscopic quantities such as individual isotopic cross sections with corresponding quantities produced by the deterministic code of interest. The results of this comparison allow the user to identify possible problems in a multigroup cross section set and to attach a level of reliability to the multigroup cross section set. More elaborate types of comparisons are occasionally carried out. For example, one analyst desired to use EPRI-CELL for the analysis of a rather complex light water reactor fuel assembly design containing fuel and blanket pins of different sizes and water holes in an unusually tight lattice.[14] This design was so heterogeneous that a true unit cell did not exist within the fuel assembly, necessitating rather extensive geometric approximations in the application of EPRI-CELL to the system. As a check on the adequacy of the final EPRI-CELL model, the entire fuel assembly was modelled exactly in a VIM calculation. This application is typical of an entire class of problems where a geometrically exact VIM calculation is used to validate a model when circumstances force a code user to exceed its intended range of application.

VIM is also used with some frequency for more general types of reactor analysis. One program that relies heavily on VIM is the Safety Research Experiment Facilities (SAREF) program. The SAREF program was formerly directed toward the development of a conceptual design for the proposed Safety Test Facility (STF) and is presently concerned with the design of an upgraded core for the Transient Reactor Test Facility (TREAT) reactor. Because this program involves all aspects of core design for an actual reactor rather than general parametric or feasibility studies of reactor types and concepts, VIM usage in SAREF tends to be varied and complex in scope. Examples of this usage will be discussed in some detail.

VIM is used for cross section benchmarking in SAREF, but the procedure becomes more complicated than in the routine unit cell calculations cited above. Because SAREF is concerned with core design for an actual reactor rather than the study of a concept, the quality of multigroup cross sections used in SAREF reactor physics calculations is particularly important. Errors which might be acceptable for a feasibility study cannot be tolerated in a program dealing with modifications to an existing reactor. Ideally, multigroup cross section methods and reactor physics calculational techniques are validated by comparison with critical experiments, but for reasons of budget and schedule, this is not possible for the current TREAT Upgrade work. Consequently, more reliance must be placed on comparisons between VIM and multigroup deterministic

calculations. One makes the same type of comparisons here as in the simpler cell calculations discussed above, but in the SAREF applications one is dealing with many distinct regions of a complex coupled-core reactor rather than a simple unit cell.

Certain unusual features of the STF conceptual design and the TREAT Upgrade design and purposes make uncommon demands on analysis methods. Both STF and TREAT Upgrade are transient test reactors intended to provide a pulsed source of neutrons with specified characteristics to irradiate a cluster of target fuel pins in a test loop at the center of the reactor core. Consequently, the fission density distribution in these target pins and the relationship of this fission density to the fission density at specified locations in the reactor core are the crucial parameters of full-core physics calculations. The target pins and some of the other regions of interest represent very small fractions of the entire core volume, so a very careful application of splitting and Russian roulette techniques is required to reduce the relevant variances in these regions to an acceptable level. Some recent calculations with and without splitting have shown that true reaction rates in the smaller regions could never be separated from statistical noise were it not for splitting.

Calculations for the SAREF reactors are further complicated by the presence of large radial and azimuthal irregularities in these cores. Both STF and TREAT Upgrade have inner and outer core regions of markedly different compositions and properties. This leads to a strong radial dependence in the core fission density and flux spectrum. A more serious non-uniformity in these cores, however, is the presence of a large cavity caused by the removal of a row of fuel assemblies between the test loop and the boundary of the reactor. This void is introduced to allow experimenters to "view" fuel displacement in the central target pins during a transient irradiation experiment. This slot causes large azimuthal flux variations and strong neutron streaming effects which in turn lead to a marked azimuthal dependence of the core fission density. The streaming effect due to this slot is the most important reason for using VIM in SAREF core analysis, since the slot void invalidates diffusion calculations and S_N calculations would require a very fine angular mesh. The presence of control rods inserted to varying positions only complicates matters further.

Because it is not practical in terms of cost or calendar time to perform VIM calculations for every core configuration or design parameter of interest, reference configuration VIM calculations are used to correct important physics paramters from the less accurate diffusion and S_N calculations. Three examples of these correction factors will illustrate this. First, deterministic codes cannot geometrically represent either target pins or the test loop, so the crucial determinations of target pin energy deposition are seriously in error. Furthermore, the fission density distribution within the target pins is an important experimental parameter which cannot be adequately calculated deterministically. By applying VIM with full geometric detail to the test assembly, correction factors are generated which apply to a class of similar situations. Finally, it is very important that the location of the hot spots in the

core be known because they set the operational limits for the core. Because diffusion and S_N calculations are not generally able to accurately account for the effects of the slot void and control rods in a three-dimensional calculation, the VIM results are used to identify and study the core hot spots. By carefully selecting representative configurations to be studied with VIM, the designer can establish sets of correction factors to be applied to classes of similar core configurations.

At times, the required accuracy for fission density estimates has made full core Monte Carlo calculations impractical. But by imposing a fixed source of magnitude, initial energy, and initial direction important with respect to the test assembly, it is possible to generate a Green's function for the target pins and the neighboring fuel assemblies. A record of initial and terminal neutron sites is written by VIM, which is then processed to yield the desired Green's function. This function can be used to determine the response of some selected portion of the system, particularly the target pins, to a partial current imposed at some boundary of interest. This current is determined from diffusion or transport calculations which are capable of representing general core characteristics but not the fine structural details of the target region. One can economically determine the response of the test assembly fission density region to changes in core conditions by varying the partial currents at the target region boundary and applying the Green's function to them.

A related procedure requires the imposition of incoming partial currents on some boundary surrounding the region of interest. These partial currents can be obtained in the same manner as for the Green's function calculation outlined above. In this case, however, the exact magnitude of the partial current is used to determine the fixed source. The source neutrons and all of their daughter neutrons generated within the region of interest are followed to the point of termination either by absorption within the region or escape from it. The resulting VIM estimates for the central region closely approximate those from a full core calculation, but are much more economical because the focus of the Monte Carlo calculation is only on the target region.

Another Argonne program that relies heavily on VIM is the Reduced Enrichment Research and Test Reactor (RERTR) program, in which many of the reactors under study have cavities and/or beam ports for the irradiation of test materials. Because many of these reactors are used principally as irradiation facilities, their designs are oriented towards creation of a high neutron flux at particular locations in the reactor core. In addition, many of these reactors are rather small physically, with very important neutron leakage and streaming effects. These reactors often exhibit such strong heterogeneity that standard diffusion and S_N codes cannot be applied without significant approximations in the geometric representations of the reactor cores. Accurate treatment of heterogeneity can be important even in relatively large, low-leakage reactors: it is even more important in small reactors where leakage can be a major factor in the neutron economy.

An adequate treatment of heterogeneity can be very difficult with deterministic codes for several reasons. First, representation of fine structure in finite difference codes can require so many mesh points as to easily exceed available core storage. Second, theoretical considerations may limit the attainable accuracy with a deterministic code, e.g., the basic approximations inherent in diffusion theory. Third, spatial heterogeneity is often accompanied by various cross section effects that are difficult to deal with in multigroup treatments, e.g. self shielding.

Sequences of design calculations with VIM are no more practical in RERTR than in SAREF, for the same reasons of time and cost. One has little choice but to accept the geometric approximations in deterministic codes for normal calculations. However, important heterogeneous features can be examined by calculating a more-or-less exact representation of the reactor core with VIM. The VIM calculation provides the data for RERTR analysts to correct the deficiencies caused by geometrical approximations and, incidentally, to correct for errors introduced by multigroup cross section treatments.[15]

VIM has also been modified for special use in the design of the Intense Pulsed Neutron Source (IPNS) at Argonne, which employs a high energy proton beam from the zero Gradient Synchrotron to generate a high flux neutron beam for nuclear physics and materials research. The proton beam generates high energy neutrons in a heavy metal target. The emergent neutrons are then scattered into neutron beam tubes by moderating materials selected to produce neutron fluxes of specified characteristics, particularly energy. The highly localized and anisotropic nature of the proton beam and the resulting neutron fluxes necessitates an exact treatment of the angular variable, and the irregular arrangement of target, moderator, reflector, and beam tube regions in the shapes of cylinders and parallelapipeds requires a flexible geometric representation. HETC[16], a high energy nucleon-meson transport code is used to track incident protons and the few neutrons emergent from the proton target with energies above 15 MeV. The site coordinates and velocities of neutrons below 15 MeV are then saved as source sites for VIM. VIM tracks the neutrons in the usual way, except that at each collision, the probability of emerging as a beam tube particle is computed. After scoring this probability times the weight, the normal tracking process resumes. The HETC/VIM results are consistent with experiment within statistics (5-10% uncertainty).

SUMMARY

For a number of years, VIM has provided a reliable computational benchmark capability at Argonne because of the extensive benchmarking of VIM itself against other analytical tools and against numerous critical experiments. The code has been applied to analysis of a wide range of fast and thermal reactors as well as to other neutron transport calculations which require either flexible geometric representations or basic ENDF cross section data up to and including version V.

References

1. L. B. Levitt and R. C. Lewis, "VIM-I, A Mon-Multigroup Monte Carlo Code for Analysis of Fast Critical Assemblies," AI-AEC-12951, Atomics International (1970).

2. M. O. Cohn et al., "SAM-CE: A Three-Dimensional Monte Carlo Code for the Forward Neutron and Forward and Adjoint Gamma Ray Transport Equations," MR-7021, Mathematical Applications Group, Inc. (1971).

3. E. M. Gelbard and R. E. Prael, "Monte Carlo Work at Argonne National Laboratory," Proc. of the NEACRP Meeting of a Monte Carlo Study Group, July 13, 1974, ANL-75-2 (NEA-CRP-L-118), p. 201, Argonne National Laboratory (1975).

4. M. Halperin, "Almost Linearly Optimum Combination of Unbiased Estimates," Am. Statis. Assoc. Journal, 56, p. 36 (1969).

5. R. E. Prael, " Application of the Probability Table Method to Monte Carlo Temperature Difference Calculations," Trans. Am. Nuc. Soc., 17, p. 261 (November 1973).

6. J. M. Otter, "UNICORN - A Program to Calculate Point Cross Sections from Resonance Parameters, NAA-SR-11980, Vol. VI (June 1966).

7. J. M. Otter, R. C. Lewis, and L. B. Levitt, "UBR, A Code to Calculate Unresolved Resonance Cross Section Probability Tables," AI-AEC-13024 (July 1972).

8. H. C. Honeck and D. R. Finch, "FLANGE II (Version 71-1) A Code to Process Thermal Neutron Data from an ENDF/B Tape," DP-1278/ENDF-152 (October 1971).

9. R. E. Prael, "Cross Section Preparation for the Continuous-energy Monte Carlo Code VIM," Proc. Conf. on Nuclear Cross Sections and Technology, NBS SP 425, p. 447 (March 3-7, 1975).

10. R. E. Prael and H. Henryson, II, "Comparison of VIM and MC^2-2 - Two Detailed Solutions of the Neutron Slowingdown Problem," Proc. Conf. on Nuclear Cross Sections and Technology, NBS SP 425, p. 451 (March 3-7, 1975).

11. S. K. Bhattacharyya, private communication, April 1980.

12. E. M. Gelbard, et al, "Calculations of Void Streaming in the Argonne Gas-Cooled Fast Reactor Critical Experiments," Nucl. Sci. Eng., 64, 624 (1977); with D. C. Wade, R. W. Schaefer and R. E. Phillips.

13. L. J. Milton, internal memorandum, Argonne National Laboratory, May 14, 1979.

14. D. J. Malloy, private communication, April 1980.

15. W. L. Woodruff, private communication, April 1980.

16. "HETC, Monte Carlo High-Energy Nuclear-Meson Transport Code," RSIC Computer Code Collection, CCC-178, Oak Ridge (1978).

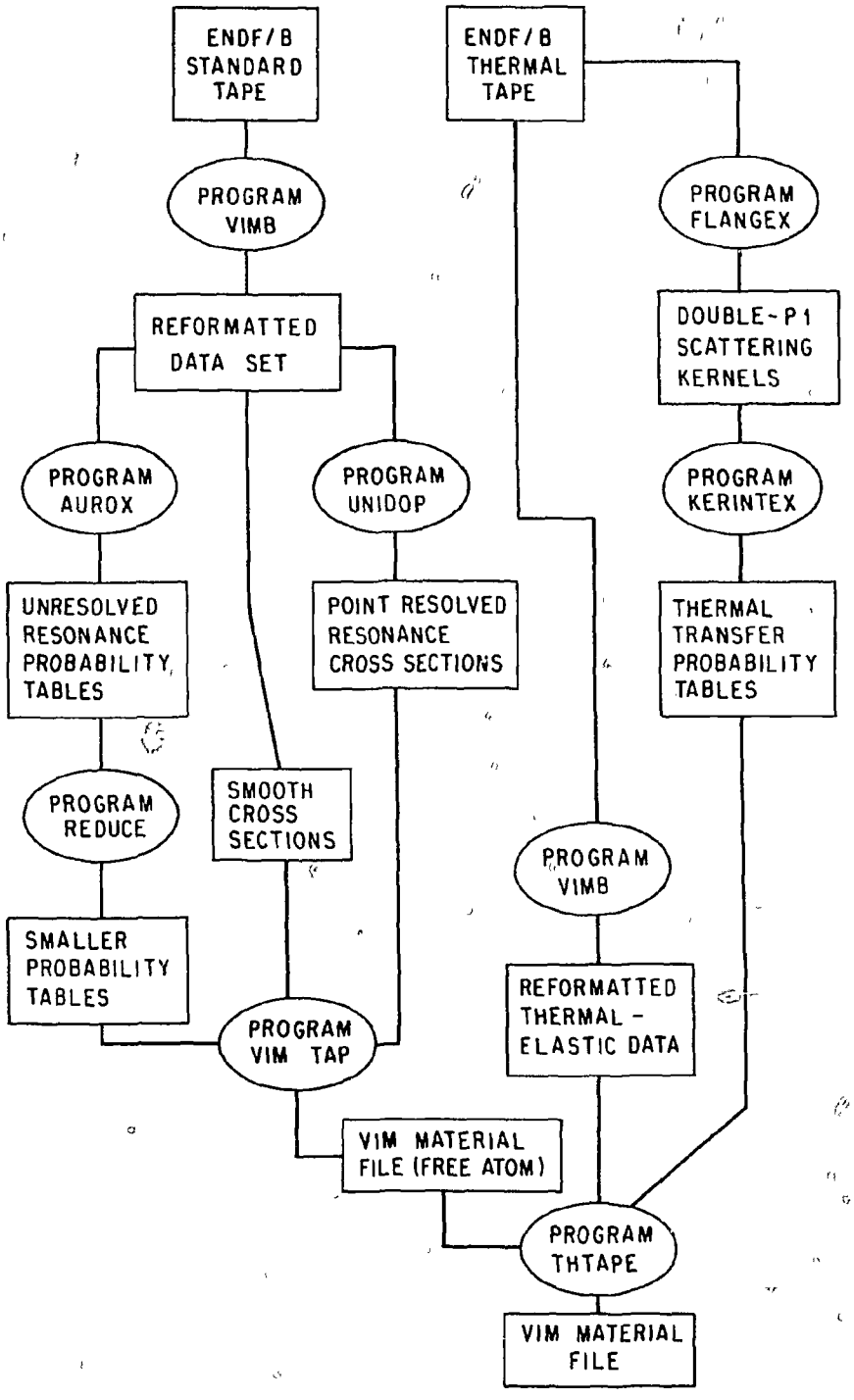

Fig. 1. VIM Cross Section Library Generation Procedure

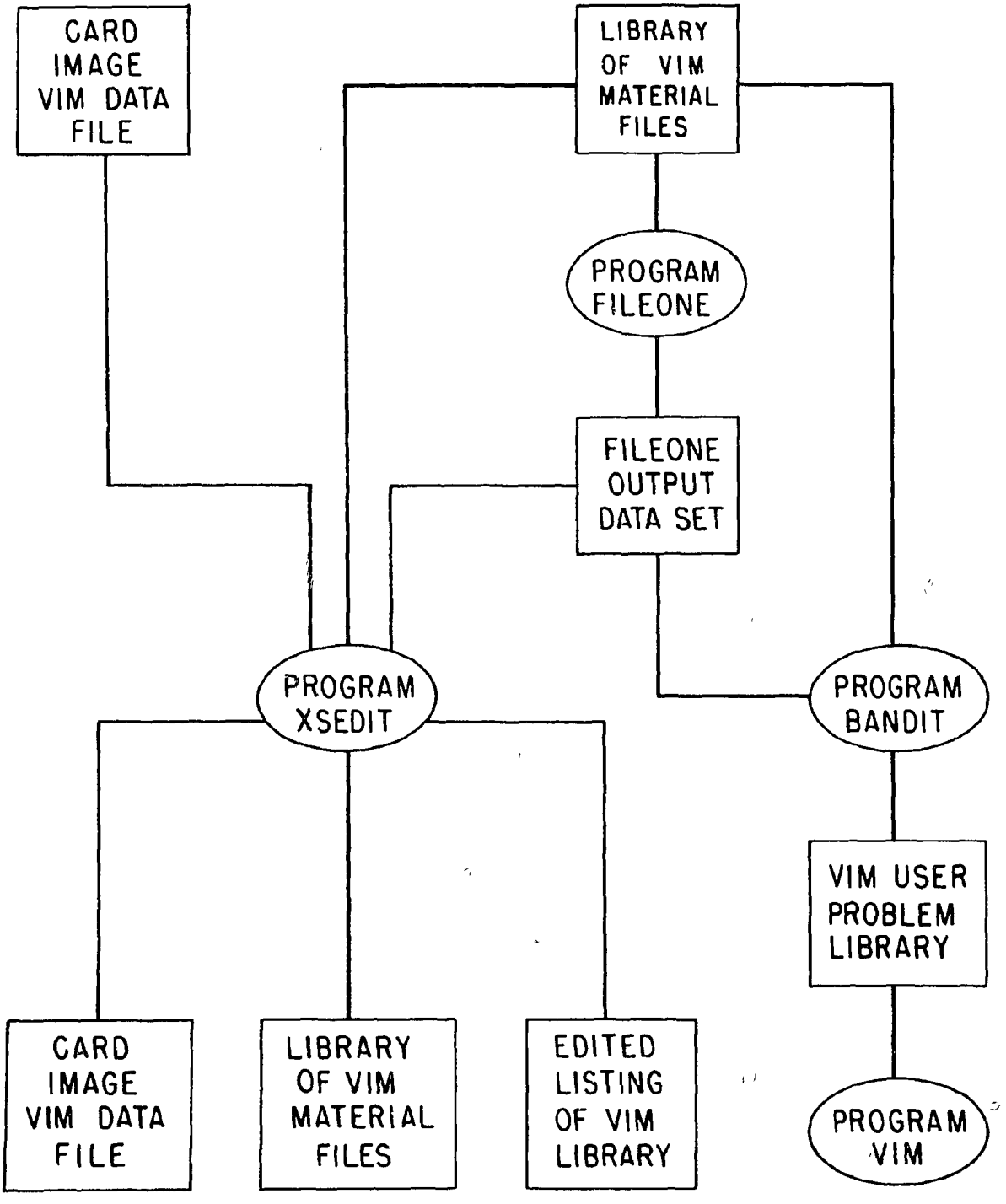

Fig. 2. VIM Cross Section Library Handling Utilities

MONTE CARLO PERTURBATION THEORY IN NEUTRON TRANSPORT CALCULATIONS

M. C. G. Hall
Imperial College of Science and Technology *
London, England

ABSTRACT

The need to obtain sensitivities in complicated geometrical configurations has resulted in the development of Monte Carlo sensitivity estimation. A new method has been developed to calculate energy-dependent sensitivities of any number of responses in a single Monte Carlo calculation with a very small time penalty. This estimation typically increases the tracking time per source particle by about 30%. The method of estimation is explained. Sensitivities obtained are compared with those calculated by discrete ordinates methods. Further theoretical developments, such as second order perturbation theory and application to k_{eff} calculations are discussed. The application of the method to uncertainty analysis and to the analysis of benchmark experiments is illustrated.

INTRODUCTION

The result of a neutron transport calculation can be very sensitive to nuclear data, and experimental error in these data may cause the result to be misleading. To determine how important this effect is, it is necessary to calculate sensitivities and combine them with covariance information to obtain the standard deviation of the result. If the uncertainty arising in this way is unacceptably large, then the nuclear data must be improved. One way to do this is to adjust on the basis of a benchmark experiment, which also involves the calculation of sensitivities. The motivation for this work is the need to calculate sensitivities in geometries which, because of their complexity, require a Monte Carlo calculation.

There are additional advantages in using a Monte Carlo method for the analysis of benchmark experiments. All the sensitivity information can be estimated simultaneously, whereas conventional methods require a separate adjoint calculation for each channel of experimental information. Also group-averaging errors can be avoided by the use of point nuclear data, so the adjustments should reflect shortcomings in the basic data, rather than difficulties in a group-averaging process. The number of

*Work performed during author's attachment to Radiation Physics and Shielding Group, Reactor Physics Division, AEE Winfrith.

sensitivity coefficients which need to be estimated though, can be as many as a thousand, so it is essential that each should be scored with very little time penalty.

The method described here has been implemented with all this in mind, although the approach has been kept as general as possible, so that different applications can be catered for.

METHOD

Any response R can be considered as an average value associated with the set P of all neutron paths:

$$R = \sum_{m \in P} r^m p^m \,. \tag{1}$$

Here p^m is the probability of path m, and r^m is the estimator for path m. If $\hat{D}$ is a linear perturbation operator, then $\hat{D}$ operating on Eq. (1) gives

$$\hat{D}R = \sum_{m \in P} \hat{D}(r^m p^m) \,. \tag{2}$$

Writing Eq. (2) in the form of Eq. (1)

$$\hat{D}R = \sum_{m \in P} dr^m \, p^m \tag{3}$$

where

$$dr^m = \{\hat{D}(r^m p^m)\}/p^m \,, \tag{4}$$

so dr^m is an estimator of $\hat{D}R$. Re-arranging Eq. (4)

$$dr^m = v^m r^m \tag{5}$$

where

$$v^m = \{\hat{D}(r^m p^m)\}/(r^m p^m) \,, \tag{6}$$

so dr^m is a weighted version of r^m.

This estimator has the disadvantage that it is bad at estimating the component of a change which is zero because of physical restrictions. For example, in a non-multiplying medium a perturbation of a cross-section at low energy usually cannot affect the flux at high energy. But even if $\hat{D}$ only operates on cross-sections at low energy and r^m only scores flux at high energy, the estimator dr^m given by Eq. (4) will still in general be non-zero, although it will have zero expectation. A more discerning estimator would itself be zero under these circumstances. To achieve this r^m and p^m are split into components associated with each trajectory of path m:

$$r^m = \sum_{i \le t^m} s_i^m \tag{7}$$

and

$$p^m = \prod_{j \le t^m} q_j^m \ . \tag{8}$$

In this context: a trajectory is a section of a path along which no collisions or boundary crossings occur; t^m is the number of trajectories in path m; s_i^m is the contribution to the estimator for path m arising from the i^{th} trajectory; q_j^m is the probability of the j^{th} trajectory, given that the $(j-1)^{th}$ trajectory has occurred. It is shown in the appendix that another estimator for $\hat{D}R$ is given by

$$dr^m = \sum_{i \le t^m} \left\{ \hat{D} \left(s_i^m \prod_{j \le i} q_j^m \right) \right\} / \prod_{j \le i} q_j^m \ . \tag{9}$$

This estimator will always be zero in the circumstances which have just been mentioned. This is because, in Eq. (9), by the time i is large enough for $\hat{D}$ to operate on s_i^m and q_j^m, the value of s_i^m is zero. Re-arranging as before

$$dr^m = \sum_{i \le t^m} \omega_i^m s_i^m \tag{10}$$

where

$$\omega_i^m = \left\{ \hat{D} \left(s_i^m \prod_{j \le i} q_j^m \right) \right\} / \left(s_i^m \prod_{j \le i} q_j^m \right) \ . \tag{11}$$

These are the key expressions used in the method. The two expressions for dr^m in Eqs. (5) and (10) can be compared by writing Eq. (5) as

$$dr^m = \sum_{i \le t^m} v^m s_i^m \ . \tag{12}$$

IMPLEMENTATION

Implementation consists of specifying $\hat{D}$, s_i^m and q_j^m of Eq. (11), evaluating the weights ω_i^m, and scoring the estimator dr^m in the same way as the estimator r^m.

Specifying $\hat{D}$

The form of $\hat{D}$ is determined by the nature of the perturbations of interest. In the analysis of a benchmark experiment it is usual to regard the result R of a calculation as a function of the nuclear data $\underline{x}$:

$$z = R(\underline{x}) \tag{13}$$

$\underline{x}$ is subject to experimental error and may be perturbed by an amount $\underline{\delta x}$. The Taylor expansion of R about $\underline{x}$ is

$$\delta R = \sum_i \delta x_i \frac{\partial}{\partial x_i} R + \frac{1}{2!} \sum_{ij} \delta x_i \delta x_j \frac{\partial^2}{\partial x_i \partial x_j} R + \dots \ . \tag{14}$$

Writing this in dimensionless terms

$$\frac{\delta R}{R} = \sum_i \frac{\delta x_i}{x_i} \frac{x_i}{R} \frac{\partial}{\partial x_i} R + \frac{1}{2!} \sum_{ij} \frac{\delta x_i}{x_i} \frac{\delta x_j}{x_j} \frac{x_i x_j}{R} \frac{\partial^2}{\partial x_i \partial x_j} R + \dots \ . \tag{15}$$

Often some of the values of $\delta x_i / x_i$ are constrained to be equal—for example they may be subject to a systematic error. Suppose for a set of integers K and associated constant c_K there is a constraint

$$\delta x_i / x_i = c_K \quad i \in K \tag{16}$$

—similarly for another set L and constant c_L. In this case Eq. (15) can be factorised:

$$\frac{\delta R}{R} = \sum_K c_K \sum_{i \in K} \frac{x_i}{R} \frac{\partial}{\partial x_i} R + \frac{1}{2!} \sum_K \sum_L c_K c_L \sum_{i \in K} \sum_{j \in L} \frac{x_i x_j}{R} \frac{\partial^2}{\partial x_i \partial x_j} R + \dots \ . \tag{17}$$

The terms which it is useful to know are

$$\sum_{i \in K} \frac{x_i}{R} \frac{\partial}{\partial x_i} R \tag{18}$$

and

$$\sum_{i \in K} \sum_{j \in L} \frac{x_i x_j}{R} \frac{\partial^2}{\partial x_i \partial x_j} R \ . \tag{19}$$

The first of these terms can be written as

$$(1/R) \hat{D} R \tag{20}$$

where

$$\hat{D} = \sum_{i \in K} x_i \frac{\partial}{\partial x_i} \ . \tag{21}$$

This is the form of $\hat{D}$ considered in this section.

Specifying S and q

The quantities S and q are determined by the type of trajectory and by the method of estimation. Suppose a trajectory starts with a neutron undergoing a reaction type α at energy E. The neutron is scattered through an angle θ to energy E', continues for a length λ and then collides. The cross-section for reaction β at energy E is x_g^β. For convenience x_g^B is defined by

$$x_g^B = \sum_{\beta \in B} , \tag{22}$$

where B is a set of partial cross-sections. The probability of the trajectory alone is given by

$$q = (x_g^\alpha / x_g^T)\, p(\theta)\, d\theta\, p(E,E')\, dE'\, \exp(-x_{g'}^T \lambda)\, x_{g'}^T\, d\lambda . \tag{23}$$

Here T is the set of all reactions making up the total cross-section and $p(\theta)\, d\theta\, p(E,E')\, dE'$ is the probability distribution function in phase-space of the secondary neutron. If a Monte Carlo code uses point nuclear data, then values such as x_g^β are used in the sampling procedure. In this case $\hat{D}$ might be given by

$$\hat{D} = \sum_{\beta \in P} \sum_{h \in G_i} x_h^\beta \frac{\partial}{\partial x_h^\beta} . \tag{24}$$

Here P is a set of cross-section types, for example non-elastic, and G_i is a set of values of h comprising an energy interval. In this case $(1/R)\hat{D}R$ would be the sensitivity of R to the non-elastic cross-section in the G^{th} energy interval.

If track length estimation is used, the contribution to the estimator for the trajectory will be given by

$$s = \lambda \sigma_{g'} , \tag{25}$$

where σ_q is a response cross-section at energy E'. If collision density estimation is used, then

$$s = \sigma_{g'} / x_{g'}^T . \tag{26}$$

Evaluating ω_i^m

The symbol δ_α^P is defined to be unity if α belongs to the set P, and otherwise to be zero. If $\hat{D}$ is given by Eq. (24) and track length estimation is used, the weight ω_i^m is given by

$$\omega_i^m = \sum_{j \le i} \left\{ \delta_\alpha^P - \delta_j^G \left(x_j^P / x_j^T\right) - \delta_j^G \left(x_{j'}^P \cdot \lambda\right) + \delta_{j'}^G \left(x_{j'}^P / x_{j'}^T\right) \right\} . \quad (27)$$

If collision density estimation is used, then

$$\omega_i^m = \sum_{j \le i} \left\{ \delta_\alpha^P - \delta_j^G \left(x_j^P / x_j^T\right) - \delta_{j'}^G \left(x_j^P \cdot \lambda\right) \right\} . \quad (28)$$

Fortunately the weights can be evaluated using a recursion formula—for example with track length estimation

$$\omega_i^m = \omega_{i-1}^m + \left\{ \delta_\alpha^P - \delta_j^G \left(x_j^P / x_j^T\right) - \delta_{j'}^G \left(x_{j'}^P \cdot \lambda\right) + \delta_{j'}^G \left(x_{j'}^P / x_{j'}^T\right) \right\} . \quad (29)$$

It can be seen from Eq. (29) why the method is so fast. The values of x_j^P, x_j^T, $x_{j'}^P$, $x_{j'}^T$ and λ are all available in an unperturbed calculation, so the weight ω_i^m only has to assemble information which is already there. In addition, the weight ω_i^m can be applied to any estimator s_i^m, which means that sensitivities to any number of responses can be scored simultaneously.

Scoring dr^m

A code called DUCKPOND[1] has been written to score the estimator dr_i^m. Full use has been made of the Winfrith Shielding Group's suite of Monte Carlo modules. This has meant that DUCKPOND has been coded with a minimum of effort yet includes the powerful capabilities familiar to users of McBEND[2]. In addition to a sensitivity capability, DUCKPOND can score a covariance matrix for all the estimated responses. This is useful in analysing benchmark experiments.

COMPARISON

Sensitivities can be obtained in limited circumstances using discrete ordinates (S_n) calculations, so an important test is to compare results of this type with answers estimated using the Monte Carlo method. The only difficulty with the comparison is that the discrete ordinates calculation may involve group-averaging errors, whereas this will not be the case with Monte Carlo estimation using point nuclear data. To determine the extent of this problem, fluxes are compared in addition to sensitivities.

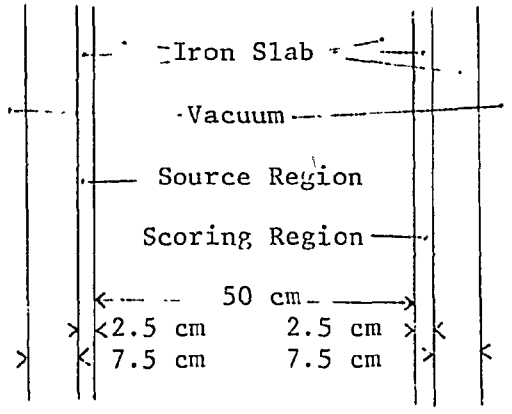

Fig. 1. The Geometry of the Test Problem.

The geometry of the test problem is illustrated in Fig. 1. The response function is for total flux per unit volume betweem 14.9 MeV and 407 KeV; the source has a fission spectrum normalised to $1{\cdot}0\ cm^{-3}\ s^{-1}$. Sensitivities to the elastic and non-elastic cross-sections of iron are calculated in forty groups of approximately equal lethargy width between 14.9 MeV and 407 KeV, corresponding to the first forty groups of the 100-group EURLIB[3] structure. Flux per unit volume in the scoring region is calculated in the same group scheme.

ANISN[4] and SWANLAKE[5] were used for the S_n calculations and DUCKPOND for the Monte Carlo estimation. Fluxes and sensitivities are compared in Figs. 2 and 3; the errors plotted for the Monte Carlo results are an estimate of one standard deviation.

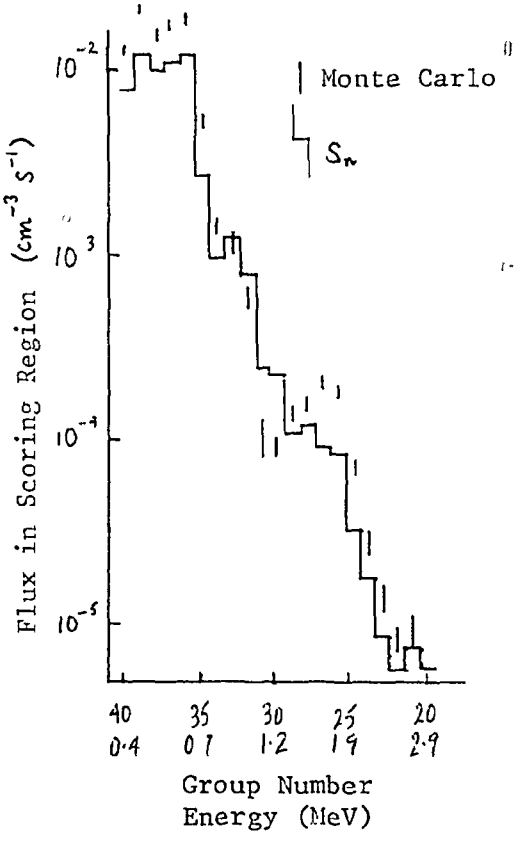

Fig. 2. Comparison of Flux in Scoring Region calculated by Monte Carlo and S_n Methods.

The Monte Carlo sensitivity estimation is working well. The agreement with the S_n method is convincing and, equally important, acceptable variances have been obtained with a workable sample size. DUCKPOND was run in this case for twenty minutes on an IBM 3033 using automatically-generated importance sampling, and the test problem is representative in scale of a realistic calculation. Moreover a comparison of running times between DUCKPOND and its non-perturbative equivalent McBEND show that sensitivity estimation typically slows down tracking by 30%. To give an example—for the same price a response might either be estimated by McBEND with a standard deviation of 10%, or estimated by DUCKPOND with a standard deviation of 11.4% but with a full set of sensitivity profiles. If the sensitivities reveal uncertainty of 20% arising from data errors, then the DUCKPOND calculation would be the more useful. It would be sensible to perform an uncertainty analysis of this kind on all Monte Carlo calculations.

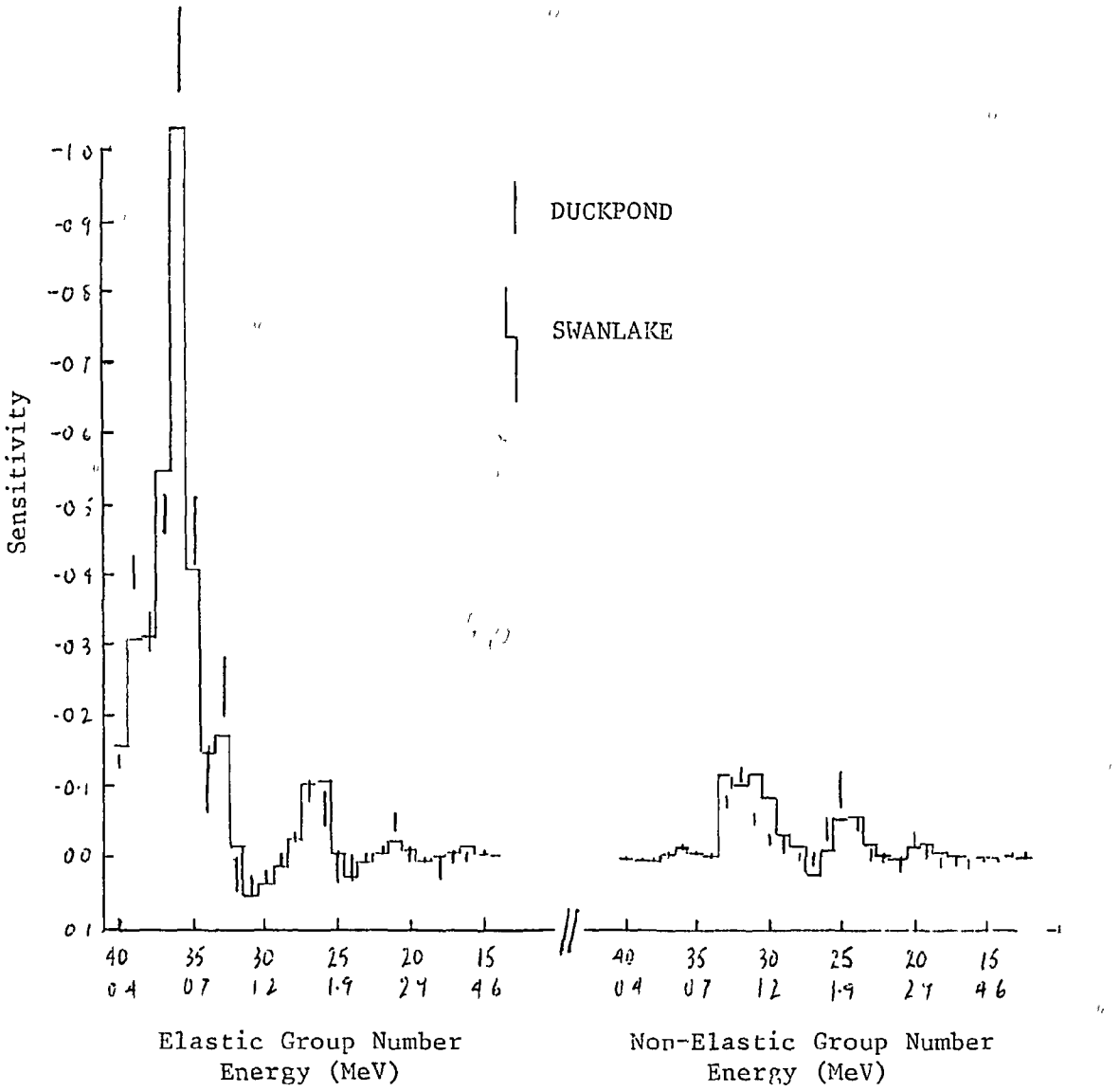

Fig. 3. Comparison of Sensitivities of Flux above 407 KeV to Elastic and Non-Elastic Cross-Sections of Iron, as calculated by DUCKPOND and SWANLAKE.

A disturbing aspect of the results is the discrepancy between the fluxes calculated by the Monte Carlo and S_n methods. The low energy flux, which is the main contributor to the total flux, is undercalculated by about 50% by the S_n method. The sensitivity profiles suggest that an explanation of this is a group-averaging overestimate of about 30% in the cross-sections for groups 35 to 39. Such an error could easily arise: the elastic cross-section of iron is rapidly changing by factors of about five in this energy range, which puts great importance on the weighting function used in the averaging process.

DEVELOPMENT

There are three interesting ways in which this method can be developed: higher order perturbation coefficients could be scored, sensitivities to geometric data obtained, and the method could be applied to eigenvalue calculations.

Higher Order Coefficients

A second order operator has already arisen in Eq. (19). Such an operator is now defined by

$$\hat{D}_{KL} = \sum_{i \in K} \sum_{j \in L} x_i x_j \frac{\partial^2}{\partial x_i \partial x_j} \quad . \tag{30}$$

It is also convenient to redefine corresponding first order operators:

$$\hat{D}_K = \sum_{i \in K} x_i \frac{\partial}{\partial x_i} \tag{31}$$

and

$$\hat{D}_L = \sum_{j \in L} x_j \frac{\partial}{\partial x_j} \quad . \tag{32}$$

The first order weights are given by Eq. (11) and turn out to be

$${}^{K}\omega_i^m = \frac{1}{s_i^m} \hat{D}_K s_i^m + \sum_{j \le i} \frac{1}{q_j^m} \hat{D}_K q_j^m \tag{33}$$

and

$${}^{L}\omega_i^m = \frac{1}{s_i^m} \hat{D}_L s_i^m + \sum_{j \le i} \frac{1}{q_j^m} \hat{D}_L q_j^m \quad , \tag{34}$$

and the second order weights are given by

$$\begin{aligned} {}^{KL}\omega_i^m = {}^{K}\omega_i^m {}^{L}\omega_i^m + \frac{1}{s_i^m} \hat{D}_{KL} s_i^m - \left(\frac{1}{s_i^m} \hat{D}_K s_i^m\right)\left(\frac{1}{s_i^m} \hat{D}_L s_i^m\right) \\ + \sum_{j \le i} \left\{ \frac{1}{q_j^m} \hat{D}_{KL} q_j^m - \left(\frac{1}{q_i^m} \hat{D}_K q_i^m\right)\left(\frac{1}{q_j^m} \hat{D}_L q_j^m\right) \right\} \quad . \end{aligned} \tag{35}$$

These equations are illustrated by referring to the specifications of $\hat{D}$, S and q appearing in the section on implementation. $\hat{D}_K$ and $\hat{D}_L$ are given by

$$\hat{D}_K = \sum_{\beta \in P} \sum_{h \in G} x_h^\beta \frac{\partial}{\partial x_h^\beta} \tag{36}$$

and

$$\hat{D}_L = \sum_{\beta \in Q} \sum_{h \in H} x_h^\beta \frac{\partial}{\partial x_h^\beta} \quad , \tag{37}$$

with a corresponding definition of $\hat{D}_{KL}$. The previous definitions of S and q still stand. For track length estimation all the terms involving S in Eqs. (33) to (35) are zero. The other terms are given by

$$(1/q_j^m)\hat{D}_K q_j^m = \delta_\alpha^P - \delta_\alpha^G (x_g^P / x_g^T) - \delta_{g'}^G (x_{g'}^P, \lambda) + \delta_{g'}^G (x_{g'}^G / x_{g'}^T), \quad (38)$$

$$(1/q_j^m)\hat{D}_L q_j^m = \delta_\alpha^Q - \delta_g^H (x_g^Q / x_g^T) - \delta_{g'}^H (x_{g'}^Q, \lambda) + \delta_{g'}^H (x_{g'}^Q / x_{g'}^T), \quad (39)$$

$$(1/q_j^m)\hat{D}_{KL} q_j^m = -(\delta_\alpha^P + \delta_\alpha^Q)(x_g^P x_g^Q)/(x_g^T x_g^T) - 2\delta_g^G \delta_j^H (x_g^P x_g^Q)/(x_g^T)^2 + \delta_{g'}^G \delta_{g'}^H (x_{g'}^P x_{g'}^Q \lambda^2), \quad (40)$$

so second order weights are not much more difficult to evaluate than first order, although there may be more of them. The most likely use of second order coefficients would be in testing the validity of a first order approximation.

Geometric Sensitivities

Suppose a geometrical configuration is defined in terms of rectangular co-ordinates r_1, r_2 and r_3. A plane with unit normal $\underline{n}$ which separates two different media may be described by the equation

$$\underline{n} \cdot \underline{r} = l . \quad (41)$$

An operator which describes a first order change in the position of the plane is

$$\hat{D} = \partial/\partial l . \quad (42)$$

Again using the previous specifications for S and q, the only variable which can depend on l is λ. If u_1, u_2 and u_3 are the direction cosines of a trajectory then

$$\partial\lambda/\partial l = K/\underline{n} \cdot \underline{u} . \quad (43)$$

Here $K = -1$ for boundary crossing at the beginning of the trajectory, $K = 1$ for boundary crossing at the end of the trajectory, and $K = 0$ otherwise. If collision density estimation is used, the weight given by Eq. (11) is

$$\omega_j^m = -K x_g^T / \underline{n} \cdot \underline{u} . \quad (44)$$

This could be used to score the geometric sensitivity $\partial R/\partial l$.

Eigenvalue Calculations

Monte Carlo eigenvalue calculations differ from shielding calculations in that superimposed on the normal processes of tracking and scoring is an iterative procedure. An eigenvalue calculation in a code such as MONK[6] will usually start with a fission source guess represented by N_0 particles. These particles are tracked to leakage, absorption or fission. N_0 of the resulting N_1 secondary particles are sampled at random and the process continues for successive generations. The ratio K_j is defined by

$$K_j = N_j / N_0 \tag{45}$$

where N_j is the number of secondary particles at the end of the j^{th} generation.

Each trajectory involved is labelled according to the particle from which it originated (m) and the generation in which it occurs (j). The probability of the i^{th} trajectory of this type is defined in the same way as before to be q_{ij}^m. The probability of all the trajectories up to and including the k^{th} generation which originate from the m^{th} particle is given by

$$p_k^m = \frac{1}{N_0} \prod_{j=1}^{k} \frac{1}{K_{j-1}} \prod_{i} q_{ij}^m \,. \tag{46}$$

If r_k^m is the number of secondaries at the end of the k^{th} generation originating from the m^{th} particle, then another expression of the ratio K_k is

$$K_k = \lim_{N_0 \to \infty} \sum_{m=1}^{N_0} r_k^m p_k^m \,. \tag{47}$$

Furthermore the eigenvalue k_{eff} is given by

$$k_{eff} = \lim_{k \to \infty} K_k \,, \tag{48}$$

so for k sufficiently large, r_k^m is an estimator of k_{eff}. If α is some perturbation parameter then

$$\frac{\partial K_k}{\partial \alpha} = \lim_{N_0 \to \infty} \sum_{m=1}^{N_0} r_k^m \frac{\partial p_k^m}{\partial \alpha} \,, \tag{49}$$

or

$$\frac{\partial K_k}{\partial \alpha} = \lim_{N_0 \to \infty} \sum_{m=1}^{N_0} dr_k^m \, p_k^m \tag{50}$$

where

$$dr_k^m = \frac{1}{p_k^m} \frac{\partial p_k^m}{\partial \alpha} r_k^m \,. \tag{51}$$

This means that dr_k^m is an estimator of $\partial K_k / \partial \lambda$ and, for k sufficiently large, $\partial R_{eff} / \partial \lambda$. Re-arranging Eq. (51)

$$dr_k^m = y_k^m r_k^m \tag{52}$$

where

$$y_k^m = \frac{1}{P_k^m} \frac{\partial P_k^m}{\partial \lambda}. \tag{53}$$

The evaluation of the weight y_k^m may be troublesome. Substituting for P_k^m from Eq. (46)

$$y_k^m = \sum_{j=1}^{k} \left(\sum_i \frac{1}{q_{ij}^m} \frac{\partial}{\partial \lambda} q_{ij}^m - \frac{1}{K_{j-1}} \frac{\partial K_{j-1}}{\partial \lambda} \right) \tag{54}$$

so

$$y_k^m = y_{k-1}^m + \sum_i \frac{1}{q_{ik}^m} \frac{\partial}{\partial \lambda} q_{ik}^m - \frac{1}{K_{k-1}} \frac{\partial K_{k-1}}{\partial \lambda}. \tag{55}$$

The difficulty is in evaluating the term $\partial K_{k-1} / \partial \lambda$. An exact value is not available, so an estimate using dr_{k-1}^m has to be used. If N_0 is not sufficiently large, the estimates of $\partial K_k / \partial \lambda$ may get progressively worse, and the method may not converge.

APPLICATION

DUCKPOND has been applied to a variety of practical problems. Preliminary results of the uncertainty analysis for the NRC Blind Test[7] have already been produced and sensitivity calculations have been carried out for the analysis of the Winfrith Iron Benchmark[8] . Some of these results are presented here.

NRC Blind Test

This test is to see how well a series of experimental reaction rates in a simulated pressure vessel can be predicted by various methods. It is useful to be able to isolate each source of error in the predictions, and DUCKPOND has been used to evaluate uncertainties arising from errors in nuclear data. The significant sensitivities of one of the reaction rates, as calculated by DUCKPOND, are illustrated in Fig. 4. These sensitivities were combined with covariance information about nuclear data[9] to obtain an uncertainty of 14%. The geometrical configuration involved in the calculation precluded an S_n method.

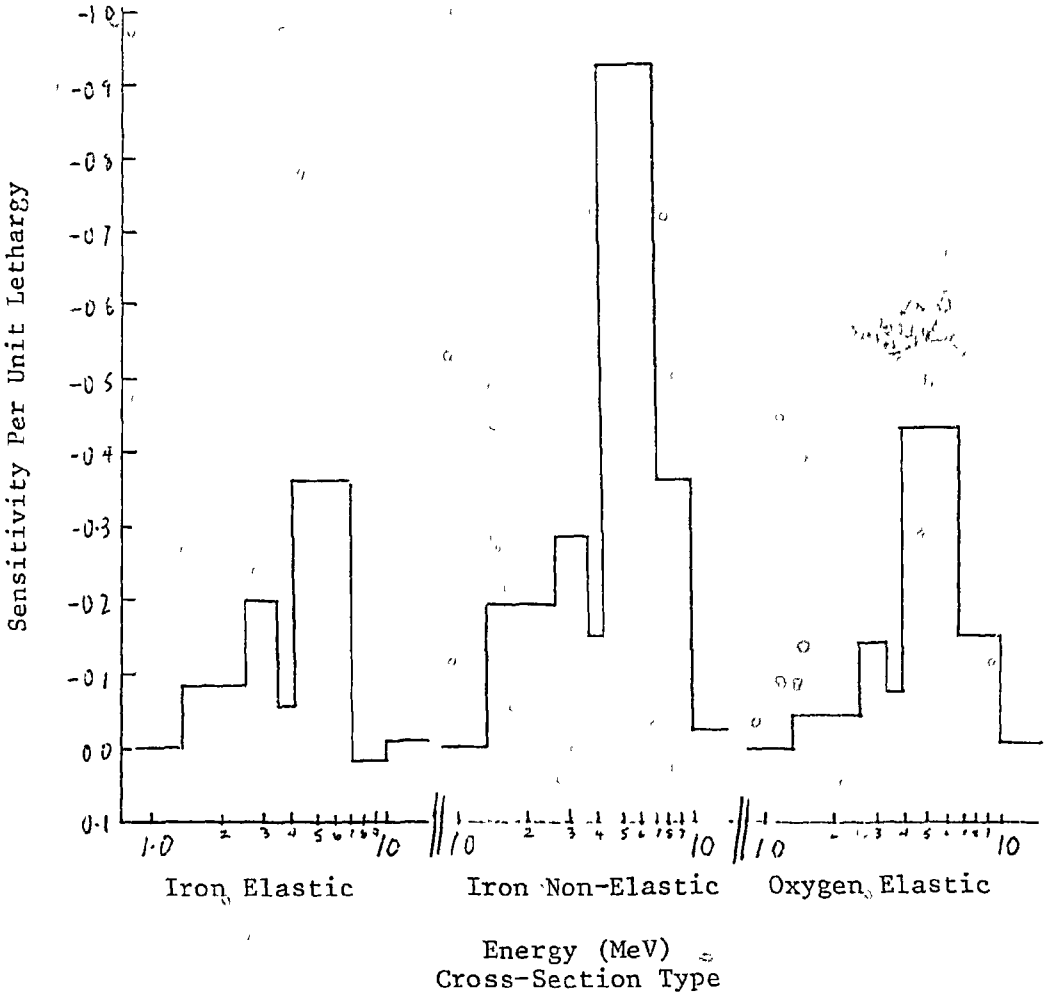

Fig. 4. Sensitivity per Unit Lethargy of $^{58}Ni(n,p)^{58}Co$ Reaction Rate in a Simulated Pressure Vessel, to Various Cross-Sections.

Winfrith Iron Benchmark

The objective of this benchmark is to adjust the evaluated cross-section of iron on the basis of count rates measured in an iron block with a fission source at one end. Each count rate is calculated along with a sensitivity profile: the sensitivities determine which adjustments would improve the agreement between calculation and experiment, and cross-section covariance information indicates which the likely adjustments are.

DUCKPOND was used for the calculations. The experimental configuration was modelled very accurately using combinatorial geometry. Sixty count rates and sensitivity profiles were scored, which involved tracking neutrons in iron to a depth of 7.5 cm and down to 5 KeV. After twenty minutes running on an IBM 3033 the statistical error on the estimated count rates

had reached the same level as the experimental error (about 15%). One of the sensitivity profiles is illustrated in Fig. 5. The pronounced positive sensitivity is probably a three-dimensional effect: an increase in the cross-section will reduce the leakage and hence increase the count rate. The results of an adjustment procedure based on this DUCKPOND calculation are shortly to be produced.

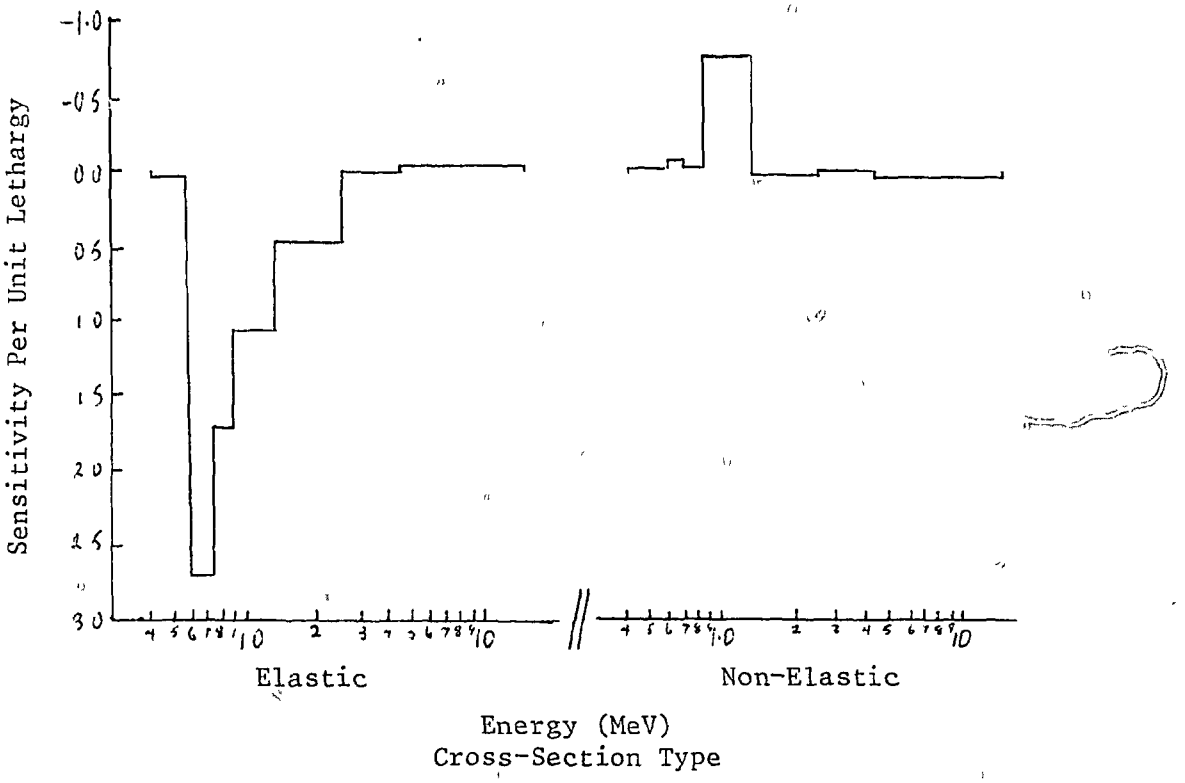

Fig. 5. Sensitivity Per Unit Lethargy of an Hydrogen/Argon Proportional Count Rate at 50 cm Penetration, to Iron Cross-Sections. (The threshold of the detector is about 4.4 MeV.)

CONCLUSION

It is now a simple and inexpensive matter to carry out the uncertainty analysis of a transport calculation, however complicated the geometrical configuration. It is also clearly feasible to analyse a shielding benchmark experiment on the basis of a Monte Carlo calculation. Application of this method to core calculations is as yet untested, and this would be a sensible option to try out. Geometric and second order developments would be easy to implement, although they might be of limited use. There is no reason why the method should not be applied to calculations using multigroup data if necessary.

REFERENCES

1. M. C. G. Hall, DUCKPOND - A Monte Carlo Code for Determining the Unknown Consequences of Known Perturbations of Nuclear Data, to be published.

2. D. E. Bendall and R. J. Brissenden, McBEND Programme Users Guide, To be published.

3. "EURLIB Library", ESIS Newsletter No. 12, January 1975.

4. W. W. Engle, A Users Manual for Anisn, a One-Dimensional Discrete Ordinates Transport Code with Anisotropic Scattering K-1673, Computing Technology Centre, Oak Ridge, Gaseous Diffusion Plant, 1967.

5. D. E. Bartine, F. R. Mynatt and E. M. Oblow, Swanlake, A Computer Code Utilising Anisn Radiation Transport Calculations for Cross-Section Sensitivity Analysis, ORNL-TM-3809, Mathematics Division, Oak Ridge National Laboratory, May 1973.

6. V. S. W. Sherriffs, Monk - A General Purpose Monte Carlo Neutronics Program, SRD Culcheth No. 86, January 1978.

7. Technical Letter for PCA Blind Test, NRC April 1979.

8. M. D. Carter and A. Packwood, The Winfrith Benchmark Experiment in Iron - Experimental Results, Proc. of Specialists Meeting on Sensitivity Studies and Shielding Benchmarks NEA/OECD, Paris, 1975.

9. J. D. Drischler and C. R. Weisbin, Compilation of Multigroup Cross-Section Covariance Matrices for Several Important Reactor Materials, ORNL-5318 Neutron Physics Division, Oak Ridge National Laboratory, October 1977.

APPENDIX

A path segment is defined to be a set of contiguous trajectories which make up the initial part of the path. R_k is the set of paths which start with segment k. ${}^kS_i$ and ${}^kq_i$ are defined by

$$ {}^kS_i = S_i^m \qquad m \in R_k \tag{56} $$

and

$$ {}^kq_i = q_i^m \qquad m \in R_k \ . \tag{57} $$

The number of trajectories in segment k is u^k. The response R can now be regarded as the average value associated with the set S of all segments:

$$R = \sum_{k \in S} {}^{k}S_{u^k} \prod_{j \leq u^k} {}^{k}q_j \quad . \tag{58}$$

$\hat{D}$ operating on Eq. (58) gives

$$\hat{D}R = \sum_{k \in S} d^k S_{u^k} \prod_{j \leq u^k} {}^{k}q_j \tag{59}$$

where

$$d^k S_{u^k} = \left\{ \hat{D} \left({}^{k}S_{u^k} \prod_{j \leq u^k} {}^{k}q_j \right) \right\} \Big/ \prod_{j \leq u^k} {}^{k}q_j \quad . \tag{60}$$

T_i is the set of segments with exactly i trajectories ($u^k = i$). The sum over segments ($\sum_{k \in S}$) is now regarded as a sum over i, and a sum over segments with exactly i trajectories ($\sum_i \sum_{k \in T_i}$). From the definition of a probability

$$\sum_{m \in R_k} \prod_{u^k < l < t^m} q_l^m = 1 \quad . \tag{61}$$

Also $u^k = i$ for $k \in T_i$. Using all this in Eq. (59)

$$\hat{D}R = \sum_i \sum_{k \in T_i} d^k S_i \prod_{j \leq i} {}^{k}q_j \left(\sum_{m \in R_k} \prod_{i < l < t^m} q_l^m \right) \quad . \tag{62}$$

Re-arranging and using Eqs. (56) and (57)

$$\hat{D}R = \sum_i \sum_{k \in T_i} \sum_{m \in R_k} ds_i^m \prod_{j \leq t^m} q_j^m \tag{63}$$

where

$$ds_i^m = \left\{ \hat{D} \left(s_i^m \prod_{j \leq i} q_j^m \right) \right\} \Big/ \prod_{j \leq i} q_j^m \quad . \tag{64}$$

Q_i is the set of paths with at least i trajectories. The sum over all such paths ($\sum_{m \in Q_i}$) can be regarded as the sum over paths which contain a segment with exactly i trajectories ($\sum_{k \in T_i} \sum_{m \in R_k}$). This double sum is replaced in Eq. (63) to give

$$\hat{D}R = \sum_i \sum_{m \in Q_i} ds_i^m \prod_{j \leq t^m} q_j^m \quad . \tag{65}$$

Re-arranging Eq. (65)

$$\hat{D}R = \sum_{m \in P} \sum_{i \leq t^m} ds_i^m \prod_{j \leq t^m} q_j^m \quad , \tag{66}$$

so an estimator of $\hat{D}R$ for paths is given by

$$dr^m = \sum_{i \leq t^m} \left\{ \hat{D} \left(s_i^m \prod_{j \leq i} q_j^m \right) \right\} \Big/ \prod_{j \leq i} q_j^m \quad . \tag{67}$$

STUDIES OF PERTURBATIONS USING CORRELATED MONTE CARLO METHOD

G. DEJONGHE - J. GONNORD - J.C. NIMAL

COMMISSARIAT A L'ENERGIE ATOMIQUE - Service S.E.R.M.A.

LABORATOIRE DE PROTECTION

SACLAY - B.P. N° 2 - 91190 GIF SUR YVETTE - FRANCE

ABSTRACT

The influence of light perturbations of cross sections on a set of neutronic responses cannot be estimated with an acceptable precision by statistically independent Monte Carlo calculations.

Differential TRIPOLI, a tridimensional, polykinetic code of Monte Carlo, permits to calculate such variations by correcting the weights of particles previously simulated by a standard TRIPOLI calculation for the non perturbed problem.

The same sample of neutrons is treated, so that a correlation factor appears, which improves the variance on the differential results.

CORRELATED SAMPLES METHOD

The neutronic properties of any medium are caracterized by the following nuclear constants :

- for each element, a set of microscopic cross sections which describes all the possible interactions between a neutron and this element, and a set of laws of the collision, determinating the energy and the direction of the particle after scattering ;
- for each composition,the atomic density of every isotope:these nuclear data, and the description of the geometry, define the linear transport operator of Boltzmann's equation.

The angular flux is the solution of this equation, for a fixed neutron source density and fixed boundary conditions.

More generally, a set of responses (scalar fluxes, currents, reactions rates, biological doses, ...) can then be calculated.

Perturbation theory is concerned with the variations of these responses when the transport operator is modified.

This theory can be applied to various problems, as concentrations, libraries or temperature effects, or sensitivity studies.

Many methods have been designed to solve the Boltzmann's equation and to calculate the influence of perturbations. They can be classified in two categories : analytical and statistical methods. We shall talk only about the second ones.

Methods of Monte Carlo

Methods of Monte Carlo solve the Boltzmann's equation by simulating the stories of a great number of neutrons.

The behaviour of one neutron is then caracterized by a chain of events $(x_0, \ldots . x_N)$ where x_i represents the coordinates $(\vec{r}_i, E_i, \vec{\Omega}_i)$ of the i^{th} collision of the neutron.

More generally, because of the use of splitting technics to improve the precision of the results, a tree of events is associated with each particle. A chain is then a sequence of consecutive events from the root x_0 (birth of the neutron) to a leaf x_N (end of simulation) of the tree.

When x_i is fixed, the next event x_{i+1} is chosen according to a law of probability which only depends on the values of the cross sections at the state x_i.

A weight ω_i is also assigned to the chain, which is brought up to date after each collision.

Statistical estimators for fluxes, currents or any response

can be defined as random variables which are function of the sequence of weights.

A response appears as the average value of such an estimator. The methods of Monte Carlo give also a statistical estimation of the relative uncertainty of the result, which is proportional to the square root of the variance of the estimator, and inversely proportional to the size of the population of source neutrons, for a number of simulated neutrons large enough.

The cost of a Monte Carlo calculation depends mainly on the number of simulated neutrons and on the average length of the chains.

Methods of Monte Carlo for the calculation of perturbations

A perturbation of the transport operator is considered, in a Monte Carlo point of view, as a modification of the laws of probability $(x_i \longrightarrow x_{i+1})$.

As for analytical methods, two independent calculations can be done to find the effect of a perturbation, by difference between the two results.

Two independent sets of trees are then created.

If this process is valid for great perturbations, it is very important to notice that infinitesimal ones cannot be reached this way :
The statistical uncertainty is inversely proportional to ΔR , where ΔR is the difference between the two responses, so that the uncertainty becomes infinite for small perturbations.

This impossibility no longer exists if the two calculations are correlated. The most natural way to insert a correlation factor is to consider that the same samples of trees have been created by both simulations.

It is obvious that, for small perturbations, the behaviour of a neutron is almost the same in both cases.

The influence of the perturbation is no more considered as a modification of the laws of collision with this model, but as a modification of the weights of the events.

Let the set of trees and the non perturbed weights be stored during the simulation of the first problem. The method used, called correlated samples method,consists in rebuilding each tree, in which each weight of each event is multiplied by a correction factor taking into account the perturbation.

This method is exact and does not make any hypothesis on the importance of the perturbation. Nevertheless, the dispersion of the corrected weights increases with its amplitude, so that the statistical uncertainty also increases.

This process has two advantages :

- a theoretical interest, because it can be proved that the uncertainty on the result is still finite when the perturbation converges uniformly to zero ;
- a practical interest, because no random processes are used, the events have been yet chosen. A deterministic correction of weight is only done. The time of calculation is improved in comparison with a standard Monte Carlo calculation.

Geometrical data are not needed, and the values of cross sections are only needed in the perturbed domain, so that the region used for computation is less important.

Several sets of perturbations can be simultaneously treated.

Scheme

The limitations of the amplitude of the perturbation only depend on the behaviour of the statistical uncertainty.

In order to explicit this dependence, we shall expose in next section two simple problems, for which the analytical expression of the uncertainty is given.

The choice of the corrections of weight in the general context of Boltzmann's equation and the study of variance do not appear in this paper.

First calculations of differential TRIPOLI, a Monte Carlist code of perturbations developped in the L.E.P., are described in the last section.

Differential TRIPOLI keeps the properties of TRIPOLI : a three dimensional treatment of polykinetic neutrons with no hypothesis on the isotropy of collisions.

The original trees of events arise from TRIPOLI.

CORRELATED SAMPLES METHOD APPLIED TO THE EXPONENTIAL AND RUSSIAN ROULETTE LAWS OF PROBABILITY

These two laws of probability are always used in Monte Carlo simulation of diffusion of particles. The random behaviour of any neutron is simulated by iterations of these elementary laws.

In infinite and homogeneous medium, and for monokinetic neutrons, their variances can be calculated. Their analytical expressions give a priori indications about the importance of permissible perturbations.

Sensitivity of the average path of a neutron to the total cross section of the medium

Original simulation

The free path of a neutron diffusing in a medium whose total cross section is σ_0, is $\frac{n}{\sigma_0}$ after n collisions.

A simple way to simulate the total travel lenght of one neutron is to choose a set of n independent values $(x_1, \ldots x_N)$, with the probability : $\sigma_0 \exp\{-\sigma_0 x_i\}\, dx_i$ for each event.

We score before each collision the quantity x_i, which is the contribution of the i^{th} event to the response.

The variance on the result is n/σ_0^2 and the statistical uncertainty $e(\sigma_0)$ is $1./\sqrt{n}$, independent of σ_0.

Let $\sigma_1 = \sigma_0 + \Delta\sigma$ be the total cross section of the perturbed medium. An independent simulation gives the response n/σ_1 with the variance n/σ_1^2.

The differential response $\Delta R = n/\sigma_1 - n/\sigma_0$ is obtained with the variance $n/\sigma_1^2 + n/\sigma_0^2$, so that the statistical relative uncertainty on ΔR is : $e(\Delta\sigma/\sigma_0) = \frac{1.}{\sqrt{n}} \cdot \frac{\sqrt{\sigma_0^2 + \sigma_1^2}}{\Delta\sigma}$, infinite when $\Delta\sigma \to 0$.

Correlated samples method

Let we now suppose that the chains still appear with the same probabilities ;

$$\prod_{i=1}^{n} \{\sigma_0 \exp(-\sigma_0 x_i)\}\, dx_1 \cdots dx_n$$

when the total cross section becomes σ_1, and assign a weight C_I to each event, determinated as follows :

$$C_0 = 1$$
$$C_i = C_{i-1} \cdot c(X_i)$$

where the value of x_i is known, and the elementary correction of weight $c(x_i)$ is the ratio of the perturbed probability : $\sigma_1 \exp\{-\sigma_1 x_i\}$ to the initial one : $\sigma_0 \exp\{-\sigma_0 x_i\}$

It can be proved that, if we score the value $C_i . x_i$ for the i^{th} collision, the average total score is the expected result n/σ_1.

The variance is no longer equal to n/σ_1^2, but is :

$$\sigma^* = 2 \cdot \frac{\sigma_1 \sigma_0}{(\Delta\sigma)^4} \left[(1-\xi)(1-\xi^n)\frac{\sigma_0}{\sigma_1} + \xi^n - n\xi + n - 1 \right] - \frac{n^2}{\sigma_1^2}$$

where $\xi = \frac{\sigma_1^2}{\sigma_0(2\sigma_1 - \sigma_0)} > 0$

It is important to notice that σ^* is undefinite when σ_1 is less than $\frac{\sigma_0}{2}$

Fig 1

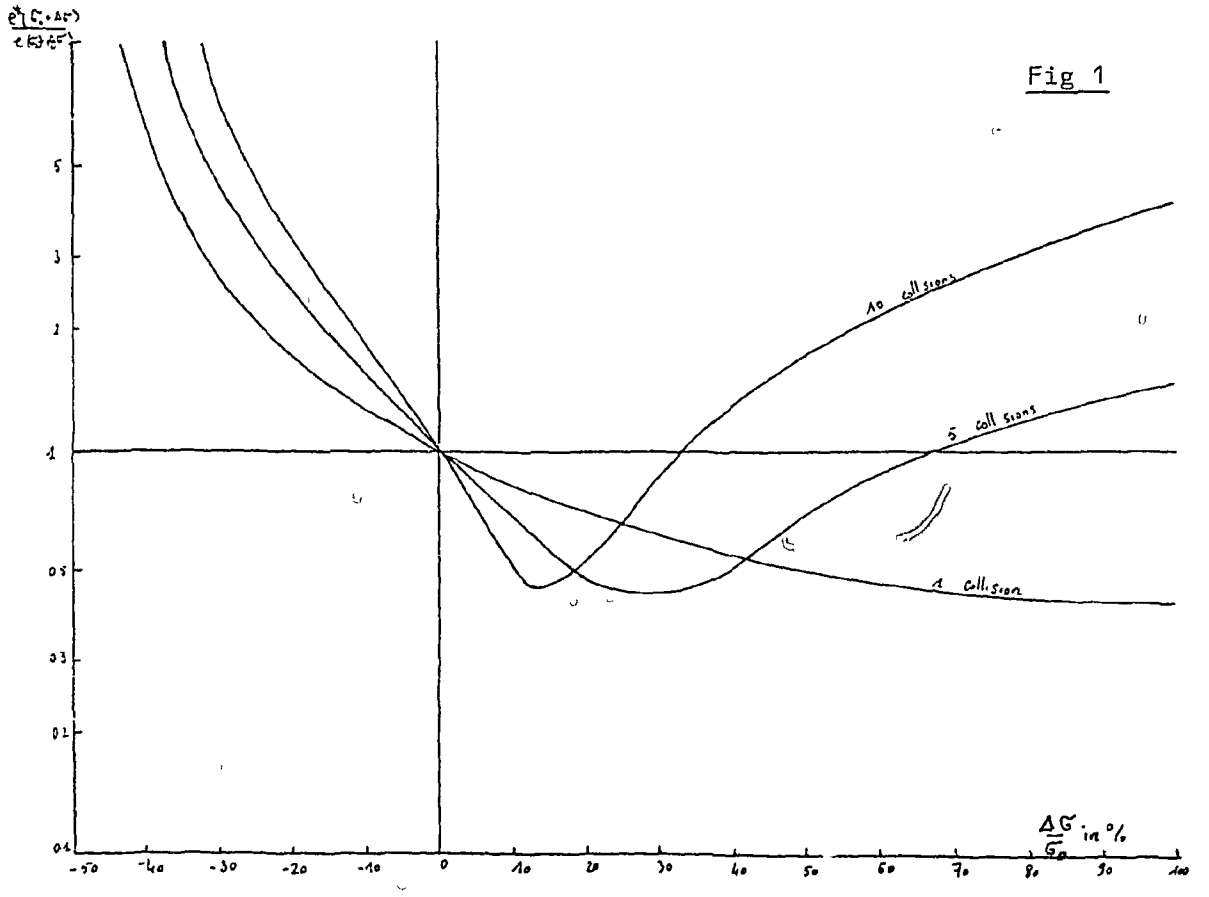

The ratio of the relative uncertainty on the response, with this estimation to the independent calculation one is showned on (fig.1). The process improves the precision when this ratio is less than 1, and is nothing else than exponential biasing technic.

Let us now consider the differential response ΔR.

The variance on ΔR is : $\sigma^*(\Delta R) = n/\sigma_0^2 + \sigma^* - 2.\,cov$

where cov covariance of the two estimators, is : $cov = \frac{n}{2\sigma_1}\left\{\frac{n+3}{\sigma_1} - \frac{n+1}{\sigma_0}\right\}$

The limit of $e^*(\Delta\sigma/\sigma_0)$, relative uncertainty on the differential effect estimated by the correlated samples method, is finite in this case when $\Delta\sigma \to 0$, and equal to :

$$e(\sigma_0).\sqrt{\frac{n^2+9n+29}{3}} \geq 3.11\, e(\sigma_0)$$

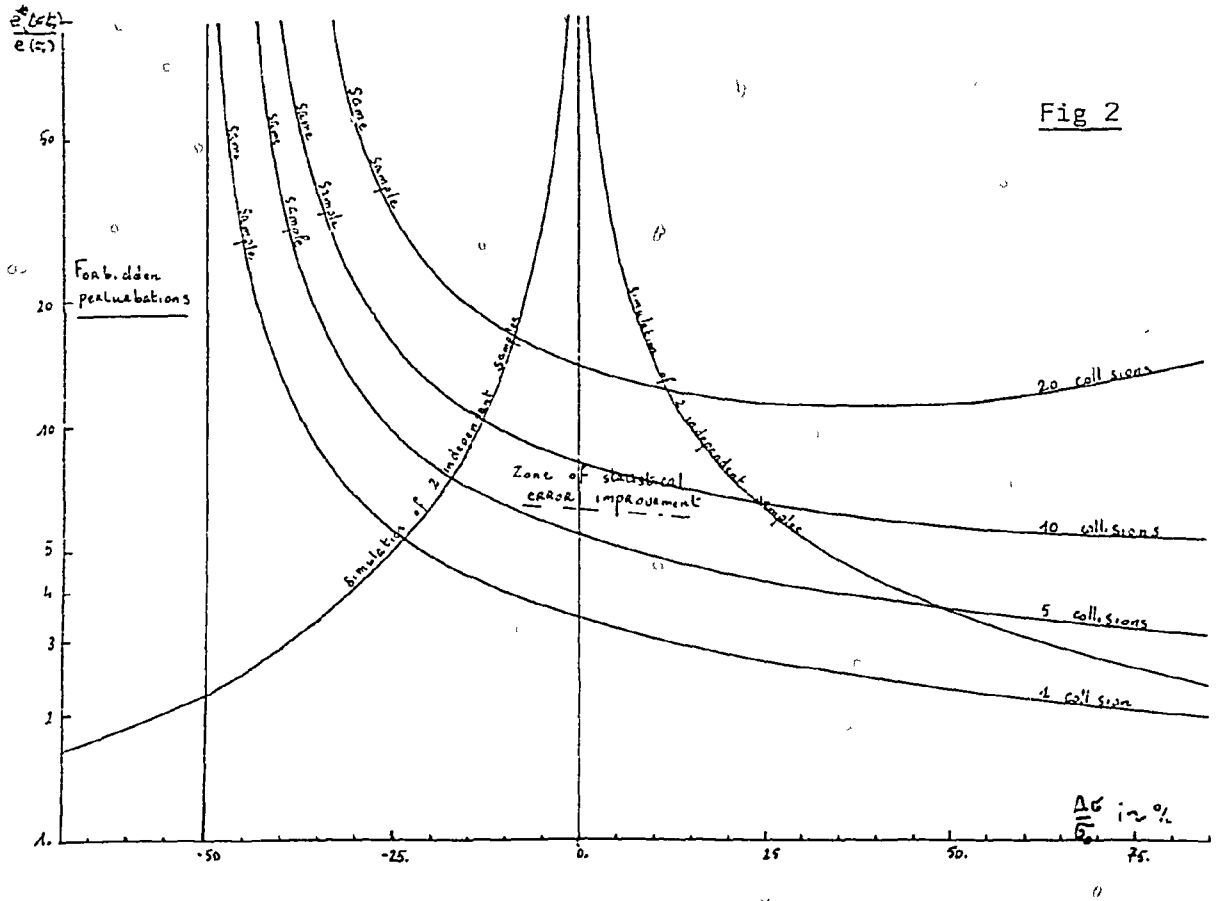

Fig 2

Fig.2 shows the variations of $e^*(\Delta\sigma/\sigma_o)/e(\sigma_o)$ for a set of values of n, number of collisions .

The uncertainty increases with the number of collisions and has important variations for negative perturbations, especially close to the asymptot .

Sensitivity of the number of collision to non capture probability

Original simulation

We create in this examples chains of variable length $(x_1 \ldots x_N)$. if c_o is the probability of non capture, the neutron survies after each collision with the probability c_o, and we add $x_i = 1$ to the total score. The neutron is killed with the probability $1.-c_o$

The probability for a neutron to have exactly n collisions is $c_o^n\,(1.-c_o)$

The average score is $\frac{1}{1-c_o}$ the variance is $\frac{c_o}{(1-c_o)^2}$ and the relative uncertainty is $e(c_o) = \sqrt{c_o}$

When the non capture probability becomes $c_1 = c_o + \Delta c$, an independent simulation gives the uncertainty :

$$e\left(\frac{\Delta c}{c_o}\right) = \sqrt{c_1(1-c_o)^2 + c_o(1-c_1)^2}\cdot\frac{1}{\Delta c}$$

on the differential response $\Delta R = \frac{\Delta c}{(1-c_1)(1-c_o)}$ which is also infinite when $\Delta c \longrightarrow 0$

Correlated samples method

We assign again a weight C_i to each event :

$$C_o = 1$$

$$C_i = C_{i-1} \times c(x_i)$$

where the elementary correction of weight $c(x_i)$ is the ratio : $\frac{c_1}{c_o}$

The average value of the perturbated score $\sum_{i=0}^{\infty} C_i x_i$ is the expected mean $\frac{1}{1-C_1}$.

The variance is then equal to :

$$\frac{C_1}{(1-C_1)^2} \cdot \frac{1-C_0}{(C_0-C_1^2)} \quad \text{for } C_1 < \sqrt{C_0}$$

The process improves the precision in comparison of an independent simulation if $C_1 < C_0$

The covariance of the two estimators is also $cov = \frac{C_1}{(1-C_1)^2}$, so that the limit of $e^*(\Delta c/c_0)$, relative uncertainty on the differential effect estimated by the correlated samples method, is still finite when $\Delta c \to 0$, and equal to :

$$e(C_0) \cdot \sqrt{\frac{5C_1 + (1-C_0)^2}{C_0^2}} \geq 2.24\, e(C_0)$$

Fig 3

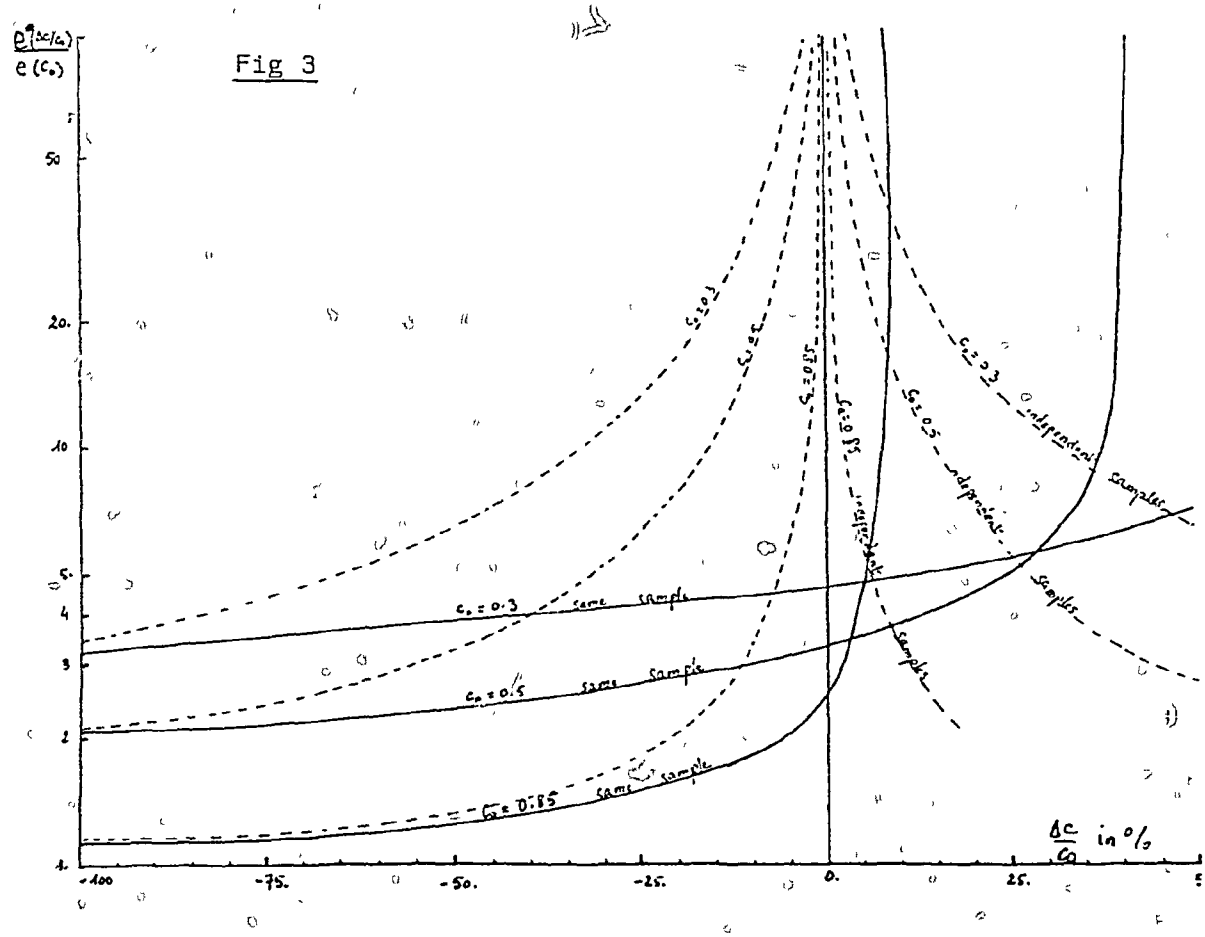

Fig 3 represents the ratio of the uncertainty of differential effects to the uncertainty of the non perturbed response. The uncertainty decreases when the value of c_o increases, for a fixed perturbation.

The precision by the correlated samples method is always better than by the independent samples estimation (dotted curve) for negative perturbations, but is quickly downgraded for positive ones because of the asymptot value $\sqrt{c_o}$.

FIRST MONTE CARLO CALCULATIONS BY DIFFERENTIAL TRIPOLI

Comparison between TRIPOLI results and analytical formulas in infinit medium and for monokinetic neutrons

Let us consider an infinite, homogeneous and non multiplicator medium in which monokinetic neutrons diffuse with isotropic collisions.

Let σ and C be respectively the total macroscopic cross section and the non capture probability of this medium.

Let the neutron source be also isotropic and localized in the plane x = 0, and S its norm.

The neutron angular flux can be obtained by solving the one dimensional Boltzmann's equation :

$$(1) \qquad \mu \frac{\partial \varphi(x,\mu)}{\partial x} + \sigma \varphi(x,\mu) = \frac{c\sigma}{2} \int_{-1}^{+1} \varphi(x;\mu)\, d\mu \qquad (x \neq 0)$$

with the boundary condition on current :

$$(2) \qquad \lim_{x \to 0} \{ \mu \varphi(x,\mu) - \mu \varphi(-x,\mu) \} = \frac{S}{4\pi}$$

Theoretical results ; analytical method

Transport theory proofs that flux integrated upon μ can be decomposed into an asymptotic term $\varphi_{as.}$ and a non asymptotic one, φ_t The first term is predominant at large distances from the source, and its analytical expression is :

$$(3) \qquad \varphi_{as.}(x,\sigma,C) = \frac{2S}{\theta[\alpha(c),c]}\, e^{-\alpha(c)\,\sigma\, x}$$

The functions $\alpha(c)$ and $\Theta(\alpha;c)$ are given by the relations :

(4) $$\text{Log}\left[\frac{1+\alpha(c)}{1-\alpha(c)}\right] = \frac{2\,\alpha(c)}{c}$$

(5) $$\Theta(\alpha,c) = \frac{2c^2}{\alpha}\left[\frac{1}{1-\alpha^2} - \frac{1}{c}\right]$$

Equation (4) can be easily solved by the numerical method of Newton with a very good precision.

Formulas (3), (4) and (5) have been computed to calculate $\varphi_{as.}$ for any values of σ, C and x.

Non perturbed problem, TRIPOLI calculation

The composition of the medium is made up of two fictitious elements, whose caracteristics are :

Element	Mass	Capture cross section (barns)	Scattering cross section (barns)	Atomic density (at/cm^3)
1	1.E 06	0.4	1.6	2.E 23
2	1.E 06	0.3	2.7	3.E 23

The atomic masses have been chosen equal to 1.E 06 so that the collisions were isotropic in the laboratory system, and the loss in energy neglectible after each collision.

The parameters of equation (3) are then :

σ_o	1.3 cm^{-1}
C_o	0.86923
$\alpha(C_o)$ given by (4)	0.59283
$K_o = \alpha(C_o) \cdot \sigma_o$	0.77068 cm^{-1}

The geometry is a 17 cm wide slab, divided in 13 meshes. The last one is 5 cm wide, with a leakage condition at the boundary, the others are 1 cm wide.

A spatial function of importance : $\mathcal{J}(x) = \exp\{+H_o x\}$ has been assigned to the medium, where K_o is the theoretical attenuation factor of the asymptotic flux, so that the number of simulated collisions is almost constant per unit of volume.

The average fluxes per mesh have been calculated from a sample of 300 neutrons, and are given in the following table:

Mesh	Asymptotic flux (from the analytical expression) neutron.cm^{-2}.s^{-1}	Flux calculated by TRIPOLI (track lenght estimator) neutron.cm^{-2}.s^{-1}	66 % relative uncertainty (in %)
1	1.397	1.743	3.41
2	6.466 E-1	6.990 E-1	4.25
3	2.992 E-1	3.107 E-1	2.27
4	1.384 E-1	1.409 E-1	1.56
5	6.405 E-2	6.270 E-2	3.33
6	2.964 E-2	2.930 E-2	3.63
7	1.371 E-2	1.352 E-2	3.35
8	6.345 E-3	6.465 E-3	4.47
9	2.936 E-3	2.952 E-3	6.89
10	1.358 E-3	1.442 E-3	5.97
11	6.286 E-4	6.310 E-4	6.80
12	2.908 E-4	2.920 E-4	3.92
13	4.903 E-5	4.926 E-5	5.99

TABLE 1 - Average scalar flux per region
for the non-perturbed problem

We verify that TRIPOLI results are in good agreement with the expected values, excepted in the two first regions, because TRIPOLI takes into account the non asymptotic term.

The concordance of the results in the 13th region shows that leakage is neglectible.

The 300 trees have been stored and can be used for further perturbation calculation.

Perturbations of the total cross section σ_o

We have calculated simultaneously the influence of fifteen perturbations of σ , for a fixed value of C_o ($C = C_o = 0.86923$)

For each perturbation, we have noted that the variance on the flux increases with x.

This effect can be explained by the study of the exponential law (§ 2) : in the first meshes close to the source, only the first collisions of the simulated neutrons contribute to the score, so that the dispersion of the corrections of weight is weaken than in the last ones.

Perturbation	φ_{AS} (from the analytical expression) neutronxcm^{-2}xs^{-1}	φ_{MC} (by differential TRIPOLI) track lenght estimator neutronxcm^{-2}xs^{-1}	66 % relative uncertainty on φ_{MC} (in %)	$\left\|\frac{\varphi_{MC} - \varphi_{AS}}{\varphi_{AS}}\right\|$ (in %)
σ : - 75 %	5.333 E-1	3.025 E-1	59.68	43.28
σ : - 50 %	1.488 E-1	1.095 E-1	18.11	26.40
σ : - 40 %	9.047 E-2	7.941 E-2	15.26	12.22
σ : - 30 %	5.536 E-2	5.268 E-2	11.51	4.84
σ : - 20 %	3.409 E-2	3.329 E-2	6.92	2.36
σ : - 10 %	2.112 E-2	2.085 E-2	4.11	1.27
σ : - 1 %	1.381 E-2	1.366 E-2	3.83	1.05
non-perturbed problem	1.316 E-2	1.315 E-2	3.53	9.44 E-2
σ : + 1 %	1.255 E-2	1.247 E-2	3.85	0.64
σ : + 10 %	8.240 E-3	8.385 E-3	3.63	1.75
σ : + 20 %	5.186 E-3	5.425 E-3	4.17	4.62
σ : + 30 %	3.278 E-3	3.541 E-3	5.44	8.01
σ : + 40 %	2.081 E-3	2.307 E-3	7.68	10.87
σ : + 50 %	1.326 E-3	1.485 E-3	11.02	12.01
σ : + 75 %	4.359 E-4	4.460 E-4	21.74	2.31
σ : + 100 %	1.459 E-4	1.094 E-4	30.57	25.03

TABLE 2 - VARIATIONS OF THE PERTURBED AVERAGE FLUX IN THE MIDDLE ZONE : 5 cm - 9 cm IN FUNCTION OF σ (C CONSTANT)

Table 2 gives average values of perturbed fluxes in the middle region 5 cm-9 cm, in which the non-asymptotic component of the fluxes and the influence of leakage are neglectible.

We notice that for perturbations from - 30 % to + 50 %, the results are correct, the ratio of the statistical uncertainties of the perturbated games to the original one does not exceed 3.

A great degradation of precision appears for $-0.75 \leq \Delta\sigma/\sigma_o \leq -0.5$ Section 2 gives the limit value of permissible perturbations :

$\sigma_{as} = \sigma^*/2 = (\sigma_o - H_o)/2$ if we take into account the function of importance.

The numerical value of $(\sigma - \sigma_{as})/\sigma_o$ is then : - 79.6 %.

Perturbations	$\frac{\Delta \varphi_{mc}}{\varphi^{\circ}_{m.c.}}$	$\Delta \varphi_{as}$ (from the analytical expression) neutron x cm^{-2} x s^{-1}	$\Delta \varphi_{mc}$ (by differential TRIPOLI) track lenght estimator neutrons x cm^{-2} x s^{-1}	66 % relative uncertainty on $\Delta \varphi_{mc}$ in %	$\left\lvert \frac{\Delta \varphi_{mc} - \Delta \varphi_{as}}{\Delta \varphi_{as}} \right\rvert$ in %
σ : - 75 %	22	5.201 E-1	2.893 E-1	62.29	44.38
σ : - 50 %	7.33	1.357 E-1	9.641 E-2	20.36	28.94
σ : - 40 %	5.04	7.731 E-2	6.625 E-2	17.93	14.30
σ : - 30 %	3.01	4.220 E-2	3.953 E-2	14.69	6.32
σ : - 20 %	1.53	2.093 E-2	2.014 E-2	10.03	3.78
σ : - 10 %	5.86 E-1	7.962 E-3	7.708 E-3	6.25	3.19
σ : - 1 %	4.64 E-2	6.341 E-4	6.108 E-4	4.86	3.67
σ : + 1 %	- 4.43 E-2	- 6.046 E-4	- 5.821 E-4	3.94	3.72
σ : + 10 %	- 3.62 E-1	- 4.918 E-3	- 4.759 E-3	3.82	3.23
σ : + 20 %	- 5.87 E-1	- 7.972 E-3	- 7.720 E-3	3.48	3.17
σ : + 30 %	- 7.30 E-1	- 9.880 E-3	- 9.604 E-3	3.22	2.79
σ : + 40 %	- 8.24 E-1	- 1.108 E-2	- 1.084 E-2	3.05	2.16
σ : + 50 %	- 8.87 E-1	- 1.183 E-2	- 1.166 E-2	3.01	1.48
σ : + 75 %	- 9.66 E-1	- 1.272 E-2	- 1.270 E-2	3.18	1.90 E-1
σ : + 100 %	- 9.91 E-1	- 1.301 E-2	- 1.303 E-2	3.39	1.67 E-1

TABLE 3 - VARIATIONS OF THE DIFFERENTIAL EFFECT $\Delta \varphi_{mc} = \varphi_{m.c.}(\sigma) - \varphi_{mc}(\sigma_o)$ IN THE MIDDLE ZONE : 5 cm - 9 cm IN FUNCTION OF σ (C CONSTANT)

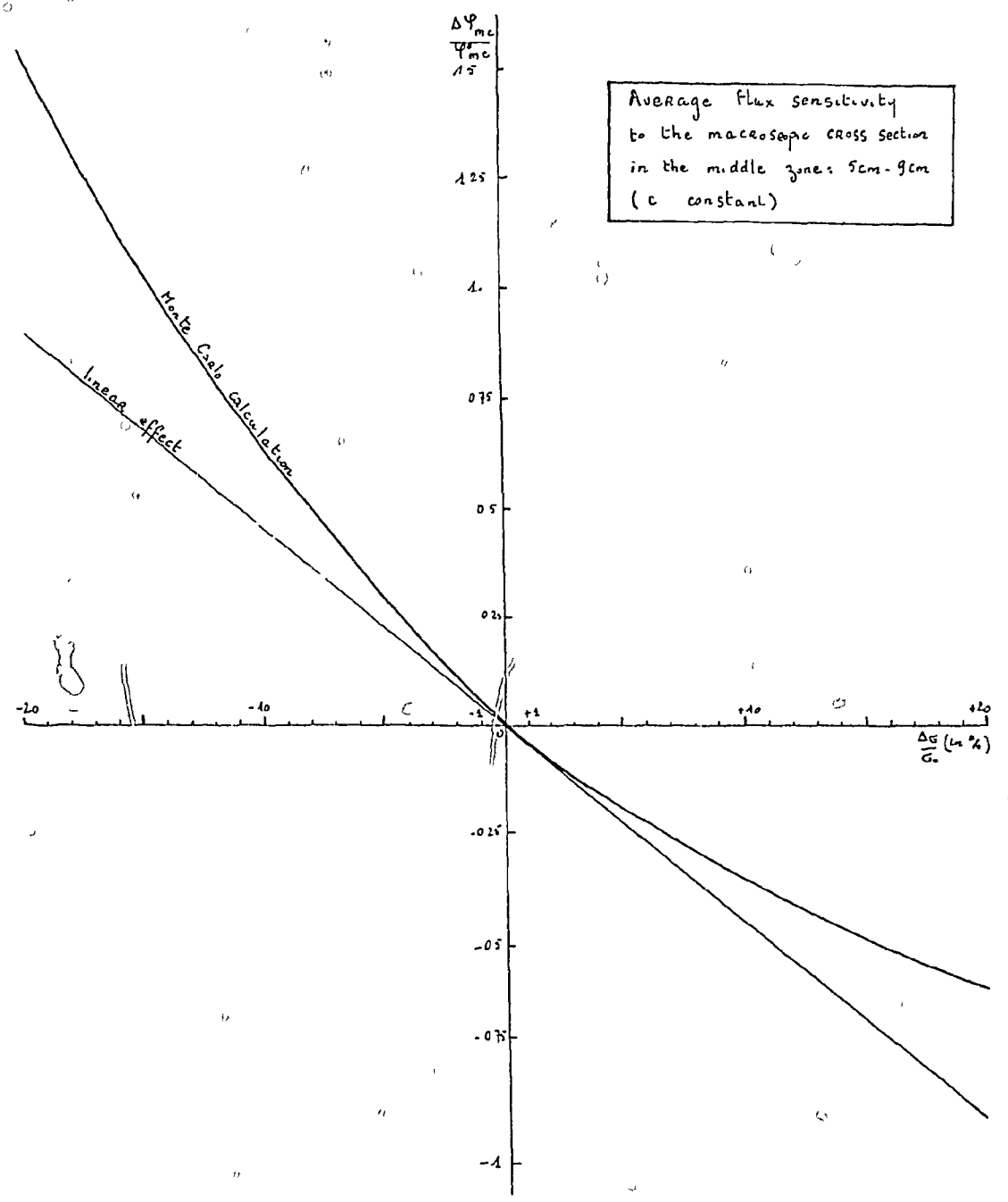
Average flux sensitivity to the macroscopic cross section in the middle zone: 5cm - 9cm (c constant)
Monte Carlo calculation
linear effect
1.5
1.25
1.
0.75
0.5
0.25
-0.25
-0.5
-0.75
-1
-20
-10
-2
+2
+10
+20
0

Fig 4

The same remarks can be done on table 3 for the differential results.

Table 3 and figure 4 prove that the method of correlated samples is still valid in a domain of iron-linearity.

Perturbations of the non-capture probability C_o

Perturbed fluxes have been calculated for a set of values of C, for a fixed value of σ.

A fixed value of C, can be obtained by several ways, by combinations of perturbations of non-capture probability of each isotope.

For highly dissymetrical perturbations of these probabilities, the uncertainty on the result is very important, even for small global perturbations of C.

Tables 4 and 5 have been calculated under the hypothesis that the microscopic total cross sections and the atomic densities of both elements are constant.

The limit of the permissible perturbations is : $\frac{\sqrt{C_o} - C_o}{C_o} = 7.26\ \%$

Perturbations	α (C)	φ_{as} (from the analytical expression) neutrons x cm^2 x s^{-1}	φ_{mc} (by differential TRIPOLI) track lenght estimator neutrons x cm^{-2} x s^{-1}	66 % relative uncertainty on φ_{mc} (in %)	$\left\lvert \frac{\varphi_{mc} - \varphi_{as}}{\varphi_{as}} \right\rvert$ (in %)
C : - 20 %	0.83302	9.550 E-4	9.589 E-4	2.17	4.08 E-1
C : - 10 %	0.73501	2.884 E-3	2.859 E-3	2.83	8.62 E-1
C : - 1 %	0.60985	1.098 E-2	1.096 E-2	3.36	1.82 E-1
C : - 0.1 %	0.59456	1.292 E-2	1.290 E-2	3.52	1.43 E-1
non - perturbed problem	0.59283	1.316 E-2	1.315 E-2	3.53	9.44 E-2
C : + 0.1 %	0.59108	1.340 E-2	1.339 E-2	3.55	7.46 E-2
C : + 1 %	0.57498	1.590 E-2	1.590 E-2	3.74	6.29 E-3
C : + 5 %	0.49364	3.802 E-2	3.799 E-2	5.22	8.55 E-2

TABLE 5 - VARIATIONS OF THE PERTURBED AVERAGE FLUX IN THE MIDDLE ZONE : 5 cm - 9 cm IN FUNCTION OF C (σ CONSTANT)

Perturbations	$\frac{\Delta\varphi_{mc}}{\varphi^{o}_{mc}}$	$\Delta\varphi_{as.}$ (from the analytical expression) neutronsxcm^{2}xs^{-1}	$\Delta\varphi_{mc}$ (by differential TRIPOLI) track-lenght estimator neutronsxcm^{-2}xs^{-1}	66 % relative uncertainty on $\Delta\varphi_{m.c}$ (in %)	$\left\lvert\frac{\Delta\varphi_{mc}-\Delta\varphi_{as.}}{\Delta\varphi_{as}}\right\rvert$ (in %)
C : - 20 %	- 9.27	- 1.220 E-2	- 1.219 E-2	3.67	8.20 E-2
C : - 10 %	- 7.82 E-1	- 1.027 E-2	- 1.028 E-2	3.81	9.74 E-2
C : - 1 %	- 1.66 E-1	- 2.175 E-3	- 2.183 E-3	4.43	3.68 E-1
C : - 0.1 %	- 1.84 E-2	- 2.406 E-4	- 2.416 E-4	4.59	4.16 E-1
C : + 0.1 %	1.88 E-2	2.462 E-4	2.470 E-4	4.62	3.25 E-1
C : + 1 %	2.10 E-1	2.746 E-3	2.757 E-3	4.79	4.00 E-1
C : + 5 %	1.89	2.486 E-2	2.484 E-2	6.14	8.05 E-2

TABLE 5 : VARIATION OF THE DIFFERENTIAL EFFECT $\Delta\vec{\varphi}_{mc} = \varphi_{mc}(c) - \varphi_{m.c}(c_o)$

IN FUNCTION OF C

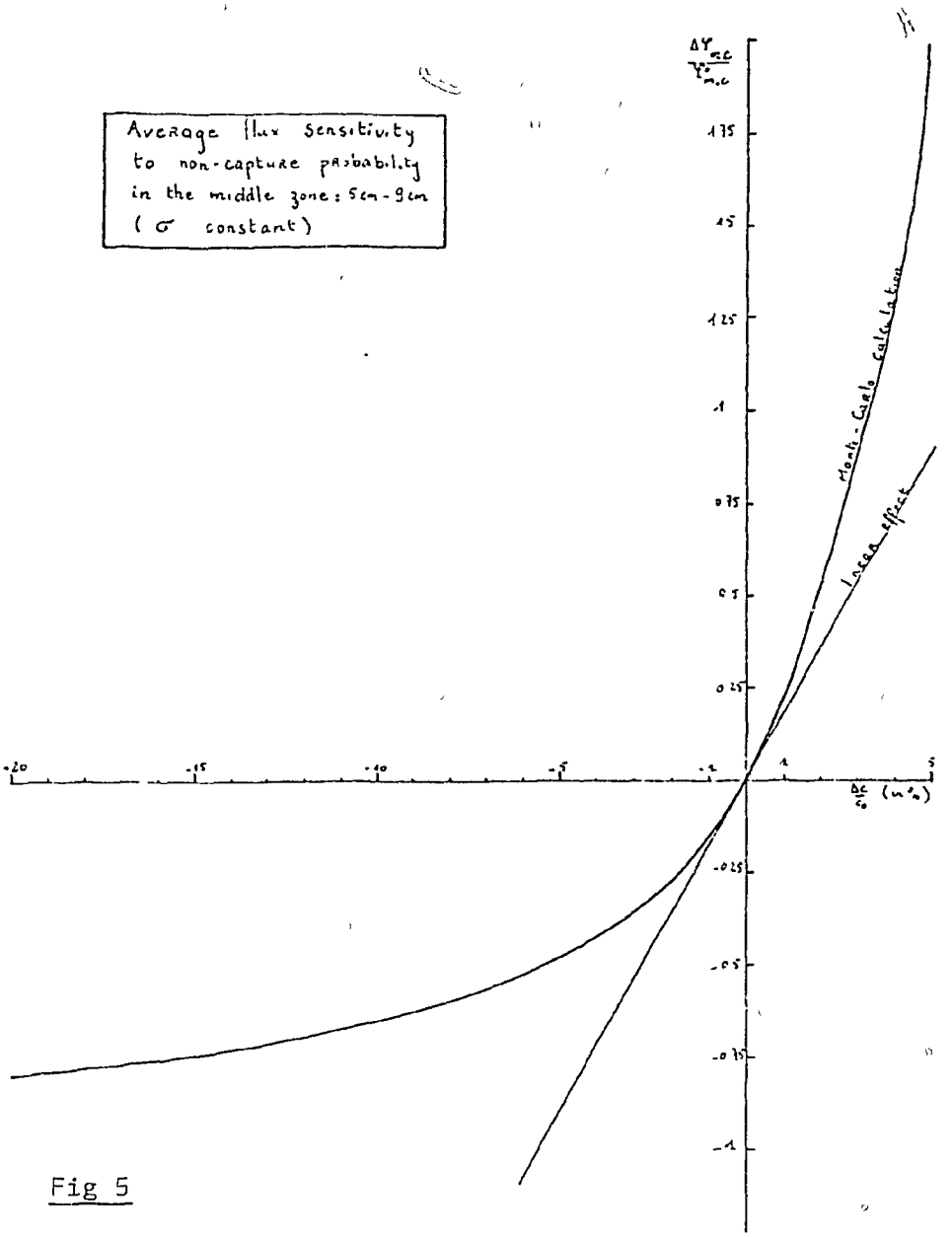

Fig 5

Similar remarks as for total cross section perturbations can be done. Figure 5 shows the non linear effects observed in the middle region and calculated by differential TRIPOLI.

Comparison between differential TRIPOLI and ANISN for polykinetic neutrons

We want to calculate the sensitivity of the biological dose at the boundary surface of a simplified shipping cask to the cross sections of iron, for a set of intervals of energy.

The geometry is a 32.2 cm wide cylinder of infinite height. The compositions are :

1. Neutron source :

The source of neutrons consists in a mixture of PuO_2.

2. Iron :

Fe	8.466 E22 at/cm^3

3. Plaster :

H	6.31 E22 at/cm^3
O	1.79 E22 at/cm^3
B10	6.60 E20 at/cm^3
C	2.15 E22 at/cm^3
Ca	3.76 E21 at/cm^3

The density of neutron source is spatially constant, and localized between the radius 0 and 6.4 cm.

The energetic spectrum is the fission spectrum of Pu corrected with (α , n) productions of neutrons on O_2.

Then follow a 12 cm wide lump of iron, a 13 cm wide lump of plaster and a 0.8 cm slab of iron.

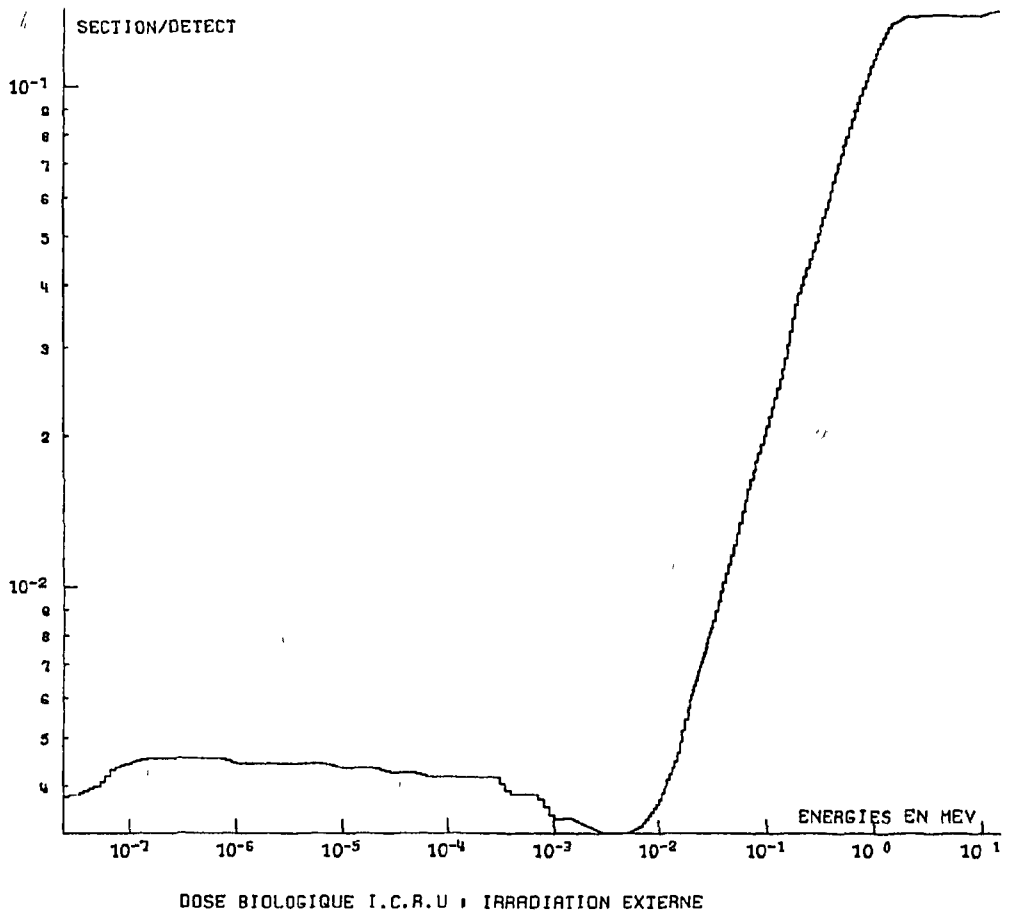

The detector r (E) is given by figure 6.

ANISN direct and adjoint calculations

Both calculations have been performed with a 100 groups standard discretization in energy.

Anisotropies are treated in P_3 approximation with S_8 quadrature. The origin of cross sections in ENDF/B3 library.

The adjoint source is a shell source localized at the radius 32.2 cm

$$S^{+}(R_{ext}; E; \mu) = \frac{r(E)}{2\pi R_{ext} \cdot \mu}$$

where μ is the cosine of the direction of the adjoint source particle and the normal to the external cylinder, of radius R_{ext}.

The integrated dose is (by both calculations) : $D(R_{ext}) = 4.49$ mrem/h.

TRIPOLI calculation

The calculation have been performed with a sample of 1500 neutrons, using exponential transform . The cross sections come from the UKNDL library and are integrated in the standard 269 multigroup mesh of TRIPOLI.

Angles of scattering are sampled from equal probabilities cosines.

The integrated dose is :

D (R_{ext}) = 6.24 mrem/h with a 3.14 % uncertainty.

Fig. 7

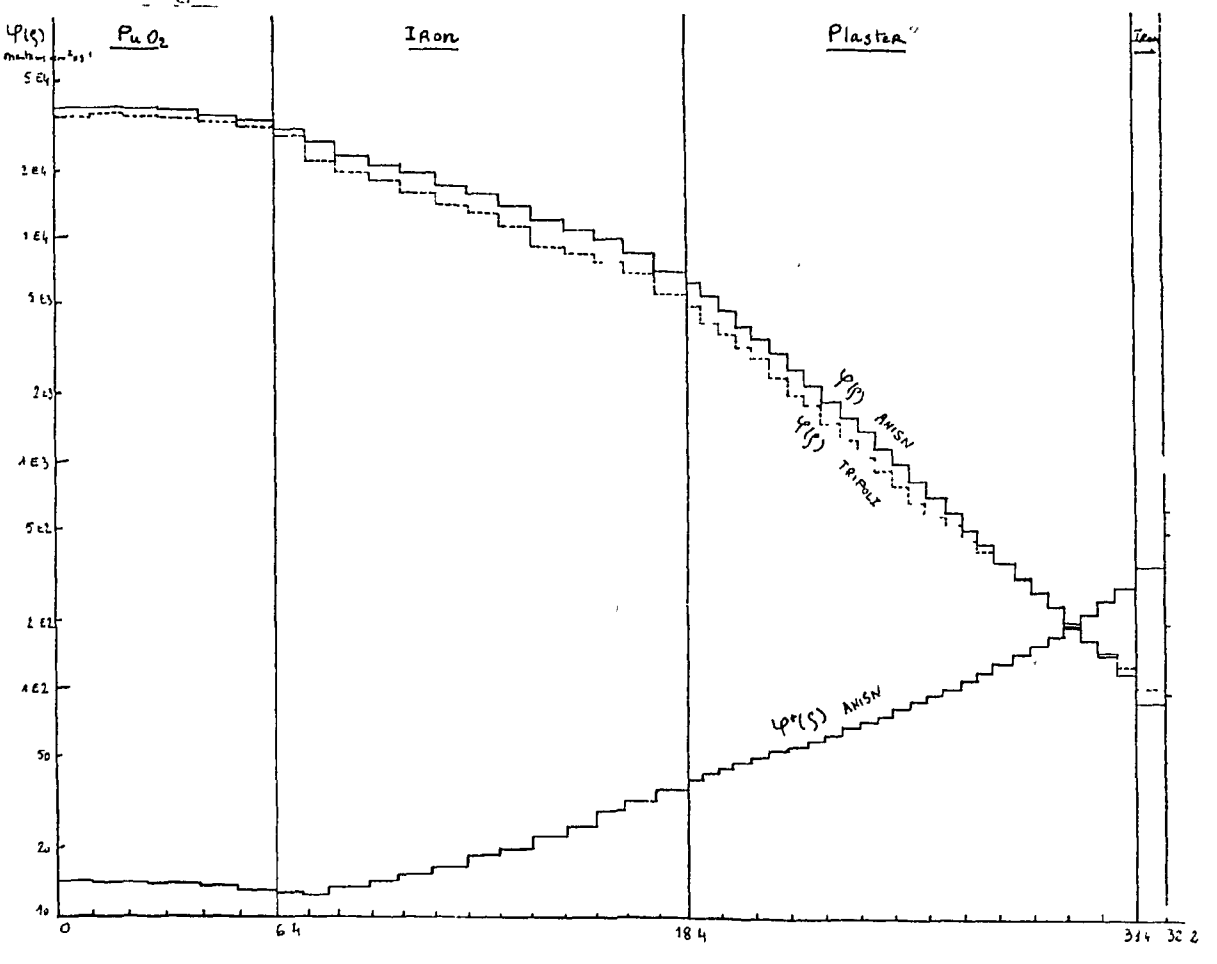

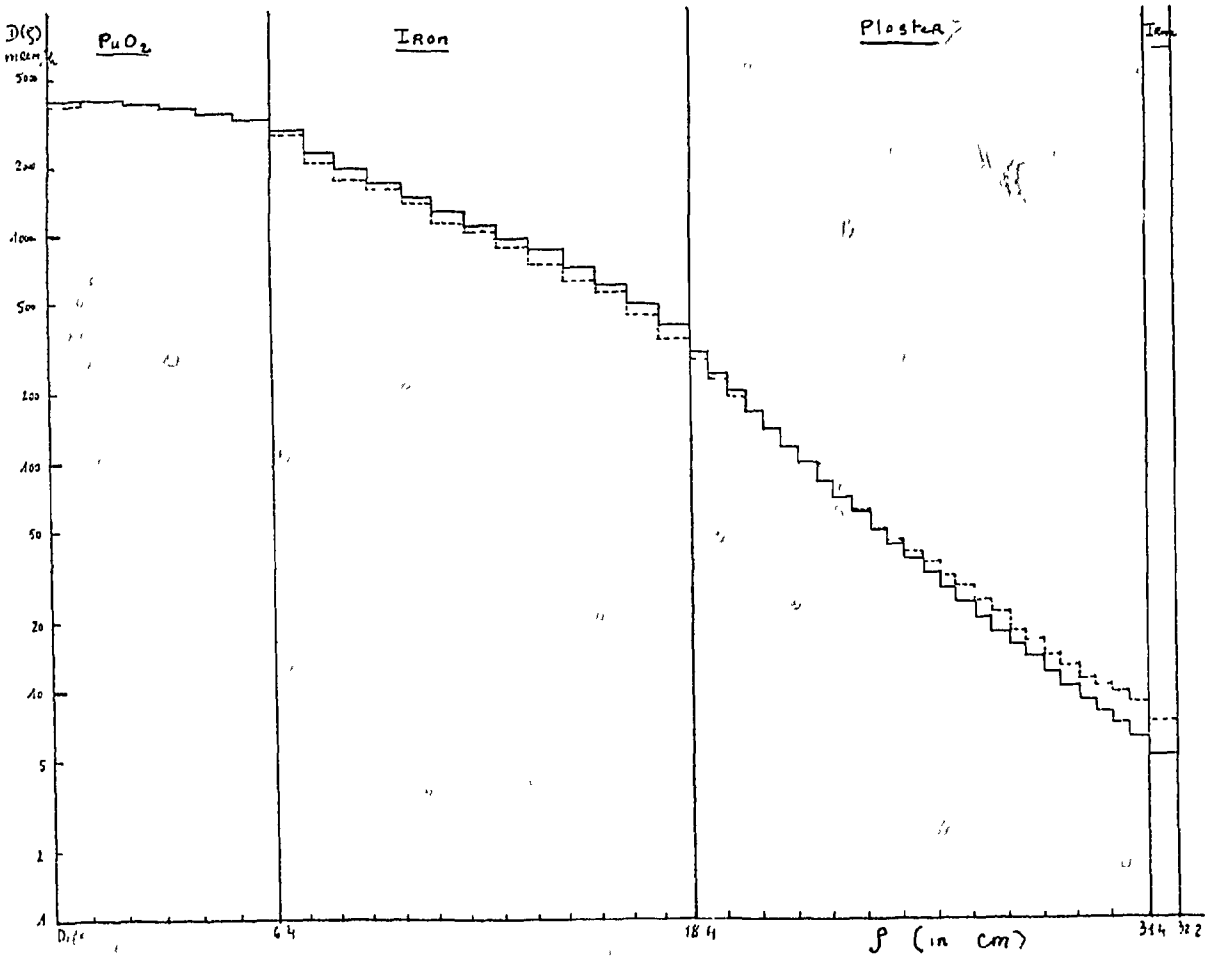

Fig 8 ------ dose TRIPOLI
——— dose ANISN

Fig 7 gives the spatial variations of the direct fluxes calculated by ANISN and TRIPOLI, and of the adjoint flux calculated by ANISN.

Fig 8 gives the spatial distribution of the dose. The difference between TRIPOLI and ANISN can be explained by the difference of microscopic data used and by the great (3 decades) attenuation.

Sensitivity calculations

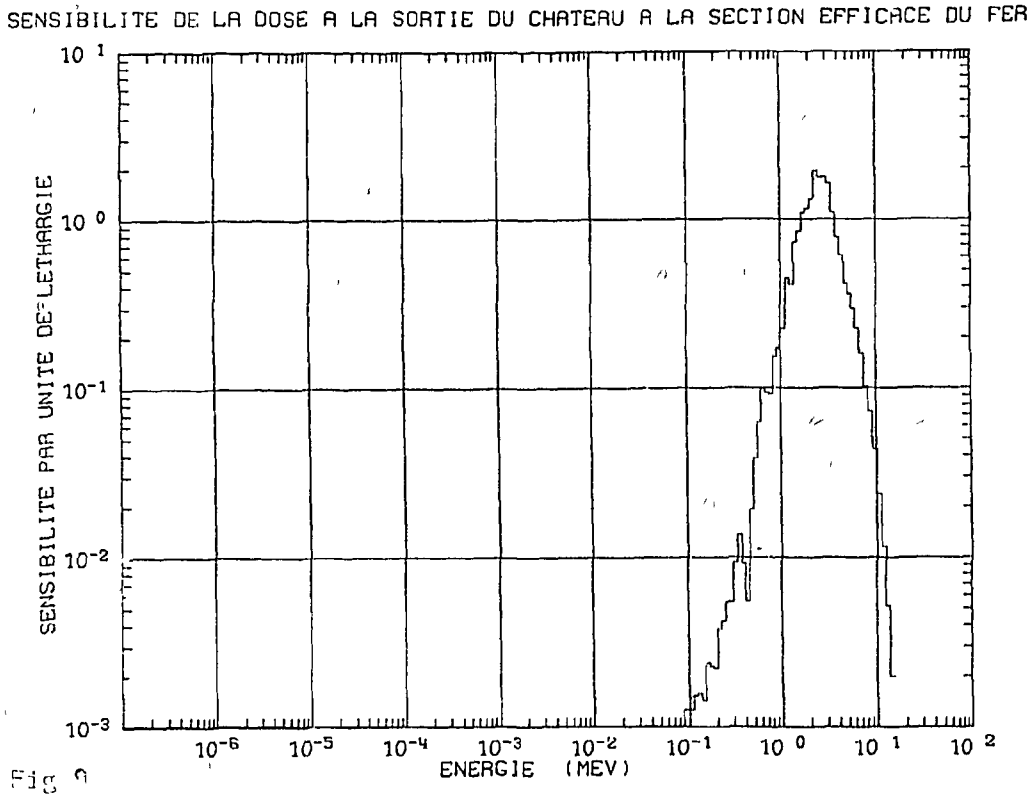

Fig 9

Figure 9 shows the sensitivity profile calculated by SWANLAKE from the angular direct and adjoint ANISN fluxes, under the hypothesis of linearity.

Energies (MeV)	Sensitivity calculated by SWANLAKE (in %)	Sensitivity calculated by Monte Carlo (in %)	66 % Relative uncertainty (in %)
14.8 - 3.35	- 4.142 E-1	- 6.654 E-1	8.33
3.35 - 2.661	- 3.882 E-1	- 3.693 E-1	13.12
2.661 - 2.239	- 3.190 E-1	- 2.497 E-1	17.77
2.239 - 1.679	- 3.451 E-1	- 2.550 E-1	12.49
1.679 -2.258 E-8	- 3.639 E-1	- 2.416 E-1	21.
14.8 - 2.258 E-8	- 1.830	- 1.783	5.79

TABLE 6 : SENSITIVITY OF THE BIOLOGICAL DOSE TO +1% PERTURBATION OF IRON CROSS SECTIONS

Table 6 is a comparison of SWANLAKE and differential TRIPOLI results for five groups.

The sensitivities per group are not in agreement, may-be because of the different origins of the libraries or the treatment of anisotropy.

For 1 % perturbation, the variance per group compared with the total variance of the non-perturbed problem is multiplied with a 2 to 4 factor.

This fact proofs that, for localized perturbations, variance is very dependent on the width of the energetical intervals, because the number of neutrons which contribute to the score is weak. Energy dependent functions of importance must be used to solve such problems to improve the variance.

The width of the iron lump is large enough to observe a non-linearity effect, when the perturbation is more important :

	SWANLAKE (in %)	MONTE CARLO (in %)	UNCERTAINTY (in %)
Perturbation of 1 % (14MeV - 0.8236 MeV)	- 1.78822	- 1.7121	5.22
Perturbation of 20 % (14MeV - 0.8236 MeV)	- 35.644	- 28.960	4.65

CONCLUSION

The first results of differential TRIPOLI are encouraging. Some problems are still to solve :

In a general context, it would be interesting to have criterions to evaluate a priori the uncertainty for light perturbations, and on the contrary to calculate the amplitude of the maximum permissible ones because the distribution of the scores per batch becomes non Gaussian so that the uncertainty is often under-estimated.

For localized perturbations, the information will be improved if more neutrons are sampled in the perturbed zone.

Biasing methods used to solve the unperturbed problem have to take into account this fact, without downgrading the precision on the non-perturbed score.

Some tests are going on to calculate variations of temperature in cells.

Blank

TRIMARAN : A THREE DIMENSIONAL MULTIGROUP P1 MONTE CARLO CODE FOR CRITICALLITY STUDIES

G. ERMUMCU - J. GONNORD - J.C. NIMAL

COMMISSARIAT A L'ENERGIE ATOMIQUE - Service SERMA

LABORATOIRE DE PROTECTION

SACLAY - B.P. N° 2 - 91190 GIF SUR YVETTE -

FRANCE

ABSTRACT

TRIMARAN is developped for safety analysis of nuclear components containing fissionnable materials : shipping casks, storage and cooling pools, manufacture and reprocessing plants. It solves the transport equation by Monte Carlo method in general three dimensional geometry with multigroup P1 approximation. A special representation of cross sections and numbers has been developped in order to reduce considerably the computing cost and allow this three dimensional code to compete with standard numerical program used in parametric studies.

As well as nuclear reactor safety, auxiliary components safety such as shipping cask, fuel storage pools and reprocessing plants has become of major importance and the restrictions requested by the safety regulations may affect the entire nuclear program.

Following actual safety regulations, all units containing fissile materials should'nt present any risk of nuclear chain reaction, and pre computation should guarantee that - even in all possible types of accident - such as : fire, handling error, flooding, geometric deformation following

falls or seism -the effective neutron multiplication constant (keff) is less than 1., all cross section and computation uncertainties evaluated.

The ever growing quantities of fissile materials to be stored, shipped and reproccessed demand more accurate calculations because large uncertainties do not allow to run such units at their optimal capacity.

Let us have a look on the following example : the effective neutron multiplication constant (keff) of a shipping cask built for 16 fuel elements is computed, assuming a total immersion in water with two methods :

A gives an uncertainty of 0.05 (3 σ)
B gives an uncertainty of 0.005 (3 σ)

Number of elements		12	14	16
method	A	0.92 ± 0.05	0.93 ± 0.05	0.95 ± 0.05
method	B	0.920 ± 0.005	0.932 ± 0.005	0.945 ± 0.005

knowing that the French safety regulation requires keff $\leq$ 0.95 all uncertainties included, we see from the table that using method A only the transportation of 12 elements may be allowed. The use of method B will allow the shipping of 16 elements, which represents a gain of 33 % of the shipping capacity.

However accurate methods demanding exact three dimensional treatment of the geometry and fine representation of cross section are quite expensive. Furthermore, to allow any type of casks or plants, the most pessimistic accidents should be evaluated, involving a lot of parametric studies such as calculation of keff function of water density, poison nature, geometric deformation and eventual presence of reflectors.....

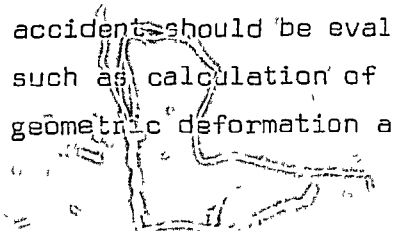

This leads to a large number of computations and a compromise must be found between cost and computational accuracy.

In order to meet this goal we have developped a simplified very fast Monte Carlo code : TRIMARAN which solves the critical Boltzmann equation in three dimensional geometry using multigroup cross sections with linear anisotropy (P1 approximation).

TRIMARAN GEOMETRY

The code uses the geometry package of the TRIPOLI system [1]. The three dimensional geometry is defined as a union of volumes filled with homogeneous composition and limited by portion of surfaces of first or second order. The geometry may be repeated by translation-rotation and symmetry and allows any type of boundary condition including albedos.

The user defines equations such as :

- general plan	$ax + by + cz + d = 0$
- special plans	$x + x_o = 0$
	$y + y_o = 0$
	$z + z_o = 0$
- general quadric	$ax^2 + by^2 + cz^2 + dxy + eyz + fzx + gx + hy + iz + j = 0$
- sphere	$(x - x_o)^2 + (y - y_o)^2 + (z - z_o)^2 - R^2 = 0$
- special cylinders	$(y - y_o)^2 + (z - z_o)^2 - R^2 = 0$
	$(z - z_o)^2 + (x - x_o)^2 - R^2 = 0$
	$(x - x_o)^2 + (y - y_o)^2 - R^2 = 0$

Then each volume will be defined by its boundary surfaces and the sign of their associated linear or quadratic forms for any point inside the volume. Any portion of boundary surface with no neighbour volume will be declared with a boundary condition such as :

- leakage
- optical reflexion
- isotropic reflexion with albedo function of energy
- symmetry
- translation
- rotation

A special and very fast processing is used for slabs which could be inserted inside every rectangular volumes.

CROSS SECTIONS

TRIMARAN solves the Boltzmann equation without external sources :

$$(1)\quad \vec{\Omega}.\vec{\nabla}\phi(\vec{r},\vec{\Omega},E)+\Sigma_t(\vec{r},E)\phi(\vec{r},\vec{\Omega},E)=$$
$$\int_{4\pi}d^2\Omega'\int_0^\infty dE'\,\Sigma_s(\vec{r},\vec{\Omega}'\to\vec{\Omega},E'\to E)\,\phi(\vec{r},\vec{\Omega}',E')+\frac{\chi_i(\vec{r},E)}{k_{eff}}\int_{4\pi}d^2\Omega'\int_0^\infty dE'\,\nu\Sigma_f(r,E')\phi(\vec{r},\vec{\Omega}',E')$$

Using the linear anisotropy collision approximation (P1) the transfer cross section may be written :

$$(2)\quad \Sigma_s(\vec{r},\vec{\Omega}\to\vec{\Omega}',E'\to E)=\Sigma_s^0(\vec{r},E\to E')+\vec{\Omega}.\vec{\Omega}'\,\Sigma_s^1(\vec{r},E\to E')$$

and in the multigroup approximation (1) becomes :

$$(3)\quad \vec{\Omega}.\nabla\phi_g(\vec{r},\vec{\Omega})+\Sigma_g^t(\vec{r})\phi_g(\vec{r},\vec{\Omega})=$$
$$\sum_{g'}\left\{\left(\Sigma^{s0}_{g'\to g}(\vec{r})+\frac{\chi_{g'}(\vec{r})}{k_{eff}}\nu\Sigma^f_{g'}(\vec{r})\right)\int_{4\pi}\phi_{g'}(\vec{r},\vec{\Omega}')d^2\Omega'+\Sigma^{s1}_{g'\to g}(\vec{r})\int_{4\pi}\vec{\Omega}.\vec{\Omega}'\,\phi_{g'}(\vec{r},\vec{\Omega}')d^2\Omega'\right\}$$

The functions $\Sigma_g^t(\vec{r})$, $\Sigma_{g\to g'}^{s0}(\vec{r})$, $\Sigma_{g\to g'}^{s1}(\vec{r})$, $\nu_g\Sigma_g^f(\vec{r})$ and $\chi_g(\vec{r})$ are constant inside a volume as defined in the geometry and are refered as the cross section library.

TRIMARAN can use any type of multigroup library with less than 256 groups. The code has its own mixing routine and may be coupled with different libraries through a simple interface.

Actually two interfaces are provided :

- one with ANISN format libraries which allows the code to use cross section processed by the AMPX system [2]
- one with a KERA library output by the cell code APPOLO[3] which computes correct self-shielded cross sections using the collision probability method.

From one of these microcopic cross section libraries, TRIMARAN computes macroscopic cross sections and probability tables :

$\sum_g^a$ absorption in group g

$\nu_g \sum_g^f$ neutron production in group g with spectrum χ_g

$$\sum_{g'\to g}^{s}(\vec{\Omega}\to\vec{\Omega}') = \sum_{g'\to g}^{s0} + \vec{\Omega}.\vec{\Omega}' \sum_{g'\to g}^{s1}$$

with $g' > g$ for the slowing down

$g' = g$ for in scattering

$g' < g$ for upscattering

in the standard 99 groups APOLLO library, 47 are with possible upscatter.

The probability tables are stored in memory in a special format presenting two important advantages :

- it reduces considerably the memory occupied by the cross sections
- the format is specially adapted to the neutron simulation by the Monte Carlo method.

SIMULATION

A batch of neutrons is simulated using the Monte Carlo method. Scoring is made for absorption, neutron production and leakage and an estimation of :

$$keff = \frac{\text{neutron production}}{\text{absorption+leakage}}$$ is computed.

In the same time, the next batch of neutrons is generated with the fission spectrum of the composition where they are created.

This process is repeated until the variance on the mean value of keff reached the user precision or the iteration limit.

To initiate the process a guess batch of neutrons is generated in fissile materials using a flat flux approximation.

Starting from a neutron characterised by :

its position $\vec{r}$ its direction Ω

its group g and its weight π

a track length is sampled. Then absorption and production rate are computed and scored along the track using two different but highly correlated ways :

- track length estimator :

$$\sum \ell * w$$

- collision estimator

$$\sum \frac{w}{\Sigma_t}$$

At the end of the track the neutron either leaves the system or has a collision. In the latter case the weight is multiplied by the probability of no absorption and a new group g' and direction are sampled from (g g') and (g, g'). If the material is fissile, neutrons for the next generation are sampled from and

The neutron history is simulated until the particle leavrs the system or its weight becomes less than .

The program offers two options :

- russian roulette
- weight transfer which seems to give a better variance.

At the end of the batch the different values of the keff estimation are used to accelerate the convergence.

The code outputs :

- absorption and production rates with their variance for each volume
- leakage through boundary surfaces
- mean value and variance of keff computed by three different ways :
- number of neutrons generated at each batch
- $keff = \frac{\text{production}}{\text{absorption+leakage}}$ from collision estimator
- $keff = \frac{\text{production}}{\text{absorption+leakage}}$ from track length estimator

SPECIAL TECHNICAL FEATURES OF TRIMARAN

The computing cost is a function of 3 parameters :

- number of input/output operations
- size of memory occupied during the execution
- central processing unit time (CPU)

The code has been specially programmed to obtain a significant reduction of the contribution to the cost of each parameter.

The input/output operations are reduced to the minimum necessary to run a computation : reading the user input, the microscopic cross sections and printing the results. All the data used during the execution is stored at the beginning in the central memory. This programming usually leads to a large utilization of the computer memory : for example, using our standard 99 groups library the cross sections matrices ( ) will occupy for only one composition 99*99*2 words. For a typical shipping cask problem where about 10 compositions are described 800 K would be necessary only to store the cross sections !

TRIMARAN uses a special binary coding which reduces the size occupied by the cross sections by a factor between 10 to 15. Using that method most of our problems can be run within a region less than 300 K.

Furthermore this coding leads us to give up nearly completely floating point operations for fixed binary operations 4 to 5 times faster on IBM machines.

This type of binary coding is specially adapted to Monte Carlo method for two reasons :

- the limited variation of numbers used during the simulation : probabilities belongs to (0,1)..

- the inherent uncertainties brung by the Monte Carlo method allows to simulate floating point operations by binary operations as long as we control the numerical uncertainties in order that their cumulated values stay neglectible in respect to the variance of the result.

In a Monte Carlo run the variance on the result decreases like the square root of the number of histories, and if it is quite easy to obtain rapidly a poor variance (10/15 %) it becomes hopeless to reach better variance than .5 to .4% in a reasonable computing time. This limit allows to use numerical methods giving uncertainties between 10^{-5} - 10^{-4} instead of the 10^{-7} - 10^{-6} of standard floating points operations, but 5 to 10 times faster. This is well shown on figure 1 where the variance is plotted as a function of time for 3 different Monte Carlo simulations of the same benchmark.

FIGURE 1

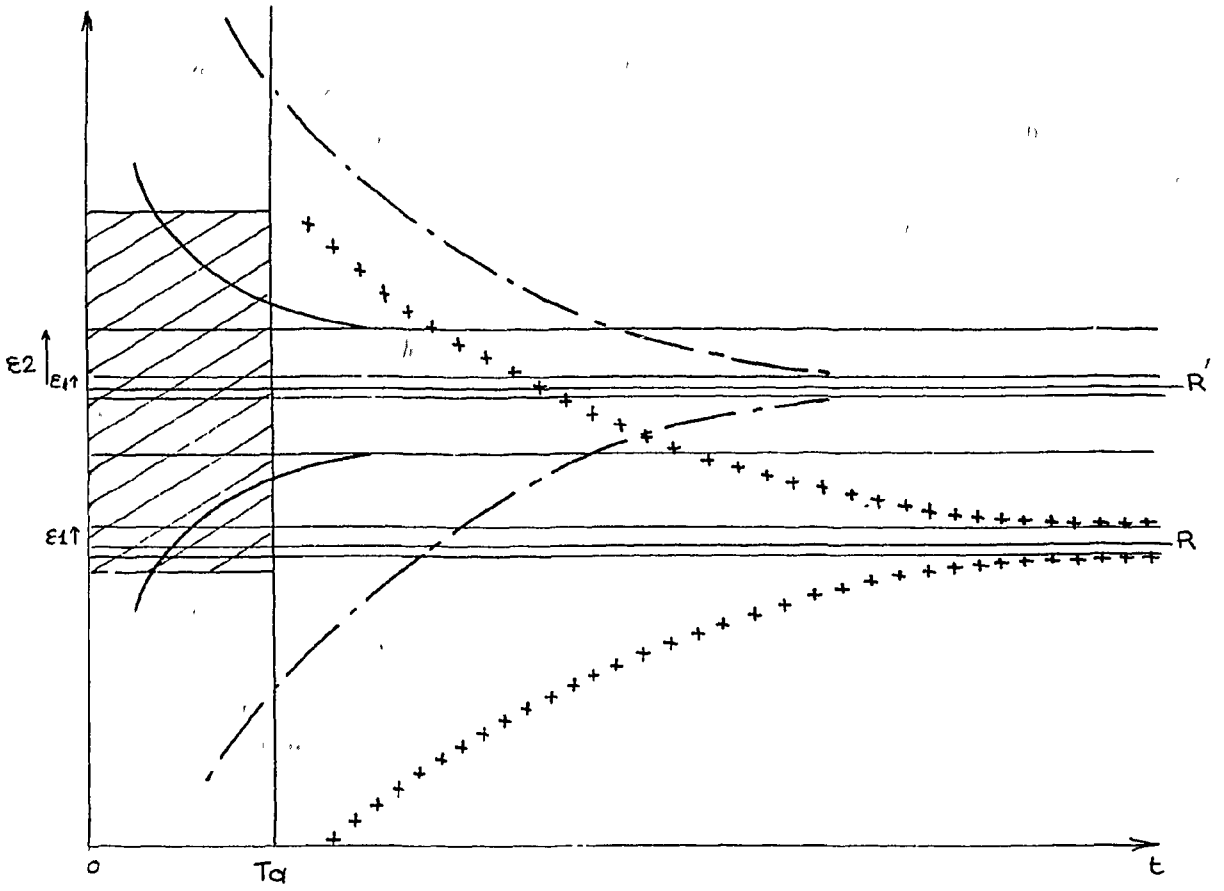

R exact result R' approximate result

ε1 numerical uncertainty from floating point operations

ε2 numerical uncertainty from binary method

Ta acceptable computing time for engineering calculations

++ exact Monte Carlo

. — multigroup P1 with floating point

—— TRIMARAN

The exact Monte Carlo computation converges very slowly to the exact result limited only by the accuracy on floating point operations -1. But the computing time limits its use to physical studies or special applications.

Simplified Monte Carlo keeping the advantages of three dimensional geometry but using approximated description of cross sections and anisotropy converges to an approximate result R' much faster but still not enough to compete with the analytical or numerical codes used in nuclear engineering.

TRIMARAN,using binary coding,falls in the range of these engineering codes, the counter part being a larger theoretical uncertainty. But anyway this theoretical uncertainty cannot be reached in the range of accuracy and computing time where the code is used. This proves the advantages of the method.

CONCLUSION

By reducing the cost of a three dimensional Monte Carlo run, as shown by preliminary results, by a factor 8 to 10 we dispose of a code able to satisfy three dimensional demands of some calculations and still in the range of price of analytical or numerical codes used in nuclear engineering.

TRIMARAN is going to be implemented in the shielding code system PROMETHEE [4] which will supply it with the input output facilities of a modular system. We think then to extend the field of this method to deep penetration problems.

BIBLIOGRAPHIE

(1) TRIPOLI 2 J.C. NIMAL

(2) AMPX II R.S.I.C.

(3) APOLLO A. KAVENOKY Note CEA n° 1610

(4) PROMETHEE J. GONNORD to be published

KENO CALCULATIONS OF LIGHT WATER FUEL LATTICS

M. J. Hebert, J. A. Handschuh, E. E. Pilat, M. Edenius
Yankee Atomic Electric Company
Westboro, Mass.

D. R. Harris
Rensselaer Polytechnic Institute
Troy, NY

J. A. Mayer
Worcester Polytechnic Institute
Worcester, Mass.

ABSTRACT

At Yankee, KENO[1] calculations of light water fuel lattices are being performed for the purpose of spent fuel rack design and as benchmarks for BWR bundle calculations.

Spent fuel rack design for Maine Yankee has utilized the well known 123 group ORNL library to verify that the close packed, poisoned fuel rack met the criterion that k be less than 0.95. The uranium 238 resonance cross sections were obtained from NITAWL[2], using dancoff factors obtained from Sauer's[3] method as implemented in LEOPARD[4]. Analysis methods were validated by performing similar KENO calculations of poisoned criticals [5,6] which have also been used to validate the SCALE SYSTEM[7]. Comparisons between experiment and calculations will be included in the presentation.

KENO calculations for BWR bundles are performed in order to verify the assumptions made in the more automated, integral transport theory calculation[8] which is used for production purposes. Although this integral transport code performs multi-group, space-dependent calculations of the bundle, a number of simplifying assumptions are necessary because of the extreme heterogeneity of the bundle. Such assumptions relate to the self-shielding of the gadolinia burnable poison present in selected fuel rods, to the definition of unit cells (the 2D transport calculation is performed on a unit cell basis), and to the representation of the boron carbide filled steel tubes which comprise the control rod, as well as to the perturbing effects of non-identical neighboring bundles. In order to make the KENO calculations as consistent as possible, they are performed with the same (ENDF/B-III) library used in the integral transport calculations. This

paper describes the reformatting of the integral transport code 25 and 69 group libraries for use in KENO, and compares k infinity values and selected reaction rates in a BWR fuel assembly as determined by the integral transport and Monte Carlo calculations.

Yankee Atomic Electric Company (YAEC) in Westboro, Mass, is currently using the Oak Ridge developed Monte Carlo code "KENO-IV: An improved Monte Carlo Criticality Program". KENO is being used as an analysis tool for spent fuel rack calculations of PWR fuel, and as a development aid for in-core BWR fuel calculations. In both cases, the Monte Carlo method is applied because of the large flux gradients.

KENO CALCULATIONS OF PWR SPENT FUEL RACKS

As applied to PWR reactors, the Monte Carlo method has been used primarily in spent fuel storage rack design calculations. Monte Carlo techniques are required for the fuel storage rack calculations because of the presence of BORAL plates in the design of Yankee racks. Diffusion theory is inappropriate in a problem with such large flux gradients. The Monte Carlo methods are available, however, for benchmarking of non-standard problems (i.e, configurations which PDQ, the standard method, might not predict. Examples include water-rod effect on power distribution, gapped fuel rod effects.)

The implementation of the Monte Carlo method is performed using the 123 group AMPX-KENO [1,2] set of calculational tools. NITAWL, using the Nordheim resonance treatment, creates the 123-group library for KENO-IV. KENO is run in restart mode until sufficient statistics are achieved.

Prior to implementation to criticality calculations, the ANS-8.11/ANSI N16.9-1975 [5,9] standard requires validation of all calculational tools to assure applicability to the problem of interest. For the fuel storage rack calculation, validation consists of comparing the results of KENO calculations to criticals. At the time of the initial work, the best available criticals that simulated fuel storage rack configuration were those performed by Bierman at Battelle Pacific Northwest Laboratories.[5,6] These criticals were performed using three subcritical clusters with and without poison plates inserted between clusters. Two different enrichments were utilized, 2.35 and 4.30 WT%, in addition, BORAL was utilized as one of the poison materials. The calculated values of these experiments are shown in Table 1. Table 1 also provides comparison to work performed by R. Westfall of ORNL[7], who generated KENO comparisons using the 123 group library for all 210 of The Bierman criticals. As

shown, the agreement between the YAEC and the ORNL work allows some bootstrapping to the complete 210 cases Westfall analyzed.

Additional verification of methods is now available from the recently published B & W criticals for arrays of nine assemblies in a fuel storage rack configuration.[10] The B & W criticals add an important aspect due to the presence of soluble boron in some of their experiments in addition to poison plates.

An interesting point that has arisen from the fuel storage rack calculation is the method used by some designers to utilize PDQ to derive sensitivities. Work preformed at YAEC on the design of SEABROOK fuel racks shows that PDQ does not provide an accurate means for deriving sensitivities. In the cases shown in Table 2, a change in the center-to-center spacing provides significant differences in relative K_{eff}. As expected, diffusion theory underpredicts the delta-K for this situation.

Table 1
Validation of KENO Methods

Enrichment & Experiement No.	Poison Plate Material	Yankee Keff	CPNL Keff
2.35-5	None	1.006 + 0.004	1.005 ± 0.004
2.35-16	Boral	1.006 + 0.004	1.007 ± 0.005
4.30-4	None	0.987 + 0.005	---
4.30-31	Boral	0.997 + 0.004	0.996 ± 0.005

Table 2
PDQ vs. KENO K_{eff}

Center-To-Center	PDQ	KENO
10.84"	0.9243	0.9418 ± 0.005
10.94"	0.9123	0.9218 ± 0.005

KENO CALCULATIONS OF BWR FUEL LATTICES

At Yankee Atomic Electric Company (YAEC), methods are currently being developed which will allow Yankee to undertake the reload licensing of Vermont Yankee. Vermont Yankee is a BWR rated at 540 MWe, which first went into operation in November of 1972.

One of the calculational tools being used is "CASMO: A Fuel Assembly Burnup Program",[8] which was developed by AB Atomenergi in Studsvik Sweden and is distributed by EPRI.

CASMO is a multigroup two-dimensional transport theory code for burnup calculations, which handles either pin-cell calculations or cylindrical fuel-pin lattices. The code has provisions to allow fuel of various compositions, fuel containing gadolinia, burnable absorber rods, cluster control rods, in-core instrument channels, water gaps, boron steel curtains, and cruciform control rods. CASMO is supplied with both 25 and 69 group cross section libraries derived from ENDF/B-III data.

One step in developing CASMO as a BWR method was the determination of how its single bundle lattices compared with multi-bundle lattices. The Monte Carlo code "KENO-IV-An Improved Monte Carlo Criticality Program",[1] develcped at Oak Ridge National Laboratory (ORNL), was employed in this effort.

BWR Fuel Lattices

A typical fuel bundle for a BWR is rather complex, particularly when compared to PWR fuel. BWR fuel bundles often contain as many as five different fuel enrichments, as well as water pins and pins containing both fuel and burnable poison. BWRs are operated with some control rods inserted creating large neutron flux depressions. Since boiling occurs within the core, water density can vary from top to bottom as well as from bundle to bundle.

In short, BWR fuel is anything <u>but</u> homogeneous. It is for this reason that the Monte Carlo technique was applied.

CASMO Description

The CASMO program performs the following sequence of events at each burnup step...

1. Macroscopic cross-sections, including effective cross-sections in the resonance region for important resonance absorbers are calculated. In the resonance calculation, Dancoff factors are used to account for the screening effect between different pins,

and the equivalence theorem relates tabulated effective resonance integrals to the particular heterogeneous problem.

2. The cross sections are used in the so-called "micro-group calculations" which provide detailed neutron energy spectra on a pin-by-pin basis for condensation and homogenization of the pin cells.

3. The discrete integral transport method is used for 1-D calculations on a cylindricalized assembly to account for such non-symmetric parameters as bypass water gap.

4. Two-dimensional transmission probability calculations are performed in as many as 12 energy groups to yield the eigenvalue and assembly flux distribution.

5. Effects of leakage are then accounted for by use of a fundamental buckling mode.

6. Isotopic depletion calculations are performed on fuel pin and burnable absorber regions. CASMO traces burnup-chains, through absorption and decay, for 22 fission products, 2 pseudo fission products, and 14 heavy nuclides.

Cross Section Library

In order to justify comparison of KENO and CASMO calculations, consistency of cross section sets was maintained. A slightly-modified CASMO 25-group cross section was used since it both contained sufficient data for both codes, and would be the standard CASMO production library.

The CASMO library contains absorption (or activation) cross sections for thirty-six nuclides as well as nu-fission, transport corrected total scattering, and P_0 scattering cross sections for thirty-four other nuclides. P_1 scattering cross sections are provided for three nuclides (Hydrogen, Deuterium and Oxygen). In addition, tables containing effective resonance integrals and burnup data are also included.

The P_0 and P_1 scattering cross sections are provided in $g \rightarrow g'$ form in a scattering matrix. The size of the matrix varies from nuclide to nuclide and group to group ranging from just one scatter cross section to full scattering over all energy groups. In some cases upscatters as well as downscatters are provided.

For some nuclides, (such as Hydrogen, Oxygen and Zircaloy), cross sections are tabulated at more than one temperature, and not all cross sections are provided at each temperature. CASMO

interpolates over available data to determine cross sections at the temperature of interest.

The CASMO cross section library has been processed in order to provide KENO-compatible format...

- Total scattering cross sections were formed from the absorption cross sections and P_0 scattering matrix.
- Nuclides with cross sections at several temperatures were broken into several pseudo-nuclides (one per temperature).
- Scattering cross sections were multiplied by a 2L + 1 factor (as expected by KENO).
- Cross sections were written into KENO card-image format. Zeroes were included as needed so that all cross sections (including full scattering) were tabulated for each nuclide.

In order to assure consistency of cross sections in the resonance-energy region, resonance group cross sections for important absorbers were taken directly from the CASMO execution for each case investigated. This necessitated the creation of several pseudo nuclides for each of these absorbers in a particular fuel lattice.

Fuel Lattice Model

Two different fuel bundles, both similar to fuel which has been loaded at Vermont Yankee (VY) have been represented. Both are 8 x 8 square pitch lattices containing fuel at five different enrichments in addition to water pins and pins containing gadolinia and fuel.

The 219 Bundle (the bundle average enrichment is 2.19%), contains fuel enrichments varying from 1.18% to 2.50%, as well as three pins which are enriched to 2.50% and contain 4.0 WT% gadolinia. The 274 Bundle enrichment ranges from 1.87% to 3.01%, and contains five pins enriched to 3.01% which contain 2.0 WT% gadolinia (figure 1).

The fuel bundle models for both CASMO and KENO are exactly identical and deviate only slightly from the actual bundles (with square as opposed to rounded channel corners, for example).

In a like manner, the control rod models are reasonably similar to the actual VY control rods. Unfortunately there are KENO geometry input requirements which necessitate that

- each succesive geometry region within a geometry "BOX TYPE" must enclose the previous one, and

- cylindrical geometry regions must be centered about their origin of its enclosing "BOX TYPE".

Together, these effectively prevent the simultaneous representation of both cylindrical fuel pins and cylindrical control rods. As a result, the KENO model contains rectangular control rods, while the CASMO model is limited to cylindrical control rods.

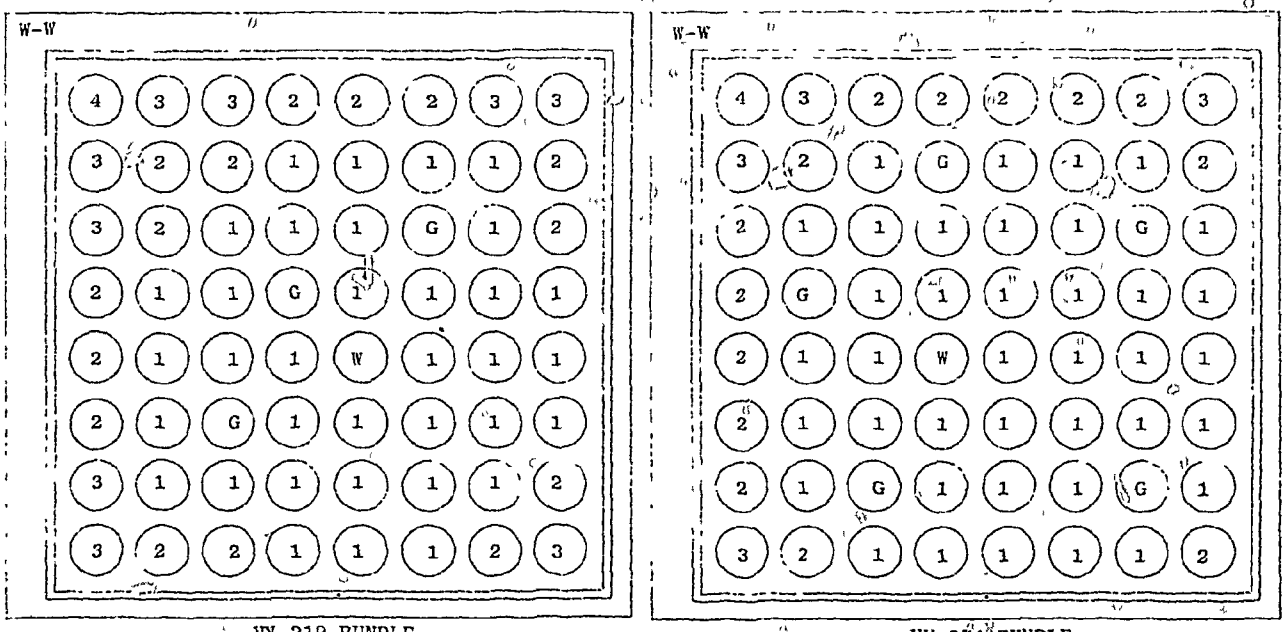

VY 219 BUNDLE
FUEL ENRICHMENT DISTRIBUTION

1	2.50% U-235	G	2.50% U-235, 4.0% Gd_2O_3
2	1.90% U-235	W	Water Pin
3	1.49% U-235	W-W	Wide-Wide Gap
4	1.18% U-235		

VY 274 BUNDLE
FUEL ENRICHMENT DISTRIBUTION

1	3.01% U-235	G	3.01% U-235, 2.0% Gd_2O_3
2	2.22% U-235	W	Water Pin
3	1.87% U-235	W-W	Wide-Wide Gap
4	1.45% U-235		

FIGURE 1

Results

Prior to executing KENO on a multi-bundle array basis, a stepwise proving procedure was undertaken. This procedure consisted of CASMO/KENO comparisons for,

- Pin cells at different tempertures
- Fuel bundles with and without burnable poison
- Fuel bundles at different void fractions
- Rodded and unrodded fuel bundles

- Fuel bundles of different enrichments

KENO was then used to investigate both rodded and unrodded four bundle fuel arrays. These arrays consisted of two each of the 219 and 274 bundles, maintaining diagonal symmetry. Throughout the analysis key parameters of interest were K-effective and local fission distribution.

KENO executes a pre-determined number of generations, the starting distribution of one depending on the fission distribution of the previous generation. The starting distribution of the first generation is determined by the user and typically is not a good approximation. Therefore, several initial generations must be skipped and the K-effective is chosen as the earliest convergence of average K-effective, as illustrated in Figure 2.

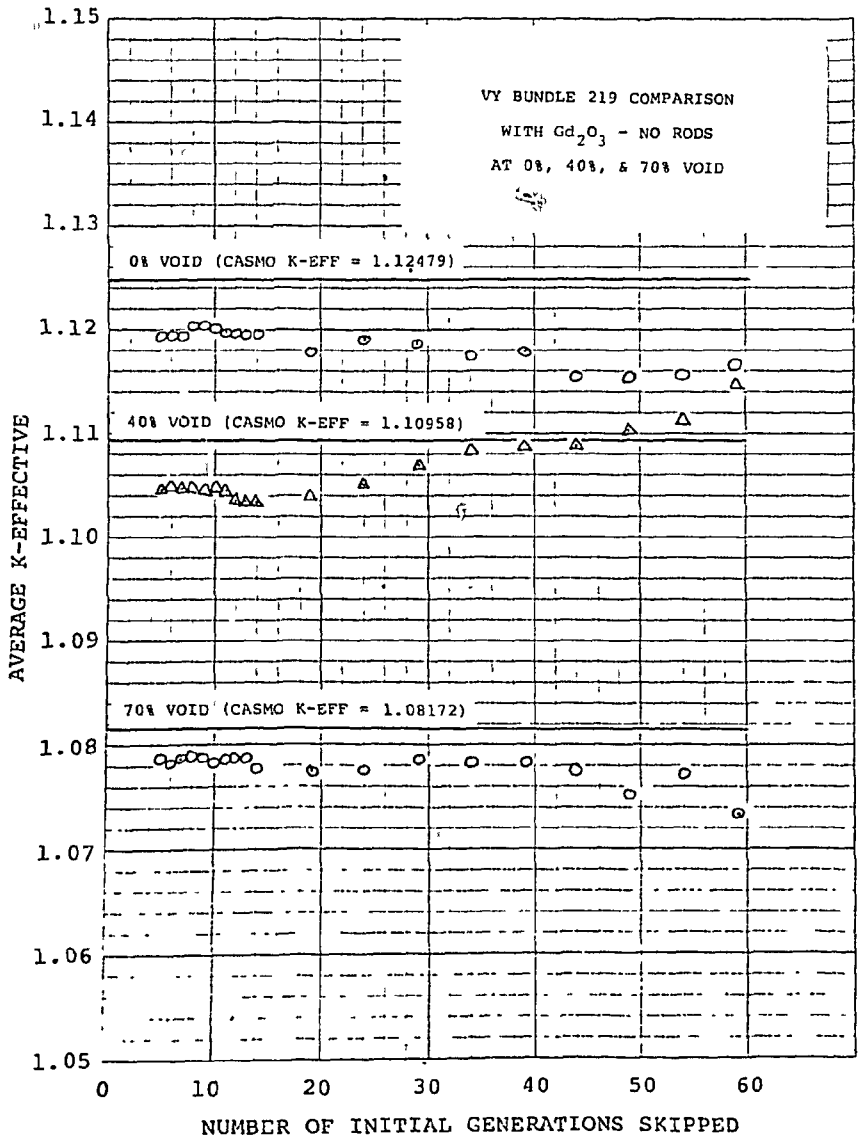

FIGURE 2

Pin cell cases were executed at 296°K and 500°K. Bundle 219 was executed without Gd_2O_3 and without control rods at 0%, 40% and 70% void; with Gd_2O_3 but without control rods at 0%, 40% and 70% void; and with both Gd_2O_3 control rods, also at the three voids. Bundle 274 was executed at 40% void, with Gd_2O_3 both controlled and uncontrolled. Table 1 presents a comparison of K-effective for each of the cases.

As can be seen from the table, KENO and CASMO K-effectives

agree within 1% for all cases. An interesting trend emerges when comparing rodded to unrodded bundles. For the rodded cases, KENO predicts a higher K-effective than CASMO by about 0.6%. For the unrodded cases (with Gd_2O_3), KENO indicates a lower K-effective by about 0.4%, when compared to CASMO. This yields a total rod bias of about a percent.

CASE	KENO	CASMO	% DEV
296°K PIN CELL	1.3739 ± .002	1.37475	-.062
500°K PIN CELL	1.3481 ± .002	1.34956	-.108
219 at 0% VOID	1.2504 ± .002	1.24939	.081
219 at 40% VOID	1.2400 ± .002	1.24150	-.121
219 at 70% VOID	1.2236 ± .002	1.21883	.391
219 w/GAD 0%	1.1198 ± .0025	1.12479	-.444
219 w/GAD 40%	1.1044 ± .002	1.10958	-.467
219 w/GAD 70%	1.0784 ± .0025	1.08172	-.307
219 RODDED 0%	0.9013 ± .003	0.89792	.376
219 RODDED 40%	0.8343 ± .003	0.82739	.835
219 RODDED 70%	0.7554 ± .0025	0.75137	.536
274 w/GAD 40%	1.0939 ± .002	1.098851	-.451
274 RODDED 40%	0.8408 ± .003	0.83473	.727

PIN & BUNDLE KENO v. CASMO K-EFFECTIVE

TABLE 1

Local fission distributions for the 274 bundles from both KENO and CASMO are presented in figures 3 & 4. Fractional differences of local fission distributions for the 219 bundles with Gd_2O_3, control rodded and un-rodded, at all void levels are presented in figures 5 & 6.

From these figures it can be seen that the deviation in the unrodded cases is fairly random, typically on the order of 2 to 3%, with only a slight bias from the wide-wide corner to the narrow-narrow. For the control rodded cases, however, the deviation is somewhat greater and the bias is more pronounced. In all cases, KENO shows an overall

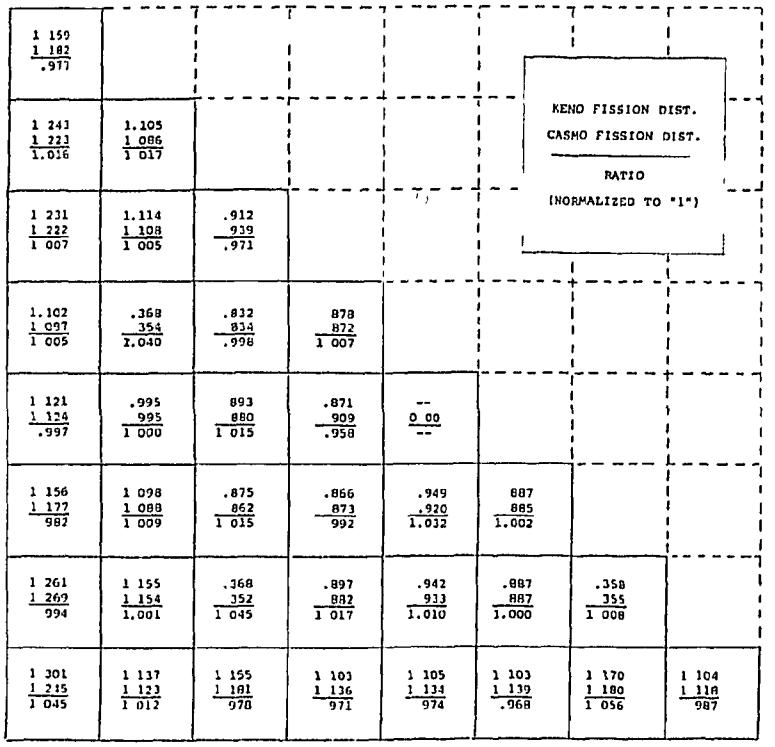

1 159 1 182 .977							
1 241 1 223 1.016	1.105 1 086 1 017						
1 231 1 222 1 007	1.114 1 108 1 005	.912 939 .971					
1.102 1 097 1 005	.368 354 1.040	.832 834 .998	878 872 1 007				
1 121 1 124 .997	.995 995 1 000	893 880 1 015	.871 909 .958	-- 0 00 --			
1 156 1 177 982	1 098 1 088 1 009	.875 862 1 015	.866 873 992	.949 .920 1.032	887 885 1.002		
1 261 1 269 994	1 155 1 154 1.001	.368 352 1 045	.897 882 1 017	.942 933 1.010	.887 887 1.000	.358 355 1 008	
1 301 1 215 1 045	1 137 1 123 1 012	1 155 1 181 978	1 103 1 136 971	1 105 1 134 974	1 103 1 139 .968	1 170 1 180 1 056	1 104 1 118 987

VY 274 BUNDLE
WITH Gd_2O_3 - 40 % VOID - NO RODS

FIGURE 3

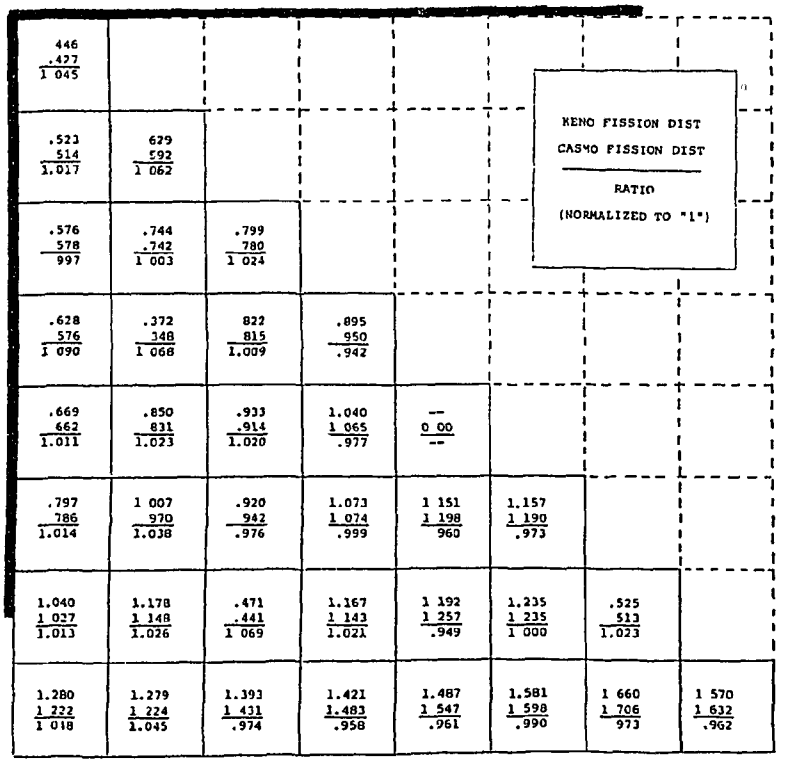

446 .427 1 045							
.523 514 1.017	629 592 1 062						
.576 578 997	.744 .742 1 003	.799 780 1 024					
.628 576 1 090	.372 348 1 068	822 815 1.009	.895 950 .942				
.669 662 1.011	.850 831 1.023	.933 .914 1.020	1.040 1 065 .977	-- 0 00 --			
.797 786 1.014	1 007 970 1.038	.920 942 .976	1.073 1 074 .999	1 151 1 198 960	1.157 1 190 .973		
1.040 1 027 1.013	1.178 1 148 1.026	.471 .441 1 069	1.167 1 143 1.021	1 192 1 257 .949	1.235 1 235 1 000	.525 513 1.023	
1.280 1 222 1 018	1.279 1 224 1.045	1.393 1 431 .974	1.421 1.483 .958	1.487 1 547 .961	1.581 1 598 .990	1 660 1 706 973	1 570 1 632 .962

VY 274 BUNDLE
RODDED - 40% VOID - WITH Gd_2O_3

FIGURE 4

These 8 x 8 bundles are symmetric about the diagonal axis.

Therefore it is sufficient to explicitly model only the lower left region (as shown), as representative of the entire bundle.

Using this convention, the wide bypass water gap lies along the left and upper sides. The narrow water gap lies along the right and lower sides.

The wide bypass water gap is the location of the cruciform control rod when present, (represented at left by a heavy solid line).

For the 4 bundle executions, the bundles are oriented so that the narrow-narrow corner is at the geometric center of the array for each bundle.

.016 .050 .043							
.064 .009 .030	.011 .028 .024						
.031 .029 -.002	.012 .066 .025	.014 -.032 .011			0% 40% 70%		
.018 .003 -.041	.007 .046 -.039	.009 .037 .048	.000 * .024 .052				
-.043 .011 .010	-.019 -.006 -.026	-.005 .011 .012	.020 .073 .037	W			
-.015 -.017 -.009	.045 .020 .016	.081 * .031 .035	-.011 -.010 .013	.004 -.050 -.018	.051 -.021 -.009		
-.008 .031 -.018	.022 .004 -.014	-.023 .003 .018	-.027 -.010 -.009	-.038 .008 .021	-.013 -.043 -.009	-.014 -.019 .035	
.032 .011 .010	-.006 .013 -.002	.025 .004 -.003	-.037 -.033 -.029	-.015 -.036 -.020	-.053 -.030 -.009	-.001 -.047 -.031	-.019 -.045 -.007

VY 219 BUNDLE FISSION DISTRIBUTION
COMPARISON AT 0%, 40% & 70% VOID
WITH Gd_2O_3 - NO RODS

*-PIN CONTAINING Gd_2O_3 W-WATER PIN

FIGURE 5

.005 .111 .081							
.003 -.008 .061	.038 .104 -.051						
.058 .032 .037	.018 .016 .047	.007 -.004 .021			0% 40% 70%		
.026 .006 .109	-.006 .034 .036	.023 -.003 .081	.056 * .107 .068				
-.012 .027 .100	.004 .013 .019	.059 .044 .049	.037 .000 .028	W			
.004 .026 .005	.025 .030 .055	.087 * .055 .077	.005 .030 .024	-.012 -.032 -.008	-.026 .001 -.035		
.052 .040 .021	.032 -.016 -.026	-.026 .014 .007	-.021 -.037 -.013	-.007 -.036 -.019	-.040 -.033 -.063	-.033 .000 -.048	
.063 .019 -.015	-.008 .015 -.004	.021 -.018 .004	-.027 -.012 -.060	-.041 -.021 -.025	-.043 -.031 -.037	-.004 -.004 -.039	-.014 -.039 -.059

VY BUNDLE 219 FISSION DISTRIBUTION
COMPARISON AT 0%, 40% & 70% VOID
WITH Gd_2O_3 - RODDED

*-PIN CONTAINING Gd_2O_3 W-WATER PIN

FIGURE 6

flatter fission distribution which corresponds to a slightly lower prediction of control rod worth, in comparision to CASMO. This in turn indicates that CASMO predicts higher local peaking factors for the rodded cases, and is therefore more conservative.

Four-bundle fuel arrays were executed consisting of two 219 bundles at 0% void and two 274 bundles at 40% void. In one case, the array was unrodded, in the other, two cruciform control rods were inserted adjacent to the 219 bundles. It should be noted that these cases are somewhat more extreme than that experienced in an actual BWR.

Local fission distribution for each bundle in each case is presented as figures 7-10. These figures represent the 4 bundle array KENO execution compared with the respective 1 bundle KENO excution, which as stated earlier, compared well with the single bundle CASMO executions. An analysis of this data indicates the greatest deviation is in the narrow-narrow corner and is on the order of 11-14%. It is interesting to note that the deviations do not change substantially between the rodded and unrodded cases.

Table 2 shows a comparison of local bundle peaking factors between the single and four bundle KENO executions. For bundle 219, the four bundle array indicates a peaking factor about 4 or 5 percent lower than the single bundle run. For bundle 274, the deviations of less than 2 percent show that the single bundle executions are in essential agreement. Considering the extreme nature of the cases and the overall agreement between KENO and CASMO single bundle executions, CASMO is seen to be slightly conservative in predicting local peaking factors for all reasonable cases.

BUNDLE-CASE	ARRAY	SINGLE
219-UNCONTROLLED	1.191	1.241
274-UNCONTROLLED	1.322	1.301
219-CONTROLLED	1.647	1.735
274-CONTROLLED	1.310	1.301

BUNDLE PEAKING FACTOR COMPARISON
4 BUNDLE ARRAY v. SINGLE BUNDLE

TABLE 2

"KENO IV - An Improved Mone Carlo Criticality Program", has proven a useful tool in developing new BWR fuel analysis methods at Yankee. By

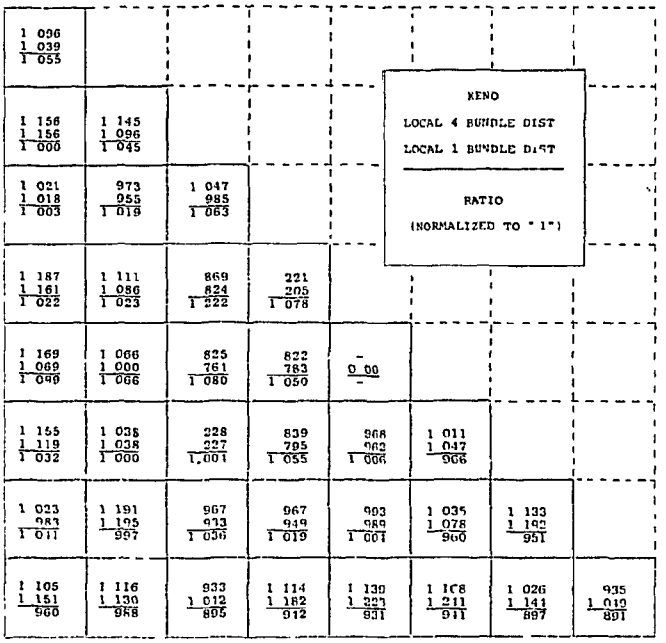

VY219 Bundle KENO From 4 Bundle Array
Bundles 274 at 40% void - Bundles 219 at 0% Void - No Rods

FIGURE 7

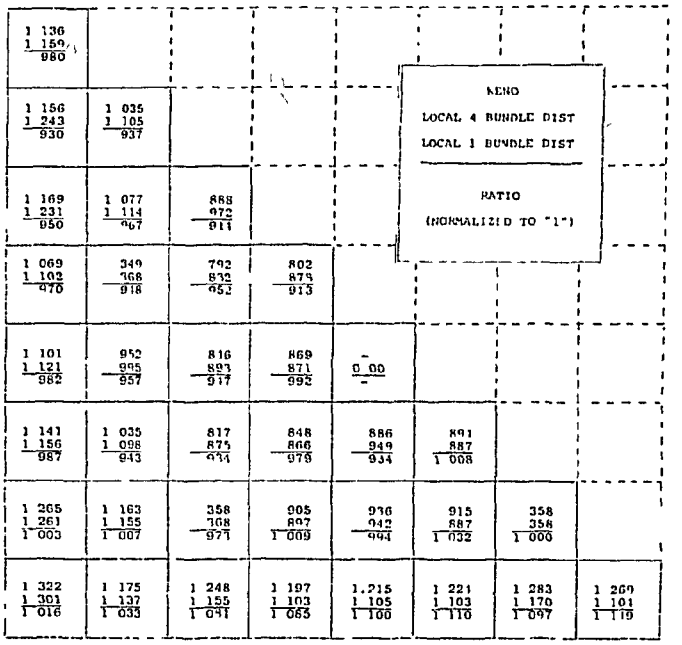

VY 271 Bundle KENO from 4 Bundle Array
Bundles 274 at 40% Void - Bundles 219 at 0% Void - No Rods

FIGURE 8

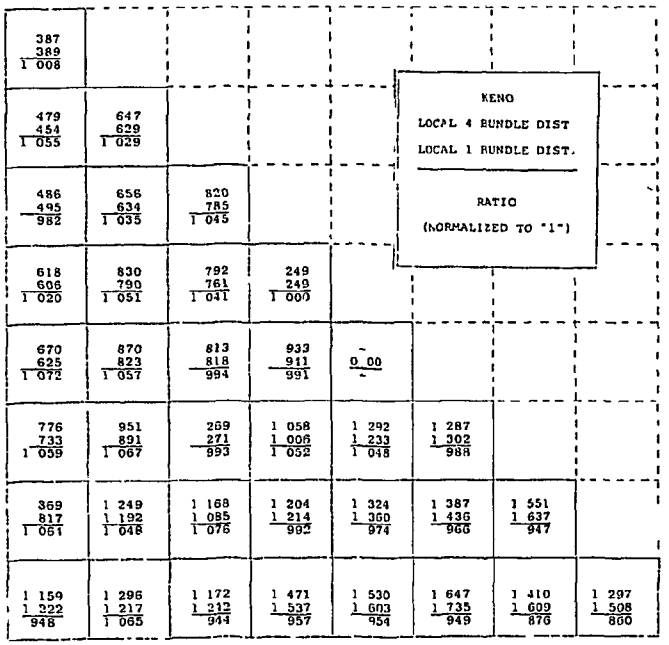

VY 219 Bundle KENO from 4 Bundle Array
Bundles 274 at 40% Void - Bundles 219 at 0% Void - Rodded

FIGURE 9

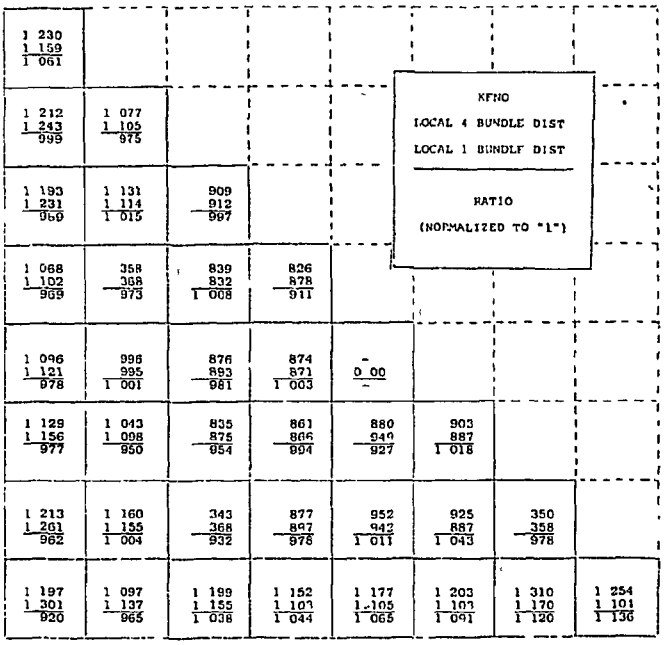

VY 274 Bundle KENO from 4 Bundle Array
Bundles 271 at 40% Void - Bundles 219 at 0% Void - Rodded

FIGURE 10

establishing relative agreement between KENO and CASMO for single bundle analysis, then extending KENO to multi-bundle cases, CASMO has been shown to be useful for multi-bundle calculation of eigenvalues and peaking factors.

References

1. ORNL-4948, KENO-IV - An Improved Monte Carlo Criticality Program, L. M. Petrie, N. F. Cross, (11/75).

2. ORNL/TM-3706, AMPX: A Modular Code System for Generating Coupled Multil-Group Neutron-Gamma Librarires for ENDF/B, N. M. Greene et. al, (3/76).

3. NSE16, 329, Approximate Escape Probabilities, A. Sauer, (1963).

4. WCAP-2759, The Revised LEOPARD Code - A Spectrum Dependent Non-Spatial Depletion Program, R. F. Barry, (3/65).

5. PNL-2438, Critical Separation Between Subcritical Clusters of 2.35 wt % 235 U Enriched UO_2 Rods in Water With Fixed Neutron Poisons, S. R. Bierman (1977).

6. NUREG/CR-0073, Critical Separation Between Subcritical Clusters of 4.29 wt % 235 U Enriched UO_2 Rods in Water With Fixed Neutron Poisons, S. R. Bierman (1978).

7. TRANS. ANS 33, 368, SCALE System Cross Section Validation with Shipping-Cask Critical Experiments, R. M. Westfall, J. R. Knight (1979).

8. AE-RF-76-4158, CASMO, A Fuel Assembly Burnup Program, Ake-Ahlin et. al. 1976.

9. ANS-8.11/ANSI N16.9-1975, "Validation of Calculational Methods for Nuclear Cirticality Safety."

10. Baldwin, et.al., "Critical Experiments Supporting Close Proximity Water Storage of Power Reactor Fuel, "BAW-1484-7, July 1979.

KENO V - THE NEWEST KENO MONTE CARLO CRITICALITY PROGRAM

N. F. Landers and L. M. Petrie
Computer Sciences Division
at Oak Ridge National Laboratory
Union Carbide Corporation, Nuclear Division
prime contractor for the
Department of Energy

ABSTRACT

KENO V is a new multigroup Monte Carlo criticality program developed in the tradition of KENO[1] and KENO IV[2] for use in the SCALE[3] system. The primary purpose of KENO V is to determine k-effective. Other calculated quantities include lifetime and generation time, energy dependent leakages, energy- and region-dependent absorptions, fissions, fluxes, and fission densities.

KENO V combines many of the efficient performance capabilities of KENO IV with improvements such as flexible data input, the ability to specify origins for cylindrical and spherical geometry regions, the capability of super grouping energy dependent data, a P_n scattering model in the cross sections, a procedure for matching lethargy boundaries between albedos and cross sections to extend the usefulness of the albedo feature, and improved restart capabilities.

This advanced user-oriented program combines simplified data input and efficient computer storage allocation to readily solve large problems whose computer storage requirements precluded solution when using KENO IV.

DATA INPUT

The KENO V data input is especially adapted for use with remote terminals. The order of input is quite flexible with the exception of the title which must be entered first; the parameters must immediately follow the title if they are entered.

A large portion of the data has been assigned default values that have been found to be adequate for many problems. Thus, the user can run a problem with a minimum of input data.

Blocks of input data are entered in the form:

READ XXXX input data END XXXX

where XXXX is the keyword for the type of data being entered. The types of data that can be entered are parameters, geometry region data, array definition data, biasing or weighting data, albedo boundary conditions, starting distribution information, cross-section mixing table and extra 1-D cross section ID's for special applications.

A block of data does not need to be entered unless it is necessary for the problem. Within the blocks of data, most of the input is activated by using keywords to override the default values.

IMPROVED GEOMETRY FEATURES

KENO V geometry input is very similar to the geometry input for KENO IV except the weighting has been rearranged to minimize storage requirements.

The geometry data for KENO IV is:

GEOMETRY WORD MIXTURE NUMBER DIMENSIONS WEIGHTS

The geometry data for KENO V is:

GEOMETRY WORD MIXTURE NUMBER BIAS ID NUMBER DIMENSIONS

The KENO IV weights are stored for each input geometry region so (number of energy groups) x (number of input geometry regions) words of storage are used. The KENO V weights are stored only for each BIAS ID NUMBER that is used. In addition, KENO V does not store region dependent data for geometry regions that are entered but not used in the problem. The storage requirements for the KENO V weights are (number of different bias ID's used in the problem) x (number of energy groups) words of storage. This can result in a significant reduction of storage space for a large problem.

One of the most important geometry improvements is the ability to specify the origin for cylinders, hemicylinders, spheres and hemispheres. This allows the use of nonconcentric cylindrical or spherical shapes and a great deal of freedom in positioning these shapes. As in KENO IV, the restriction that each geometry region must completely enclose the previous region is mandatory.

Another geometry convenience is a choice of the method used to specify the array definition (mixed box orientation) data. The method

used in KENO IV is available in KENO V. A second method allows the data to be entered by stringing in the unit or box types starting at x=1, y=1, z=1, and varying x then y and then z. This input is entered by using ANISN[4]-like input options for filling the array.

SUPER GROUPING

An important feature of KENO V is the capability of super grouping the energy dependent information such as cross sections and fluxes. This automatic feature is activated when the computer storage is insufficient to hold all the problem data at once. The energy dependent data is then broken into super groups that are written on a direct access device and moved in and out of core as necessary. A problem cannot be super grouped if the energy-dependent data associated with any energy group is too large to fit in the available storage.

The advantage of super grouping is that larger problems can be run on smaller computers. This capability is gained at the expense of running time and increased I/O's. The more super groups, the more I/O's are used and the slower the problem will run because of the banking, sorting, and use of direct access devices in the solution of the problem.

P_n SCATTERING

KENO V treats anisotropic scattering by using discrete scattering angles. The angles and associated probabilities are generated in a manner that preserves the moments of the angular scattering distribution for the selected group-to-group transfer. These moments can be derived from the coefficients of a P_n Legendre Polynomial expansion. All moments through the 2n-1 moment are preserved for n discrete scattering angles. A one-to-one correspondence exists such that n Legendre coefficients yield n moments.

If the cross-section data has fewer coefficients than the requested number of discrete scattering angles, higher moments are generated by using zeros for the higher order coefficients. The method of generating the angles and probabilities is appropriate only if the moments are for a valid probability distribution. If extending the coefficients with zeros results in an invalid distribution, the code will generate angles and probabilities that will preserve the available valid data. A warning message is printed whenever incorrect moments are encountered. A large number of these messages may be generated if the code has to extend the cross-section coefficients.

KENO V treats the case of zero and one scattering angle in a special manner. It can recognize that the distribution is isotropic even if the user specified multiple scattering angles, and therefore selects from a continuous isotropic distribution. If the user specified one scattering angle, the code performs semi-continuous scattering by picking scattering angles uniformly over some range between -1 and +1. The probability is zero over the rest of the range.

EXTENDED USE OF DIFFERENTIAL ALBEDOS

KENO IV can use differential albedos to simulate tracking in a reflector. These differential albedos are expensive and time consuming to generate because an ANISN calculation must be made for all polar angles at each energy group. Thus 64 ANISN calculations were involved in generating each differential albedo currently available for use with KENO. These albedos were generated using the Hansen-Roach 16 energy group structure and can only be used in conjunction with cross sections having the Hansen-Roach 16 energy group structure if KENO IV is used.

KENO V is not limited by this restriction. It matches lethargy boundaries between the albedos and cross sections so the appropriate energy transfers can be made. This is done by creating lethargy boundary tables for both the albedo group structure and the cross section group structure and determining the lethargy interval corresponding to the desired transfer (cross section group structure to albedo group structure or vice versa) based on a uniform distribution over the lethargy interval. Therefore, KENO V can use the existing differential albedos with any cross section energy group structure. When the energy group boundaries of the cross sections and albedos are different, approximations are made by the code. The results should be scrutinized by the user to evaluate the effects of the approximations until an adequate information base is established.

RESTART

KENO V has an improved restart capability. It is much easier to use than the KENO IV restart option. Certain pieces of input data can be overridden to be different from the original case. To restart a problem, the original case must be flagged to write a restart data set. The restarted problem uses data from the restart data set.

When restarting a problem, a new random number can be entered to change the random sequence and the calculations involving fluxes and fission densities can be turned off.

CALCULATIONS

The use of KENO V to solve criticality problems has been limited due to incomplete documentation. The report and data guide are currently being written and should be available sometime this year. KENO V has calculated k-effectives comparable to those obtained by KENO IV for the usual criticality problems used to validate our codes. It has also been used to calculate critical assemblies that are beyond the scope of KENO IV on our computers. The EPRI water-reflected uranium oxide arrays[5] using 218 group ENDF/B-IV cross sections have been calculated using KENO V. These problems cannot be run with KENO IV because the vast amount of storage exceeds the capacity of our computers.

Recent calculations of a Los Alamos critical experiment[6] involving a small water reflected uranium sphere have illuminated a subtle shortcoming involving the P_1 scattering treatment used in KENO IV. A sketch of the experiment is shown in Figure 1. The results of the KENO IV, KENO V, and XSDRN calculations are tabulated in Table 1. The KENO IV results were consistently lower than XSDRN due to the single discrete angle scattering. The Hansen-Roach 16 group water cross sections have a P_2 correction applied to the total cross section. This correction increases the effective mean free path in water so that neutrons exiting the sphere travel farther from the fuel before scattering. The small solid angle subtended by the fuel sphere coupled with the preferentially forward scattering of hydrogen place a severe test on the KENO scattering model in calculating the worth of the water reflector. The single angle model for P_1 scattering has been found to be not as effective as the distributed angle P_1 model described in the section entitled P_n Scattering. A bulletin will be forthcoming in the Radiation Shielding Information Center (RSIC) newsletter to explain the problem and present the modification for the KENO IV code.

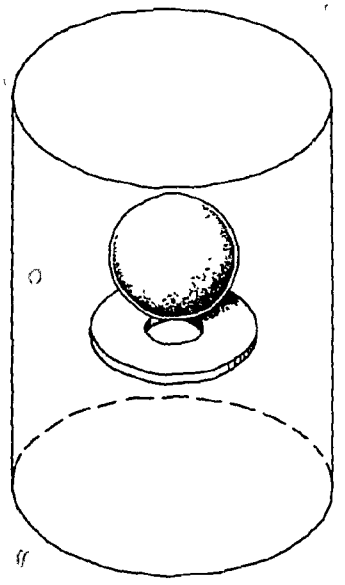

Figure 1. Highly enriched uranium sphere on a plexiglas collar with a cylindrical water reflector.

Table 1. Comparison of KENO and XSDRN for Small Reflected Uranium Sphere.

Number of Energy Groups	Number of Discrete Angles	KENO IV*	Histories	KENO V*	Histories	XSDRN	Quadrature	Convergence
16	1			0.9292 ± 0.0045	50,000	0.9944	32	1.0-8
16	1	0.9830 ± 0.0046	28,800	0.9867 ± 0.0032	89,000	0.9949	32	1.0-6
16	1	0.9809 ± 0.0047	28,800	0.9868 ± 0.0029	89,000	0.9988	8	1.0-4
16	1			0.9902 ± 0.0053	30,000			
16	2	—	—	0.9805 ± 0.0035	70,000			
16	4	—	—	0.9906 ± 0.0057	30,000			
16	0	—	—	1.1144 ± 0.0046	30,000	1.1098	16	1.0-6
16	0	—	—	1.1116 ± 0.0067	12,999			
27	0	—	—	1.1988 ± 0.0056	30,000	1.2079	16	1.0-6
27	1	—	—	0.9870 ± 0.0054	30,000	0.9822	16	1.0-6
27	2	—	—	1.0000 ± 0.0051	30,000	1.0013	16	1.0-6

*Single angle P_1 treatment was used in the calculations having one discrete angle.

The 27 group KENO V results for this experiment were in good agreement with XSDRN but show that P_1 scattering is inadequate for cross sections that do not have higher order corrections applied to them. The KENO V calculation using two discrete scattering angles and the P_3 XSDRN calculation for the 27 group cross sections agree well with the experiment.

At the present time extensive timing studies have not been made for KENO V. The only recent timing comparison between KENO IV and KENO V are for the four aqueous four metal critical experiment shown in Figure 2. The following results were obtained:

KENO IV 30,000 histories $k_{eff} = 0.9959 \pm 0.0056$ in 65.02 seconds
KENO V 30,000 histories $k_{eff} = 0.9994 \pm 0.0051$ in 48.94 seconds

KENO IV used 180 IO's and KENO V used 2088 IO's in the calculations. The problem was run as one super group in KENO V. If it used multiple super groups, both the number of IO's and the running time would increase. KENO V will not always compare so favorably with KENO IV, depending on the type of problem. In general KENO V can be expected to be a little slower and use more IO's than KENO IV.

Figure 2. Four aqueous four metal critical experiment.[7,8]

REFERENCES

1. G. E. Whitesides and N. F. Cross (Landers), KENO - A Multigroup Monte Carlo Criticality Program, CTC-5 (1969).

2. L. M. Petrie and N. F. Cross (Landers), KENO IV - An Improved Monte Carlo Criticality Program, ORNL-4938 (November 1975).

3. R. M. Westfall et al., SCALE - A Modular Code System for Performing Standardized Cask-Analyses for Licensing Evaluation, ORNL/NUREG/CSD-2, to be published.

4. W. W. Engle, Jr., A User's Manual for ANISN - A One-Dimensional Discrete Ordinates Transport Code with Anisotropic Scattering, UCC-ND, K-1693 (March 1967).

5. N. F. Cross (Landers), R. M. Westfall, K. R. Turnbull, and P. B. Fox, "Validation of Criticality Safety Broad-Group Library Using Uranium Systems," Trans. Am. Nucl. Soc., 27, 406 (November 1977).

6. Cleo C. Byers et al., "Critical Measurements of a Water-Reflected Enriched Uranium Sphere," Trans. Am. Nucl. Soc., 27, 412, (November 1977).

7. J. T. Thomas, "Critical Three-Dimensional Arrays of U(93.2)-2 Metal Cylinders," Nucl. Sci. Eng., 52, 350, (November 1973).

8. J. T. Thomas, Critical Three-Dimensional Arrays of Neutron-Interacting Units, Part II, ORNL/TM-868 (July 1964).

GEOMETRY MODELING FOR SAM-CE MONTE CARLO CALCULATIONS

H. A. Steinberg and E. S. Troubetzkoy
Mathematical Applications Group, Inc.
3 Westchester Plaza
Elmsford, New York 10523

ABSTRACT

Three geometry packages have been developed and incorporated into SAM-CE, for representing in three dimensions the transport medium. These are combinatorial geometry - a general (non-lattice) system, complex combinatorial geometry - a very general system with lattice capability, and special reactor geometry - a special purpose system for light water reactor geometries. Their different attributes are described.

1. INTRODUCTION

The treatment of radiation, transport or reactor, problems is most difficult when the geometry of the problem is truly three dimensional. For this situation, the Monte Carlo method, as implemented in computer codes, has been found to be the only practical approach to solution.

A major technical question, in the design and implementation of a code, is the means for representing the geometry. This problem which is mathematically rather simple, is complicated by the conflicting requirements of ease of usage, generality of application, and computer time requirements.

In SAM-CE[1], to answer this question, three packages have been developed, combinatorial geometry (CG), complex combinatorial geometry[2] (CCG), and special reactor geometry (SRG). CG is a general purpose system for representing arbitrary, non-repetitive configurations. CCG extends the CG capability to include lattices, with variable attributes at different lattice sites, in a hierarchical structure, e.g., lattices of lattices. SRG is a fast special purpose system for representing reactor assemblies.

The simulation of particle paths, consisting of straight line segments, through the medium, is the primary geometry problem in Monte Carlo codes (the tracking problem). The solution is made up of a sequence of determinations of two items, the distance to a boundary and the identity of the next region of space. In the following, each geometry is described in terms of representation capability and how the tracking problem is handled.

2. REPRESENTATION CAPABILITY

For all three geometries, space is divided into regions, which are individually homogeneous. All properties, physical (composition, density) and mathematical (scoring, sampling weight) are defined to be constant throughout any region. Finally, all of space must be defined (within some finite limit).

Combinatorial Geometry

Regions are defined as Boolean combinations (unions, intersections, differences) of realizations of geometry primitives (bodies), spheres, boxes, cones, etc. The current library of bodies in SAM-CE has about two dozen types. In addition, a region may include other (previously defined) regions in its descriptive definition. The realizations of the bodies are defined by specific geometric parameters, e.g., for a sphere, the location of the center and the radius. Since each region is defined individually, the requirement that all of space be defined and the avoidance of double definition, are user responsibilities.

Complex Combinatorial Geometry

In its representation capability, CCG is a superset of CG. Specifically, regions - defined by the method described above - are arranged in an hierarchical structure, with additional geometric attributes, such as lattice repetition and translation. Thus, a specified region may be used to define more than one volume of space.

To establish the hierarchical structure, the concept of complex regions is used. A complex region consists of a collection of components, which can be ordinary regions or lattices. A lattice component is actually a repeated geometric pattern of components, which are not necessarily physically identical. Furthermore, any component may, in turn, be a complex.

For example, a reactor core can be defined as a lattice of assemblies, with different properties, e.g., age, and further, each assembly (as a complex) can be modeled as a lattice of rods, allowing variations such as different enrichments, water holes, control rods, etc.

As in the case of CG, the space filling and overlap avoidance responsibility are the user's.

Special Reactor Geometry

This geometry (independent of the others) is designed to represent parts of light water reactor cores. Specifically, an assembly, including a cruciform control rod for BWRs may be modeled. The assembly is defined as a square array of rods, where each rod consists of three concentric cylinders (fuel, gap and clad). The radii may vary from

rod to rod. In general the geometry is three dimensional, but when the cruciform is omitted, it becomes two dimensional.

Since the geometric structure is precisely defined, the space filling and overlap avoidance problems are not present.

3. TRACKING

For all three geometries, the logic is set up so that a sequence of calls to the tracking routines can be made for a given ray (defined by a starting position and a direction), where at each call, the distance to the current region boundary and the identity of the region beyond it is returned. If the ray has a predetermined end point (e.g., to a point detector when estimating flux at a point), as a time saving feature, the next region identity is not determined. Unless terminated by other means (e.g., Russian Roulette), the tracking proceeds until a specially designated region, called the "escape" region, is encountered, except in case of SRG, where a reflecting surface is used. In CG and CCG, rays hitting the "escape" region can be treated as either true escapes or reflections, depending on input.

Combinatorial Geometry

As an aid to the tracking logic, each (user) region, whenever the union operator is used, is defined to be a combination (union) of (internal) regions, which are described by means of intersections and differences only. The two track items (distance and neighbor identity) are obtained for the given internal region, and if the neighboring internal region is part of the same user region, the process simply proceeds without returning to the calling routine. The internal region tracking has two main components, initial and continuing.

The initial portion, used at the beginning of a ray, consists first of the calculation of the distance to the boundary for the known internal region. For an internal region, this is the minimum of the exiting distance for all bodies defined as positive (i.e., intersection) and entering distance (infinite for miss) for all bodies defined as negative (i.e., difference). The identities of the particular body and surface determining the distance are obtained also.

The continuing portion of the code, which uses the cumulative distance traversed, checks all candidate regions for the possibility that at the current position, the ray is about to enter, while at the same time, the distance to the next boundary is obtained. Specifically, the cumulative distance is compared to the entering and exiting distances along the ray for each body defining the region. This cumulative distance should be between the body intersections for a positive and outside the body intersection interval for a negative. If the body is not

convex more than one interval may have to be checked. If the cumulative distance satisfies all the necessary inequalities, the region is considered to be the neighbor, with the distance to the next boundary being obtained in the process, with the defining body and surface.

The logic of this process is such that the geometry code is one step ahead of the calling routine in the determination of distance to the boundary, permitting a simple return with no further calculation, when the next region identity is not needed.

To control the computer time required for tracking, the number of candidate regions examined during the continuing portion must be kept to a minimum. In CG a learning process is used. Initially the complete region list is used as the candidate list for neighbor determination; with processing terminating at the first success. The identity of this neighbor is saved in the region description, associated with the body. Subsequently, when a ray leaves a region through a surface determined by that body, the saved region is checked first. If the saved region is not the neighbor, the full list is then checked and the newly ascertained neighbor is added to the save list for future priority checking. Thus, the number of times the full region list must be checked (a very time consuming task) is kept to a minimum.

Complex Combinatorial Geometry

The arithmetic aspect (distance calculation) of CCG is identical to that of CG. However, the logical aspects, i.e., which regions to check, memory features, etc., are quite different, because of the complex hierarchical structure. In addition, arithmetic and logical analyses are needed when tracking through lattice structures. There is one additional similarity to CG in that the neighbor identity and distance to the (neighbor) region boundary are determined together, while the data furnished to the calling program are the neighbor identity and distance to the current region boundary.

The tracking logic is built around the hierarchical structure, i.e., the logical placement of a point in space requires the definition of a sequence of regions, each of which is a component of the previous complex region, terminating in a region that is not a complex*. Furthermore, when a component is a lattice, the specific cell indices are required.

The tracking consists of an initialization and a continuation. During the initialization phase, the hierarchical sequence is determined, starting with the "real world", and for each region, the distance to the boundary is determined. The minimum of all such distances is the one returned to the calling program.

*The system allows the possibility that the last two regions in the chain are not complexes, when "virtual" and "subordinate" regions are used. In practice, this option is seldom used.

The continuation along the track requires first the determination of the level where the region boundary is further than the minimum. If there is none, tracking proceeds in the real world. Otherwise tracking proceeds among the components of the complex at the determined level. Here, there are two possibilities, depending on whether or not the next lower level component was a lattice. If it was, then the logic will go to the next cell along the track, unless exiting from the entire lattice. In that case, or when the component was not a lattice, the remaining components are checked for entry. If the region entered is a complex, then the chain must be extended by examining its components to determine which one is being entered, with the process continuing until a component which is not a complex is encountered.

In order to control the amount of checking required to ascertain neighbor identity, two learning processes, one similar to that in CG, are used. The CG process is used for "real world" regions and components where the union operator is used. For the latter case, the eligible internal regions are only those which belong to the same user region. For components of complexes, the order of checking is determined by the order of initial encounter.

Special Reactor Geometry

SRG deals with a special case which can be handled by CCG. As indicated previously, it is restricted to typical BWR and PWR, and specifically to infinite reactors consisting of identical assemblies exhibiting four-fold symmetry.

The tracking logic is similar to that of CCG, but much stronger use is made of analytic tracking. The improvement in running time efficiency results from the fact that a substantial part of the information needed during tracking is assumed rather than either retrieved from input data, or obtained by logical tests. A detailed description is given in Appendix A.

4. CONCLUSION

SAM-CE has available three different geometry packages, where the choice of a particular package depends on the application.

REFERENCES

1. H. Lichtenstein, et. al., "The SAM-CE Monte Carlo System for Radiation Transport and Criticality Calculations in Complex Configurations (Revision 7.0)", MR-705207 (Jan. 1979).

2. H. Steinberg, "Complex Combinatorial Geometry", Trans. Amer. Nucl. Soc. 23, 207 (June 1976).

APPENDIX A

Special Reactor Geometry

The tracking logic SRG is similar to that of CCG, but, as SRG deals with a special geometrical case, many logical tests and data retrieved tasks are bypassed.

As in the case of CCG, physical regions are defined by a chain of simpler geometrical definitions. SRG deals with chains of length up to four.

The first level (Figure 1) deals with the vertical range of the reactor. The region between two given horizontal planes is a complex region containing the entire configuration. The two planes are reflection surfaces. This level is bypassed in the case of absence of cruciform control rod, as the geometry becomes effectively two dimensional.

The second level consists of four nested squares (see Figure 2). The entire configuration is within the outermost square. The outermost square itself is a reflection surface. Let the interior of the inner square be region 1, and let regions 2, 3, 4 be the regions defined by the next square annuli, in the outward order. Region 1 is complex. Regions 2 and 3 are physical regions containing moderator, and can material, respectively. Region 4 is complex if and only if it contains a cruciform control rod.

The third level in region 4 (see Figure 3) consists of the cruciform and of the coolant outside the cruciform. Each of these two regions are physical regions.

The third level in region 1 consists of an array of square cells (see Figure 4) completely filling region 1. Each cell is a complex region.

Finally, the fourth level in each cell is defined by three coaxial cylinders. The inner cylinder, the two cylindrical shells, and the region in the cell outside the largest cylinder are all four physical regions (Figure 5).

The method of tracking through the array departs somewhat from the CCG method and is as follows. The tracking in level 1 is trivial.

Both level 2 and level 4 involve two dimensional tracking through convex, nested, non-intersecting curves (nested squares and nested circles). Assume the surfaces are numbered 1, 2, ..., n starting from the innermost one, in the outward direction. If the track starts in the shell between surfaces i and i+1, first test whether it intersects surface i. If it does not, mark the track as outgoing. If the track originates inside surface 1, mark it as outgoing.

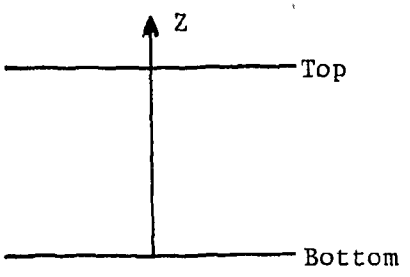

Figure 1

Level 1 - Vertical Range

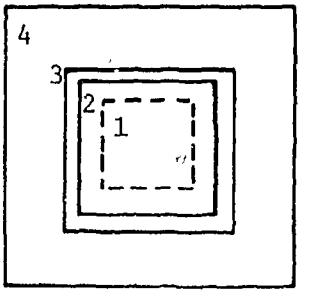

Figure 2

Level 2 - The Nested Squares

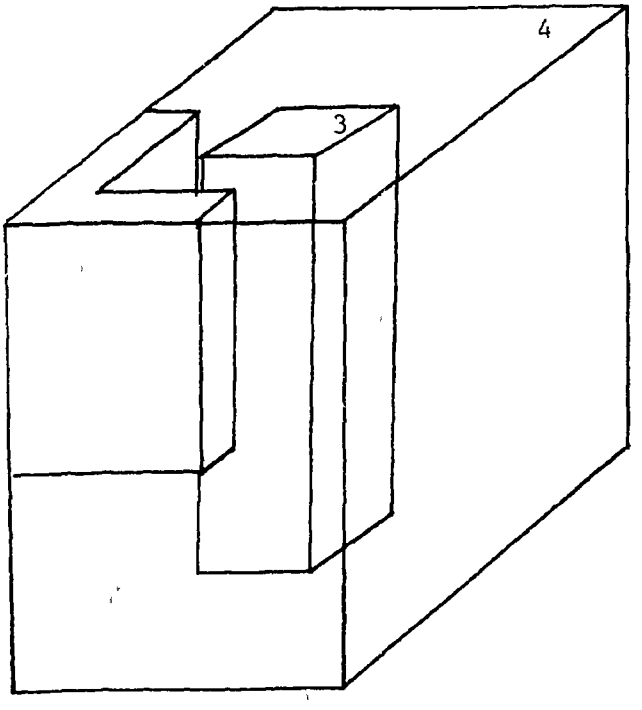

Figure 3

Level 3 - The Cruciform

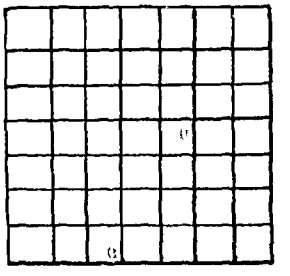

Figure 4

Level 3 - The Array of Cells

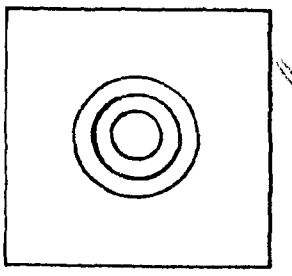

Figure 5

Level 4 - The Nested Cylinders

For non-outgoing tracks, calculate the distance of entry and exit to surface i. The track enters the region inside surface i and outside surface i-1, if any.

Once labeled outgoing, the track remains outgoing. The case of a track originating outside surface n is impossible in level 2 (level n is the reflection region) and treated as explained below in the case of circles.

Tracking in level 3 of region 1 (array) is done as follows. The tracking from cell to cell is performed internally, and terminates as soon as the first of the following conditions is met: the track enters the outermost cylinder of a cell, or a distance limit is reached. This distance limit is preset as the minimum of the distance to leave the array (as calculated in tracking through the previous levels) and a limit (which may be infinite) communicated by the calling program (e.g., distance to point detector).

Finally, tracking in level 3 of region 4 (cruciform) is done exactly as in CG.

NUCLEAR DATA TREATMENT FOR SAM-CE MONTE CARLO CALCULATIONS

H. Lichtenstein, E. S. Troubetzkoy, M. Beer
Mathematical Applications Group, Inc.
3 Westchester Plaza
Elmsford, New York 10523

ABSTRACT

The treatment of nuclear data by the SAM-CE Monte Carlo code system is presented. The retrieval of neutron, gamma production, and photon data from the ENDF/B files is described. Integral cross sections as well as differential data are utilized in the Monte Carlo calculations, and the processing procedures for the requisite data are summarized.

1. INTRODUCTION

The SAM-CE[1] Monte Carlo code system uses ENDF/B[2] as its nuclear data source. The SAM-X component of SAM-CE serves as the principal nuclear data processor, which, together with several auxiliary code modules, extracts the data required for the Monte Carlo analyses. These data include neutron, gamma production, and photon cross sections, as well as differential data, such as angular distributions and secondary energy distributions.

The SAM-X code evolved from ENDTS[3], which itself was an adaptation of ENDT[4]. This evolutionary process, whose duration has already exceeded a decade, has paralleled the development of ENDF/B to its current version V. Aside from keeping pace with ENDF/B format changes, SAM-X has been expanded to include the treatment of thermal neutron scattering data, and, most recently, fission neutron spectra. In addition, as the sheer volume of data included in ENDF/B grew, the SAM-X algorithms have been redesigned to provide increasingly accurate processed data sets. The goal of these developments has been to provide the Monte Carlo component of SAM-CE, SAM-F, nuclear data derived from ENDF/B with virtually no degradation of accuracy. Since most of the nuclear data is linearly interpolated in the Monte Carlo stage (for speed), and ENDF/B can, and often is, tabulated using non-linear interpolation rules, our goal for SAM-X can only be approached within a user specified tolerance. Nevertheless, these tolerances can be quite small (i.e., 0.1%), and certain data (such as fission neutron spectra) are utilized with no degradation of accuracy from the ENDF/B source.

This paper describes the treatment and utilization of the major categories of nuclear data by SAM-CE. Since details of the processing

2.3 Resonance Parameters

For nuclides with cross section resonances, ENDF/B provides resolved and unresolved resonance parameters. These data are to be combined with the corresponding smooth cross sections to yield the complete cross section representation in the resonance energy range.

These data can be treated by SAM-X in several ways. The originally developed approach uses the resonance parameters to generate point values (distribution-averaged values in the unresolved range); these are subsequently combined with the smooth background value. These originally implemented algorithms have been superseded by an adaptation of the RESEND code[6]. These algorithms process ENDF/B resonance parameters (both resolved and unresolved) and combine the resulting point values with the smooth background to produce a complete pointwise tabulation in the resonance range (distribution-averaged values in the unresolved range). All the formalisms invoked by ENDF/B to represent the resolved resonances (i.e., single level and multilevel Breit-Wigner, Reich-Moore, and Adler-Adler) are treated.

An alternative treatment for the unresolved range has been provided by an adaptation of the U3R code[7]. These algorithms generate probability tables (uniform in probability) for the total cross section, and average value partials tabulated as a function of total cross section. This choice of treatment for the unresolved range is optional; the user's decision should be based on a judgment, weighing the investment of an additional processing step versus the gain in accuracy of representation.

2.4 Angular Distributions

Angular distribution data are retrieved for elastic and discrete inelastic scattering. Probability tables (uniform in probability), for cosine of scattering angle in the center-of-mass, are tabulated. The transformation to the lab system is performed analytically in the collision treatment algorithms of the Monte Carlo code.

2.5 Secondary Energy Selection for Inelastic Scattering

The selection of the secondary neutron energy for inelastic scattering is based on the partial cross sections for the discrete levels, and probability distributions for the continuum. The SAM-CE treatment for the discrete levels is analogous to the hierarchical procedure for choosing, first between scattering and absorption, then, if scattering, between elastic and inelastic. Thus, the partial cross sections for the levels are accumulated, such that, for each level, the cumulative values of the partials up to that level number (ordered by increasing threshold) are tabulated on the cross section energy mesh.

and utilization algorithms are amply provided in the SAM-CE user's manual[5], a narrative style will be assumed herein.

2. NEUTRON DATA

2.1 Preliminary Remarks

An ENDF/B data set for one nuclide is subdivided into principal sections, termed "files". The first few files deal primarily with neutron data; for convenience, these may be termed the "neutron files". These files may include the following types of data:

(1) smooth cross sections (total and partials);

(2) resonance parameters (resolved and unresolved);

(3) angular distributions (elastic and discrete inelastic);

(4) secondary energy distributions;

(5) fission spectra (prompt and delayed);

(6) thermal neutron scattering data, termed $S(\alpha,\beta)$ data.

Although other types of neutron data are sometimes available also, the foregoing are the principal types utilized by SAM-CE.

2.2 Smooth Neutron Data

A SAM-CE neutron data set for a specific nuclide will contain tabulations of integral cross sections on an "appropriate" energy mesh. The appropriateness of the energy mesh is defined in terms of the requirement that linear interpolation between mesh points yield cross section values which do not deviate from the implied ENDF/B value by more than a user specified tolerance. The tabulations include total, total scattering, inelastic, and fission cross sections (where relevant). In addition, neutron multiplicities of inelastic scattering, stemming from "(n,2n)-like" reactions, are tabulated on the same energy mesh.

These meshes vary in length for different nuclides, for obvious reasons. For example, a hydrogen data set may be tabulated on an energy mesh of several hundred entries, whereas a data set for ^{238}U may require tens of thousands of energy mesh points to preserve the same degree of accuracy for linear interpolation. This approach of generating unique energy meshes for each nuclide data set offers substantial savings in memory for the Monte Carlo stage, where many nuclides may be present in the problem description.

The choice between levels and continuum is based on the fraction of inelastic cross section which exceeds the cumulative value tabulated for the highest explicit level. Thus the continuum event is initially treated as an implicit highest level.

Given that a continuum inelastic event is selected in the Monte Carlo, the secondary energy is sampled from cumulative probability tables (uniform in probability), which are also tabulated on the same energy mesh used for the integral cross sections. These tabulated secondary energy values are given by ENDF/B as angle decoupled values in the lab system. To introduce an energy-angle coupling, these values are interpreted by SAM-CE as average values, from which an excitation energy, Q, is computed using the relation

$$Q = \left(\frac{A}{A+1}\right)\ (E-\bar{E}) \qquad (1)$$

where E is the incident neutron energy, $\bar{E}$ is the sampled average, and A is the mass of the nuclide. Thus, the treatment of the continuum reduces to the treatment of a discrete level, with a "sampled" excitation, Q.

2.6 Thermal Scattering Data

For certain evaluations (such as hydrogen bound-in-water), ENDF/B provides thermal scattering data to account for molecular binding effects. These data, usually referred to as $S(\alpha,\beta)$, are utilized by SAM-CE to generate two dimensional sampling tables, coupling the momentum (α) and energy (β) transfer of a thermal scattering event. Through numerical integration and interpolation, SAM-CE allows the sampling of all physical points in the (α,β)-domain.

Since the numerical integration becomes a substantial fraction of the Monte Carlo computing time for problems characterized by thermal molecular scattering, the $S(\alpha,\beta)$ processing and sampling algorithms in SAM-CE will be completely overhauled in the near future. An order of magnitude improvement in speed is anticipated by a judicious change of variables (from α and β), which will obviate numerical integration in the Monte Carlo sampling stage.

2.7 Fission Spectra

The most recent additions to the collection of ENDF/B neutron data utilized by SAM-CE are fission spectra, both prompt and delayed. The data is retrieved from ENDF/B with no degradation of accuracy. This is accomplished via a departure from the normal requirement for linear interpolation in the Monte Carlo sampling. The sampling algorithms incorporate all valid ENDF/B interpolation schemes, and are cognizant of all defined formalisms (the tabulations, as well as the analytic probability functions). The inclusion of a treatment for the delayed neutron spectra is believed to be unique among the foremost neutronics codes in the field.

3. GAMMA PRODUCTION DATA

The ENDF/B "gamma production" files are, essentially, tabulations of photon yields for various non-elastic neutron interactions, and corresponding photon angular distributions. These data are processed by SAM-X in a manner analogous to the treatment for smooth neutron cross sections, as described above. The algorithms have not changed significantly from those described in Reference 3.

4. PHOTON INTERACTION CROSS SECTIONS

Point value cross sections are generated from ENDF/B file 23. These data govern photon transport and interactions, as well as the generation of secondary electrons. Once the energy mesh is established, using criteria for linear interpolation, as for smooth neutron cross sections, the Compton cross section is computed analytically, and the pair production and photoelectric partials are retrieved from ENDF/B.

5. MISCELLANEOUS

Several auxiliary data processing utilities and procedures deserve mention. These include: (1) BCDEAN, a utility for transfering processed libraries (which are utilized in binary form) between, possibly, different computer architectures; (2) an adaptation of the PLOTEF[8] code, to enable graphic display of SAM-X processed neutron cross sections; (3) the *a priori* energy mesh enrichment algorithms necessitate some *a posteriori* "weeding", which is provided for neutron, photon, and gamma production data; (4) Doppler broadening of neutron cross sections is performed by initially producing a "cold" data set from the ENDF/B, and then "heating" up the processed data to any requested temperature; (5) the approximate treatment of electron transport (straight ahead/continuous-slowing-down) in SAM-F utilizes the photon interaction cross sections as electron production data, and uses built in range-energy relations; (6) the secondary photon producing processes of Bremsstrahlung and electron-positron annihilation are treated in the photon transport.

REFERENCES

1. E. S. Troubetzkoy, et al., "The SAM-CE Monte Carlo System for Radiation Transport and Criticality Calculations in Complex Configurations (Rev. 7.60), EPRI CCM-8, Prepared by MAGI (Jan. 1980).

2. D. Garber, C. Dunford and S. Pearlstein (eds.), "Data Formats and Procedures for the Evaluated Nuclear Data File, ENDF", BNL-NCS-50496/ENDF102 (Oct. 1975).

3. H. Lichtenstein, et al., "Processing ENDF Cross Sections for the Monte Carlo Solution of Radiation Transport Equations", Trans. Am. Nucl. Soc., 15, 571 (1972).

4. S. Kellman, "ENDT: A Fortran Program to Prepare Cross Section Data for UNC-SAM-3 from ENDF/B Tapes", DASA-2337/UNC-5243, United Nuclear Corp. (Jan. 1970).

5. E. S. Troubetzkoy, et al., op. cit.

6. O. Ozer, "RESEND: A Program to Preprocess ENDF/B Materials with Resonance Files into a Pointwise Form", BNL 17134 (1973).

7. R. Prael, Atomic International, private communication.

8. Program PLOTEF, distributed by the National Neutron Cross Section Center, Brookhaven National Laboratory.

MONTE CARLO METHODOLOGY AS IMPLEMENTED IN SAM-F

E. S. Troubetzkoy and H. A. Steinberg
Mathematical Applications Group, Inc.
3 Westchester Plaza
Elmsford, New York 10523

ABSTRACT

The variance reduction techniques implemented in SAM-F are discussed. This includes importance sampling as a function of position, direction, energy and time, and judicious use of quota sampling.

I. INTRODUCTION

The quantities estimated by SAM-F[1] include flux and reaction rates at specified points, or averaged over specified geometrical regions, averaged over specified energy and time ranges. In eigenvalue problems, several (biased) estimators of the eigenvalue are also available.

As indicated by its acronym, SAM-F, (Stochastic-Aleatory Method, Forward Mode) the code utilizes the Monte Carlo method. The source is sampled. Collision points are sampled from the transport kernel and, at these points, the collision kernel is sampled. Estimation is performed when tracks reach point detectors or cross detector regions. The sampling is importance-biased, with bias removed by weight adjustment, and features a judicious use of generalized-quota sampling.

II. ESTIMATION

Consider a track originating either at the source or at a collision point. If the semi-infinite track enters a convex detector region a distance r from its origin, and leaves that region a distance r' from its origin, the analytical expression for the flux contribution of that track to the region average is:

$$E = \frac{A}{V} \frac{1-e^{-\mu(r'-r)}}{\mu} \qquad (1)$$

where μ is the total cross section in the region, V is the volume of the region, and

$$A = W\, e^{-\int_0^r \mu(s)ds} \tag{2}$$

where W is a weight carried by the particle, adjusting for importance sampling.

The familiar "track length" and "collision" estimators, as well as their "minimum variance" linear combination, are all valid estimators of (1). All three have a finite variance. In SAM-F, the zero variance "exponential" estimator is implemented: expression (1) is evaluated numerically. Russian roulette on the track is played, however, when the value of A falls below a pre-determined, importance-dependent, cutoff value A_0. This introduces a finite variance for finite A_0.

For a point detector a distance r away from the track origin, the estimator is

$$E = A/r^2 \tag{3}$$

This is also calculated numerically. As mentioned below, the biasing is such that the estimator (3) is bounded: W removes the $1/r^2$ singularity.

III. IMPORTANCE SAMPLING

All sampling distributions are importance biased by a user specified importance function, which may be a function of space, time, energy, and direction, with no restriction on separability. The direction-dependence is restricted to be a function of the angle between the direction of flight and a specified "aiming vector" which may be itself a function of space, time, and energy. The dependence of the importance function on each of its variables is restricted to be piecewise constant.

In the presence of point detectors, an additional importance function[2] is internally defined. It has a $1/r^2$ singularity, where r is the distance to the point detector.

We are going to describe our method of importance sampling. To introduce our notation, we write the Boltzmann equation as

$$\psi(P'') = S(P'') + \int K(P'' \leftarrow P')T(P' \leftarrow P)\psi(P)dP \tag{4}$$

where ψ is the density of particles coming out of collisions, S is the source, K is the collision kernel, and T is the transport kernel. To avoid a cumbersome notation, we consider a time-independent problem and define:

$$P = \{\vec{X},\vec{\Omega},E\}$$

$$P' = \{\vec{X}',\vec{\Omega},E\} \tag{5}$$

$$P'' = \{\vec{X}'',\vec{\Omega}'',E''\}$$

where $\vec{X}$ is the position, $\vec{\Omega}$ the direction, and E is the energy.

Finally, let

$$\text{Importance function} = I(P) \tag{6}$$

III.1 Importance Sampling of the Source

The source term of Equation (4) is normalized. We rewrite it in the form:

$$S(P'') = W \cdot \tilde{S}(P'') \tag{7}$$

where $\tilde{S}(P'')$ is the importance-biased source:

$$\tilde{S}(P'') = I(P'')\ S(P'')/S_0 \tag{8}$$

$$W = S_0/I(P'') \tag{9}$$

$$S_0 = \int I(P'')\ S(P'')dP'' \tag{10}$$

The calculation of the normalization (10) and of the sampling tables for $\tilde{S}$ is performed once at input time.

At the start of each history, one samples $\tilde{S}$ for P'', and calculates W from Equation (9). According to Equation (7) the sample P'' weighed by W is a valid sample of S(P'').

III.2 Importance Sampling of the Transport Kernel

The transport kernel

$$T(P' \leftarrow P) = e^{-\int_0^S \mu(S')dS'} / \mu \ , \tag{11}$$

where

$$S = (\vec{X}''-\vec{X}) \cdot \vec{\Omega}, \tag{12}$$

is normalized. The biased sampling of the transport kernel, conceptually, could be treated exactly as the sampling of the source term. A difficulty arises, however, in the evaluation of the normalization

$$\int I(P')T(P' \leftarrow P)dP', \tag{13}$$

which requires tracking to infinity. That calculation cannot be carried out exactly in infinite lattices, for instance.

Instead of defining a normalized biased kernel, we define an unnormalized one.

Let

$$T(P' \leftarrow P) = W_T \cdot \tilde{T}(P' \leftarrow P) \tag{14}$$

where

$$\tilde{T}(P' \leftarrow P) = I(P')T(P' \leftarrow P)/I(P) \tag{15}$$

$$W_T = I(P)/I(P') \tag{16}$$

Equation (15) can be more clearly written in terms of the variable S (Equation (12)):

$$\tilde{T}(S) = I(S) \cdot e^{-\int_0^S \mu(S')dS'} / (\mu \cdot I(0)) \tag{17}$$

A method to sample such unnormalized kernels has been devised[3]. The problem of obtaining a single sample of a normalized distribution with a weight proportional to the normalization is replaced by obtaining N samples, the expected value of N being the normalization. A completely stratified sampling reduces the fluctuation of N to a minimum. The necessity to track to infinity is eliminated by introducing Russian roulette, preserving completely the exact nature of the calculation.

The N samples P_i', i=1,N, carry transport weight factors given by Equation (16):

$$W_{Ti} = I(P)/I(P_i') \ , \ i=1,N \tag{18}$$

and total weights

$$W_i = W \cdot W_{Ti} \quad , \quad i = 1,N \tag{19}$$

The N samplea and their total weights are stored into a "latent" list. The samples represent the density of particles going into collision.

III.3 Importance Sampling of the Collision Kernel

The samples of particle going into collision are picked up, one at a time. Consider particle i. Let $P' = P'_i$ and $W = W_i$.

As in the case of the source distribution, we define a normalized biased kernel K through:

$$K(P'' \leftarrow P') = W_K \tilde{K}(P'' \leftarrow P') \tag{20}$$

where

$$\tilde{K}(P'' \leftarrow P') = I(P'')K(P'' \leftarrow P')/K_0 \tag{21}$$

$$W_K = K_0/I(P'') \tag{22}$$

$$K_0 = \int I(P'')K(P'' \leftarrow P')dP'' \tag{23}$$

The calculation of the normalization (23), which is P'-dependent, is performed at sampling time. The method does not depend on K being normalized: the normalization of K itself is correctly taken into account through Equation (23) and (22): the presence of reactions like n2n is treated by sampling a single outgoing neutron, but with a high weight.

A single outgoing particle P" is sampled from $\tilde{K}$. The weight W_K is calculated. As shown by Equation (20) the sample P" weighted by W_K represents an unweighted sample of K.

The total weight W is set equal to $W \cdot W_K$. The set (W,P") represents a contribution to the density of particles coming out of collision.

Several treatments of absorption are available, with option specified on input. The normal treatment is to consider absorption as a reaction which, when sampled, terminates the history branch.

Another option (which we recommend only in special situations) is to exclude absorption as a reaction: the normalization of K is reduced, leading to reduced values of the collision weight factor W_K. In this option, neutrons never die, but rather, like old soldiers, they just fade away* as the total weight eventually becomes vanishingly small.

*and, with apologies to MacArthur, undergo Russian roulette.

Finally, the option exists to treat schizophrenic neutrons, with absorption both allowed and suppressed. The use of that option will become apparant in Section IV.1 below.

IV. Generalized Quota Sampling

Generalized Quota Sampling[4] (GQS) is a powerful variance reduction technique when applied judiciously.

When running a Monte Carlo calculation consisting of N histories, the histories are combined into n statistical aggregates, or batches, of n histories each, so that $N=m\cdot n$.

Each history of an aggregate is a random sample of variables in phase space. GQS preserves that property but its ultimate goal is that each of the n histories of the same aggregate, sample an independent but equally probable region of phase space. This reduces the variance by making the variance for N histories less than 1/N times the variance for one. The degree of success of GQS depends on how that subdivision is defined in the sampling scheme.

IV.1 GQS of the Source

In the case of fixed (input-specified) source problems, the position, direction, energy, and time variables of the source term are always sampled using GQS.

The case of eigenvalue problems is different. The source term is the eigenfunction. Our general approach to the problem is to perform Monte Carlo calculations generation by generation, with fission neutrons produced in one generation playing the role of source neutrons in the next generation. A more detailed discussion follows.

In the course of processing the histories of a generation, in addition to performing all requested estimates of flux and reaction rate, we store, at each collision entered, the parameters P', and the weight W multiplied by $\nu\mu_f/\mu_T$, together with the identifier of a fissionable nuclide appropriately sampled from the ones locally present. When completed, the list, together with fission spectral information, completely specifies the next generation source. The size, and therefore, the statistical quality of the list can be improved by using the option of absorption suppression. In fact, as mentioned in Section III.3 above, we can suppress absorptions just for the purpose of creating this list, and still allow absorptions for the purpose of scoring reaction rates.

Let us now return to the subject of this subsection, and discuss source sampling given such a list produced in the preceding generation. To utilize GQS, the user subdivides all of space into simple geometrical

regions (e.g., cylindrical annuli). If the size of the statistical aggregate is n, n samples will be drawn from the list, satisfying (up to the undivided remainder) the quotas in each region, with weight inversely proportional to the fixed, input specified importance at the sampled position. All weights are equal to 1 in the usual case of unit importance everywhere. Finally, the energy is sampled from the appropriate fission spectrum (in most cases by random sampling), and an isotropic direction is sampled using GQS.

IV.2 GQS of Absorptions

The technique of stratified absorption[5] has been made compatible with GQS. The technique is simple both to grasp and to implement in the absence of any importance biasing.

Consider a history corresponding to an analog Monte Carlo technique: A particle is sampled from the source, and is transported to collision, and then from collision to collision until an absorption occurs. This can be simulated by sampling, at each collision, a reaction type: a scattering with probability μ_S/μ_T or an absorption with probability μ_a/μ_T. The same game of chance can be played differently. At the beginning of the history, let W=1, and sample a random number ξ. Suppress absorption at collision, but decrease the survival weight by setting $W=W\cdot\mu_S/\mu_T$. Stop the history at the first collision for which $W\leq\xi$ and call the last event absorption. The game of chance is identical, but the technique offers the possibility of useful stratification. If n is the size of the statistical aggregate, n stratified random numbers can be presampled at the start of the aggregate, satisfying $(i-1)/n\leq\xi_i<i/n$. GQS delivers a random permutation of such numbers.

The usefulness of the technique is most apparent for thermal reactor calculations. The technique drastically reduces the fluctuation of the number of neutrons degrading into the thermal energy range, and therefore of all estimates of interest, including criticality.

V. Biased Estimators

The flux and reaction rate estimators presented in Section II are completely unbiased in the case of fixed source calculations.

Eigenvalue problems are treated generation by generation. Each generation is treated as a fixed source calculation, with the source obtained from the previous iteration. The method leads to a bias of all estimates. This bias cannot be removed. The only bias reduction technique implemented in SAM-F is the option to initiate estimation only after a certain number of generations have been completed.

V.1 Estimation of Eigenvalue

Several estimators are available for the eigenvalue. The one which falls into the category of Section II is the exponential flux estimator times $\nu(E)\mu_f(E)$. In addition, a collision estimator and an absorption estimator are available.

In addition to all other reaction rates requested on input, the following quantities are also estimated: absorption, excess neutron due to (n,2n),(n,3n) reaction, and leakage. The quantity: absorption plus leakage minus excess neutron has unity for expected value. A fourth, definitely biased eigenvalue estimate is obtained by dividing, at the end of each generation, this quantity into the exponential $\nu\mu_f$ estimate. We observe that, for thermal reactors, the fluctuations of that ratio are much smaller than those of the numerator. We also observe that the bias is small, in the sense that the average of the ratio is well within the standard deviation of the numerator.

Finally, a fifth biased estimate is evaluated. It is that linear combination of the first four which minimizes the variance. This estimate becomes meaningful only for well converged runs.

We observe that the minimum variance estimate is usually extremely close to the absorption eigenvalue estimate if stratified absorption is used. The minimum variance itself is usually only slightly smaller than the variance of the absorption eigenvalue estimates.

References

1. E. S. Troubetzkoy, H. Lichtenstein, H. A. Steinberg, M. O. Cohen, M. Beer, "The SAM-CE Monte Carlo System (Rev. 7.60)", MAGI report, EPRI-CCM-8 (January 1980).

2. H. A. Steinberg and M. Kalos, "Bounded Estimation of Flux at a Point", Nucl. Sci. & Eng. 44, 406 (1971).

3. E. S. Troubetzkoy, UNC-SAM-2, UNC-5157 (September 1966).

4. H. A. Steinberg, Generalized Quota Sampling, Nucl. Sci. Eng. 15, 142 (1963).

5. E. S. Troubetzkoy, "Monte Carlo Calculation of Resonance Escape Probability in Uranium and Uranium Oxide Lattices", Trans. Am. Nucl. Soc. 11, 163 (1968).

RADIATION STREAMING WITH SAM-CE

N. De Gangi, M. O. Cohen, E. Waluschka and H. A. Steinberg
Mathematical Applications Group, Inc.
Elmsford, New York U.S.A.

ABSTRACT

The SAM-CE Monte Carlo code has been employed to calculate doses, due to neutron streaming, on the operating floor and other locations of the Millstone Unit II Nuclear Power Facility. Calculated results were compared against measured doses.

A problem of significant interest to the Nuclear Power industry is the prediction of dose levels due to radiaton which emerges from the pressure vessel of an operating reactor. These predictions should not require excessive costs either in setting up the calculations or in running the problems, but should, at the same time, be accurate enough so that costly retro-fitting will not be required.

Locations of most interest are those where personnel may be found during operation (e.g., on the operating floor) and where radiation reaches the site primarily by neutron streaming (e.g., through the reactor cavity).

Mathematical Applications Group, Inc. (MAGI) has performed a set of calculations to demonstrate that:

(1) with the SAM-CE Monte Carlo[1] radiation transport code,

(2) with a reasonably detailed geometric model (omitting, however, considerable fine detail),

(3) and with affordable computer running times,

adequate prediction of the radiation dose levels can be achieved.

The calculations were performed with the SAM-CE (ENDF/B-based, point energy cross sections) Monte Carlo code using the experimental results obtained at the Millstone II power plant[2], as a means of comparison. The Millstone II configuration was simulated, in SAM-CE, by the Combinatorial Geometry technique[3] with 130 identifiable and selected geometric regions. For importance sampling purposes (see below) these simulated geometric regions were, in many cases, subdivided so that the final computer model had 190 regions.

Simulated detectors were placed at several locations which corresponded to measurement points at Millstone. Specifically, we examined selected locations on the operating floor, on the missile shield, and looking down into the refueling cavity. Both neutron and secondary gamma ray doses were obtained, but since the neutron dose levels significantly exceed the gamma ray levels, heaviest concentration of effort was placed on the neutron results. In addition, we calculated the dose levels on the operating floor that would be present with an additional shield (water tank) at the top of the cavity.

A pressure vessel current surface source was used to start Monte Carlo calculation. Neutron energy-angular distribution were determined with ANISN[4]. The axial distribution was obtained from the Millstone Unit II Final Safety Analysis Report.

Those familiar with Monte Carlo techniques know that proper importance sampling is required to speed the convergence of the solutions. SAM-CE offers the user the opportunities to importance sample in all aspects of phase space, that is, in space, direction, energy and time. Of these options, the first three were used in this effort.

Of particular interest is SAM-CE's capability of biasing transport with respect to the direction of the radiation particle. This angular biasing can be with respect to either a point in space, a line in space, or a fixed direction; with free choice of option being available for each geometric region. The proper use of angular biasing enabled us to "force" radiation back into the cavity without the need for albedo data sets.

The "transmission" region option provided another tool to enhance the speed of the Monte Carlo calculation. This option eliminated time consuming point detector estimates when sampling was occurring at locations that do not contribute significantly to the point detectors. Further, geometric perturbations were permitted without recalculating the complete problem.

Figures 1 and 2, from the Millstone report[5], identify the measurement locations. Encircled sites represent points considered by our calculational program.

Measured and calculated data are presented in Table 1. The measurements were reported to be uncertain by up to a factor of two[6]. The uncertainties in the computed results (percent) are provided in parentheses. The computed results were those provided directly from SAM-CE. The ratios of these results to the measurements are given. We have also considered normalizing all computed results so that the fluxes predicted at the mid-core level in the cavity (slight variation from run to run), which are highly dependent upon the source terms agree with the measured data at this location. These "normalized" doses lead to the "normalized ratios", also given in Table 1, and are the best indicators of the ability of SAM-CE to predict radiation streaming.

DETECTOR LOCATIONS

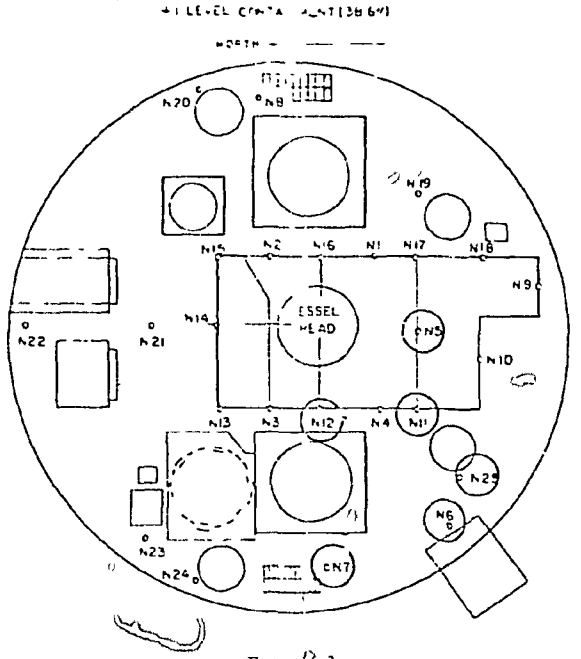

Figure 1

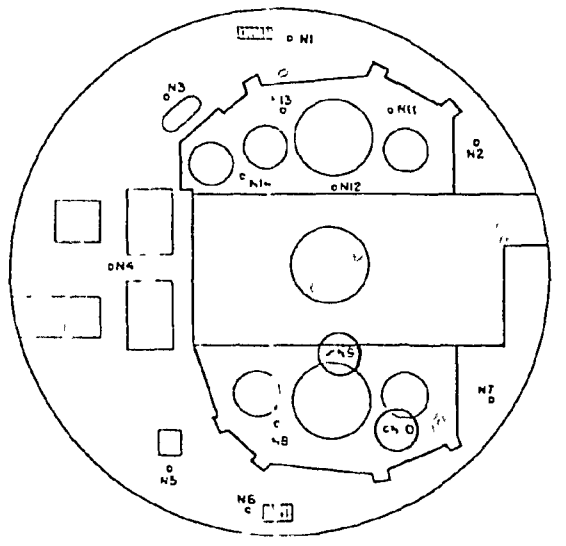

Figure 2

TABLE 1

Millstone II - Radiation Levels

Locatio	Detector	Radiation Type	Dose (rem/hr) Calculated		Measured	Ratio (C/M)	Normalized Ratio (C/M)
OF-CAV*	5	neutron	62.1	(21)	65	.96	.90
		gamma ray	3.8	(20)	10	.38	.34
		total	65.9	(20)	75	.88	.83
OF	6	neutron	3.71	(17)	4	.93	.83
		gamma ray	0.64	(32)	0 45	1.42	1.32
		total	4.35	(15)	4.45	.98	.88
OF	7	neutron	1.36	(18)	1.5	.91	.81
		gamma ray	0.13	(32)	0.23	.57	.53
		total	1.49	(17)	1.73	.86	.78
OF-CAV	11	neutron	29.5	(26)	10	2.95	2.79
		gamma ray	1.6	(19)	2.5	.64	.53
		total	31.1	(25)	12.5	2.48	2.34
OF-MS*	12	neutron	8.44	(19)	6	1.41	1.26
		gamma ray	1.18	(27)	1.5	.79	.66
		total	9.62	(17)	7.5	1.28	1.14
OF	25	neutron	3.32	(18)	3	1.11	.99
		gamma ray	0.86	(33)	0.45	1.91	1.80
		total	4.18	(16)	3.45	1.21	1.09
SGC**	9	neutron	50.18	(27)	30	1.67	1.22
SGC	10	neutron	6.37	(23)	1.5	4.24	3.10
OFW***	6	neutron	0.035	(29)	0.04	.88	.70
OFW	7	neutron	0.020	(27)	0.01	2.00	1.60
OFW-MS	12	neutron	0.296	(29)	N.A.	--	--
OFW	25	neutron	0.059	(24)	0.04	1.47	1.23

NOTES

* OF = operating floor, CAV = overlooking cavity, MS = on missile shield

** SGC = steam generator cubical

*** OFW = operating floor with water tank in place

It is seen in Table 1 that some of the calculated-to-measured ratios are less than unity whereas others are greater. In all cases agreement for the normalized ratios is within a factor of about three and in most cases the agreement is much closer than that.

The entire program required about 10 hours (CP) of CDC 6600 computer time. However, one-third of this time was spent establishing proper importance sampling techniques and need not be required for similar reactor configurations.

REFERENCES

1. H. Lichtenstein, et al., "The SAM-CE Monte Carlo System for Radiation Transport and Criticality Calculations in Complex Configurations (Revision 7.0)", EPRI CCM-8 (July 1979).

2. "Radiation Survey Results in and around Millstone Unit II Containment Building", Docket No. 30-336 (April 1976).

3. H. Lichtenstein, et al., op. cit., Section 3.2.1.

4. W. W. Engle, Jr., "A User's Manual for ANISN", K-1693, Oak Ridge Gaseous Diffusion Plant (1967).

5. N. De Gangi, et al., "Validation of a Monte Carlo Code for Radiation Streaming Analyses", MR-7068 (December 1979).

6. Private Communication, John Doroski, Radiation Assessment Section, Radiological Assessment Branch, Northeast Utilities (April 1979).

Blank

TRX AND UO2 CRITICALITY BENCHMARKS WITH SAM-CE

M. Beer, E. S. Troubetzkoy, H. Lichtenstein
Mathematical Applications Group, Inc.
3 Westchester Plaza
Elmsford, New York 10523

P. F. Rose
Brookhaven National Laboratory
Upton, New York 11973

ABSTRACT

A set of thermal reactor benchmark calculations with SAM-CE which have been conducted at both MAGI and at BNL are described. Their purpose was both validation of the SAM-CE reactor eigenvalue capability developed by MAGI and a substantial contribution to the data testing of both ENDF/B-IV and ENDF/B-V libraries. This experience also resulted in increased calculational efficiency of the code and an example is given.

The benchmark analysis included the TRX-1 infinite cell using both ENDF/B-IV and ENDF/B-V cross section sets and calculations using ENDF/B-IV of the TRX-1 full core and TRX-2 cell. BAPL-UO2-1 calculations were conducted for the cell using both ENDF/B-IV and ENDF/B-V and for the full core with ENDF/B-V. In these calculations the modeling of the full core lattices was accomplished by use of Complex Combinatorial Geometry. Eigenvalues, reaction rates and reaction rate ratios are given for these cases and the results discussed.

1. INTRODUCTION

This paper describes a set of Monte Carlo calculations with SAM-CE involving thermal reactor benchmarks. The calculations were performed recently at MAGI and at Brookhaven National Laboratory (BNL). They involved both full core and infinite cell cases, utilizing both the ENDF/B-IV and the ENDF/B-V libraries.

The dual major purpose of the calculations was the validation of the SAM-CE reactor capabilities that are described in other papers at this session and a contribution to the testing of data pertaining to reactors in the ENDF/B libraries.

Efforts were also made to utilize the experience gained in running problems with SAM-CE to improve the overall efficiency of the Monte Carlo calculations.

It is useful to briefly mention one example of improved efficiency before turning to the major considerations of this paper - the calculations and results. We refer to variance reduction by application of a posteriori statistical methods to several estimators of the same parameter. In particular, SAM-CE estimates k_{eff} in four ways, utilizing track length and collision type estimators. In the course of these calculations, the maximum likelihood-minimum variance procedure was first applied to the case of several eigenvalue estimators[1] and later implemented within SAM-CE directly[2]. The method was also applied to the case of two estimators of the same reaction rate in some of the later benchmark calculations.

2. CALCULATIONS AND METHODOLOGY

We now turn to consideration of the calculations. These involved the TRX-1, TRX-2 and BAPL-UO2-1 benchmarks. Results were obtained for the cases shown in Table 1. Note that calculations of TRX-1 and TRX-2 cells and the TRX-1 full core were conducted utilizing an available SAM-X processed library of ENDF/B-IV elements[3]. These calculations proved very useful in the code validation.

The BAPL-UO2-1 calculations for the cell were performed with both the ENDF/B-IV library and a recently processed ENDF/B-V SAM-CE library[4]. A full core ENDF/B-V calculation has also been performed. These SAM-CE benchmarks offered useful comparison of results involving both ENDF/B-IV and ENDF/B-V.

It should be noted that calculations involving the ENDF/B-V library utilize the fission spectra specified for the individual isotopes by ENDF/B-V at a particular neutron energy. The ENDF/B-IV calculations assumed fission spectra to be represented by that for ^{235}U thermal neutrons.

Geometry and composition for the problems are as specified in the "CSEWG Benchmark Specifications"[5]. Reflective boundary conditions were used for the cell combinatorial geometry. Full core calculations utilized complex combinatorial geometry.

All the benchmarks were run on CDC 7600 computers. The BAPL-UO2-1 ENDF/B-V benchmark was also run on a PDP-10 computer*. The BAPL-UO2-1 full core calculation was conducted at MAGI, the remainder at BNL.

*The results given herein for this benchmark are those obtained on the PDP-10.

TABLE 1

Benchmark Criticality Calculations
Conducted with SAM-CE

	Cell Calculation		Full Core	
Benchmark	ENDF/B-IV	ENDF/B-V	ENDF/B-IV	ENDF/B-V
TRX-1	Yes	No	Yes	No
TRX-2	Yes	No	No	No
BAPL-UO2-1	Yes	Yes	No	Yes

3. RESULTS

The TRX-1 and TRX-2 cell eigenvalue and reaction rate ratios are given in Table 2 for SAM-CE calculations as well as comparison results obtained from the RECAP and VIM Monte Carlo codes*. Generally good agreement is found between the codes. Table 3 gives 4 group** reaction rates for ^{235}U and ^{238}U obtained for both the TRX-1 and TRX-2 cells.

We now turn to the TRX-1 full core results. Table 4 gives k_{eff} and inner core reaction rate ratios for SAM-CE and comparison BNL results for RECAP[6] and Hardy's RCP01 results[7]. The SAM-CE inner core was chosen to conform to the largest region shown by Hardy[7] to yield reaction rate ratios imperceptibly different from core center results.

The important deviations of calculated and experimental values occur for k_{eff} and ρ_{28} for which all three codes agree fairly well with each other. The effect is better seen in Figure 1 in which the SAM-CE and RECAP points have been added to the other points plotted previously by Hardy[6]. The deviations of k_{eff} and ρ_{28} from experiment clearly are artifacts of the ENDF/B-IV data.

The BAPL-UO2-1 calculations allow comparisons to be made between ENDF/B-IV and ENDF/B-V results. Table 5 contains values for k_{eff} and reaction rate ratios for the 3 cases considered. (Inner core reaction rates are given for the full core results.) Note first the good agreement obtained between the full core ENDF/B-V values and experiment. On the other hand, comparison of the cell results indicates a seemingly significant increase in the k_{eff} value from ENDF/B-IV to ENDF/B-V ($\sim$.6%) in conformity with the TRX results (low k_{eff} for ENDF/B-IV full core).

Turning to the reaction rates, Table 6 gives reaction rates for ENDF/B-IV and ENDF/B-V cell calculations in the CSEWG group structure. The significant changes in this case involve a decrease in ^{238}U fast capture and an increase in fast ^{238}U fission from ENDF/B-IV to ENDF/B-V. Reaction rates for ENDF/B-V results were also obtained in a second four group structure specified by EPRI***. These were divided by the group fluxes to obtain the EPRI group cross sections given in Table 7 for ENDF/B-V cell and full core calculations. Good agreement is obtained between full core inner core and cell results for all cases.

---

*Uncertainties in all the tables are either standard deviations or percent standard deviations when indicated.

**Upper energy boundaries of the four groups are 10 MeV, 67.379 keV, 3.355 keV, 0.625 eV. These will be referred to as the CSEWG group structure.

***Upper energy boundaries of the four groups are 10 MeV, 821 keV, 5.53 keV and 0.625 eV.

TABLE 2

Eigenvalues and Reaction Rate Ratios
for TRX-1 and TRX-2 Cell Calculations

LATTICE PARAMETERS	TRX-1			TRX-2		
	RECAP	SAM-CE	VIM	RECAP	SAM-CE	VIM
k_∞	1.1721 ± .0019	1.1751 ± .0016	1.1721 ± .0030	1.1578 ± .0026	1.1605 ± .0015	1.1613 ± .0032
ρ_{28}	1.334 ± .46%	1.324 ± .8%	1.328 ±1.2%	.8244 ± .75%	.8139 ±1.1%	.8344 ±1.0%
δ_{25}	.0963 ± .52%	.09526± .7%	.09693± .87%	.05843± .82%	.0585 ± .9%	.05917± .86%
δ_{28}	.08903± .56%	.09206± .7%	.08866± .81%	.06473± .80%	.06450± .7%	.06487± .75%
C*	.7910 ± .31%	.7882 ± .4%	.7899 ± .78%	.6351 ± .43%	.6314 ± .5%	.6391 ± .58%

TABLE 3

CSEWG 4 Group Reaction Rates for TRX-1 and TRX-2 Cells
For ENDF/B-IV

Group	U-235			U-238		
	Capture	Fission	Neutron Production	Capture	Fission	Neutron Production
			TRX-1 Cell SAM-CE			
1	4.059-4 (.4%)	3.3806-3 (.3%)	8.8013-3 (.3%)	1.9124-2 (.3%)	4.0174-2 (.6%)	.11312
2	5.8811-4 (.7%)	1.5780-3 (.7%)	3.8208-3 (.7%)	2.3463-2 (.7%)	3.0653-7 (1.4%)	7.1361-7 (1.4%)
3	1.5904-2 (.9%)	.032998 (.6%)	7.9818-2 (.6%)	.15338 (.8%)	0	0
4	6.8756-2 (.4%)	.39846 (.4%)	.96381 (.4%)	.14799 (.4%)	0	0
			TRX-2 Cell SAM-CE			
1	2.5792-4 (.5%)	2.2535-3 (.4%)	5.8910-3 (.4%)	1.2370-2 (.5%)	2.8790-2 (.6%)	8.1126-2 (.6%)
2	3.5808-4 (.9%)	9.5908-4 (.9%)	2.3221-3 (.8%)	1.4222-2 (1.0%)	1.7960-7 (.23%)	4.1812-7 (2.3%)
3	1.0504-2 (1.2%)	2.1486-2 (.8%)	5.1973-2 (.8%)	9.9864-2 (1.1%)	0	0
4	7.2275-2 (.4%)	.42167 (.4%)	1.0199 (.4%)	.15537 (.4%)	0	0

TABLE 4

TRX-1 Full Core k_{eff} and Reaction Rate Ratios
For the Inner Core Region

PARAMETER	EXPERIMENT	RCPO1	RECAP	SAM-CE
k_{eff}	1	.9837 ± .0008	.9827 ± .0013	.9839 ± .0026
ρ_{28}	1.320 ± .021	1.396 ± .004	1.415 ± .021	1.390 ± .018
δ_{25}	.0987± .0010	.1009 ± .0005	.1015 ± .0016	.09989± .0013
δ_{28}	.0946± .0041	.0972 ± .0003	.09707± .0016	.09939± .0012
C*	.797 ± .008	.809 ± .001	.8167 ± .0095	.8070 ± .0056

TABLE 5

BAPL-UO2-1 Values for k_{eff} and Reaction Rate Ratios
for ENDF/B-IV and ENDF/B-V Data

Parameters	Cell ENDF/B-IV	Cell ENDF/B-V	Full Core ENDF/B-V	Experiment
k	1.137 ± .0017	1 1433 ± .0019	0.9958 ± .0032	1
ρ_{28}	1.385 ± .011	1.392 ± .011	1.429 ± .062	1.39 ± .01
δ_{25}	0.0801 ± .0006	0.0806 ± .0005	0 0801 ± .0024	0.084 ± .002
δ_{28}	0.0710 ± .0004	0.0727 ± .0006	0.0764 ± .0027	0.078 ± .004
C*	0.8022 ± .0041	0.8058 ± .0038	0 819 ± .020	--

TABLE 6

BAPL-UO2-1 ENDF/B-IV and ENDF/B-V CSEWG Four Group Cell Reaction Rates

	ENDF/B-IV				ENDF/B-V PDP-10			
	^{235}U		^{238}U		^{235}U		^{238}U	
Group	Capture	Fission	Capture	Fission	Capture	Fission	Capture	Fission
1	3.186-4 (.34%)	2.628-3 (.30%)	1.467-2 (.32%)	3.086-2 (.48%)	3.177-4 (.37%)	2.643-3 (.35%)	1.430-2 (.37%)	3.1410-2 (.71%)
2	4.946-4 (.57%)	1.322-3 (.57%)	2.024-2 (.66%)	<1.-6	5.000-4 (.55%)	1.312-3 (.58%)	1.996-2 (.75%)	<1.-6
3	1.394-2 (.74%)	2.825-2 (.61%)	.1672 (.73%)	0	1.421-2 (.83%)	2.831-2 (.71%)	.16841 (.42%)	2.152-6 (12%)
4	6.932-2 (.36%)	.4027 (.36%)	.1463 (.35%)	0	6.895-2 (.25%)	.4003 (.25%)	.1457 (.25%)	0

TABLE 7

EPRI Four Group Cross Sections (barns)
for BAPL-UO2-1 Cell and Full Core
Using the ENDF/B-V Library

		Cell	Full Core (Inner)	Full Core - Cell
U235 Absorption	σ_1	1.2920 ± .0010	--	--
	σ_2	2.0750 ± .0039	--	--
	σ_3	38.478 ± .233	--	--
	σ_4	453.76 ± 1.47	--	--
U235 Fission	σ_1	1.2302 ± .0008	1.227 ± .00154	-.0032 ±.00173
	σ_2	1.6188 ± .0024	1.612 ± .0064	-.0068 ±.0068
	σ_3	25.644 ± .152	24.63 ± .387	-1.014 ±.419
	σ_4	387.09 ± 1.25	386.6 ± 2.98	-.49 ±3.25
U238 Absorption	σ_1	.43333 ± .00163	.4295 ± .00292	-.00383 ±.00334
	σ_2	.2422 ± .00097	.2427 ± .0060	.0005 ±.0061
	σ_3	2.0842 ± .0174	2.075 ± .0504	-.0092 ±.0533
	σ_4	1.8959 ± .0060	1.894 ± .0597	-.0019 ±.0600
U238 Fission	σ_1	.37870 ± .00171	.3746 ± .0035	-.0041 ±.0039
	σ_2	4.56-4 ± .032-4	4.55-4 ± .12-4	-.01-4 ±.124-4
	σ_3	2.6303-5 ± .339-5	2.33-5 ± 1.03-5	-.3-5 ±1.08-5
	σ_4	--	--	--

Figure 1 - k_{eff} vs Rho 28 for TRX-1 Full Core

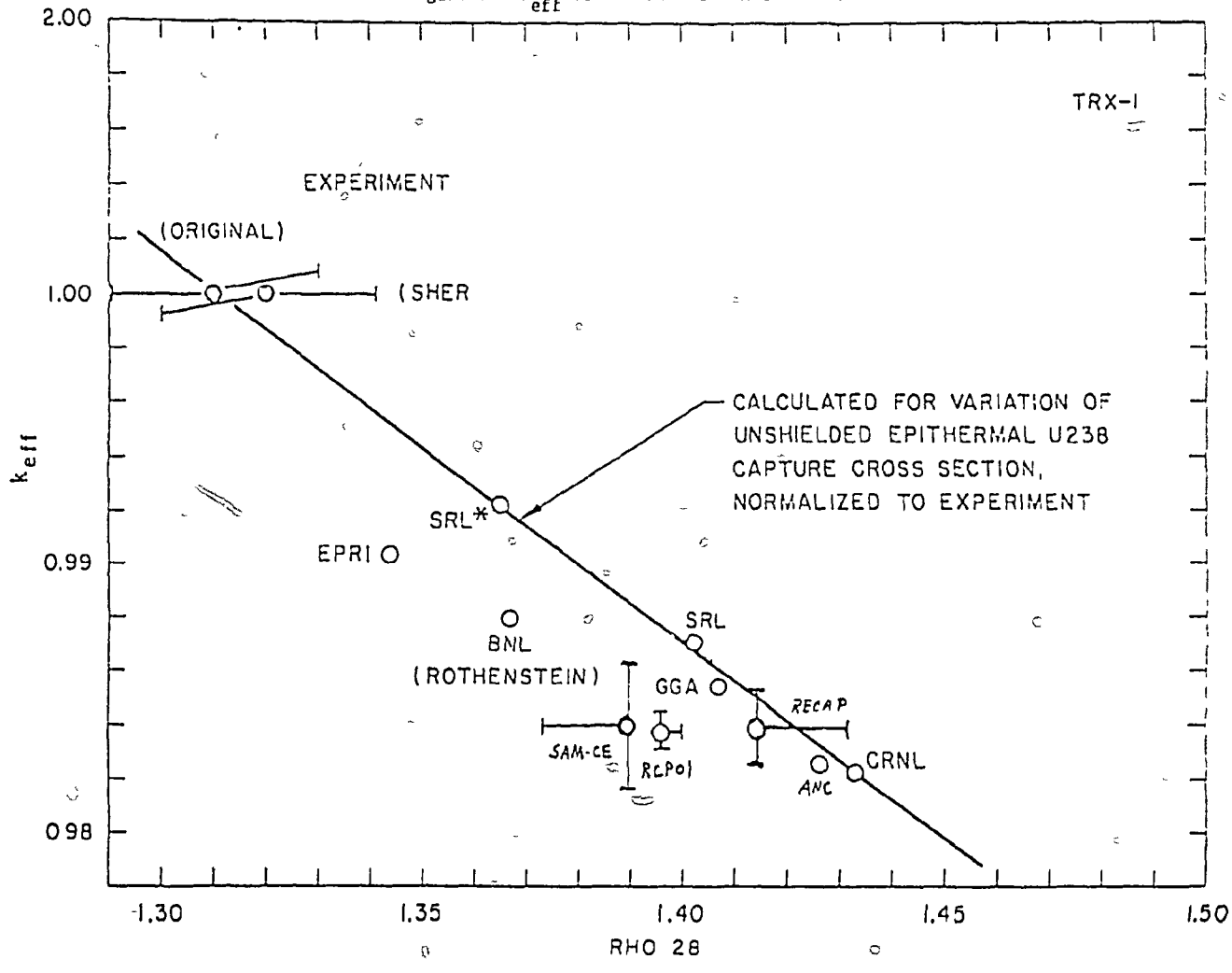

The agreement is a result of interest. We have given a direct comparison of group cross sections obtained from cell and full core calculations and have found the two sets to be fully consistent.

In conclusion, it can be stated that the value of SAM-CE for reactor calculations has been demonstrated and valuable data has been obtained for testing the accuracy of ENDF/B-IV and ENDF/B-V libraries for reactor calculations.

REFERENCES

1. M. Beer and P. F. Rose, "Monte Carlo Infinite Cell Calculations for TRX-1 and TRX-2 Benchmarks", Trans. Am. Nucl. Soc. 32, 775 (1979).

2. E. S. Troubetzkoy et al., "The SAM-CE Monte Carlo System for Radiation Transport and Criticality Calculations in Complex Configurations (Revision 7.60)", EPRI CCM-8 (Jan. 1980).

3. H. Lichtenstein et al., "Development of the Criticality Capability For the SAM-CE Monte Carlo System", EPRI NP-1042 (April 1979).

4. M. Beer and P. F. Rose, "Implementation of the SAM-CE Monte Carlo Benchmark Analysis Capability for Validating Nuclear Data and Reactor Design Codes", EPRI report to be published.

5. National Neutron Cross Section Center, "Cross Section Evaluation Working Group, Benchmark Specifications", BNL 19302 (ENDF-202) (1974).

6. L. Levitt, B. Magurno, P. F. Rose, "Improvement of Reference Nuclear Data for Commercial Power Reactor Analysis and Design", EPRI NP-556 (Oct. 1977).

7. J. Hardy, Jr., "Monte Carlo Analyses of TRX Slightly Enriched Uranium-H_2O Critical Experiments with ENDF/B-IV and Related Data Sets", WAPD-TM-1307 (Dec. 1977).

Blank

THE RECURSIVE MONTE CARLO METHOD FOR DEEP-PENETRATION PROBLEMS

M. Goldstein*
Oak Ridge National Laboratory
Oak Ridge, Tennessee
and
E. Greenspan*
Nuclear Engineering Program, University of Illinois
Urbana, Illinois 61801, U.S.A.

ABSTRACT

The Recursive Monte Carlo (RMC) method developed for estimating importance function distributions in deep-penetration problems is described. Unique features of the method, including the ability to infer the importance function distribution pertaining to many detectors from, essentially, a single M.C. run and the ability to use the history tape created for a representative region to calculate the importance function in identical regions, are illustrated. The RMC method is applied to the solution of two realistic deep-penetration problems - a concrete shield problem and a Tokamak major penetration problem. It is found that the RMC method can provide the importance function distributions, required for importance sampling, with accuracy which is suitable for an efficient solution of the deep-penetration problems considered. The use of the RMC method improved, by one to three orders of magnitude, the solution efficiency of the two deep-penetration problems considered: a concrete shield problem and a Tokamak major penetration problem.

1. INTRODUCTION

The Recursive Monte Carlo (RMC) method is being developed for the estimation of adjoint functions distributions in general three-dimensional geometries; these adjoint distributions are aimed for importance sampling in the course of solution of deep-penetration problems using Monte-Carlo (M.C.) techniques. The idea for a RMC method to calculate adjoint functions was first proposed by Steinberg, Kalos and Troubetzkoy[1] who also looked at its feasibility for the solution of a simple one-dimensional (slab geometry) problem. Their effort was focused on an attempt to develop an automatic algorithm for the generation of equi-

*On leave from Nuclear Research Center-Negev and Dept. of Nuclear Engineering, Ben-Gurion University, Beer-Sheva, Israel.

importance surfaces in general 3-D problems - a task which was found to be inefficient[2]. Our approach is to divide the system, intuitively, into regions of convenient geometry, and estimate the value of the importance function on the surfaces separating these regions. More on the background of the RMC method, its theoretical foundation and strategy for implementation can be found in Ref. 3. That reference considers monoenergetic examples only. The primary purpose of this work is to illustrate the applicability of the RMC method for the solution of realistic multi-group deep-penetration problems.

For the convenience of the reader we start with a brief review of the theoretical foundation of the RMC method (Section 2) and the strategy for its application (Section 3). The RMC method is then applied for the solution of two deep-penetration problems having streaming ducts: the right circular concrete shield problem studied by Tang et al.[4] (Section 4) and a blanket-shield problem with a major penetration as encountered in Tokamak reactor designs[5] and proposed as a benchmark problem[6] (Section 5).

All of the RMC calculations reported on are performed using the recently developed REMOP code.[7] The detectors' responses are calculated with MORSE[8] (using the RMC results for importance sampling). The computer times quoted are of a CYBER-73 computer.

2. THEORETICAL FOUNDATION

Consider radiation transport problems the objective of which is to find the value of a performance parameter (or a detector response, or system characteristics) that can be expressed as

$$R = \int \chi(p) f(p) dp \tag{1}$$

where $\chi(p)$ is the neutron birt -rate density distribution - the density of neutrons coming out from collisions per unit phase space volume, dp, at $p \equiv (\underline{r}, E, \underline{\Omega})$, per unit time; it is the solution of the Boltzmann equation

$$\chi(p) = S(p) + \int \chi(p') K(p' \rightarrow p) dp' \tag{2}$$

in which S(p) is the source density distribution, K(p' p) is the Boltzmann kernel which can be expressed as

$$K(p' \rightarrow p) = T(\underline{r}' \rightarrow \underline{r}\ E' \underline{\Omega}') C(E' \underline{\Omega}' \rightarrow E\underline{\Omega} | \underline{r}) \tag{3}$$

where $T(\underline{r}' \rightarrow \underline{r} | E' \underline{\Omega}')$ is the transport kernel and $C(E' \underline{\Omega}' \rightarrow E\underline{\Omega} | \underline{r})$ is the collision kernel. Finally

$$f(p) = T(\underline{r} \rightarrow \underline{r}_d | E\underline{\Omega})\ \eta(E, \underline{\Omega}) \tag{4}$$

where $\eta(E, \underline{\Omega})$ is the response function (or efficiency) of the detector and $\underline{r}_d$ denotes a position vector in the active volume of the detector.

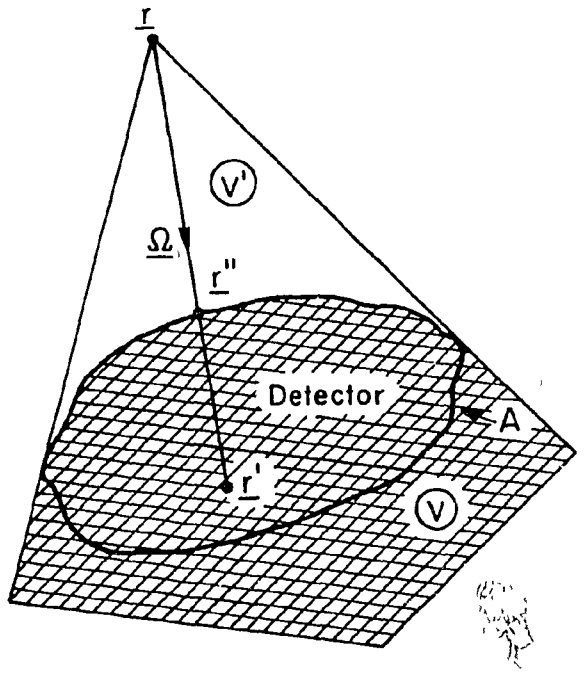

Fig. 1. A schematic illustration of the division of the configuration space to subregions. The importance function on surface A dividing V and V' is known.

The optimum biasing function for the solution of Eq. (2) for the purpose of calculating the performance parameter of Eq. (1) is (see, for example, Ref. 9-11) the importance function - the solution of the adjoint equation

$$\chi^*(p) = f(p) + \int K(p \to p')\chi^*(p')dp' \qquad (5)$$

In terms of this importance function the performance parameter of Eq. (1) can be expressed as

$$R = \int \chi^*(p)S(p)dp \quad . \qquad (6)$$

Suppose the importance function distribution is known on a surface A (in the configuration space) which separates the detector from the volume V (represented by the radius vector $\underline{r}$; see Fig. 1). Dividing the spatial integration in Eq. (5) into the two regions V and V' we find

$$\chi^*(\underline{r},E,\underline{\Omega}) = S^*(\underline{r},E,\underline{\Omega};\underline{r}") + \int_{V'} d\underline{r}' \int dE' \int d\underline{\Omega}' T(\underline{r}\to\underline{r}'|E\underline{\Omega})C(E\underline{\Omega}\to E'\underline{\Omega}'|\underline{r}') \chi^*(\underline{r}',E',\underline{\Omega}') \qquad (7)$$

where the first term on the right side of Eq. (7) is obtained as follows:

$$\int_V d\underline{r}' T(\underline{r}\to\underline{r}'|E\underline{\Omega}) \int dE' \int d\underline{\Omega}' C(E\underline{\Omega}\to E'\underline{\Omega}'|\underline{r}')\chi^*(\underline{r}',E',\underline{\Omega}') + f(\underline{r},E,\underline{\Omega})$$
$$= U(\underline{r}\to\underline{r}"|E\underline{\Omega}) \int_V d\underline{r}' T(\underline{r}"\to\underline{r}'|E\underline{\Omega}) \int dE' \int d\underline{\Omega}' C(E\underline{\Omega}\to E'\underline{\Omega}'|\underline{r}')\chi^*(r',E',\underline{\Omega}') + f(\underline{r},E,\underline{\Omega})$$
$$= U(\underline{r}\to\underline{r}"|E\underline{\Omega})\,[\chi^*(\underline{r}",E,\underline{\Omega}) - f(\underline{r}",E,\underline{\Omega})] + f(\underline{r},E,\underline{\Omega}) = U(\underline{r}\to\underline{r}"|E\underline{\Omega})\chi^*(\underline{r}",E,\underline{\Omega})$$
$$\equiv S^*(\underline{r},E,\underline{\Omega};\underline{r}") \qquad (8)$$

and

$$U(\underline{r}\to\underline{r}"|E\underline{\Omega}) \equiv T(\underline{r}\to\underline{r}"|E\underline{\Omega})/\Sigma_t(\underline{r}",E) \quad . \qquad (9)$$

The adjoint source term $S^*(\underline{r},E,\underline{\Omega};\underline{r}")$ is the importance of neutrons coming out at $(\underline{r},E,\underline{\Omega})$ which reach the reference surface A uncollided.

Consider now the importance function at phase space point $p_0 \in V'$ expressed as a detector response [the equivalent of Eq. (6)],

$$\chi^*(p_o) = \int_{V'} \chi^*(p)\delta(p-p_0)dp \quad . \qquad (10)$$

We can express it using the distribution function formulation [the equivalent of Eq. (1)] getting

$$\chi^*(p_0) \equiv \chi^*(\underline{r}_0, E_0, \underline{\Omega}_0) = \int_{V'} d\underline{r} \int dE \int d\underline{\Omega} J(\underline{r}, E, \underline{\Omega}; p_0) S^*(\underline{r}, E, \underline{\Omega}; \underline{r}'') \qquad (11)$$

where J is the solution of the equation for the distribution function due to the point source at p_0,

$$J(p; p_0) = \delta(p - p_0) + \int_{V'} dp' J(p') K(p' \to p) \quad . \qquad (12)$$

In other words, Eqs. (11), (12), (7) and (10) are the equivalent of, respectively, Eqs. (1), (2), (5) and (6). Eqs. (11) and (12) imply that the value of the importance function at phase space point p_0 can be calculated by solving the forward (or distribution function) equation in subregion V' subjected to a source $\delta(p-p_0)$, and weight the flux of neutrons which reach, uncollided, the reference surface A with the value of the importance function on that surface (assumed known).

The value of the importance function averaged over a phase space region $\Delta p = (\Delta \underline{r}, \Delta E, \Delta \underline{\Omega})$, (with $\Delta \underline{r} \varepsilon V'$),

$$\chi^*_{\Delta p} \equiv \int_{\Delta \underline{r}} d\underline{r} \int_{\Delta E} dE \int_{\Delta \underline{\Omega}} d\underline{\Omega} \chi^*(\underline{r}, E, \underline{\Omega}) \Big/ \int_{\Delta \underline{r}} d\underline{r} \int_{\Delta E} dE \int_{\Delta \underline{\Omega}} d\underline{\Omega} \quad , \qquad (13)$$

can similarly be calculated from the expression

$$\chi^*_{\Delta p} = \int_{V'} d\underline{r} \int dE \int d\underline{\Omega} J_{\Delta p}(\underline{r}, E, \underline{\Omega}) S^*(\underline{r}, E, \underline{\Omega}; r'') \qquad (14)$$

where $J_{\Delta p}$ is the solution of the forward equation

$$J_{\Delta p}(p) = S_{\Delta p}(p) + \int_{V'} dp' J_{\Delta p}(p') K(p' \to p) \qquad (15)$$

subjected to an external source of neutrons uniformly distributed in Δp,

$$S_{\Delta p}(p) \equiv 1/\Delta p \equiv [(\Delta \underline{r})(\Delta E)(\Delta \underline{\Omega})]^{-1} \quad . \qquad (16)$$

3. THE RMC METHOD

The RMC method consists[3] of the following ingredients: (1) The system is divided into relatively small geometrical regions, typically one mean-free-path (mfp) in thickness. (2) The forward transport equation is solved for each region subjected to an isotropic source of neutrons distributed uniformly on the surface of the region farthest from the detector. The histories of the source neutrons are followed throughout the volume of the region and a buffer zone adjacent to it (from the other side of the source surface). (3) The average importance of the source neutrons is calculated by summing the probabilities of the neutrons coming out of collisions in the region (and the buffer zone) to cross, uncollided, the preceeding surface (obtained from forward Monte Carlo calculations) weighted with the value of the importance function at the

crossing point, which is known from the previous step. The result is the average importance function of the source neutrons; it is assigned to the source surface which provides the "reference" surface for the next step. (4) This procedure is repeated recursively, starting with the closest-to-detector region and continuing towards the external source. The surface averaged values of the importance functions are then used for importance sampling in the course of the M.C. calculation (forward) of the detector response.

In the following subsections we shall discuss a number of issues related to the practical application of the RMC method.

3.1 Region Geometry

Consider the system illustrated schematically in Fig. 2a. The problem is to estimate the adjoint function distribution corresponding to the detector throughout the system (up to the external source surface). Towards this end the system is divided (fictitiously) by surfaces, as illustrated in Fig. 2b. Let us suppose that the importance function is known on surface A_3 and examine the procedure to be used for calculating the average importance function on surface A_4.

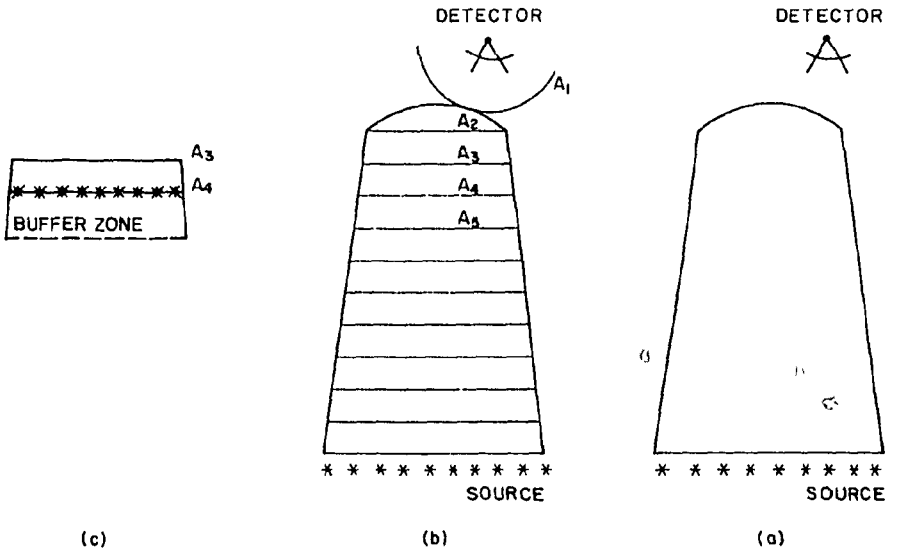

Figure 2. A schematic illustration of the division of the system (a) into regions (b) and of the subsystem considered in each recursion step (c).

Following the forumulation of Sec. 2 we are to assign a uniform isotropic source of neutrons to surface A_4 and solve the forward Boltzmann equation subjected to that fictitious source throughout the volume of the system excluding that part between reference surface A_3 and the detector. Such an undertaking is both impractical and

unnecessary. Remembering that the solution looked for is the value of the importance function on A_4, and realizing that neutrons reaching a few mean-free-path from A_4 (away from the detector) have a very low probability to reach reference surface A_3 (and hence, to contribute to surface A_4 importance function) it is apparent that it is sufficient to consider a truncated V', as illustrated in Fig. 2c. This truncated V' consists of the geometrical region (between A_4 and A_3) and a buffer zone (from the other side of A_4).

The larger the thickness of the geometrical region the longer it will take to get the importance function on A_4 with a given level of accuracy but the smaller number of recursion steps will be necessary for the solution of a given problem. Similarly, the thicker the buffer zone the longer it will take to follow the histories of a given number of source neutrons; beyond a certain thickness the added accuracy resulting from a further increase in the buffer zone thickness becomes negligible.

Investigating the effect of the region and buffer zone thickness on the accuracy and efficiency of the RMC method (considering monoenergetic problems) we found[3] that region and buffer zone thicknesses of the order of one mean-free-path appear to be near the optimum. Recently we got an indication that for certain problems it might be possible (and efficient) to do without a buffer zone. Further investigation is needed before the optimal thickness of the region and buffer zone for different problems could be identified.

3.2 Sample Size and Statistical Accuracy

A question of primary concern to the practicality of the RMC method is that of the propagation of statistical errors in problems having a large number of recursion steps. Figure 3 compares the importance function calculated with the RMC method for a simple one-dimensional deep-penetration problem with the results from deterministic calculations obtained with ANISN. The system consists of a homogeneous sphere having a central spherical detector surrounded by a 22 mfp thick shield (extending from a radius of 28 cm to 200 cm). The problem is monoenergetic with isotropic scattering. An S_8 (symmetric) angular quadrature was used for the ANISN calculations. For the purpose of the RMC calculations the system is divided into 50-1/2 mfp thick regions. The solid angle is divided into the eight quadratures used for the ANISN calculations thus enabling a direct comparison between the RMC and the ANISN results. A buffer zone, 1 mfp in thickness, is attached to each region. The detector response function was taken to be unity. The importance function on the closest-to-detector reference surface was obtained from a simple ANISN run. (It can also be calculated, straightforwardly, by hand; note that only angular components of the importance function pointing towards the detector need to be known.) The sample size of the neutron source assigned to each surface for the RMC calculations was 3000. Figure 3 shows a very good agreement between the RMC and the ANISN results throughout the system, with no indication for propagation of errors. It ought to be mentioned, though, that we did observe propagation of errors

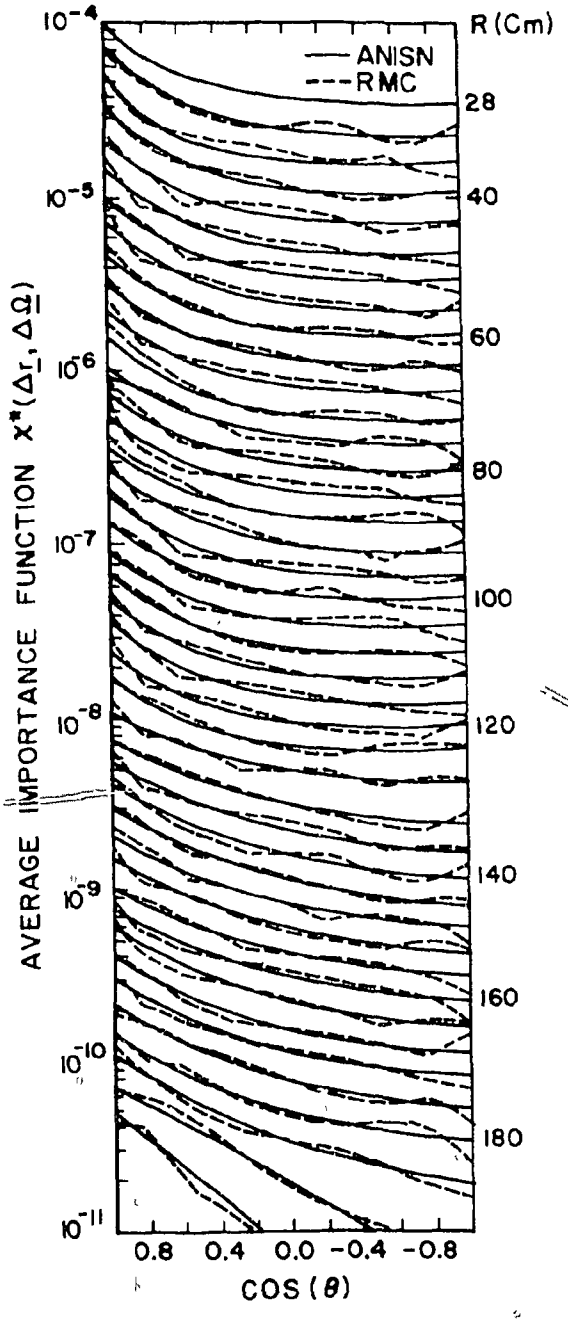

Fig. 3. A comparison of the importance function calculated by the RMC method (broken lines) with ANISN results (solid lines). Sample size for the RMC calculations is 3000 neutrons.

when using, for the same problem, a sample size of 1500 neutrons and volumetric (rather than surface) sources.[3]

The efficiency of the importance sampling technique (judged by the computer time required for the estimation of the detector response at a given degree of accuracy) depends on the accuracy of the importance function used for biasing. The higher the accuracy required, the more time is needed, however, for the adjoint calculation. The efficiency and usefulness of the RMC method should therefore be judged by the overall computation time needed for the two phases of the solution - the RMC calculation of the importance function distribution, and the calculation of the detector response (using importance sampling). We shall refer to the overall procedure as the "RMC procedure." The first phase will be referred to as the "adjoint calculation" whereas the second phase as the "detector calculation."

To examine the sensitivity of the efficiency of the RMC procedure to the accuracy of the importance function distribution we define a figure of merit,

$$\gamma = \sigma^2 T \qquad (17)$$

where σ^2 is the variance of the final result for the detector response, and T is the overall computation time, such that

$$T = T_a + T_d \qquad (18)$$

where T_a and T_d are the time required for the calculation of, respectively, the importance function and the detector response. In conventional applications of

M.C. techniques, in which T stands for the time it takes to perform the M.C. calculations (the equivalent of T_d in the RMC procedure), Y is constant. The figure-of-merit was calculated as a function of two parameters: the batch size of source neutrons used for the RMC calculation (S_a) and for the detector response (S_d).

The parametric study was performed for a shielding problem similar to (although smaller than) that considered by Tang, et al.[4] The shield, illustrated in Fig. 4, is a right circular cylinder of a uniform homogeneous composition having a central duct along its axis. A plane isotropic source is located at the base of the shield, from the other side of the detector. The problem was treated as monoenergetic with isotropic scattering. The cross sections were taken to be $\Sigma_t = 1.0$ cm^{-1} and $\Sigma_s = 0.9$ cm^{-1}.

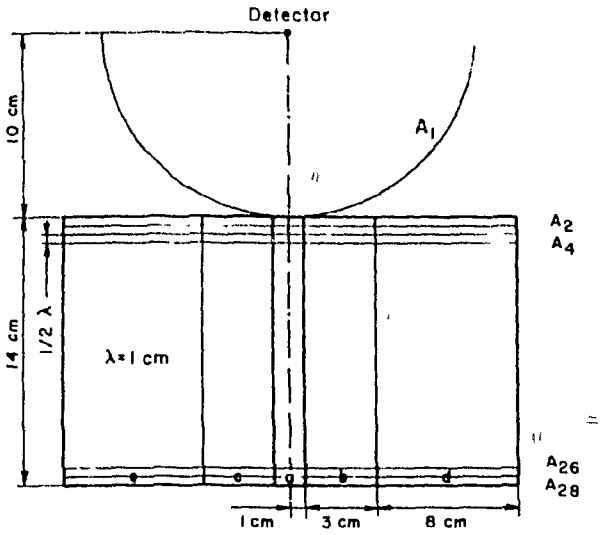

Fig. 4. The geometry of the 2-D shield problem of Ref. 4.

For the purpose of the recursive solution, the shield is divided into 28 half-mfp thick regions, by planes perpendicular to the cylinder axis (see Fig. 4). Each plane is partitioned, somewhat intuitively, into five sections, a thru e, as illustrated in Fig. 4. In setting this partition we have taken into account the anticipation that most of the contribution to the flux in both detectors is likely to come through the axial duct and through regions adjacent to it. The distinction between the right and left sides of the system is to enable accounting for the asymmetry of the problem in the case of the side detector (considered in Ref. 3, but not in the present example). The first step in the solution is to calculate the importance function distribution on spherical surface A_1 centered in the axial detector (see Fig. 4). This is done with a simple ANISN run.

The importance function in the five sections of surface A_2 is then calculated using A_1 as the reference surface. A one mfp thick buffer zone is attached to the region for the adjoint calculations. The computation time for the average importance of the five sections of surface A_2 was 1 min. 8 sec., when using a source of 1500 neutrons per section. Geometrical imaging[3] (see also Sec. 3.3.2) was applied to the next 27 regions which are identical to the first one. The time per recursion step (just for weighting a given histories tape with the appropriate adjoint function) was 4.18 sec. for the 1500 n/section source. The last two regions are different from the reference region by the thickness of their buffer zone. We could still apply, nevertheless, the histories tape of the reference region to the edge region, by ignoring the contribution to the importance function, of neutrons colliding in the missing sections of

the buffer zone. The total computation time needed for the calculation of the importance function was 2 min. 53 sec. for the 1500 n/section source case. Without geometrical imaging the solution would have taken 11 times longer. The importance function distribution thus calculated is used for biasing of the external neutron source, for the Russian roulette, splitting, as well as for the generalized exponential transform.[13] For this purpose, the average importance function calculated for a surface is assigned to the volume extending 1 4 mfp in both sides of the surface.

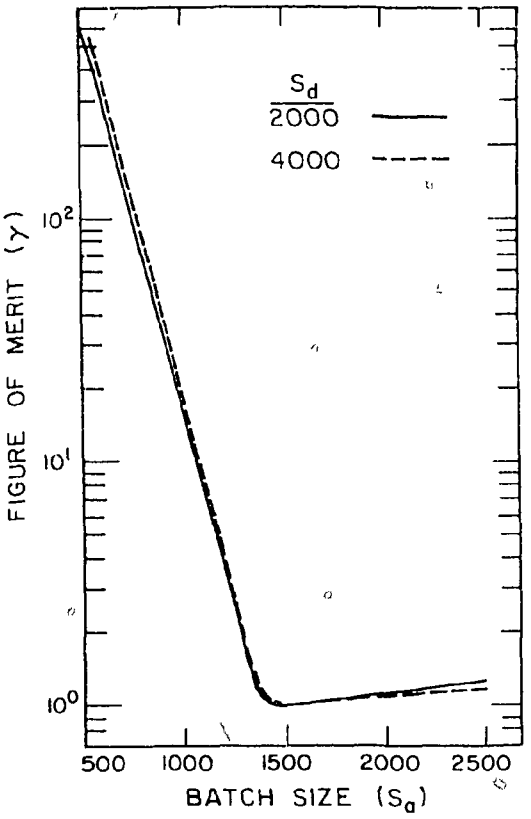

Fig. 5. Effect of batch size in the adjoint calculation on the figure of merit for the RMC procedure.

The results obtained for the central detector are summarized in Fig. 5. The figure of merit is found (Fig. 5) to have a clear minimum; to be strongly correlated with S_a; and almost independent of S_d. The γ - S_a plane of Fig. 5 is divided into two distinct domains: in the high S_a domain $[S_a > (S_a)_{opt}]$ the improvement in the accuracy of the importance function distribution does not improve the efficiency of the importance sampling so that T and therefore γ, increase essentially linearly with S_a. In the $S_a < (S_a)_{opt}$ domain, on the other hand, the accuracy of the importance function distribution degrades significantly with the decrease in S_a, causing a dramatic loss in the accuracy of the calculated detector response. At the optimum, corresponding in the problem considered to $S_a \approx 1500$, the time required for the adjoint calculation is smaller than the time required for the calculation of the detector response.

An important question associated with the practical application of the RMC method is how to determine, a priori, the optimal source batch size for the adjoint calculation. This bath size is expected to be problem dependent. In all the problems we have solved so far with the RMC procedure, we found that a bath size of 1500 neutrons was adequate. Much more numerical experimentations, covering a wide variety of problems, is necessary, nevertheless, before a reliable recipe could be determined.

3.3 Special Features of the RMC Method

3.3.1 Simultaneous Solution of Multi-Detectors Problems

To each detector in a given system there corresponds a different importance function distribution. Consequently, to find the importance function pertaining to N different detectors in a given system, it is necessary to repeat the solution N times. The RMC method, on the other hand, enables getting the solution for all N detectors from, essentially, a single run (provided these detectors can be enclosed by the first reference surface).

In the RMC method the adjoint calculations consist of two phases: (1) the calculation of the probability of the source neutrons to reach the reference surface (as a function of location on that surface and of direction of arrival), and (2) weighting this "arrival probability" with the corresponding value of the importance function. The first phase is detector independent; once we know the arrival probabilities pertaining to a given detector, we know these probabilities for all other detectors in the same system (provided the system is divided the same way for all different detectors). The importance function distribution pertaining to each of the detectors can then be calculated just by weighting these arrival probabilities with the appropriate importance functions. The detector dependency comes only through the assignment of the importance function to the first reference surface.

3.3.2. Geometrical Imaging

When two regions are identical in geometry and composition (i.e., they are the image of each other), the histories of the source neutrons pertaining to each region (i.e., the arrival probability) are the same. Consequently, the histories generated for a representative region are directly applicable for all the images of that region. The application of this procedure will be referred to as geometrical imaging.

Geometrical imaging can significantly reduce the computation time for the solution of deep-penetration problems using the RMC method. The solution of the adjoint equation in certain deep-penetration problems can be transformed, with this feature, to the order of difficulty required for the solution of simple one mean-free-path type transport problems.

3.3.3. Estimation of the Importance Function in Low Importance Regions

In solving the adjoint equation for deep-penetration problems using the adjoint (conventional) M.C. method it is difficult to get a reliable estimate of the importance function in regions in which this function has relatively low values (usually the regions farthest away from the detector). Importance sampling applications require proper knowledge of the importance function throughout the system; too much a distortion in the adjoint distribution may lead to a significant error in the calculated detector response.[11] (See also Sec. 4.) The accuracy of the estimation of the detector response becomes more sensitive to the value of the

importance function in low-importance regions the higher is the relative flux of neutrons in these regions. (More details on this issue along with an illustrative example can be found in Ref. 12).

As the RMC method involves the solution of the forward equation corresponding to a source of neutrons assigned to each region (of phase space), this method "picks up" the value of the importance function in low importance region as reliably as it does in high importance regions. This feature is particularly important for problems characterized by relatively high fluxes in regions of relatively low importance.[12]

4. A CONCRETE SHIELD PROBLEM

So far we have considered mono-energetic problems only. As the first illustration for the application of the RMC method to realistic multigroup problems, we apply it to the solution of the concrete shield problem of Tang et al.[4] (Fig. 6). The problem is to find the total neutron fluence at the two point detectors. The 14 energy group structure along with the group constants library of Ref. 4 are used for the present study. The scattering anisotropy is described using the P_3 approximation.

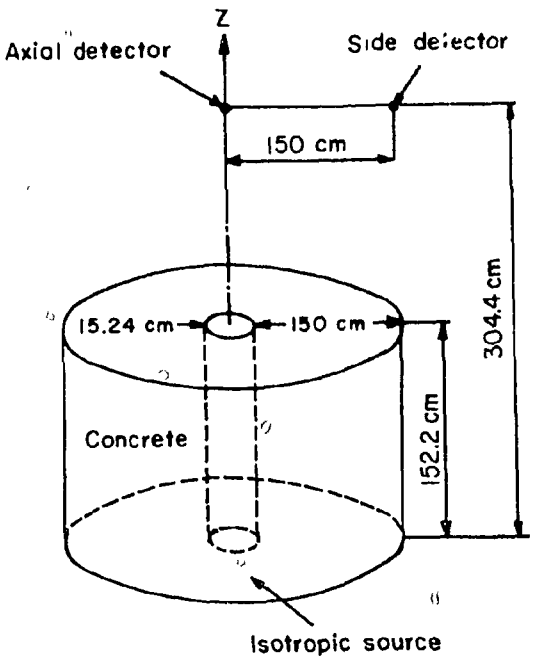

Fig. 6. The geometry of the concrete shield problem.

The first phase of the solution is the estimation of the importance function distribution throughout the shield. Towards this end we divide the shield into 100 equally thick regions by planes perpendicular to the cylinder axis (as in Fig. 4). This gives a region thickness of 1.52 cm, which is smaller than the mfp pertaining to any of the energy groups (ranging from 2.36 cm to 8.37 cm). A buffer zone, 8.37 cm thick (i.e., equal to the largest mfp in this problem), is attached to each region for the purpose of the adjoint calculations (see Fig. 7). Each surface is partitioned into five sections (following the rationale described in Sec. 3.2) as follows (see also Fig. 7):

section a:	$0 < R < 7.62$ cm
sections b and c:	$7.62 < R \leq 16$ cm
sections d and e:	$16 < R \leq 150$ cm

The solution starts with the calculation, using ANISN, of the importance function distribution on the spherical surface A_1 centered at the

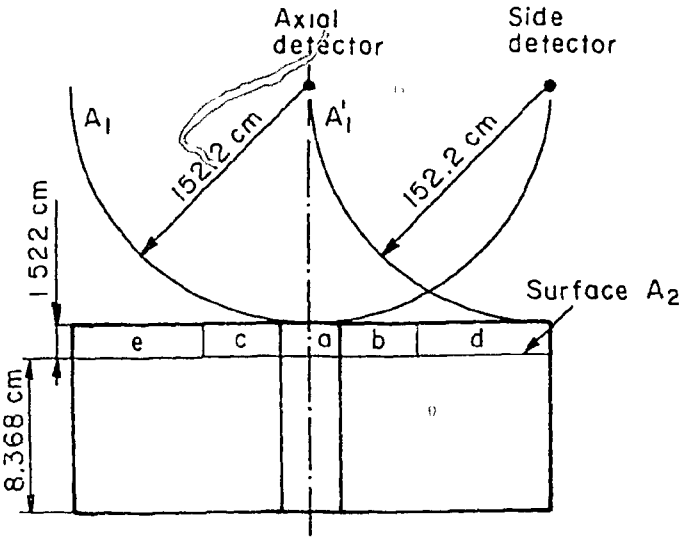

Fig. 7. The geometry of the effective geometrical region used for the first RMC calculation step of the concrete shield problem.

axial detector (see Fig. 7) using an adjoint source term of unity at the detector point, for each of the 14 energy groups. Then we calculate the importance function in the five sections of surface A_2 with A_1 serving as the reference surface (Fig. 7). In order to save time following neutrons in relatively low importance regions of relatively thick buffer zones (which can be, in this problem, as large as 4 mfp) the buffer zone is divided into four subregions onto which splitting and Russian roulette is applied. An isotropic source is uniformly distributed on the surface of each section in each of the energy groups. The sample size of the source neutrons was 21000 per section, corresponding to 1500 neutrons for each energy group. The time for calculating the average importance function on the first five sections (surface A_2) was 6 min 28 sec. Without Russian roulette and splitting, this computation time was longer by a factor of 2.6.

Capitalizing on the similarity of all the regions the system is divided to, we used the geometrical imaging procedure (see Sec. 3.3.2) for calculating the importance function in the rest of the regions. The last six regions (95-100) have a thinner than nominal buffer zone. We applied geometrical imaging to these regions as well, accounting for the difference in the buffer zone thickness by ignoring the histories in the "excessive zones" (see Sec. 3.1). The computation time for a single recursion step was approximately 12 sec, making the total time needed for estimating the importance function distribution pertaining to the central detector 26 min 18 sec.

The calculation of the importance function distribution pertaining to the side detector followed the same procedure, with only two small modifications: the first reference surface was A_1' rather than A_1 (Fig. 7) and there was no need to calculate a new neutron histories tape for the first region - the tape created for that region during the calculation of the central detector importance function was used. Also notice that the importance function distribution on the reference surface A_1' is identical to that on A_1 (remember that we are interested in the forward directions only). Using geometrical imaging, the total computation time needed for the estimation of the importance function distribution pertaining to the side detector was 20 min 3 sec.

The importance function distributions obtained for each of the detectors were then used during the calculation of the corresponding detector's reading for biasing of the external source, Russian roulette, splitting and for the generalized exponential transform.[13] For this purpose, the value of the average importance function at a given surface is assigned to a region centered around this surface. To examine the sensitivity of the RMC procedure to the accuracy of the importance function distribution used for importance sampling, we also calculated the side detector response using the importance function distribution pertaining to the axial detector. Fifty batches of 400 source neutrons were used for the M.C. calculations of the response of each detector. No attempt was made to optimize the batch size used for the RMC procedure.

Table 1 compares the results obtained with the RMC procedure with "exact" results obtained[3] from deterministic calculations (using the two-dimensional S_n code DOT) and with the M.C. results of Ref. 4 obtained using the importance function distribution for the central detector calculated[4] with DOT. The results from the RMC procedure are seen to agree well with those from DOT, when the appropriate importance function distribution is used for importance sampling. Moreover, the RMC calculated standard deviations for the central and the side detectors are, respectively, 1.8 and 9.3 times smaller than those obtained in Ref. 4 using the DOT importance function, while the overall effective computation time appears to be smaller.†

Table 1. Comparison of the Results from the RMC Calculations With Those Obtained With Other M.C. and Discrete-Ordinates Methods

Computation Method	Response of Axial Detector	Response of Side Detector	Computation Time (min)		
			Importance Function	Detector Response	Total
S_n* (DOT)	2.453×10^{-9}	1.408×10^{-11}	-	50**	50**
M.C. + Adjoint S_n (DOT)*	3.093×10^{-9} (±4.8%)	1.062×10^{-11} (±43%)	52**	60**	112**
M.C. + RMC (for the axial detector)	2.540×10^{-9} (±2.6%)	-	26.3	19.3	45.6
M.C. + RMC (for the side detector)	-	1.560×10^{-11} (± 4.6%)	20.1	23.6	43.6
M.C. + RMC (for the axial detector)	-	0.910×10^{-11} (±50%)	26.3	31.8	58.1

*Data from Ref. 4
**CPU-time of IBM - 360/91[14]

†To the best of our knowledge, the CPU speed of the IBM 360/91 used in Ref. 4 is about a factor of 4.5 faster than that of the CYBER-73.

With the axial detector importance function used for importance sampling, the RMC standard deviation of the side detector response was a factor of 10.8 greater than when the side detector importance function is employed for importance sampling. A similar standard deviation for the side detector was obtained in Ref. 4. It is thus seen that, in the problem under consideration, the use of an importance function distribution from 2-D calculations for importance sampling in a 3-D problem (which differ from the 2-D problem in the location of the detector only) leads to a reduction in the overall efficiency of the M.C. calculation of the side-detector response, by about two orders of magnitude. This example indicates to the sensitivity of the M.C. method efficiency to distortions in the importance function used for importance sampling.

5. A TOKAMAK MAJOR PENETRATION PROBLEM

As a second test of the efficiency of the RMC method for the solution of realistic deep-penetration problems we applied it to a three-dimensional Tokamak blanket-shield major penetration problem recently studied by Jung and Abdou[5] and proposed for a benchmark.[6] A cut through the system considered is shown in Fig. 8 and the thickness and composition of the different zones are summarized in Table 2.

Table 2. Dimensions and Compositions of the Tokamak Blanket/Shield Major Penetration Problem

Zone	Outer Radius cm	Thickness cm	Material Composition
1	210	210	Plasma
2	240	30	Vacuum
3	241	1	Stainless Steel
4	256	15	Stainless Steel
5	261	5	Boron Carbide
6	276	15	Stainless Steel
7	281	5	Boron Carbide
8	291	10	Stainless Steel
9	301	10	Boron Carbide
10	311	10	Stainless Steel
11	321	10	Boron Carbide
12	331	10	Stainless Steel
13	340	9	Boron Carbide
14	351	11	Stainless Steel
15	361	10	Boron Carbide
16	371	10	Stainless Steel
17	430	59	Vacuum
18	490	60	50% SS + 50% Cu

Following Ref. 5, the toroidal geometry is approximated by a cylindirical one, with the X-axis designating the centerline. The first wall, blanket, shield and Toroidal Field Coils (TFC) are of cylindrical cross section in the Y-Z plane (see Fig. 8), and the vacuum duct cross section is in the X-Y plane. This duct, 20 cm in diameter, is lined with a 1 cm thick stainless steel tube. A 5 cm thick stainless steel disc provides an end-cap to the duct (Zone 25, Fig. 8). The TFC are divided into concentric rings, 5 cm thick each (Zones 18, 19, 20 etc.), bounded (following Ref.5) by the $y = +100$ cm planes (with the centerline of the duct being at $y=0$). The problem is to calculate the total flux in the end-cap (Zone 25) and in the two inner zones (Zones 18 and 19) of the TFC due to a uniform isotropic shell source of 14 MeV neutrons coming from the surface of the plasma region.

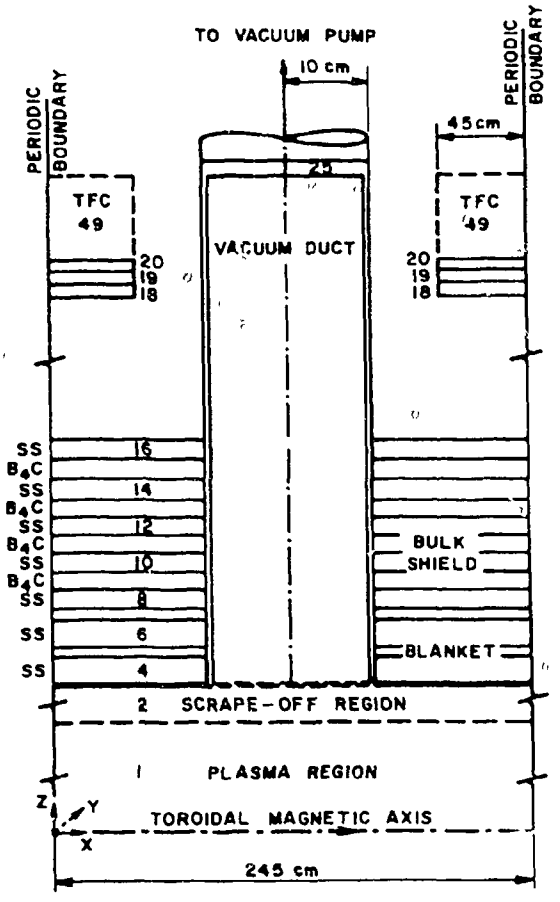

Fig. 8. The geometry of the Tokamak blanket/shield deep-penetration problem.

Twenty-two energy groups (the group structure for which is summarized in Table 3), P_3 scattering anisotropy and S_8 angular quadrature are used for the solution of the Tokamak problem. The 22 group constants were generated by collapsing, with ANISN, the 100 group DLC-2 library using ANISN calculated flux (for a representative 1-D mockup of the problem) for the weighting spectrum. The boundaries of the angular quadratures used are cos = 0.0, $\pm$.41555, $\pm$.69105, $\pm$.8934 and $\pm$1.0.

For the purpose of the adjoint calculations (in the RMC procedure) we neglected the curvature around the X-axis. This approximation enables using geometrical imaging (and thus improve the efficiency of the RMC procedure) and is not expected to significantly distort the importance function distribution* (due to the relatively large radius of curvature of the problem). The division of the system into "small" regions poses a more difficult problem than in the previous example (Sec. 4) not only because of the heterogeneous structure of the blanket/shield but also due to the large spread in the value of the mfp pertaining to the different compositions and energy groups used (see Table 3); the smallest mfp (0.004 cm) is less than one thousandths of the largest mfp (5.8 cm). Anticipating that most of the contribution to the detectors reading will come from the MeV and upper KeV energy ranget (the first 13 energy groups), we divided the blanket/shield (by planes parallel to the first wall) into 2.5 cm thick regions (or 1/2 to 1 mfp in thickness for the first 13 energy groups). No buffer zones were used in this problem.#

Each surface (used for the RMC calculations) is divided into three sections (similar to the division in Sec. 4, except that now we do not have a distinction between left and right):

*There is no difficulty in applying the RMC method to curved geometry.
†An indication which we also got from the 1-D ANISN run.
#The buffer zones appeared to have only very small effect on the results of this problem. The buffer zone issue deserves additional examination.

section a: $0 < R \leq 11$ cm
section b: $11 < R \leq 31$ cm
section c: $31 < R \leq$ system boundaries in the X-Y plane.

Table 3. Energy Boundaries and Mean-Free-Paths of the 22 Group Structure Used for the Tokamak Problem

Group Number	Upper Boundary (eV)	Mean-Free-Path (cm) B_4C	SS	TFC
1	1.4918 + 7	5.38	4.59	4.28
2	1.3499 + 7	5.36	4.19	3.76
3	1.0000 + 7	5.54	3.63	3.45
4	8.1873 + 6	5.23	3.33	3.20
5	6.0653 + 6	5.80	3.21	3.14
6	4.9659 + 6	4.46	3.20	3.19
7	4.0657 + 6	4.05	3.36	3.39
8	3.0119 + 6	3.36	3.42	3.55
9	2.4660 + 6	3.92	3.63	3.72
10	2.2313 + 6	3.62	3.72	3.79
11	1.8268 + 6	3.35	3.94	3.82
12	1.1080 + 6	2.22	3.98	3.48
13	5.5023 + 5	1.60	2.91	2.54
14	1.1109 + 5	1.35	1.26	1.23
15	3.3546 + 3	0.49	0.97	1.26
16	5.8295 + 2	0.23	0.76	0.85
17	1.0130 + 2	0.11	1.07	1.23
18	2.9023 + 1	0.063	1.11	1.23
19	1.0677 + 1	0.037	1.10	1.21
20	3.0590	0.021	1.09	1.19
21	1.1254	0.013	1.07	1.16
22	4.1399 - 1	0.004	0.97	1.03

The adjoint calculations proceed as follows: First, the collision tapes pertaining to the three regions which can represent the system - a stainless steel region (Zones 4, 6 etc., including the portion of the vacuum duct in these zones, see Fig. 8), a B_4C region (Zones 9, 11, etc.) and vacuum space (Zone 17), are generated (using the RMC approach). Fifteen hundred source neutrons per surface section, energy group and angular bin are used for these calculations. Then the importance function pertaining to the end-cap detector is found on the first reference surface, taken to be the plane passing through the basis of this cap (parallel to the first wall). Geometrical imaging is then used to find, recursively, the average importance function (per group and angular bin) on each of the reference surfaces down to the fusion neutron source plane. The total computation (CPU) time until this phase was 80 min. Starting with the first reference surface for the TFC detector (regions 18 and 19, see Fig. 8), located at the outer surface of Zones 18 and 19, the importance function pertaining to this detector was then calculated with the RMC method, using the collision tapes already available. The CPU time required for this phase of the work was 48 min.

The importance functions thus obtained are used, in the detectors calculation (using MORSE), for biasing of the external neutron source, Russian roulette, splitting and for the generalized exponential transform. The detectors response (i.e., total neutron flux in the detector region) were calculated using a track length estimator. Six thousand source neutrons were used for the calculation of each detector's response, requiring 53 min and 75 min of CPU time for, respectively, the end-cap and TFC detectors.

Table 4 summarizes the results for the detectors response, as obtained using the RMC procedure described above, and compares them with the corresponding results obtained by Jung and Abdou[5] (J & A), using 50,000 source neutrons for each detector (or region). It is seen that even

Table 4. The Total Neutron Fluxes at the End-Cap and TFC Dectectors as Calculated With the RMC Method, in Comparison With the M.C. Results of Ref. 5

Region	Total Neutron Flux* ($n/cm^2 sec$)	
	RMC Procedure	Ref. 5
25	10.87×10^{11} ($\pm$7%)	5.35×10^{11} ($\pm$100%)
18	5.60×10^{9} ($\pm$13%)	1.10×10^{10} ($\pm$56%)
19	3.52×10^{9} ($\pm$15%)	8.04×10^{9} ($\pm$70%)

*normalized to a neutron wall loading of 1 MW/m^2

though J & A followed about one order of magnitude more source neutrons per detector than used for the RMC calculations, the results from the latter method exhibit substantially lower standard deviation. Even when the time required for the adjoint calculations (which is of the same order as the time for the direct calculations) is taken into account, the efficiency of the RMC procedure is found to be significantly higher than that of a "brute-force" M.C. calculation; for the J & A method of calculation to provide a standard deviation of 7% for region 25, for example, it had to process about 1600 times more source neutrons than in the RMC procedure (the detector calculation phase).

The differences in the average value of the detectors response obtained between the RMC and J & A methods, even though within the statistical uncertainty, may be due, in part, to some differences in the representation of the problem. The isotropic shell source used for the RMC calculations, for example, ought to be replaced by a more realistic angular distribution. In addition, the presence of the TFC (and neutron interactions with them) should also be taken into account for the RMC calculations. These and other (such as accounting for the curvature in the poloidal direction) refinements are not expected, however, to affect substantially the applicability and accuracy of the RMC method.

6. CONCLUDING REMARKS

The experience gained so far with the RMC method confirms the need for importance sampling for efficient solution, using M.C. techniques, of deep penetration problems (see, for example, Ref. 10). It also confirms the need for accurate enough knowledge of the importance function distributions used for importance sampling; using an importance function from two-dimensional calculations for importance sampling in a three-dimensional problem (different from the 2-D one only in the location of the detector) led to a reduction in the efficiency of the M.C. solution of the concrete shield problem (considered in Sec. 4) by about two orders of magnitude.

The RMC method appears practical and efficient for the estimation of the importance function distributions in realistic deep-penetration problems with an accuracy suitable for importance sampling applications (and it ought to be realized that the solutions, with the RMC procedure,

of the deep-penetration problems described in Secs. 4 and 5 were not optimized). It thus might enable applying the M.C. technique to the solution of realistic complicated deep-penetration problems otherwise found very difficult to solve (see, for example, Refs. 5 and 6).

Many more numerical experimentations are, nevertheless, required before the practicality and efficiency of the RMC procedure could reliably be assessed, and in order to devise recipes for the optimal application of this procedure to a wide range of problems.

The recursive approach developed for the RMC calculations could, in principle, also be applied with deterministic methods for the solution of the transport equation. The deterministic methods are expected to have not ony a limited range of applicability (usually to 2-D regions) but may also be less efficient than the RMC method; they require a solution of GxSxA equations per region (i.e., recursive step) where G is the number of energy groups, S is the number of sections a reference surface is divided into and A is the number of angular bins used.

The RMC procedure has been incorporated within the MORSE Monte Carlo system. The resulting code, named REMOP, is to become available through the Radiation Shielding Information Center of the Oak Ridge National Laboratory.

REFERENCES

1. H. A. Steinberg, M. H., Kalos and E. S. Troubetzkoy, "Machine Generation of Monte Carlo Sampling Functions," p. 771 in Proc. Conf. New Developments in Reactor Mathematics and Applications, CONF-710302 (1971).

2. M. H. Kalos, H. Steinberg and E. Troubetzkoy, Automatic Computation of Importance Sampling Functions for Monte Carlo Transport Codes - Phase III, Final Report, Defence Nuclear Agency Report DNA-2890F (1972).

3. M. Goldstein and E. Greenspan, "A Recursive Monte Carlo Method for Estimating Importance Function Distributions in Deep-Penetration Problems," Nucl. Sci. Eng., to be published.

4. J. S. Tang, P. N. Stevens and T. J. Hoffman, Methods of Monte Carlo Biasing Using a Two-Dimensional Discrete Ordinates Adjoint Flux, Oak Ridge National Laboaratory Report ORNL/TM-5414 (June, 1976). See also NS&E 62, 617 (1977) and NS&E 64, 837 (1977).

5. Jungchung Jung and M. A. Abdou, Radiation Shielding of Major Penetrations in Tokamak Reactors, Argonne National Laboratory Report ANL/FPP/TM-107 (March, 1978).

6. E. M. Gelbard and H. Henryson II, "New Areas for Benchmark Computation," Nucl. Sci. Eng. 64, 124 (1977).

7. M. Goldstein and E. Greenspan, REMOP - A Recursive Monte Carlo Code for the Estimation of Importance Function Distributions in Three-Dimensional Systems (to be published).

8. W. A. Straker, P. N. Stevens, D. C. Irving and V. C. Cain, The MORSE Code - A Multigroup Neutron and Gamma Ray Monte Carlo Transport Code, Oak Ridge National Laboratory Report ORNL-4586 (1970).

9. H. Kahn, Application of Monte Carlo, USAEC Report AECU-3259 (1954).

10. G. Goertzel and M. H. Kalos, "Monte Carlo Methods in Transport Problems," p. 315 in Progress in Nuclear Energy, Series I, 1958.

11. M. H. Kalos, F. R. Nakache and J. Celnick, "Monte Carlo Methods in Reactor Computations," p. 365 in Computing Methods in Reactor Physics, H. Greenspan, C. H. Kebler and D. Okrent, Eds., Gordon and Breach Science Publishers, 1968.

12. M. Goldstein, A Recursive Monte Carlo Method for Generating Importance Functions in Deep-Penetration Problems, Ph.D. Thesis, Dept. of Nuclear Engineering, Ben-Gurion University of the Negev, Beer-Sheva, Israel.

13. M. Goldstein and D. Shvarts, "Monte Carlo Shielding Calculations Using a Generalized Exponential Transform Biasing," Trans. Israeli Nucl. Soc. 5, 207 (1977).

14. J. S. Tang, Personal Communication.

Blank

THE MONTE CARLO LATTICE PROGRAM KIM

E. Cupini, A. De Matteis, and R. Simonini
Comitato Nazionale Energia Nucleare
Bologna, Italy

ABSTRACT

The Monte Carlo program KIM solves the steady-state linear neutron transport equation for a fixed-source problem or, by successive fixed-source runs, for the eigenvalue problem, in a two-dimensional thermal reactor lattice. Fluxes and reaction rates are the main quantities computed by the program, from which power distribution and few-group averaged cross sections are derived. The simulation ranges from 10 MeV to zero and includes anisotropic and inelastic scattering in the fast energy region, the epithermal Doppler broadening of the resonances of some nuclides, and the thermalization phenomenon by taking into account the thermal velocity distribution of some molecules. Besides the well known "combinatorial" geometry, the program allows complex configurations to be represented by a discrete set of points, an approach greatly improving calculation speed.

1. INTRODUCTION

KIM (k-infinite-Monte Carlo) is a program which solves the steady-state linear neutron transport equation for a fixed source problem or, by successive fixed-source runs, for the eigenvalue problem, in a two-dimensional infinite thermal reactor lattice using the Monte Carlo method[1]. A characteristic feature of the program is its approach to the lattice geometry. In fact, besides the usual continuous treatment of the geometry, using the well-known "combinatorial" description of domains, the program allows complex configurations to be represented by a discrete set of points whereby the calculation speed is greatly improved.

This code includes in its body much of the programming work developed at the CNEN's Computing Centre in the field of Monte Carlo reactor calculations. This work has also allowed preparation and checking of large parts of the nuclear data library accompanying the program. The program has been widely used for BWR's and PWR's and also for heavy-water moderated, light-water cooled reactors.

The coding language is essentially Fortran-IV for IBM computers of the series 360, 370, exploiting the half-word addressability. Computer memory requirement is problem-dependent, through dynamic core allocation

at running time for the most critically-sized arrays (as, for example, thermalization kernels and the map of the discretized domain). However, most cases run in about 1000 kbytes. The time needed on the IBM 370/168 to obtain the infinite multiplication factor with precision of about 0.3%, for a typical 8x8 rod element of a BWR, is about 40', corresponding to 40,000 histories. This time refers to geometry treated in the discrete mode; the continuous mode requires almost double the time.

2. SIMULATION OF THE PHYSICAL EVENTS

2.1 The Physical Model

The problem of time evolution of the neutron distribution towards an equilibrium, defined as an invariance of the distribution shape, can be reduced to a sequence of stationary problems. The process simulated to reach the equilibrium is iterative and can be summarized as follows: starting from a first-generation neutron source, that is, from a given neutron distribution, one computes the distribution of neutrons born by fission, this being then considered as the second-generation source: fission is the only reaction which separates generations of neutrons and, together with radiative capture, determines the exhaustion of a generation. Iterations stop when the shape of the fission source distributions of successive generations are statistically invariant within a required accuracy. This invariance will point out that equilibrium has been reached. The multiplication factor is then computed as the ratio of the number of neutrons born in two successive generations. One iteration has normally been found sufficient when starting from a uniform source in the fuel.

The tracing of the neutron history takes into account both the slowing down and the thermalization phenomenon. Partly due to its development in time, and partly for reasons of memory saving, the program is organized in three sections for fast, epithermal and thermal simulation. Each section implements a particular model: indeed, both numerical techniques and cross-section representation vary with the energy section. The total energy interval, from 10 MeV to zero, is divided into the three ranges of Tab.1. In the same table the approximations used for cross

Table 1. Cross section representation

Range	Bounds	Approximation
1. Fast	10 MeV-46 KeV	16 groups
2. Epithermal	46 KeV-5 eV	64 groups and continuous treatment for some resonance nuclei
3. Thermal	5 eV-0 eV	256 points and scattering kernels (55x55 energy points x 9 cosine points) with interpolation

section representation are given. The upper bound of the epithermal range has been chosen so as to confine within the first energy range the simulation of anelastic and anisotropic elastic scattering from stationary nuclei. In the thermal range a cross section interpolation, linear above 1 eV and bilogarithmic below, is performed.

In the fast energy range 10 MeV-46 keV, cross sections are averaged in 16 groups, although energy varies continuously during the simulation. Nuclear reactions considered in this range are: i) radiative capture; ii) elastic scattering. For each group of incoming energy the anisotropy is described by a table of 17 values of the cosine μ_B of the scattering angle in the center of mass system (CMS) corresponding to 16 equiprobable intervals. A value of μ_B is obtained from this table through a random access and a linear interpolation; iii) inelastic scattering, treated according to three different models: excitation of known discrete energy levels, evaporation model, transition matrices. Isotropy in CMS is assumed; iv) fission. The energy of a fission neutron is assumed to be independent of the incoming energy and of the nucleus hit and is selected according to the Watt spectrum. The yield for each fissile nucleus is described by a linear law with parameters assumed constant within three energy ranges.

In the epithermal range 46 keV-5 eV it is possible at running time to take into account the Doppler broadening of the resonances of some nuclides with spacing between resonances much greater than the resonance widths (in the present library Pu-240, U-238, Th-232, In-115, Ag-109, Ag-107). Cross sections of all other nuclides are described by 64 energy groups. The reactions considered are elastic scattering isotropic in CMS, fission with a constant yield, and capture. For the resonance nucleus in thermal motion we assume a maxwellian distribution of its velocity as a function of the temperature. Only s-wave resonances are taken into account, assuming that resonances can be described by the single-level Breit-Wigner formula. Cross sections are computed at the current energy by adding the contributions of the nearest left and right resonances. Parameters of up to 100 resolved resonances are stored for each reconance nucleus in the library. For higher energies, the neutron width is randomly generated during the simulation, and it is assumed that the unresolved resonances are equispaced and have a constant capture width.

The thermal energy range, 5 ev-0, is divided into 256 energy points to represent scattering, fission and capture cross sections. At the current neutron energy,cross sections are computed through linear interpolation above 1 eV and bilogarithmic interpolation below. Between 5 and 1 eV all nuclei are considered as free. Below 1 eV we consider the thermal motion of some molecules which are particularly important for the thermalization process such as light or heavy water and oxygen. The scattering kernel of a thermalizing nuclide is described pointwise. In the present library, thermalization kernels at several temperatures are given for water, heavy water and oxigen. The energy kernel is described through a 55x55 matrix between 1 eV and zero; for each energy transition the angular distribution is described by 8 values.

2.2 Numerical Techniques

The generator of the pseudo-random numbers y_i is Lehmer's multiplicative congruential scheme:

$$y_i \equiv y_{i-1} \cdot 41475527 (\mathrm{mod} 2^{28}),$$

whose multiplier has been divised and tested by Ahrens et al.[2]. Although the period of the generated sequence, 2^{26}, is rather small, its good statistical properties have been confirmed both theoretically and experimentally[2].

Simulation of the history of a particle begins at an energy randomly chosen from the fission spectrum with an initial unitary statistical weight. The index of the starting region r is assigned by a semi-stratified sampling as follows: if F(r) is the mean number of particles to be started from region r, then the program deterministically assigns the region index r to $[F(r)]$ starting particles, while the remaining particles are randomly distributed among the regions with pdf proportional to $\{F(r)\}$, where $[\cdot]$ and $\{\cdot\}$ denote the integral and the fractional part, respectively.

Position of the starting point within a chosen region is selected uniformly according to standard techniques, except in a special case: if the geometric domain is discretized and the source is not on rods, a rejection technique using Halton's "quasi-random" numbers[3] is used. For Halton's generator, unlike Lehmer's, the following important property holds: as the number of tosses increases, the probability that no point falls in a given small (but machine-representable) area vanishes. This property also ensures that the rejection process surely ends, however small the source region whose index is imposed by the stratified sampling.

When a particle exhausts its path the types of both the collided nuclide and the reaction undergone are to be determined. To better describe how this is performed by the program it is convenient to separate the fast and the epithermal interval from the thermal one:

a) Fast and epithermal interval. If σ_s and σ are the macroscopic scattering and total cross section of the material at the collision point, the fraction σ_s/σ of the particle undergoes scattering with the i-th nuclide which is chosen on the basis of the probability $\sigma_s^{(i)}/\sigma_s$, with $\Sigma_i \sigma_s^{(i)} = \sigma_s$. In the fast range the type of scattering (elastic or inelastic) for the selected nuclide is subsequently decided. If the weight falls below a certain cut-off threshold in the fast interval, the history terminates. In the epithermal interval, instead, a Russian roulette game decides on history termination.

b) Thermal interval. The weight of the particle is never changed in this section: a game based on absorption probability of the mixture decides at each collision whether a particle is absorbed. The nuclide hit is chosen as above. We have chosen this analog history termination because of the usually large number of collision in this energy interval; however, fluxes and reaction rates are estimated through expected-value techniques.

To improve statistics in regions either important or seldom visited by particles, it is possible to split up histories according to a number of branches given for each region. Besides, to allow a different number of histories to be run in each of the three energy ranges of the program, thinning of the source particles in each of the three parts is foreseen. This is performed by a Russian-roulette game just at birth in each range on the basis of decimation ratios given in input.

Flux computation in KIM implements a known expected-value technique: the flux estimator τ in a given region is the product of the mean free path by the expected number of collisions in that region. Scoring of τ is performed at birth, at emersion from reactions and on entering a new region. Some quantities which are linear transformations of the flux are directly computable through the flux estimator τ . For example, reaction rate of the i-type reaction is estimated by scoring the product $\sigma_i \tau$. In this way also reaction rates of nuclides present in very small concentrations are evaluated. In a similar way, cross sections averaged over regions and energy intervals are obtained. Where anisotropic elastic and/or inelastic scattering are present, removal cross sections between the three energy parts of the program (and between other input-given intervals) are computed by scoring the statistical weight of the particle removed (by scattering) from that interval. Where scattering is instead only elastic isotropic in CMS, the removal probability from an energy interval is computed analytically.

At the end of the life cycle simulation, the fission map is given, i.e. the ratio between fissions in a region and average fissions over fissile regions. Besides the fission map the power map is also given, taking account of the different energy released by fission from the different fissile nuclides.

3. TREATMENT OF THE GEOMETRY

3.1 Continuous and Discrete Approach

In the usual (or "continuous" as it will often be called here) approach to geometry in Monte Carlo, a particle walk is simulated by computing the intersection of the flight line with the nearest boundary. In terms of computer time the cost of the algorithms solving this problem increases with the geometric complexity. In KIM, besides the continuous approach, a new one has been introduced. Planar regions can in fact be represented by a finite (and, therefore, approximating) set of area-points obtained by overlaying a square lattice upon the given configuration; a "discretization algorithm" decides which region index is to be assigned to each grid point. The transport is simulated by moving the particle from one grid point to another, keeping as close as possible to the actual trajectory. The algorithm performing this function and detecting the region boundary crossing is the "scanning algorithm". By this "discrete"

approach, the tracing of particle flights becomes independent of the geometric complexity of the configuration since it essentially reduces to simple checking operations to verify whether a point belongs to a subset. Although only a few bits are necessary to code information about the nature of the region (i.e. the region index), a large number of core memories is needed to represent the configuration with sufficient approximation, dependent on the lattice pitch compared to the mean free path. In our IBM version of the program this information is stored in a half word.

The question of the approximation error has not been considered theoretically. However, it is partially answered by the internal agreement of computations carried out with and without discretization by our program.

"Combinatorial" geometry description is used for the continuous approach . The subroutines used in the program are adapted from those developed for the shielding Monte Carlo code SAM-CE[4]. Modifications include reduction from three to two dimensions with the implementation of some fundamental elementary figures, implementation of boundary conditions, speeding up of the initial learning process concerning neighbouring regions, dynamic allocation, squeezing of data.

The program can handle an infinite array of planar elements with a largely arbitrary internal configuration. These elements can be either rectangles with periodicity or reflection boundary conditions, or hexagons with the periodicity condition alone.

3.2 The Scanning Algorithm

The particle transport in the discrete domain is simulated by the scanning algorithm which determines the grid points visited in succession. Let the mesh-size h be the unit of the length, x_0, y_0 the integer coordinates of the starting point, ℓ the free-flight, x_f, y_f the integer coordinates of the end point, θ the direction of motion between these two points. In the case $0 \leq \theta \leq \pi/4$, the scanning procedure along the path from (x_0,y_0) to (x_f,y_f) may be essentially described as follows. Denoting by $[q]$ the integral part of q, the point visited at the n-th step is

$$x_n = x_{n-1} + 1 = x_0 + n$$

$$y_n = y_0 + [n\mathrm{tg}\theta + 0.5] .$$

The scanning goes on until (x_f,y_f) is reached, unless a grid point with a region index different from that of (x_0,y_0) is encountered. In this last case the control passes to the physical treatment subroutines to determine the length of the free path in the new region, unless the element boundary is met. The y_n coordinate is the grid coordinate nearest to $y=y_0+(x_n-x_0)\mathrm{tg}\theta$; the grid points scanned are thus the nearest to the segment linking (x_0,y_0) to (x_f,y_f).

Two types of direct transition from one grid point to another are thus possible: along one of the coordinate directions and along the diagonal of a grid cell. Therefore (for $0 \leq \theta \leq \pi/4$), for $x = x_n$ only one point is scanned: thus, paths with the same projection on the x-axis need scanning of the same number of points. This invariance shows that the scanning time is proportional to the square root of the number of lattice points.

3.3 Distance Travelled and Boundary Crossing

Along with the discrete (integer) coordinates, another pair of real coordinates in the continuum is associated to the moving particle, from birth on. The birth-place itself, (x'_b, y'_b), is first selected in the continuum and then the nearest grid point (x_b, y_b) is determined. If a particle flight, starting from (x'_0, y'_0), ends in (x'_f, y'_f) without region boundary crossings, the distance travelled is the actual distance in the continuum and not the rounded one between the two nearest corresponding grid points (x_0, y_0) and (x_f, y_f). In this way also those displacements so small as to leave the integer coordinates unchanged are recorded; in other words, particle migration in homogeneous media is not biased from the discrete approximation.

The discretization biases instead the detection of region boundary crossing: indeed, this event is detected by the scanning algorithm, which does not generally know the actual continuous region boundaries. The crossing point is then conventionally assumed in the program at the middle of the last two scanned points. When applied to fuel rods in energy ranges with very small mean free path, this approximate approach to crossing has sometimes shown itself to be inadequate: for instance, systematic errors of the order of some tenths per cent have been observed for fuel rods in the epithermal resonance energy range. To overcome these errors, circular (or annular) regions can also be treated in a special way. The program memorises the true physical boundaries of these regions, which are still discretized but only for crossing detection. When an entry in one of these regions is detected by the scanning algorithm, the true entry point is computed and the path is simulated in the continuum until the particle leaves this region.

This last approach is actually a "mixed" continuous-discrete mode of simulation and, together with the introduction of the continuous coordinates accompanying the discrete ones, is the main improvement to an earlier algorithm[5].

3.4 Geometry-Routine Performance

To evaluate the efficiency of the discrete approach, the case of an 8x8 rod BWR element has been analyzed. To this end, a 40,000-history computation for this element has been carried out in both discrete and combinatorial geometry. The domain has been discretized with 100,000

points, the mesh size being approximately 0.05 cm , while in the combinatorial description each rod has been embedded in a square of a chessboard covering the element, in order to speed up boundary crossing identification.

The time needed for the geometry simulation alone has been separately evaluated as follows. We assumed that in the discrete tracing the bulk of the geometric computation is the map scanning; since the scanning time is, as already said, proportional to the square root of the number of points, the proportionality constant has been obtained by carrying out the discrete computation twice, with different mesh sizes. A third computation, with a different mesh size, confirmed the validity of the hypothesis on the tracing time.

For the map with 100,000 points the geometric tracing has been found to require 5' out of the total running time, 42'. The time for the non-geometric simulation thus being known, the time needed by the combinatorial-geometry tracing has then been estimated as 47' out of 84'. The conclusions for this reference computation are the following:
i) the discrete geometry tracing is about one order of magnitude faster than the combinatorial one;
ii) the whole running time with a discrete approach is half the other.

Similar conclusions hold also for cluster configurations of CANDU-like heavy water reactors. The use of the "mixed" approach does not essentially alter the above conclusions.

REFERENCES

1. E. Cupini, A. De Matteis, and R. Simonini, KIM- A Two-Dimensional Monte Carlo Program for Thermal Reactors, Italian Report CNEN RT/FIMA(80)2.

2. J. H. Ahrens, U. Dieter, and A. Grube, "Pseudo-Random Numbers. A New Proposal for the Choice of Multiplicators," Computing 6, 121 (1970).

3. J. H. Halton, "On the Efficiency of Certain Quasi-Random Sequences of Points in Evaluating Multi-Dimensional Integrals," Numer. Math. 2, 84 (1960).

4. M. O. Cohen et al., SAM-CE: Monte Carlo Time-Dependent Complex Geometry, Report CCC-187 Oak Ridge Nat.Lab.-Contributed by MAGI, Mathem. Appl. Group. Inc., New York (1973).

5. E. Cupini and A. De Matteis, "A Discrete Approach to Complex Planar Geometries," p.70 in Proceedings of the NEACRP Meeting of a Monte Carlo Study Group, ANL-75-2/NEA-CRP-L-118, Argonne, Illinois, U.S.A. (July, 1974).

AN ANALYSIS OF EXCORE DETECTOR RESPONSE TO CORE WATER LEVEL USING MONTE CARLO TECHNIQUES

R. D. Lucier, R. J. Cacciapouti
Yankee Atomic Electric Company

D. R. Harris, D. Napolitano
Rensselaer Polytechnic Institute

ABSTRACT

In response to U. S. Nuclear Regulatory Commission requirements, each commercial reactor must have a method of indicating core water level. This paper presents a calculation of excore neutron detector response using Monte Carlo techniques to determine core water level. An increase in excore detector response of a factor of about 3 has been calculated for a half voided core. Using this approach the operating staff at a Nuclear Power Station can determine core water level in the event of an incident causing voids in the primary loop.

INTRODUCTION

In the interim since TMI, the U.S. NRC has made several rules to mitigate possible problems observed at TMI. One of the "Lessons Learned"[1] requirements is that every pressurized water reactor must have a method of determining reactor vessel water level. Boiling water reactors already have this capability incorporated in their design.

This paper presents the methodology to determine reactor vessel water level in the Yankee Nuclear Power Station. The Yankee Nuclear Power Station is a 600 MWth Westinghouse pressurized water reactor. Yankee Rowe is located in the Northwest corner of Massachusetts. The plant was completed in July 1960 and achieved initial criticality in August 1960.

MEASUREMENT METHODS

There are at least three methods that can be used to measure water level. They are:

1) Differential pressure cells (DP)

2) Incore thermocouples

3) Radiation measurement (neutron or gamma)

The differential pressure cell system requires penetrations into the top and bottom of the vessel as well as into the outlet pipes. The DP cell system measures a differential pressure between two or three points within the vessel. This information is correlated to known temperature and pressures in the system to determine the void content of the water near the detector. This is further correlated to a water level in the vessel. The expected accuracy is $\pm$ 20%.[2]

The DP cell system has been ruled out for Yankee Rowe. The main reason is that penetrations must be available in the bottom of the vessel. Unlike current Westinghouse designs, there are no available penetrations in the bottom of the vessel and there is no access to this area.

The second method, incore thermocouples, would measure local temperatures axially and radially throughout the core. These measurments would be coupled with pressure information to provide an indication of voiding.

A thermocouple system, in the event of an accident similar to TMI, would undergo tremendous thermal shock and possible mechanical damage. Therefore, the reliability of this system is suspect. Also, for an application to Yankee Rowe, installation may require a redesign of the fuel elements. Furthermore, more penetrations may have to be made in the vessel head.

The third method, radiation measurements, can be accomplished without any penetrations in the reactor vessel. As observed at TMI[3], the excore neutron detectors measured a count rate of 3-10 times more than the expected count rate. These readings have been correlated to the times of most probable core uncovery.

Predicting the detector response to core water level can be done experimentally and through computation. Experimentally dropping the reactor vessel water level could be hazardous. Computationally determining the response can be very expensive and yield poor accuracy. However, for an application at Yankee Rowe, this appears to be the better method. There are currently three excore source range neutron detectors in place. Therefore, additional equipment is

not required. Consequently, greater emphasis can be placed on the computational methodology.

All of these methods assume that there is a defined water level to measure. This, most probably, is not the case. If the reactor coolant pumps are not operating, there may be a transition region from water to steam. If the pumps are operating, there may be a circulating void with no defined water level. According to NUREG-0578, each pressurized water reactor should have a saturation meter on its control board by 1/1/80. This meter indicates pressure or temperature above or below the saturation point. This meter is used as the primary indicator of voids in the system. If voids are present, the operating staff will consult the information provided to him from this project to obtain an approximate water level.

CALCULATIONAL METHODOLOGY

As this situation closely resembles a shielding problem, the two obvious calculational methods were discrete ordinates and Monte Carlo. Due to the physical size of the problem and the desire to have three-dimensional effects included, Monte Carlo was chosen. A two- or three-dimensional discrete ordinates calculation of this magnitude was beyond the computer limits (CDC-CYBER175) and beyond resonable costs.

To perform this calculation, ANDYMG3[4] was chosen for two reasons. First, ANDYMG3 was available in house. Secondly, it has the ability to treat neutrons and photons.

ANDYMG3 is a three-dimensional multi group neutron-photon transport Monte Carlo code. It has a generalized geometry routine which handles any topologically sound combination of planes, cylinders, ellipsoids, cones, and spheres. Cross sections are read in Sn format with scattering pattern components up to P-3. A flux at a point estimator routine was added to obtain the detector response. Importance splitting and Russian roullette were also added to improve efficiency by splitting particles travelling towards the detector and killing particles travelling towards the core.

THE MONTE CARLO MODEL OF YANKEE ROWE

The first step in modelling a system is to define all surfaces necessary to bound all regions. The second step is to define surface segments which are cut from the surfaces. The surface segments are used in defining regions. A region is a spatial domain in which macroscopic cross sections are uniform.

The Yankee Rowe geometry contains 32 surfaces: 18 concentric cylinders and 14 planes. From these surfaces, 64 surface segments are cut in order to describe 27 regions. The concentric cylinders are also used as splitting planes.

A uniform source with a fission spectrum was used within the core.

For cross sections, the CASK[5] data set was used. CASK is a 40 group (22 neutron, 18 gamma) coupled P-3 cross section library. CASK was chosen for two reasons. First, gamma-n reactions with deuterium may be a significant source of neutrons after shutdown.[6] Secondly, if gamma detectors are desired, the data necessary to calculate a response will have been calculated.

ASSUMPTIONS

In the calculation, four assumptions were made:

1) The reactor core was at beginning of life

2) The reactor was just scrammed

3) There was an instantaneous change in water level

4) A fission source spectrum existed in core.

RESULTS AND APPLICATION

The detector response in the calculation is an average of four symnetrically positioned detectors. For ray tracing purposes, a collision within 115 cm of the detector causes a response. This choice of 115 cm is arbitrary.

The calculations to date are preliminary but are useful for discussion purposes. From Table 1, even though the deviation is high, an increase of factor of almost 3 in the response can be seen when the core is half voided.

TABLE 1

Case	Response	Deviation	No. of Neutron Starters
Full System	.69370E-9	.27349E-9	5,000
Top Half Voided	1.8008E-9	.44792E-9	5,000

This type of information will be used in the event of an indication of voids in the primary system. For example, a typical source range detector count rate reads 70 cps at 6 hours after shut down. If at this time, voids are indicated in the system and the count rate increases to 190 cps, the operating staff will consult information provided by this project. The ratio of count rates in this example is 2.7, i.e., 190/70. This indicates a core that is almost half voided. With further calculations, a more complete and accurate set of data will be provided.

CONCLUSIONS

Even though the results provided are not yet complete, the use of Monte Carlo techniques appear to be a reasonable approach to solve the water level indication problem in the core.

As this work is still preliminary, further effort must be concentrated on:

1) A better model of the source both spatially and spectrally.

2) A correlation of void fraction and water level height.

3) Larger samples to improve statistics.

REFERENCES

1. NUREG-0578, TMI-2 Lessons Learned Task Force Status Report And Short Term Recommendations, Section 2.1.3.b, USNRC (1979)

2. Westinghouse Owner's Group Meeting, 18 January 1980, Pittsburgh, PA.

3. NSAC-1, Analysis of Three Mile Island - Unit 2 Accident, Appendix CI (1979)

4. LA-4539, ANDYMG3, The Basic Program of a Series of Monte Carlo Programs for Time - Dependent Transport of Particles and Photons, D. R. Harris, (11/70

5. DLC-23, CASK 40 Group Coupled Neutron And Gamma-Ray Cross-Section DATA, ORNL, (1978)

6. D. R. Harris, Natural Reactor Sources in A. Radosky, Ed., Naval Reactors Physics Handbook, Volume 1, USAEL, (1964)

Blank

ADJOINT MONTE CARLO TECHNIQUES AND CODES FOR ORGAN DOSE CALCULATIONS

László Koblinger
Health Physics Department
Central Research Institute for Physics
P.O. Box 49, Budapest, H-1525, Hungary

ABSTRACT

Adjoint Monte Carlo simulations can be effectively used for the estimation of doses in small targets when the sources are extended in large volumes or surfaces. The main features of two computer codes for calculating doses at free points or in organs of an antropomorphic phantom are described here. In the first program /REBEL-3/ natural gamma emitting sources are contained in the walls of a dwelling room, in the second one /POKER-CAMP/ the user can specify arbitrary gamma sources with different spacial distributions in the environment: in /or on the surface of/ the ground and in the air.

INTRODUCTION

The determination of the doses absorbed in various parts of the human body is one of the main tasks of health physics. Whether measurements or calculations are carried out for such purposes, first a model of the human body, i.e. an antropomorphic phantom, has to be selected. For photon dose calculations W. Snyder and his co-workers defined a heterogeneous phantom in the 60's[1,2] that was later slightly modified[3] and we will refer to this 1974 version hereafter as the ORNL phantom.

The ORNL phantom has a relatively simple geometrical shape. The external surfaces and the boundaries of the more than 20 organs are defined by secondary order equations. Each organ is considered to be homogeneous although different elemental compositions and densities are used for the skeleton, the lungs and the remainder of the phantom.

There are many gamma and X-ray dose studies carried out using this phantom for the determination of organ doses from internal or external gamma or X-ray sources /e.g. Refs 2, 3, 4, 5, 6, 7/ and all the calculations known by us are based

on direct Monte Carlo simulations.

For several years we have been facing the problem of the determination of organ doses and shielding factors /i.e. ratios of organ doses to doses measured by point-like detectors/ in [illegible] fields of different environmental sources. In these conf[illegible]tions the targets are small /or even zero-volume poin[illegible]n comparison with the spacially extended sources, therefore the adjoint Monte Carlo method was chosen which is more efficient in such cases.

THE PHYSICAL MODELS

Two types of geometries are discussed here. In the first case the point detector or the ORNL phantom is placed into a dwelling room /Fig. 1/. The room is a rectangular block with doorless and windowless homogeneous walls. The gamma emitters - the ^{40}K, and the elements of the U/Ra/-series and the Th-series - are assumed to be distributed in the walls uniformly.

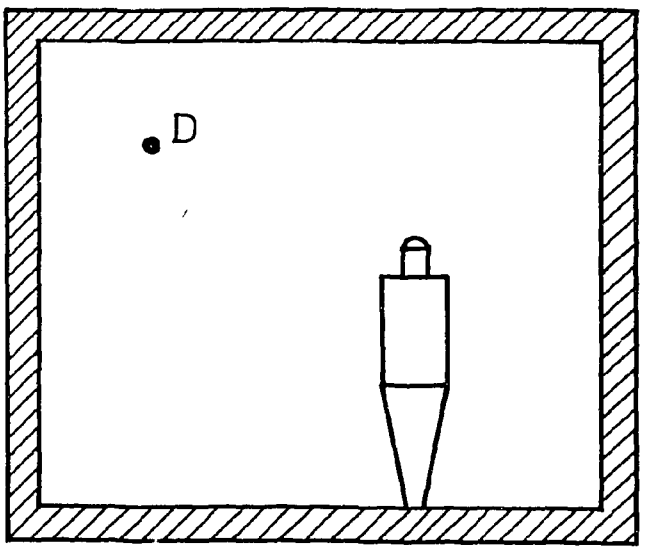

Fig. 1. The phantom in the room.

In the REBEL-3 /Radiation Emitted by Building ELements - 3rd version/ code written for the calculation of doses in dwellings the geometrical data of the room and the material of the walls are the main input data. Any number of neighbouring rooms can also be specified.

From these input data specific dose rates are calculated - (μGy/h)/(Bq/kg) - so the doses can be predicted if the specific activities of the building materials are known. The ratios of the organ doses to the point detector dose can well be used in the interpretation of data measured in existing rooms.

In the second problem the environment is modelled by three regions. The air and the ground regions are semi-infinite and a layer with arbitrary thickness can be placed onto the ground. This layer can be used for modelling grass, snow etc., or simply to take into account a change in the composition of the soil. The phantom stands on the soil region/s/ or a point detector is placed to any height in the air or even into the earth.

The radioactive sources are assumed to be distributed uniformly or exponentially in any of the three regions or plane sources can be placed on the bulk or layer surface or into the air /Fig. 2/. The natural radioactive sources have generally uniform spacial distribution, isotopes of the fall-out are deposited as plane sources on the ground surface and e.g. isotopes of the fall-out washed in by rains can have specific activities decreasing approximately exponentially by depth.

In the POKER-CAMP /Point or Organ Kermas from Environmental Radiations - Code by Adjoint Monte Carlo Processes/ code the following quantities are the most important input data:

- layer thickness,
- elemental compositions and densities,
- source geometry /any combinations of the above mentioned possibilities/,
- source energies and line intensities /for the most important isotopes and decay series there is a built in catalogue/,
- specific activities.

The output of POKER-CAMP is the dose rate, first given separately for each source, then the total sum is also printed.

Results obtained by this code can well be used e.g. for determination of doses in the vicinity of nuclear power stations.

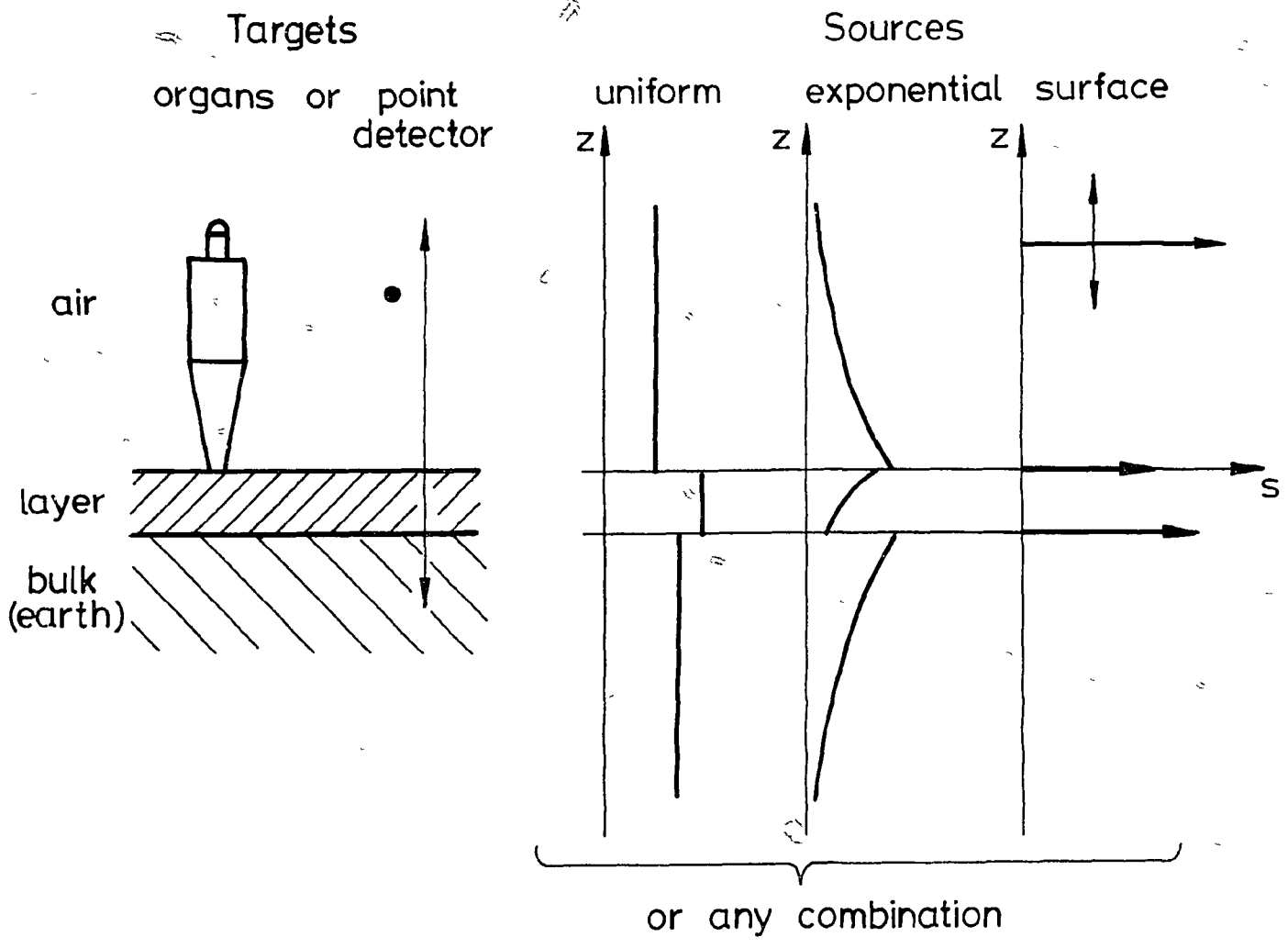

Fig. 2. The source distribution possibilities in the POKER-CAMP code.

In both programs the doses absorbed in the whole body, in the testicles, ovaries, red /active/ or yellow marrow or in the lungs of the CRNL phantom; or in the air at the detector site can be calculated.

The fluxes and energy spectra are also determined, if needed. These quantities have special importance when the calculated values are compared with measured data.

THE ADJOINT MONTE CARLO METHOD

Several types of derivation of the adjoint transport equations are known from the literature therefore only a brief summary is given here. The formalism applied is very similar to that used by D.C. Irving[9], so those who are interested in details should see his original review. To simplify the notation the symbol $\bar{E}$ is used instead of $(E, \bar{\omega})$: the energy and the unit vector of the direction of motion.

Let us denote the density of photons entering a collision at $\bar{r}$ with incoming velocity $\bar{E}$ by $\psi(\bar{r}, \bar{E})$, and the source density by $S(\bar{r}, \bar{E})$ then the integral equation for the collision density is

$$\psi(\bar{r},\bar{E}) = S_c(\bar{r},\bar{E}) + \int\int d\bar{E}'\, d\bar{r}'\, T(\bar{r}',\bar{r}\,|\,\bar{E})\, C(\bar{E}',\bar{E}\,|\,\bar{r}')\, \psi(\bar{r}',\bar{E}')$$

where

$$S_c(\bar{r},\bar{E}) = \int d\bar{r}'\, T(\bar{r}',\bar{r}\,|\,\bar{E})\, S(\bar{r}',\bar{E}),$$

is the first collision source.

In the transport kernel:

$$T(\bar{r}',\bar{r}\,|\,\bar{E}) = \mu(\bar{r},E)\, \exp\left(-\int_{\bar{r}'\to\bar{r}} \mu(\bar{r}'',E)\, ds\right) \frac{\delta\left(\bar{\omega}\,\frac{\bar{r}-\bar{r}'}{|\bar{r}-\bar{r}'|} - 1\right)}{|\bar{r}-\bar{r}'|^2}$$

$\mu(\bar{r}, E)$ is the total linear attenuation coefficient of the material at $\bar{r}$ for photon energies E.

The collision kernel is

$$C(\bar{E}',\bar{E}\,|\,\bar{r}) = \frac{\mu_s(\bar{r},\bar{E}'\to\bar{E})}{\mu(\bar{r},E')}$$

where $\mu_s(\bar{r}, \bar{E}' \to \bar{E})$ is the differential linear scattering coefficient. In our calculations only one type of scattering effects: the Compton scattering, as described by the Klein-

Nishina formula, is taken into account[10] where the angle of scattering is determined by the energy change, i.e.

$$C(\bar{E}',\bar{E}|\bar{r}) = C_E(E',E|\bar{r})\,\delta\left[\bar{\omega}'\bar{\omega} - g(E',E)\right]$$

and

$$g(E',E) = 1 + \frac{\varepsilon}{E'} - \frac{\varepsilon}{E},$$

where $\varepsilon = m_e c^2 \cong 0.511$ MeV.

Physical quantities of interest (λ) can be calculated as functionals of the collision density:

$$\lambda = \iint d\bar{r}\, d\bar{E}\, P_\psi(\bar{r},\bar{E})\,\psi(\bar{r},\bar{E}),$$

where P_ψ is the pay-off function.

In our case, when we calculate the flux at a point: $\lambda = \varphi(\bar{r}_0)$, then by taking into account the

$$\psi(\bar{r},\bar{E}) = \mu(\bar{r},E)\,\varphi(\bar{r},\bar{E})$$

relation,

$$P_\psi(\bar{r},E) = \frac{1}{\mu(\bar{r},E)}\,\delta(\bar{r}-\bar{r}_0).$$

For the derivation of the adjoint equations let us define a new function $\psi^*(\bar{r}, \bar{E})$ to be the value for a particle just entering a collision at $\bar{r}$ with energy $\bar{E}$. The value is a sum of two terms: the immediate pay-off and the pay-off expected to result from all future collisions:

$$\psi^*(\bar{r},\bar{E}) = P_\psi(\bar{r},\bar{E}) + \iint d\bar{E}'\, d\bar{r}'\, C(\bar{E},\bar{E}'|\bar{r})\, T(\bar{r},\bar{r}'|\bar{E}')\,\psi^*(\bar{r}',\bar{E}'). \qquad (1)$$

Now the physical quantity can be determined as:

$$\lambda = \iint d\bar{r}\, d\bar{E}\, \psi^*(\bar{r},\bar{E})\, S_c(\bar{r},\bar{E}).$$

A more comfortable integral-equation can be obtained by the following transformations:

$$\hat{\psi}(\bar{r},\bar{E}) = \mu(\bar{r},E)\,\psi^*(\bar{r},-\bar{E}),$$

$$\hat{P}_\psi(\bar{r},E) = \mu(\bar{r},E)\,P_\psi(\bar{r},-\bar{E})$$

and:

$$\hat{C}(\bar{E},\bar{E}'|\bar{r}) = C(\bar{E},\bar{E}'|\bar{r})\,\frac{\mu(\bar{r},E)}{\mu(\bar{r},E')}\,.$$

By these new quantities:

$$\hat{\psi}(\bar{r},\bar{E}) = \hat{P}_{\psi}(\bar{r},\bar{E}) + \iint d\bar{E}'d\bar{r}'\,\hat{C}(\bar{E},\bar{E}'|\bar{r})\,T(\bar{r}',\bar{r}|\bar{E}')\,\hat{\psi}(\bar{r}',\bar{E}') \qquad (2)$$

and

$$\lambda = \iint d\bar{r}\,d\bar{E}\,\hat{\psi}(\bar{r},\bar{E})\,\frac{S_c(\bar{r},\bar{E})}{\mu(\bar{r},E)}\,. \qquad (3)$$

For the calculation of the flux at a point:

$$\hat{P}_{\psi} = \delta(\bar{r}-\bar{r}_o). \qquad (4)$$

Equations like (1) or (2) are generally /but not strictly correctly/ called as adjoint equations and their solutions by Monte Carlo method are called adjoint Monte Carlo procedures.

In our Monte Carlo simulations pseudo-photons start from the point $\bar{r}' = \bar{r}_o$, with random direction and with an energy $E' \in [E_t;\ E_M]$, where E_t is the low energy threshold of the calculation and E_M is the maximum energy of interest /the maximum source energy/. Thus the pseudo-photons start with a weight of $4\pi(E_M - E_t)$. In the consequent steps the new collision sites /$\bar{r}$/ are chosen from the

$$\frac{T(\bar{r}'\bar{r}|E')}{\int d\bar{r}\,T(\bar{r}',\bar{r}|\bar{E}')}$$

probability density function and new energies /E/ from

$$\frac{\hat{C}_E(E,E'|\bar{r})}{\int dE\,\hat{C}_E(E,E'|\bar{r})}\,. \qquad (5)$$

The new direction is always selected with the condition $\bar{\omega}\bar{\omega}' = g(E,\ E')$. The statistical weight is multiplied by

$$\int d\bar{r}\,T(\bar{r}',\bar{r}|\bar{E}')$$

and then by

$$\int dE\,\hat{C}_E(E,E'|\bar{r}), \qquad (6)$$

after the above mentioned steps, respectively.

Biasing of the adjoint collision kernel

The simulation procedure mentioned above is theoretically correct but the denominator of formula (5) becomes infinite if the energy of the pseudo-photon before the collision /E'/ exceeds $1/2\varepsilon$ /~0.255 MeV/. For such cases we developed a biasing technique[11], where the collision kernel

$$\tilde{C}_E(E,E'|\bar{r}) = \frac{E'}{E}\hat{C}_E(E,E'|\bar{r})$$

replaces the original one. Now, the

$$\int dE\, \tilde{C}_E(E,E'|\bar{r})$$

normalizing factor is finite for all E'-s.

For the selection of the new energy from $\tilde{C}_E$ a quite simple and fast algorithm is developed[11] and if the statistical weight is multiplied by E/E' after each collision, the final estimation will be unbiased.

SCORING

In the subsequent steps of the Monte Carlo simulation of Eq. (2) a Neumann series of $\hat{\psi}$ is generated:

$$\hat{\psi}(\bar{r},\bar{E}) = \hat{\psi}_0(\bar{r},\bar{E}) + \sum_{i=1}^{\infty}\hat{\psi}_i(\bar{r},\bar{E}) = \hat{\psi}_0(\bar{r},\bar{E}) + \hat{\psi}'(\bar{r},\bar{E})$$

where the first term is

$$\hat{\psi}_0(\bar{r},\bar{E}) = \hat{P}_\psi(\bar{r},\bar{E}).$$

Accordingly, the physical quantity (3) - the flux at a point in our case - is also a sum of two terms:

$$\lambda = \lambda_0 + \lambda',$$

where the source contribution is

$$\lambda_0 = \iint d\bar{r}\,d\bar{E}\;\hat{P}_\psi(\bar{r},\bar{E})\,\mu^{-1}(\bar{r},E)\;S_C(\bar{r},-\bar{E}), \qquad (7)$$

and the contribution of the scattered particles is

$$\lambda' = \iint d\bar{r}\,d\bar{E}\,\hat{\psi}'(\bar{r},\bar{E})\,\mu^{-1}(\bar{r},E)\;S_C(\bar{r},-\bar{E}). \qquad (8)$$

Source contribution

In the case of uniform monoenergetic source distributions:

$$S(\bar{r},\bar{E}) = \begin{cases} S_o \frac{1}{4\pi} \delta(E-E_o) & \text{if } \bar{r} \in V_S, \\ 0 & \text{if } r \notin V_S, \end{cases}$$

where V_S is the source volume, Eq.(7) leads to:

$$\lambda_o = S_o \int d\bar{\omega} \frac{1}{4\pi} \int d\bar{r}' \mu^{-1}(\bar{r}_o, E_o)\, T(\bar{r}', \bar{r}_o | E_o, \bar{\omega}),$$

i.e. if an initial direction $\bar{\omega}_o$ is selected from the uniform distribution, then the score is:

$$L(\bar{r}, E_o, \bar{\omega}_o) = S_o \int_{V_S} d\bar{r}' \mu^{-1}(\bar{r}, E_o)\, T(\bar{r}_o, \bar{r}' | E_o, \bar{\omega}_o); \qquad (9)$$

S_o times the expected value of the track length in the source region.

If the source density is exponentially decreasing along, say, the z direction:

$$S(\bar{r}) \sim S_o \exp(-z/\zeta),$$

then in the source region μ have to be replaced by $\mu - \omega_z/\zeta$ and S_o by $S_o \exp(-z_o/\zeta)$, where ω_z is the z direction component of the $\bar{\omega}_o$ vector and z_o is the z coordinate where the path enters the source region, and the path length type score (9) holds.

Similarly, it can be derived that for plane sources the expected path length is replaced by the probability that the pseudo-particle crosses the source surface, divided by the cosine of the angle between $\bar{\omega}_o$ and the surface normal.

Contribution of scattered particles

Since in the adjoint simulation $\hat{\psi}(\bar{r}, \bar{E})$ is the collision density of the pseudo-photons just leaving a collision at $\bar{r}$ with energy and direction $\bar{E}$, we can define its counterpart $\hat{\chi}(\bar{r}, \bar{E})$ as the collision density of the pseudo-photons entering a collision at $\bar{r}$ with energy and direction $\bar{E}$:

$$\hat{\chi}(\bar{r},\bar{E}) = \int d\bar{r}'\, T(\bar{r}', \bar{r} | \bar{E})\, \hat{\psi}(\bar{r}', \bar{E}) \qquad (10)$$

From Eqs (2), (8) and (10):

$$\lambda' = \iint d\bar{r}\, dE\, \hat{\chi}(\bar{r}, E)\, \frac{1}{4\pi}\, \hat{C}_E(E_o, E|\bar{r}) \int d\tau\, L(\bar{r}, E_o, \bar{\omega}'), \qquad (11)$$

where $L(\bar{r}, E_o, \bar{\omega}')$ is the track length type quantity defined by Eq.(9) for uniform source distribution and has to be modified for the other two source types as described at the source contribution. The directions $\bar{\omega}'$ has to be chosen in accordance to the

$$\bar{\omega}\,\bar{\omega}' = g(E_o, E)$$

relation. This condition determines the angle of scattering only, therefore L has to be integrated over all azimuths (τ). This integration for τ can be carried out by an inner Monte Carlo estimation: a single azimuth is chosen randomly from the uniform distribution on $(0, 2\pi)$.

Briefly summarizing the evaluation of (11): the score is calculated before each pseudo-collision event by a product of a quantity $/\hat{C}_E/$ proportional to the probability that the pseudo-particle's energy will be scattered to E_o and a track length type quantity /L/ belonging to a such scattered pseudo-photon.

SPECIAL TECHNIQUES USED IN THE CODES

Calculation of the track length type quantities

The integrals describing the expected values of the track length type quantities of the scores are evaluable analytically but, in practice, if a path crosses the inhomogeneous phantom, then because of the necessary determination of the boundaries where the attenuation coefficient is changing /i.e. the determination of crossing points of the path with the second order surfaces separating the phantom regions/, the analytical calculation becomes extremely complicated and time consuming.

In view of this, the expected path scores are used if the point detectors are considered. If the phantom is standing in the room, then, in the REBEL-3 code, actual lengths of selected paths replace the expected values. /In other words, the expected paths are determined by an internal Monte Carlo procedure - consisting of just a single sampling/.

In the POKER-CAMP code the type of estimation is selected in every case /Fig. 3/. If the actual path does not cross the phantom, then the expected values are calculated analytically. For paths crossing the phantom expected values are calculated

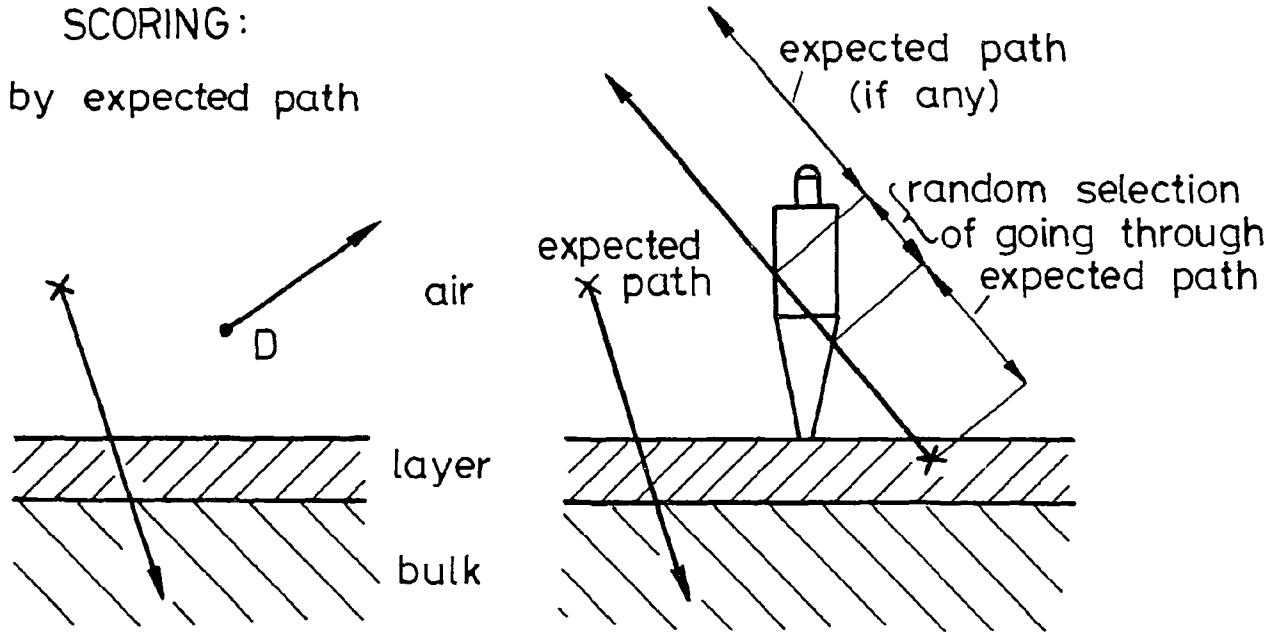

Fig. 3. A sketch of the track length type score calculations.

for the path before the phantom /if there is such a section/, then a random selection decides whether the path continues over the phantom, and if so, the calculation goes on again by analytical determination of the expected values.

Transport Inside the Phantom

The transport within the phantom is always simulated by the maximum cross section technique[12], i.e. potential sites are selected by using the maximum attenuation coefficient (μ_{max}), in our case the coefficient of the bone. Then the ratio $p = \mu_{pot} / \mu_{max}$ is calculated /μ_{pot} denotes the attenuation coefficient at the selected potential site/ and with probability of p the site is regarded as a real collision point, while with the probability 1-p a new path, starting from the previous potential site, is selected.

Calculations for More than One Sources

In the REBEL-3 code there are three types of sources: the ^{40}K /with a single gamma line/, the U/Ra/ and the Th series /their gammas are represented by 24 and 20 lines, respectively/, while in the POKER-CAMP the user can specify maximum 10 sources with not more than 250 lines altogether.

The fluxes are calculated separately for the different sources and also for the source and collided parts, but the random walk of the pseudo-particles is simulated commonly, i.e. the scores are calculated to all the lines before each collision.

Dose Calculations

As in most low energy photon dose calculations only interactions of the photons are followed, i.e. the energies of the secondary charged particles are assumed to be deposited at the sites of their creation. In other words it means that we approximate the absorbed dose by the kerma. This approximation is quite reasonable for energies below about 3 MeV.

The connection between the fluence rate and dose rate is given by

$$\dot{D} \simeq \dot{K} = \frac{\mu_K(E)}{\rho} E \varphi ,$$

therefore the initial statistical weight of the pseudo-particles is multiplied by

$$\frac{\mu_K(E)}{\rho} E$$

for the dose rate calculation.

We have only one problematic point with the ORNL phantom: that relating to the bone marrow, since there is no geometrically separated marrow region in the phantom. The marrow dose in the original Monte Carlo calculations with this phantom was estimated simply by taking the weight proportional fraction of the bone doses. Now, in our adjoint model this method has been modified in such a way that while the bone is still considered to be a homogeneous medium during the random walk simulation of the pseudo-particles, at the fluence to kerma conversions the mass energy transfer coefficients (μ_K/ρ) are calculated for the real bone marrow material - taken after the "reference man" of ICRP[13].

In the phantom dose calculations the physical target organ is assumed to be homogeneous, i.e. in the adjoint simulation the pseudo-photons start from all points with equal probability.

The skeleton of the phantom is divided into 13 segments /bones and bone parts/ having different marrow contents, and the distribution of the marrow tissues is uniform within each segment. Thus, in the case of the marrow dose calculation first a bone segment is selected /with a probability proportional to its marrow content/, and then the starting point is chosen from its volume.

The whole body of the phantom is inhomogeneous, the densities of the three types of tissues are different from each other. In principle, starting points should be selected with higher probabilities from the denser part but for sake of easy computation uniform random selection is carried out for the whole phantom volume but the initial statistical weight is multiplied by the density of the region where the selected point lies.

For the actual selection direct samplings /inverting the c.d.f./ or rejection techniques are used.

- x -

Finally we should like to mention here that the REBEL-3 code is deposited at the Radiation Shielding Information Center /ORNL/ and several representative results calculated by it are published[14,15]. The development of the POKER-CAMP code is just in the final stage, full documentation of it together with the publication of the first results may be

expected in the near future.

REFERENCES

1. H. L. Fisher and W. S. Snyder, "Distribution of Dose in the Body from a Source of Gamma Rays Distributed Uniformly in an Organ", Proc. 1st International Congress Radiation Protection, Pergamon Press, Oxford, p. 1773 /1968/

2. W. S. Snyder, M. R. Ford, G. G. Warner and H. L. Fisher, MIRD Pamphlet No. 5, J. Nucl. Med., 10, Supplement No. 3, 1 /1969/

3. W. S. Snyder, M. R. Ford, G. G. Warner and S. B. Watson, A Tabulation of Dose Equivalent per Microcurie-Day for Source and Target Organs of an Adult for Various Radionuclides, ORNL-5000, Report of the Oak Ridge National Laboratory, 1974.

4. L. Koblinger and P. Zaránd, Phys Med. Biol., 18, 4 /1973/

5. L. Koblinger, Monte Carlo Calculation on Chest X-ray Examinations. Results for Monoenergetic Beams, KFKI-73-19, Report of the Central Research Institute for Physics, Budapest, 1973.

6. K. O'Brien and R. Sanna, Health Phys., 30, 71 /1976/.

7. K. O'Brien and R. Sanna, Health Phys., 34, 107 /1978/.

8. L. Koblinger, REBEL-3: A Code for Calculating Doses in the Organs of a Phantom Standing in a Dwelling Room. KFKI-1980-07, 1980.

9. D. C. Irving, Nucl. Eng. Des., 15, 273 /1971/.

10. R. D. Evans, Compton Effect. Encyclopedia of Physics /Ed. S. Flügge/, Vol. XXXIV, Springer Verlag, Berlin, 1958.

11. L. Koblinger, A New Energy Sampling Method for Monte Carlo Simulation of the Adjoint Photon Transport Equation, KFKI-76-57, 1976.

12. W. A. Coleman, Nucl. Sci. Eng., 32, 76 /1968/.

13. Report of the Task Group on Reference Man, ICRP Publication 23. Pergamon Press, Oxford, 1974.

14. L. Koblinger, Health Phys., 34, 459 /1978/.

15. L. Koblinger, "Phantom Organ Shielding Factors for Radiation from Walls of Buildings" submitted for publication to the Health Phys.

Blank

CALCULATIONAL PROBLEM FOR DEEP PENETRATION OF NEUTRONS THROUGH A ONE-BEND SODIUM DUCT

Enrico Sartori*
Nuclear Energy Agency Data Bank, Saclay
Gif sur Yvette, France

ABSTRACT

This problem features a two-dimensional geometry representing a sodium duct surrounded by concrete that can easily be modeled with both Monte Carlo and two-dimensional S_N codes. The neutron source is placed on an external duct surface, has a uniform spectrum over the energy range of 5-2 MeV and is forward peaked with a cosine distribution. The average distance covered by a neutron leaving the duct surface at the exit is about 360 cm.

The importance sampling method of the Monte Carlo code TRIPOLI-2 is used. Fluxes and detector responses are tabulated for several surfaces defined along the neutron path in the sodium. A population of approximately 5000 neutrons undergoes about one million collisions giving flux and current at the duct exit with a standard error of 7.5 per cent.

INTRODUCTION

An important part of the activity of computer code centers is the implementation, verification and packaging of computer programs. Verification ensures that a program runs for selected problems in the same way as in the originating author's computer installation.

A further validation of a program can be made by comparison with other programs for a set of standard problems. Such benchmark tests and standard problem exercises are of particular interest to the N.E.A. Committees on Safety of Nuclear Installations (CSNI) and Reactor Physics

*Staff member of the IAEA, Vienna, on detachment at the NEA Data Bank.

(NEACRP), and can also help the NEA Data Bank to improve the computer program service. Computer programs and standard problems suitable for such comparative calculations are selected after consultation with members of these committees, with preference given to the benchmark problem collection of the ANS Standards Committee.

Results are presented here for the program TRIPOLI-2, applied to a two-dimensional geometry shielding problem. Other Monte Carlo codes, and eventually an S_N code, will also be run on the same problem.

DESCRIPTION OF THE PROBLEM

Geometry and Compositions

The geometry of the problem is depicted in Fig. 1. It is characterized by a two-dimensional one-bend sodium duct, 80 cm wide, surrounded by concrete walls, 40 cm thick. The length of the short leg is 160 cm, the length of the long leg 250 cm. The external boundary conditions are of no incoming flux. An infinite third dimension is simulated by prescribing reflective boundary conditions at two surfaces, normal to the third direction, two meters distance from each other. The densities and components of the materials are shown in Table I.

Source-Detectors

A boundary neutron source is placed at the external sodium surface of the short leg. Its surface density is of 1 neutron/cm^2 sec. The spectrum is uniform over the energy range of 5-2 MeV. Its angular distribution is an inwards directed cosine, normal to the boundary surface (Fig. 1.).

Table I. Material Compositions (293.6°K)

Material	Density (g/cm^3)	Component	Mass percentage
Sodium	0.9700	^{23}Na	100.
Concrete	2.380	Si	27.518
		^{16}O	53.949
		^{1}H	0.722
		Ca	17.810
		^{10}B	0.00153

The detectors' characteristics are given in Table VI. Microscopic cross-section data are used. ^{58}Ni and ^{103}Rh are used to detect fast neutrons down to 1 MeV and 50 keV, respectively. Thermal and epithermal neutrons are detected by means of the ^{55}Mn and $^{55}Mn/Cd$ detectors.

CALCULATIONAL METHODS AND RESULTS

Cross-Section Data

Group cross-section data,[1] based on the UKNDL evaluation, are used. The 269 groups have an equal lethargy width of 0.0575 from 15 MeV to 1 keV, with the exception of the interval of 32-20 keV, where half width is used. From 1 keV to thermal this width is doubled. A constant weighting was used when generating the group cross sections. Neutron slowing down and the cross-section anisotropy are treated in a continuous way. In the simulation, individual target nuclei are chosen with which the neutron will collide.

Biasing

In deep penetration problems, variance reduction techniques have to be used if realistic computing times are to be achieved.

The importance sampling method[1,2] of TRIPOLI-2 is used.

The biased Monte Carlo game consist of the following:

- A continuous weighting function (inversely proportional to the importance) is defined, taking into account the geometry, the materials, and the source-detector configuration and characteristics of the problem.
- The neutron population emitted at the source is transported together with its changing weight from the source to the detector region. Its size is kept under control in order to achieve effectiveness.
- The collision process is biased in such a way as to give birth to uncorrelated neutron histories.

The weighting function is of the following form:

$$\Pi(\vec{r},\vec{\Omega},E)=\Pi_1(\vec{r})\cdot\Pi_2(\vec{\Omega})\cdot\Pi_3(E)$$

where

$$\Pi_1(\vec{r})=\Pi_\circ(\vec{r}_\circ)e^{-k\vec{\Omega}_\circ\cdot(\vec{r}-\vec{r}_\circ)}.$$

$\vec{\Omega}_o$ is a unit vector specifying the preferred direction in which one wants the neutrons to move; k is the logarithmic slope of the spatial weights in direction $\vec{\Omega}_o$.

$$\Pi_3(E)=f\cdot E^{-\alpha}$$

where f is a normalizing factor and α is an energy dependent function.

$\Pi_2(\vec{\Omega})$ is selected by the program in such a way that the weight of the neutrons before each collision is independent of the direction and point of departure of the neutron.

The parameters used for $\Pi_1(\vec{r})$ and $\Pi_3(E)$ are given in Tables II and III. The isoweight contour lines of $\Pi_1(\vec{r})$ are shown together with the preferred directions in Fig. 2. These parameters were obtained by trial and error on a small sample of the neutron population.

The following considerations were made during the parameter tuning process:

- The number of collisions in the concrete should be limited as these will lead to insignificant contributions to the final tallies; the neutron population should migrate from the source to the detectors in the sodium around the bend.
- In order to have good statistics, a sufficient number of collisions should occur in the target area. In this specific problem the chosen target area is the duct outlet and the last 150 cm of the duct.
- The construction of a continuous weighting function reduces the need for splitting and russian roulette to a minimum, thus avoiding correlated and useless histories which lead to higher variance and lower efficiency.

By applying the exponential transform a biased total cross section is utilized,

$$\Sigma_t^* = \Sigma_t - k\vec{\Omega}\cdot\vec{\Omega}_o$$

where $\vec{\Omega}$ is the flight direction of the neutron.

Neutrons traveling in the preferred direction see a smaller cross section than those moving in the opposite direction. Successive collisions thus make the neutron population migrate toward regions of higher importance. The higher k compared to Σ_t the faster the population grows during the migration and slowing down process. $\Pi_3(E)$, however, is chosen in such a way as to cancel this population increase. In fact, higher importance is assigned to fast neutrons when compared to intermediate and epithermal neutrons.

The exponential transform causes more neutrons to be transported in the preferred than in the opposite direction. The biasing of the collision[1] forces neutrons to be transported independently of their direction after collision, thus increasing the independency of the histories and decreasing the variance. During the simulation the population size is controlled inside regrouped energy intervals called weighting groups.

An appropriate tuning of $\Pi_1(\vec{r})$ and $\Pi_3(E)$ minimizes this control thus avoiding russian roulette and splitting (see Table III).

Results

The calculation was carried out for ten batches, each of a population of about 500 neutrons which undergoes on the average 10^5 collisions. The current at the duct outlet, for neutrons with energies from 5 MeV to thermal is $5.8\ 10^{-5} \pm 7.5\%$ n/cm^2 sec and the flux $9.7\ 10^{-5} \pm 7.6\%$ n/cm^2 sec.

The 269-group spectrum, averaged over the last mesh (16cm), and the standard errors in per cent for each energy decade are shown in Fig. 3.

The surface flux, obtained by summing up the weights of the neutrons hitting the surface, the average mesh flux calculated by the track length estimator, and the absorption at different surfaces parallel either to the source or to the duct outlet surface are given in Table IV. Table V shows the detector responses at the same surfaces. In order to demonstrate the effect of tuning of the importance parameters, the responses over the whole duct length are presented. The chosen target area, however, is delimited by the last 150 cm of the long leg. The variance of the tallies is less than 10 per cent in this area. Whereas the fast neutron tallies have a low variance over the whole length of the duct, the corresponding epithermal and thermal variance decreases as the duct outlet is approached.

The computing time necessary for this calculation was 28 minutes on an IBM 3033. About 20 per cent of this time was spent in the thermal group.

CONCLUSION

TRIPOLI-2 is a flexible tool for solving deep penetration problems by the Monte Carlo method. With its importance sampling technique, complicated shielding problems can be calculated with efficiency.

ACKNOWLEDGMENTS

I am indebted to the authors of TRIPOLI-2 for many fruitful discussions and suggestions.

REFERENCES

1. A. Baur, L. Bourdet, G. Dejonghe, J. Gonnord, A. Monnier, J. C. Nimal, and T. Vergnaud, "Programme de Monte Carlo Polycinetique a Trois Dimensions TRIPOLI-02," CEA/SERMA/LEP Saclay (1980.

2. M. H. Kalos, F. R. Nakache, and J. Celnik, "Monte Carlo Methods in Reactor Computations," Computing Methods in Reactor Physics, Gordon and Breach Science Publishers, Ch. 5 (1968).

Table II. Space dependent weighting function $\pi_1(\vec{r})$

Region	k (cm^{-1})	direction of unit vectors (relative to x-axis) (degrees)	geometry
Sodium 1	0.044	position dependent focus on cylinder axis (140,140)	cylindrical
Sodium 2	0.044	0.	planar
Concrete 1	0.0792	20.	planar
Concrete 2	0.0792	0.	planar
Concrete 3	0.0792	304.	planar
Concrete 4	0.088	60.	planar
Concrete 5	0.0812	55.	planar
Concrete 6	0.0924	152.	planar

Table III. Weighting groups and energy dependent weighting function $\pi_3(E) = f \cdot E^{-\alpha}$

Upper Energy limit (MeV)	α	$\pi_3(E)$	imposed neutron population
14.8	1.0	1.00	500
4.217	1.0	3.41	500
1.0	0.25	14.4	1000
0.1995	0.25	27.9	750
4.467E-2	0.25	40.7	500
1.0E-2	0.1	59.2	500
1.995E-3	0.05	69.8	500
4.467E-4	0.05	75.3	500
1.0E-4	0.05	81.0	500
1.995E-5	-0.1	87.9	500
3.990E-7	-0.1	83.7	500
8.966E-8	0.0	57.3	500

Table IV. Neutron flux and absorbtion as a function of position

Location*) (cm)	$\sigma_a \phi$ (n/sec 10-24)	standard error %	surface flux (n/cm^2 sec)	standard error %	mesh averaged flux (n/cm^2 sec)	standard error %
+28	3.7E-2	61	2.4	18	2.5	7
+51	3.7E-2	35	1.6	11	2.0	12
+74	5.2E-2	31	1.1	10	1.4	10
+97	3.2E-2	29	0.70	12	0.90	10
+120	2.3E-2	30	0.40	12	0.56	11
+140	9.3E-3	30	0.28	17	0.29	12
-177	5.1E-3	15	6.3E-2	10	8.8E-2	11
-154	2.7E-3	12	3.1E-2	9	4.7E-2	10
-131	1.5E-3	9	1.7E-2	8	2.3E-2	9
-108	8.2E-4	8	8.5E-3	7	1.2E-2	8
-85	4.4E-4	11	4.2E-3	10	6.1E-3	9
-62	2.5E-4	7	2.1E-3	7	3.1E-3	9
-39	1.2E-4	8	9.6E-4	7	1.5E-3	8
-16	4.6E-5	8	3.7E-4	7	6.3E-4	7
-0	1.1E-5	9	9.8E-5	7	2.4E-4	8

*) + distance from the inlet

- distance from the outlet

Table V. Detector responses
$\sigma_D \phi$ /n/sec 10^{-24}/

location*) (cm)	detector 1	standard error %	detector 2	standard error %	detector 3	standard error %	detector 4	standard error %
+28	1.1	58	0.944	3.5	0.68	67	0.139	2.3
+51	1.2	32	0.403	2.8	0.58	37	4.78E-2	2.0
+74	1.9	31	0.190	8.1	0.86	44	1.76E-2	4.4
+97	1.6	24	7.84E-2	3.8	0.96	35	6.94E-3	5.4
+120	0.71	28	3.23E-2	3.7	0.27	19	2.43E-3	4.6
+140	0.38	28	1.43E-2	4.9	0.25	45	9.38E-4	4.5
-177	0.17	13	1.70E-3	4.7	6.8E-2	11	2.10E-5	4.8
-154	8.5E-2	9	6.22E-4	3.0	3.0E-2	14	2.70E-5	4.9
-131	4.8E-2	8	2.17E-4	4.0	1.6E-2	10	8.59E-6	6.1
-108	2.7E-2	10	8.00E-5	5.5	1.1E-2	15	2.86E-6	4.3
-85	1.4E-2	10	2.97E-5	5.4	4.8E-3	11	1.03E-6	4.3
-62	7.6E-3	8	1.10E-5	6.0	2.4E-3	10	3.70E-7	4.8
-39	3.5E-3	8	4.07E-6	4.7	1.1E-3	9	1.35E-7	6.9
-16	1.4E-3	8	1.38E-6	6.2	4.5E-4	10	4.92E-8	9.0
-0	3.5E-4	8	4.13E-7	5.6	1.2E-4	7	1.80E-8	7.7

*+ distance from the inlet - distance from the outlet

Table VI . Detector Characteristics

Detector identification no.	Characteristics
1	$^{55}Mn(n,\gamma)$ UKNDL 70 /thickness=0/σ_{th}=13.4 barns/
2	$^{103}Rh(n,n^1)$ UKNDL 70; equivalent fission flux /σ_f=0.720 barns/
3	Mn/Cd(n,γ) UKNDL 70 /thickness=0/ resonance integral I=15.44 barns
4	$^{58}Ni(n,p)$ Perkin data /σ_f=0.1119 barns/

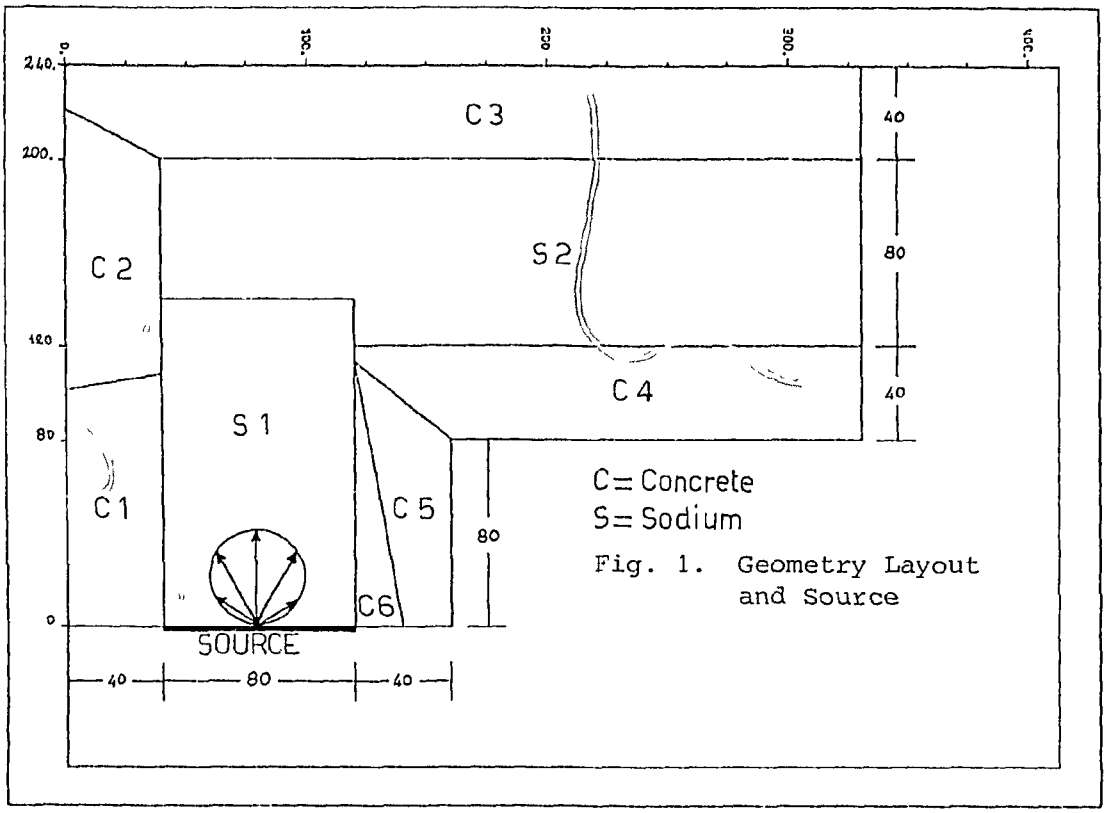

Fig. 1. Geometry Layout and Source

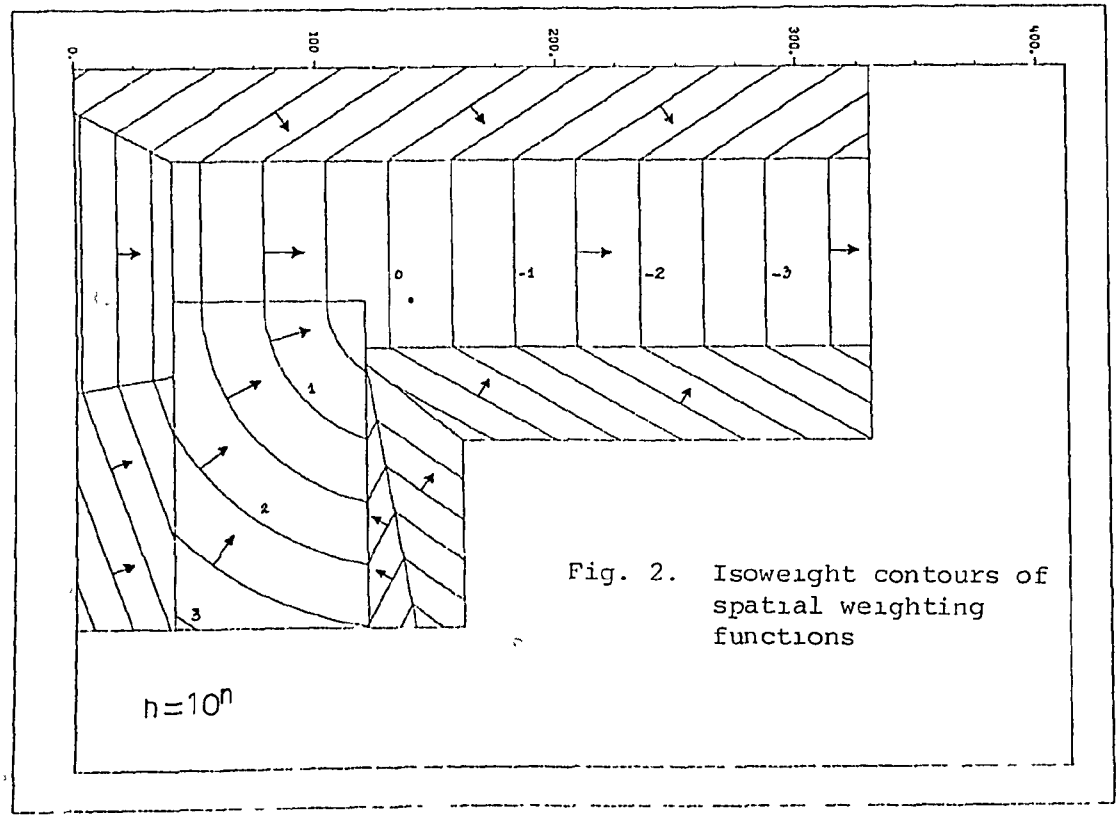

Fig. 2. Isoweight contours of spatial weighting functions

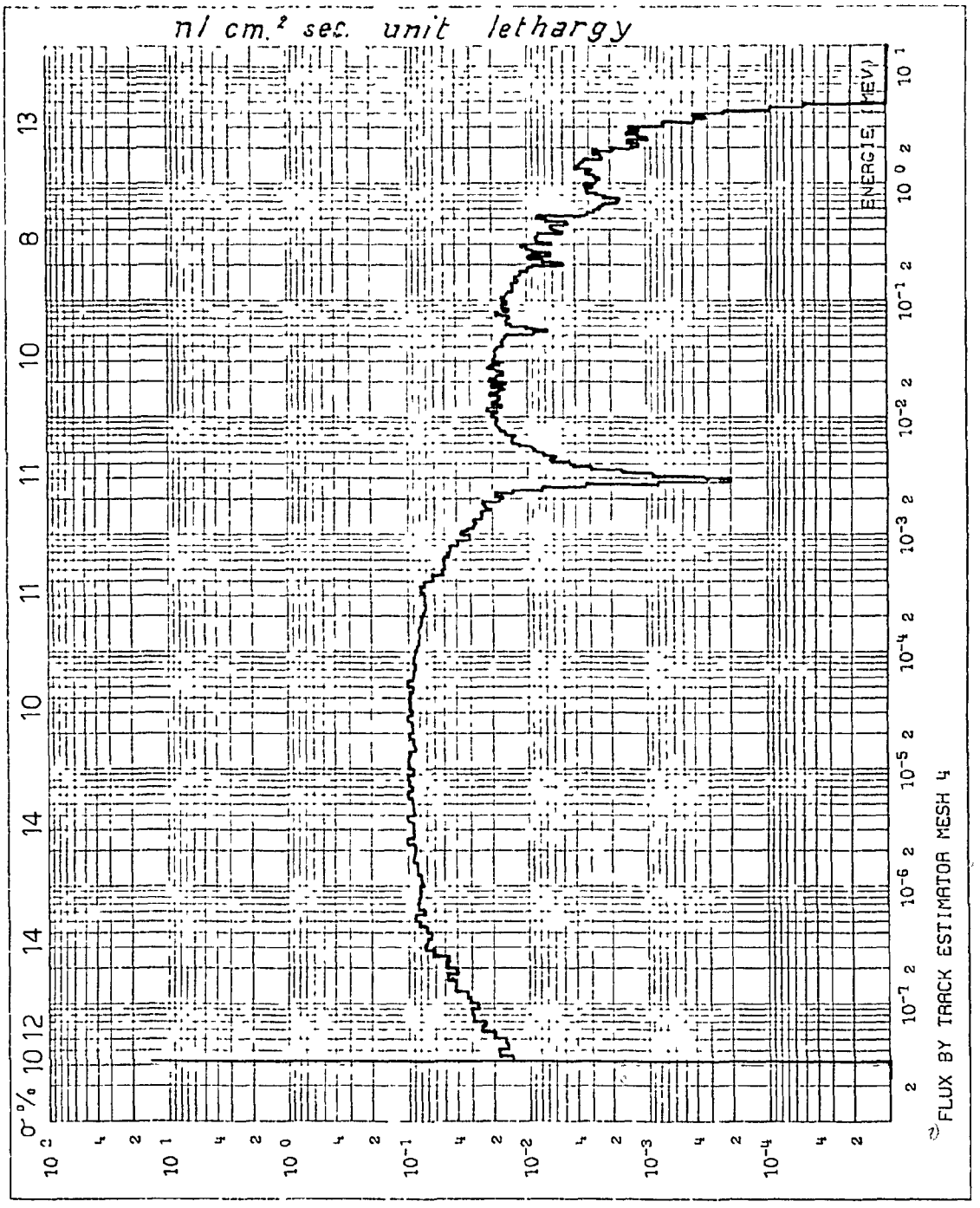

Fig. 3. 269 group spectrum in the sodium duct averaged over the interval 0 - 16cm from the outlet.

Blank

THE STATUS OF MONTE CARLO AT LOS ALAMOS

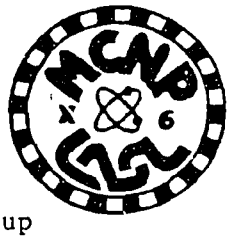

William L. Thompson and Edmond D. Cashwell
Group X-6
Monte Carlo, Applications, and Transport Data Group
Theoretical Applications Division
Los Alamos Scientific Laboratory
Los Alamos, New Mexico 87545

ABSTRACT

At Los Alamos the early work of Fermi, von Neumann, and Ulam has been developed and supplemented by many followers, notably Cashwell and Everett, and the main product today is the continuous-energy, general-purpose, generalized-geometry, time-dependent, coupled neutron-photon transport code called MCNP. The Los Alamos Monte Carlo research and development effort is concentrated in Group X-6.

MCNP treats an arbitrary three-dimensional configuration of arbitrary materials in geometric cells bounded by first- and second-degree surfaces and some fourth-degree surfaces (elliptical tori). MCNP has its own cross-section libraries plus it allows two thermal neutron models: the free-gas and $S(\alpha,\beta)$ treatments. There is a wide variety of standard sources plus a very easy-to-use and extensive tally structure. MCNP is quite rich in variance-reduction schemes, including three different techniques for estimating flux at a point. Other features include being able to calculate eigenvalues for both sub- and super-critical systems, an elaborate plotter for checking geometry setups, calculation of cell volumes and surface areas, and good documentation.

Monte Carlo has evolved into perhaps the main method for radiation transport calculations at Los Alamos. MCNP is used in every technical division at the Laboratory by over 130 users about 600 times a month accounting for nearly 200 hours of CDC-7600 time. However, MCNP is just the parent code. In addition to MCNP, major variants supported by Group X-6 include a multigroup forward and adjoint code, a code allowing geometrical perturbations, and a code that allows cell boundaries to change as a function of time. In addition, Group X-6 is involved in electron and high-energy nucleon/meson transport by Monte Carlo.

INTRODUCTION

We are happy to report that Monte Carlo is alive and well at Los Alamos. Our main code, MCNP,[1] is used by about 130 users in virtually every technical division at the Laboratory over 600 times a month, accounting for nearly 200 hours of CDC-7600 computer time. Monte Carlo, and in particular MCNP, is possibly the main method for radiation transport calculations at Los Alamos today. MCNP is also actively supported by Group X-6 on the Magnetic Fusion Energy computer network where it is used by a number of people throughout the country. Although Monte Carlo has widespread use at Los Alamos, the main research, code development and maintenance, user support, documentation, and nonroutine applications are concentrated in Group X-6 in the Theoretical Applications Division (X-Division). The purpose of this paper is to tell you a little about X-6 and its codes, with emphasis on MCNP.

GROUP X-6

Group X-6, presently consisting of 22 members, has as its title "Monte Carlo, Applications, and Transport Data." From this title, it is clear we have three areas of concern: (1) Monte Carlo methods and code development, (2) applications requiring particle transport by Monte Carlo, and (3) cross-section data. A strength of the group lies in the interaction of these three areas and their support of one another. To a very large extent, all the people in X-6 are conversant in each of these areas and appreciate the requirements and problems of each. The magnitude of the Monte Carlo expertise that resides in X-6 is likely unrivaled.

Activities in each of these areas will be discussed, but to help clarify the role of Group X-6 relative to some other activities at Los Alamos that you may be familiar with, the role of two groups from the Theoretical Division will be briefly mentioned. Group T-1, headed by D. J. Dudziak, is where the Laboratory's S_n expertise is concentrated. They are responsible for codes like ONETRAN[2] and TRIDENT.[3] Like X-6 they also are involved in applications but specialize in S_n and occasionally use the X-6 Monte Carlo codes as we in X-6 occasionally use their S_n codes. Basically though, we in X-6 solve transport problems randomly and T-1 solves transport problems discretely. Group T-2, headed by P. G. Young, is the Laboratory's nuclear data group. Among other activities, T-2 evaluates cross sections and processes data sets with their codes such as NJOY;[4] X-6 does not evaluate cross sections but extensively tests them and then makes them available in proper form for direct use by many of the major transport codes at LASL.

Monte Carlo Methods and Code Development

X-6 responds to requests from throughout the Laboratory for new methods and techniques to help solve individual problems. The requests are

frequently very specific and limited in scope (such as how to sample from some exotic distribution), but the requests may lead to a new feature that becomes a permanent part of our codes. Furthermore, X-6 originates many new methods and code improvements based on its knowledge of Monte Carlo and applications.

Some of the recent accomplishments include an S(α,β) thermal treatment, a more general analytical volume and surface-area calculator,[5] a very general tally structure, a once-more-collided point detector routine with a bounded variance, the addition of the union and complement operators for geometry specification, new standard sources with improved directional biasing into a fixed cone or in a continuous manner by means of an exponential function, a way to deterministically transport particles during their random walk (DXTRAN), many more user-oriented features and safeguards, plus a long list of miscellaneous items. A major accomplishment has been in the area of code documentation with the publishing of the 411-page MCNP manual[1] that contains over a hundred pages each of theory, cookbook examples, and details of the coding.

In the area of Monte Carlo theory, the theory of errors is a significant topic in X-6,[6-9] and a major work on relativistic effects has just been published.[10]

A new area of code development and physics for X-6 is the transport of high-energy (GeV range) protons, pions, mesons and the complete cascade of secondary particles down to the thermal-energy range. Applications will include energy deposition calculations in tissue in conjunction with the Los Alamos Meson Physics Facility research in cancer treatment plus shielding and materials damage studies. Our work is based on a modification to the HETC[11] code with an interface to MCNP.

In addition to the parent code MCNP, other X-6 codes include MCMG[12] which is a multigroup version of MCNP that also has an adjoint capability, MCNPPER that allows geometrical perturbations for calculating derivative information, MCGE which is a coupled electron-photon code that addresses the complete electron-photon cascade in the energy range from 20 MeV to 100 keV, a code that allows geometrical boundaries to change as a function of time, and numerous special versions of MCNP with which we evaluate new techniques and solve specialized problems.

About 40% of our effort is spent in this area.

Applications

X-6 serves two roles in the area of applications: (1) we work closely with MCNP users to help them with their applications, and (2) we do many applications ourselves that require our expertise and experience. Both these roles are valuable because they give us feedback on the use of MCNP and how best to improve it, and they broaden our own experience with a variety of applications.

Many applications are related to data verification and will be mentioned in that context.

An ongoing responsibility that we have for the Laboratory is calculating the biological dose from the intrinsic radiation (from the various natural decay modes of plutonium and uranium isotopes) emitted from the nuclear material used in nuclear weapons. This is of concern when military personnel are required to be in the proximity of the weapons for extended periods of time as is the case on a submarine. We also perform many calculations related to the vulnerability and effects of nuclear weapons.

X-6 has done extensive neutronics calculations for magnetic fusion reactor designs such as the Elmo Bumpy Torus (EBT),[13] Linus,[14] Reversed Field Pinch Reactor (RFPR)[15] and Fast-Liner Reactor[16] concepts. Furthermore, studies were made on Tokamak designs to evaluate the effect of geometrical simplifications in calculations.[17] Figure 1 is a Tokamak reactor geometry set up for MCNP; the surfaces marked by asterisks are tori. We would like to increase our role in the magnetic fusion area.

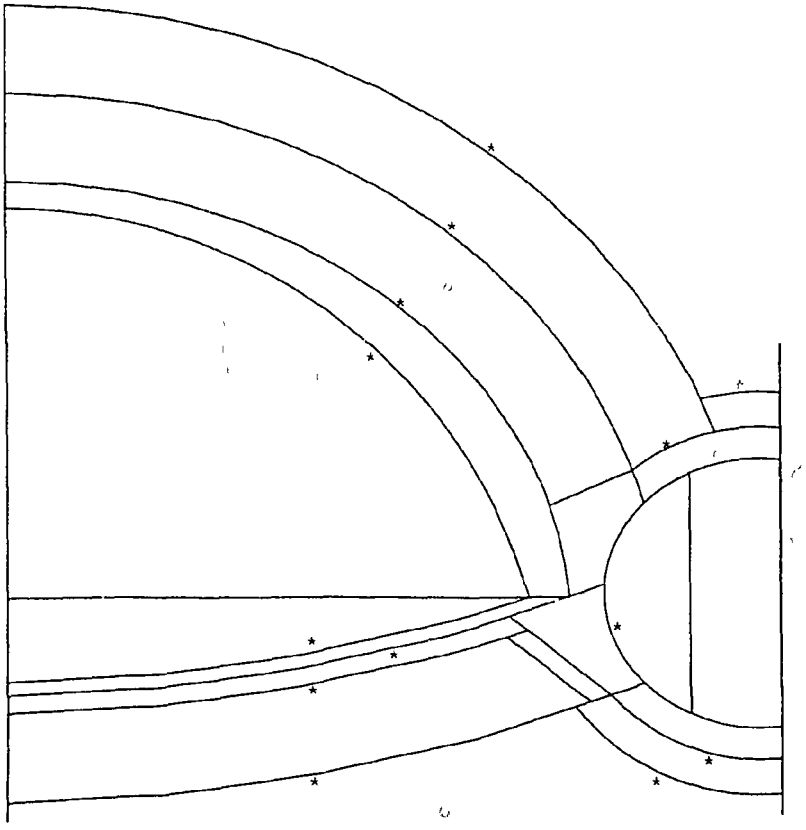

Figure 1. Tokamak Geometry.

The shielding designs for new facilities to be built at Los Alamos are frequently done by X-6. Recent examples include shielding from bremsstrahlung for a new electron accelerator to be built by the Physics Division and for the Antares Laser Fusion facility being built by the Laser Division. The Monte Carlo bulk-shielding calculations were done for Antares during the early design of the facility.[18] The basic building has been constructed, and we are now doing a radiation mapping inside the Target Building to ascertain material and instrumentation damage plus activation analysis of the target-chamber components. Figure 2 is the MCNP representation of the Antares target-insertion mechanism.

An activation analysis code, using the LASL GAMMON library,[19] is coupled with MCNP and calculates gas production (H,D,T, and He), material activation, and photon sources. The photon sources can be used in MCNP to calculate dose rates at points of interest.

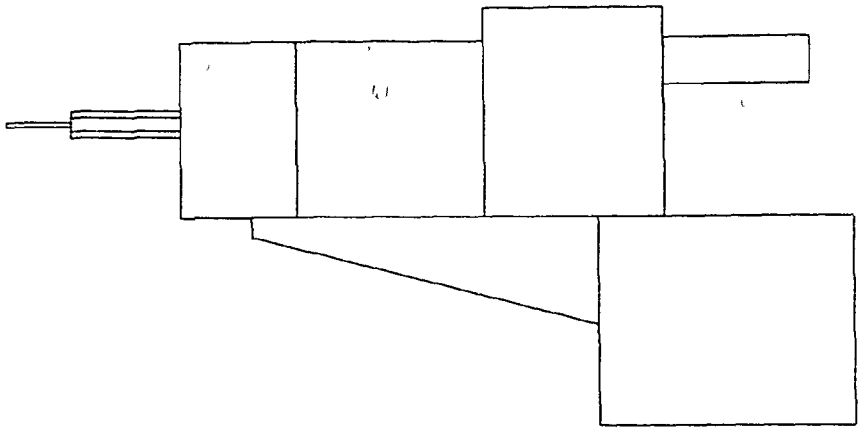

Figure 2. Antares Target-Insertion Mechanism.

Many interesting calculations have been done for the Health Division that involve instrument design[20,21] and radiation safety. One project involved the design of the gloveboxes at the new Plutonium Facility at Los Alamos, and another project just completed was a criticality study for the Slagging Pyrolysis Incinerator Facility (SPI) to be built at Idaho Falls.[22]

A recent series of calculations was completed as part of the review of the design of the Fusion Material Irradiation Test Facility (FMIT) to be built at Hanford.

X-6 works closely with the Nuclear Safeguards (assay and accountability) groups at Los Alamos in the designing of instrumentation, helping to understand the physics and Monte Carlo simulation of their experiments, and providing special versions of MCNP to account for delayed neutrons and to simulate coincidence counters.[23] Calculations in this area are invaluable to optimize an instrument design and to understand or extrapolate a calibration curve in the assay of unknowns.

About 35% of X-6's effort is spent in the area of applications.

Transport Data

X-6 is responsible for the X-Division nuclear cross sections and does partial processing of cross-section data provided by Group T-2. This includes continuous-energy, multigroup, and radiochemistry data used not only in the X-6 Monte Carlo codes but also in other transport codes used in X-Division and throughout the Laboratory.

The major effort in this third area of X-6 work is the testing of cross-section data.[24] The data are verified by two methods: (1) differential testing involving spectra, and (2) integral testing involving critical mass calculations of Los Alamos assemblies like Godiva and Jezebel. As part of this cross-section work, X-6 has been calculating and analyzing the latest experiment designed to measure the neutron spectrum and tritium production, and to check specific cross sections at various locations in a system consisting of a 93.5% enriched uranium sphere surrounded by ^{6}LiD. The Livermore pulsed-sphere experiments are also calculated for integral testing of cross-section data.

Extensive thermal benchmark calculations have recently been completed to test the integrity of MCNP, its thermal treatments, and its data.[25] MCNP calculations are now making significant contributions to the thermal data-testing program.

We have recently completed the monumental task of thinning, testing, and assembling in suitable form the ENDF/B-V and Livermore ENDL79 data. These data are now being used at Los Alamos.[26-28]

This final area accounts for about 25% of the group's effort. We find having this cross-section effort an integral part of X-6 to be a very valuable arrangement. It gives those of us doing applications a greater appreciation and awareness of the data. Furthermore, great resources can be immediately brought to bear on questions of transport data - as illustrated in the following paper on deep-penetration calculations by Thompson, Deutsch, and Booth.

MCNP

As mentioned earlier, Group X-6 is the author of MCNP, and MCNP is the backbone and main product of X-6.

MCNP is a very mature and reliable Monte Carlo code. It represents over two hundred man-years of effort and is the culmination of the original Monte Carlo work at Los Alamos by Fermi, von Neumann, and Ulam. Cashwell and Everett, over a period of almost thirty years, have contributed most to the development of MCNP. The first book on Monte Carlo was written by Cashwell and Everett.[29]

MCNP is a general-purpose, continuous-energy, generalized-geometry, time-dependent, coupled neutron-photon Monte Carlo transport code. It may be used in any of three modes: (1) neutron transport only, (2) combined neutron-photon transport, or (3) photon transport only. The capability to calculate eigenvalues for critical systems is also a standard feature of MCNP.

The following few sections will point out the main features of MCNP but will not go into detail. The MCNP manual, in addition to explaining how to use the code, contains the details of the physics, mathematics, and nuclear data aspects of MCNP. Another short publication,[30] which is just a reprint of the first part of the manual, summarizes the code. Finally, Carter and Cashwell's book[31] is not only a good general reference on radiation transport by Monte Carlo, but it is based upon MCNP in many aspects.

For most applications of MCNP, the user has to supply no more than an input file describing a problem. All of the input to MCNP is in free format. There is a variety of standard sources to choose from, and the tally structure is very general and elaborate. There is no need for a user to compile cross-section libraries for problems; X-6 maintains and provides all the data needed by MCNP.

Nuclear Data and Reactions

MCNP is a continuous-energy Monte Carlo code that makes no gross approximations regarding data. Linear interpolation is used between energy points with a few hundred to several thousand points typically required to reproduce the original data within a specified tolerance (in fact, usually within 0.1 to 0.5%). The only significant difference between the MCNP data libraries and the ENDF/B library (from which it is derived with the NJOY processing code) is that resonance data are represented in MCNP as linearly interpolated pointwise data that are Doppler broadened to a specific temperature. All reactions given in a particular neutron cross-section evaluation are accounted for in the energy range from 20 MeV to 10^{-5} eV. Users can choose from data with prompt or total fission ν's as well as

having the option to use a set of discrete-reaction cross sections in which the reaction cross sections have been collapsed into 240 energy groups to save computer memory. Users have the choice of data from the ENDF/B, British AWRE, Livermore ENDL, or special LASL libraries.

There are two thermal treatments in MCNP. One is the free-gas model in which, for elastic collisions, light atoms (Z = 1 through 8) are assumed to be in a Maxwellian distribution with some thermal temperature that may be a function of time. Secondly, the $S(\alpha,\beta)$ scattering model is available which accounts for chemical binding and crystalline effects at very low energies. Typically, when going down to room temperature, the free-gas model is used from around 10 eV to 4 eV, and then the $S(\alpha,\beta)$ model is used below that.

Photon interactions are accounted for in the range of 100 MeV to 1 keV. MCNP accounts for both incoherent and coherent scattering, fluorescent emission following photoelectric absorption, and pair production.

Geometry

The geometry of MCNP treats a general three-dimensional configuration of arbitrarily-defined materials in geometric cells bounded by first- and second-degree surfaces and some special fourth-degree surfaces (elliptical tori). The cells are defined by the intersections, unions, and complements of regions bounded by the surfaces.

Surfaces are easily defined by supplying coefficients to the analytic surface equations or by indicating known points located on the surfaces. For example, the surface y - D = 0 is represented in MCNP by the mnemonic PY with the single entry D. Therefore, a plane normal to the y-axis at y = 4 is defined by the simple input line of

```
PY    4
```

MCNP has 26 such mnemonics available.

Figure 3 is a geometry set up to test the analytical volume calculator in MCNP (the volume was calculated analytically and also stochastically by using a track-length estimator). This geometry of a fancy fish with a weird sun is actually only three cells in the MCNP problem: (1) the disjoint regions of the fish plus the sun (which appears as four regions), (2) everything else inside the sphere, and (3) everything outside the sphere. The geometry was specified by portions of twenty-three surfaces consisting of six tori, two hyperboloids, two ellipsoids, seven cones, one cylinder, two spheres, and three planes.

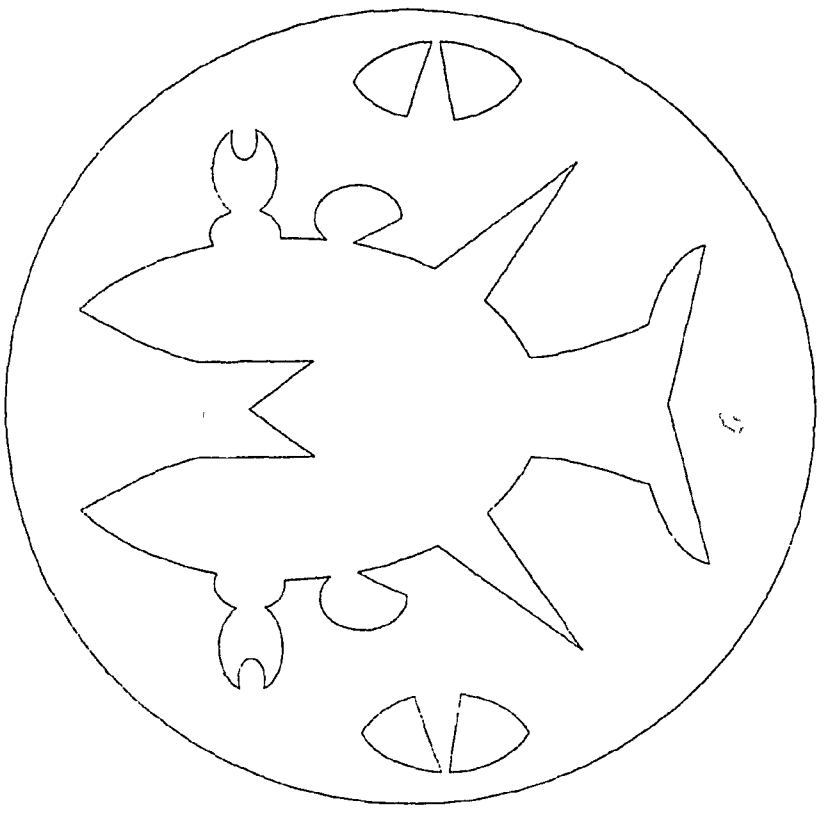

Figure 3. Example of MCNP Geometry.

Figure 4 is another example of MCNP geometry. This geometry consists of two cells and fifteen surfaces. The numbers in the figure refer to surface numbers: surface 1 is a cylinder; 3 is a cone; 12 and 13 are planes; 6, 7, 14 and 15 are ellipsoids; and 2, 5, 9, 10, and 11 are planes of two sheets.

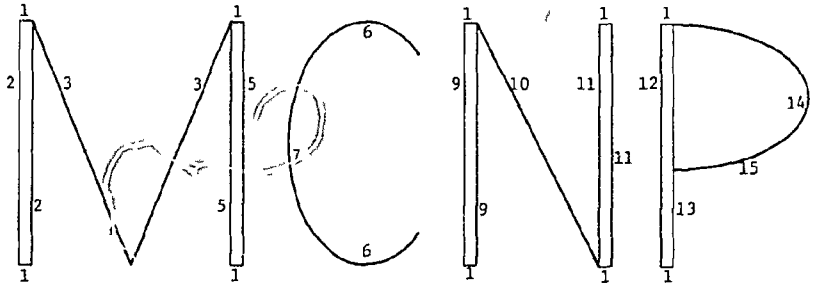

Figure 4. Example of MCNP Geometry.

More details about the MCNP geometry are given in the following paper by Godfrey. The significant additions of the union and complement operators to our geometry vocabulary are products of Godfrey's work. Cells that are now routinely specified with the union operator that are illegitimate when using intersections only are now in fact called "Godfrey cells" by us.

Variance Reduction

This one area alone makes MCNP a superb Monte Carlo code; MCNP is rich in variance-reduction techniques. The following two papers by Cashwell and Schrandt and by Thompson, Deutsch, and Booth will illustrate some of these techniques. More details are available in Refs. 1 and 31.

In addition to obvious ways to save computer time like using energy and time cutoffs, MCNP offers geometry splitting with Russian roulette, analog capture or survival biasing with weight cutoff and Russian roulette, correlated sampling, the exponential transformation, energy splitting, forced collisions, flux estimates at points by three methods (next-event estimator, ring detector, and once-more-collided estimator), track-length estimators, source biasing in direction and energy, and a combination random walk/deterministic scheme called DXTRAN. Furthermore, a Russian roulette game can be played with detector or DXTRAN contributions as a function of mean free path that can save substantial computer time.

X-6 is always evaluating new variance-reduction techniques and improving existing ones. Examples are (1) angle biasing which we look at from time to time but to date have not found a scheme that has anything substantial to offer over other methods already in MCNP, and (2) a weight window that looks quite promising (see paper by Thompson, Deutsch, and Booth). Furthermore, we are looking at generalized phase-space splitting.

Tallies

An important part of the MCNP output that the user has little control over (except for all of it or a fixed subset of it) is summary and diagnostic information. This information is valuable for determining the characteristics of a problem and the effect of variance-reduction techniques. Examples are (1) a complete breakdown of all energy and weight creation and loss mechanisms averaged over the entire problem and also individually by cell, (2) the number of tracks entering a cell and the track population in a cell, (3) the average energy, weight, number of collisions, and mean free path in a cell, (4) the volume, mass, and surface area of a cell, and (5) the activity (i.e., collisions, collisions times weight, and weight lost to capture) of each nuclide in each cell.

In addition to this summary information, MCNP has an elaborate and easy-to-use tally structure that allows the user to tally almost anything conceivable. Choices include, as a function of energy and time,

(1) current as a function of direction across a surface, (2) flux across a surface, (3) flux at a point, (4) average flux in a cell, and (5) energy deposition (or heating) in a cell by neutrons, photons, and products of neutron reactions. Surfaces or cells may be subdivided into segments for tallying purposes. In addition, particles may be flagged when they cross specified surfaces or enter designated cells, and the contributions of these flagged particles to the tallies are listed separately. The user has available a special subroutine by which the standard tallies can be modified in almost any desired way.

Reactions such as fission, absorption, tritium production, or any product of the flux times the approximately one hundred standard ENDF/B reactions plus several nonstandard ones may be tallied very simply.

Printed out with each tally is also its estimated relative error corresponding to one standard deviation of the mean.

Other Features

MCNP has the capability to calculate eigenvalues for critical systems. Three estimators (in various combinations) are used to calculate k_{eff}: absorption, collision, and track-length estimators.

For debugging input and geometries, MCNP makes extensive and elaborate checks for consistency. A plotting capability is in MCNP that provides an arbitrary cross-sectional view of the input geometry on several output devices (all figures in this paper plus slides used in the oral presentation were generated by the plotter). If a track gets lost during its transport, diagnostics are automatically printed for that track which include an event log. The event log is a print of the complete life of the track from event to event (birth, collisions, surface crossing, etc.).

A feature is available to allow the user to translate and/or rotate surfaces from one coordinate system to another. For example, it is a nontrivial task to determine the coefficients for the general quadratic equation needed to define an ellipse with its origin off somewhere in space and its axes at some skewed angle. However, an ellipse can be easily defined centered about the coordinate-system origin with axes parallel to the coordinate axes. It is then an easy procedure to move the simple ellipse to another place with another orientation.

For tallying purposes, cell volumes and surface areas are analytically calculated for polyhedral cells and for any cell bounded by surfaces of revolution (regardless of axis of symmetry). Surfaces of revolution generally account for the majority of cells, but irregular volumes and surface areas can also be easily calculated stochastically.

A convenient mechanism is provided to specify information to be written to a file for post-processing, such as for plotting results or to generate a source for a subsequent problem.

Full restart capabilities are available that are used for machine failure or continuing a run to obtain better statistics.

Future Work

We are the first to recognize that MCNP does not do everything for everybody. We are cautious about what goes into the code and put something in only for a good reason and after it has been carefully evaluated. However, X-6 frequently creates special versions of MCNP for the one-time requirements of special calculations or for the special requirements of a limited number of users.

The two most obvious shortcomings for use outside of Los Alamos are a lattice geometry specification and a better treatment of unresolved resonances. The lattice capability has not been of overriding importance to us at Los Alamos, but if others are interested in this feature we could be persuaded to increase the priority of it.

As mentioned earlier, we are always improving the existing variance-reduction techniques and devising new ones. We are interested in photo-neutron transport, but this is mainly a problem of data. Work is presently in progress on a three-dimensional plotter; our geometries have become so complicated it is hard to comprehend them with two-dimensional slices. Graphical techniques are being explored for post-processing of output data and for visual aids to help understand the characteristics of a problem (i.e., where are the particles going and how does a variance-reduction technique influence them). Studies of Monte Carlo vectorization are underway to see how we can take advantage of modern computer architecture (such as the CRAY-1) or future computers with parallel, independent processors.

MCNP is not a static code. It is under constant scrutiny and development by X-6. We release a new version about once a year with the current code being Version 2A. If MCNP ever becomes static, it will be so because there is no further use for it. We do not anticipate this happening; rather, the opposite seems to be the case.

MCMG

The multigroup code MCMG has basically the same features as the continuous-energy code MCNP, but it relies on the same user-supplied multigroup, multitable cross-section data that are used in discrete ordinates codes. Unlike the data for MCNP, the multigroup data treatment results in problem-dependent cross sections that can place a burden on the user to assemble and understand. MCMG can be applied to standard shielding

problems, to problems in reactor physics including the use of thermal upscatter matrices, to problems in accelerator or cosmic-ray shielding at very high energies, to problems in neutral atom transport in plasmas, and to any other problem in linear transport for which multigroup data have been developed.

An added feature of MCMG is that it is also an adjoint code. A cell- and energy-dependent scalar flux is automatically generated during a forward-mode calculation, and this information is used for importance sampling of adjoint collisions and for an energy-dependent geometric splitting and Russian roulette game in the adjoint tracking.

The distribution of scattering angles for group-to-group transfer is represented by either continuous, equiprobable cosine bins or by MORSE-type discrete-scattering angles, both of which preserve all of the moments of the truncated Legendre representation.

MCMG has an advantage over discrete ordinates codes in that it does not suffer from geometrical restrictions. Like discrete ordinates codes, however, it can be limited by the approximations that are inherent in the multigroup data that can, for example, result in masking the existence of self-shielding effects.

CONCLUSION

In our opinion (admittedly biased in the true nature of Monte Carlo), Group X-6 is a very strong, experienced, and versatile Monte Carlo group. Our code MCNP is a leading Monte Carlo code because of its maturity, generality, ease of use, reliability, richness of variance-reduction techniques, documentation, cross-section libraries, and active support and development by the expertise of X-6.

REFERENCES

1. LASL Group X-6, "MCNP - A General Monte Carlo Code for Neutron and Photon Transport," LA-7396-M, Revised (November 1979).

2. T.R. Hill, "ONETRAN, A Discrete Ordinates Finite Element Code for the Solution of the One-Dimensional Multigroup Transport Equation," LA-5990-MS (June 1975).

3. T.J. Seed, "TRIDENT-CTR User's Manual," LA-7835-M (May 1979).

4. R.E. MacFarlane, R.J. Barrett, D.W. Muir, and R.M. Boicourt, "The NJOY Nuclear Data Processing System: User's Manual," LA-7584-M (December 1978).

5. J.S. Hendricks, "Calculation of Cell Volumes and Surface Areas in MCNP," LA-8113-MS (January 1980).

6. R.J. Juzaitis and T.E. Booth, "Minimizing Splitting Costs in Monte Carlo Particle Transport," Transactions of the ANS, 33, 713 (1979).

7. T.E. Booth and E.D. Cashwell, "Prediction of Computing Costs in Monte Carlo Transport Calculations," Transactions of the ANS, 33, 321 (1979).

8. C.J. Everett and E.D. Cashwell, "Cost of Splitting in Monte Carlo Transport," LA-7189-MS (March 1978).

9. T.E. Booth and E.D. Cashwell, "Analysis of Error in Monte Carlo Transport Calculations," Nuclear Science and Engineering, 71, 128 (1979).

10. C.J. Everett and E.D. Cashwell, "A Relativity Primer for Particle Transport, A LASL Monograph," LA-7792-MS (April 1979).

11. K.C. Chandler and T.W. Armstrong, "Operating Instructions for the High-Energy Nucleon-Meson Transport Code HETC," ORNL-4744 (January 1972).

12. O.L. Deutsch, "MCMG User's Guide," Internal X-6 Document (March 1979).

13. R.A. Krakowski and C.J. Bathke, "Reassessment of the Elmo Bumpy Torus Fusion Reactor Concept: Phase I, Physics Design," (P.D. Soran, Neutronics Design), LASL report in preparation.

14. R.W. Miller and R.A. Krakowski, "Reassesment of the Slowly-Imploding Liner (Linus) Fusion Reactor Concept," (P.D. Soran, Neutronics Design), LASL report in preparation.

15. R.L. Hagenson, R.A. Krakowski, G.E. Cort, "The Reversed-Field Pinch Reactor (RFPR) Concept," (P.D. Soran, Neutronics Design) LASL report LA-7973-MS (August 1979).

16. R.W. Moses, R.A. Krakowski and R.L. Miller, "A Conceptual Design of the Fast-Liner Reactor (FLR) for Fusion Power," (P.D. Soran, Neutronics Design), LASL report LA-7686-MS (February 1979).

17. J.L. Macdonald, E.D. Cashwell, and C.J. Everett, "Calculation of Toroidal Fusion Reactor Blankets by Monte Carlo," Proceedings of the Fifth International Conference on Reactor Shielding, Science Press, Princeton, 622 (1977).

18. W.L. Thompson, "A Neutron/Photon/Electron Shielding Study for a Laser Fusion Facility," Proceedings of the Fifth International Conference on Reactor Shielding, Science Press, Princeton, 628 (1977).

19. M.E. Battat, R.J. LaBauve, and D.W. Muir, "The GAMMON Activation Library," LA-8040-MS (September 1979).

20. D.A. Close and T.E. Booth, "In Situ Nondestructive Plutonium Assay for an Electropolishing Bath," Transactions of the ANS, 33, 423 (1979).

21. J.S. Hendricks and D.A. Close, "^{3}He Detector Design for Low-Level Transuranic Waste Assay," Transactions of the ANS, 28, 137 (1978).

22. D.A. Close, T.E. Booth, J.T. Caldwell, "Criticality Calculations and Criticality Monitoring Studies of the Slagging Pyrolysis Incinerator Facility," LA-8336-MS (April 1980).

23. J.E. Stewart, N. Ensslin, R.G. Schrandt, "Removing Multiplication Effects from Neutron Coincidence Counting Using Monte Carlo," Transactions of the ANS, 33, 442 (1979).

24. R.E. Seamon, "Cross Sections for Monte Carlo Calculations," X-6 Activity Report, LA-8232-PR, 34 (July-December, 1979).

25. R.E. Prael, "Thermal Reactor Benchmark Calculations with the MCNP Monte Carlo Code," Transactions of the ANS, 33, 846 (1979).

26. P.D. Soran and R.E. Seamon, "Integral Data Checking of ENDF/B-V and ENDL79," Internal X-6 memo (March 18, 1980).

27. G.P. Estes and J.S. Hendricks, "Integral Testing of Some ENDF/B-V Cross Sections," Transactions of the ANS, 33, 679 (November, 1979).

28. L.L. Carter and J.S. Hendricks, "Computational Benchmark for Deep Penetration in Iron," Transactions of the ANS, 33, 663 (1979).

29. E.D. Cashwell and C.J. Everett, "A Practical Manual on the Monte Carlo Method for Random Walk Problems," Pergamon Press, Inc., New York (1959), also LA-2120 (1957).

30. W.L. Thompson, "MCNP - A General Monte Carlo Code for Neutron and Photon Transport, A Summary," LA-8176-MS (December 1979).

31. L.L. Carter and E.D. Cashwell, "Particle-Transport Simulation with the Monte Carlo Method," ERDA Critical Review Series, TID-26607 (1975).

GEOMETRY IN MCNP

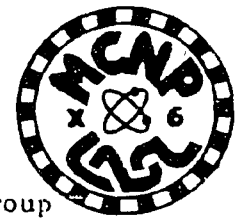

Thomas N.K. Godfrey
Group X-6
Monte Carlo, Applications and Transport Data Group
Los Alamos Scientific Laboratory
Los Alamos, New Mexico, USA

ABSTRACT

MCNP is a general-purpose neutron and photon Monte Carlo code developed by group X-6 at LASL. The geometry cells in MCNP are defined as regions of space bounded by user-specified second-degree surfaces and certain tori. Until recently cells had to have only convex edges. Now the geometry description is entirely general: cells may have concave edges and any sort of connectivity. The new general geometry description is a substantial improvement over the surface list and combinatorial geometry methods and includes the best features of both. It makes a big difference in the ease of setting up problems that contain features such as nested boxes, rooms with ells, and irregular slabs.

Another recent addition to the geometry description capability of MCNP is that certain kinds of surfaces of revolution can be defined by a few points on the surface rather than by the coefficients of the equation of the surface.

MCNP has long automatically calculated the volumes of rotationally symmetric cells. It now also calculates the volumes of polyhedral cells.

I will start with an example of how geometry is described in the setup of a problem for MCNP. I will then explain the vocabulary and syntax of the setup and show how tracking is done in the code. Finally, I will describe some of the other geometry features of MCNP and our plans for future improvements.

EXAMPLE OF GEOMETRY DESCRIPTION

In Fig. 1, cell 1 is a room with thick walls. The walls, including the columns, are collectively cell 2. There are other cells in the system that are not shown in the figure. The origin of coordinates is inside the

lower left column. The background grid consists of 1-meter squares. The portions of the problem input file for MCNP that describe cells 1 and 2 are shown in Table 1.

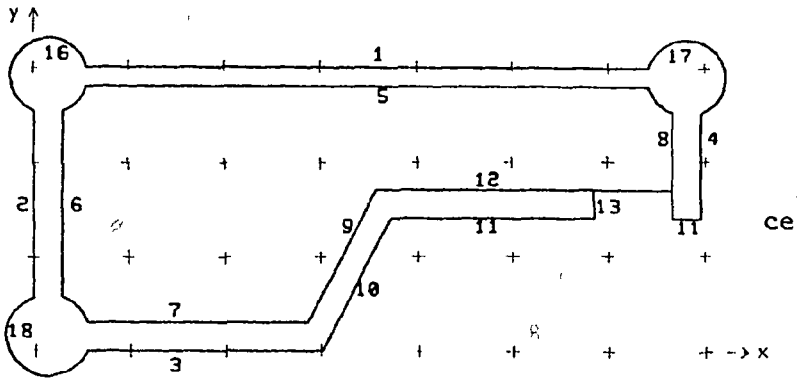

Fig. 1. Example of MCNP Geometry

Table 1. Input File for Geometry of Fig. 1

```
cells
1     6 -5 -8 7 (12:-9) 16 17 18 14 -15
2     (2 -1 -4 3 :-16:-17:-18) #1 #(13 -12 -8) #(-11 10) 14 -15

surfaces
1     PY 300
2     PX 0
3     PY 0
4     PX 690
5     PY 280
6     PX 30
7     PY 30
8     PX 660
9     P 2 -1 0 540
10    P 2 -1 0 600
11    PY 140
12    PY 170
13    PX 580
14    PZ 0
15    PZ 310
16    C/Z 15 290 40
17    C/Z 675 290 40
18    C/Z 15 15 42.7
```

Each surface in the system is assigned a number. The specification of each surface is written on the line after the surface number. The specification of a surface consists of a symbol for the kind of surface

followed by the coefficients for the surface. For example, surface 1 is specified to be a plane perpendicular to the Y-axis (PY) at Y=300 cm. Surface 9 is a plane satisfying the equation

$$E(X,Y,Z) = Ax + By + Cz - D = 0$$
$$\text{with } A = 2,\ B = -1,\ C = 0,\ \text{and } D = 540. \qquad (1)$$

Every point in space has a positive or negative sense with respect to each surface, unless it is actually someplace on the surface. The sense arises from the way the surfaces are required to be specified. Each kind of surface is described by an equation which is built into the code,

$$E(X,Y,Z) = 0. \qquad (2)$$

All points (X,Y,Z) for which the expression E(X,Y,Z) is greater than zero have a positive sense with respect to that surface. For example, the equation of surface 4 is

$$E(X,Y,Z) = X - D = 0 \quad \text{where } D = 690. \qquad (3)$$

So points to the right (large X) of surface 4 are positive with respect to surface 4, and points to the left of the surface are negative.

Cell 1 is specified as consisting of the intersection of the spaces to the right of surface 6, below surface 5, to the left of surface 8, above surface 7, and either above surface 12 or above and to the left of surface 9. The spaces where the columns encroach are excluded, and the cell is further limited by the floor and ceiling, surfaces 14 and 15. Cell 2 is the space enclosed by surfaces 2, 1, 4 and 3, plus the three columns, but excluding cell 1 and excluding the space enclosed by surfaces 13, 12, and 8. The space below surface 11 and to the right of surface 10 is excluded, and it is limited by the floor and ceiling.

VOCABULARY AND SYNTAX

The scheme used here is the combinatorial geometry of regions which are defined by simple surfaces. The regions are in most cases infinite, but in combination they define finite cells. The union operator is represented by the colon, the intersection operator is implicit, and the complement operator is represented by #. Where the complement operator is followed immediately by a number, the number is interpreted as a cell number. Otherwise all of the numbers are surface numbers. The region of space whose points have positive sense with respect to a surface is represented by the surface number. The region on the negative side is represented by the negative of the surface number. Parentheses are used

where necessary to change the order of execution of the operators. Unless dictated otherwise by parentheses, complementation is done first, then intersection, and union is last, which is the conventional hierarchy for operators of this kind.

The surfaces available in MCNP include all of the surfaces of second degree in three dimensions plus certain tori. The general second degree surface is available. Its symbol is GQ and its equation is

$$E(X,Y,Z) = Ax^2 + By^2 + Cz^2 + Dxy + Eyz + Fzx + Gx + Hy + Jz + K = 0 \qquad (4)$$

A user specifies it by an input line like this:

surface no. GQ A B C D E F G H J K

Special simpler expressions with fewer coefficients are available for certain simple, frequently-used second degree surfaces. These include planes and cylinders, as shown in Fig. 1 and Table 1, and also spheres and cones.

The tori available are ones with elliptical cross section and with the axis parallel to one of the coordinate axes. They are rather handy in problems with inherently toroidal shapes, such as magnetically-confined-fusion machines.

TRACKING

When a particle comes out of the source or out of a collision, it is necessary to find the point where its track first intersects the boundary of the cell it is in. In Fig. 2, the collision is at K, and the track intersects the surfaces of the cell at A, B, C, and D. Intersection C is the required intersection with the cell boundary. MCNP calculates the intersections A, B, C and D by solving equations and accepting positive real roots. It then examines each intersection in increasing order of distance from the collision to find the cell boundary intersection. The algorithm used is shown by example in Fig. 2. A logical expression is set up parallel to the cell description but with the surface numbers replaced by true or false, depending on whether the collision point is on the designated side of the surface. At the collision point K, the value of the logical expression is, of course, true. As each intersection is examined, the logical values corresponding to the surface at the intersection are flipped and the expression is evaluated. As long as the intersections are still inside the cell, the value of the expression remains true. When it turns false, the cell boundary intersection has been found.

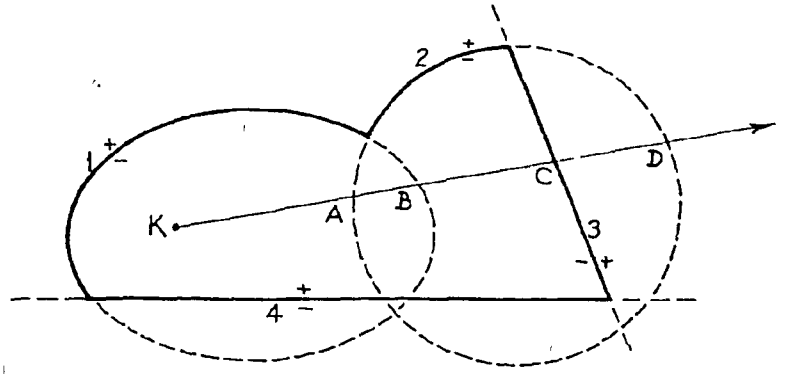

Logical expressions:

geometrical description of the cell:	(-1	: -2)	-3	4	
at collision point K:	(T	: F)	T	T	= T
across surface 2 at A:	(T	: T)	T	T	= T
across surface 1 at B:	(F	: T)	T	T	= T
across surface 3 at C:	(F	: T)	F	T	= F

Fig. 2. Tracking

COMPARISON WITH OTHER GEOMETRY SCHEMES

The geometry scheme that MCNP once had was like the one described above except that it had no union or complement operators. I call it the surface list scheme since if the only operator is intersection, the specification of a cell is just a list of its bounding surfaces. The complement operator does not add a new capability, but it is a significant convenience. The union operator makes it possible to describe cells with concave edges and cells that consist of disconnected regions. Without the union operator, the two cells in Fig. 1 would have had to be eleven cells. A larger number of cells is not only more trouble to set up, which leads to setup errors, but in some cases complicates the tallying and the interpretation of the tallies.

In comparison with the other combinatorial geometry scheme with which I am familiar, the MCNP scheme differs mainly in the nature of the basic building blocks. In MCNP they are at once simpler and more general. I imagine that the scheme that turns out to be better for setting up a problem depends on the specific nature of the problem. The greater generality of the MCNP surfaces is a help in some cases. Also it must often happen that a body in combinatorial geometry is used for the sake of only one or two of its surfaces. The other surfaces then become parasites in tracking.

OTHER FEATURES

In some problems the geometry, or a significant part of it, is rotationally symmetric about some axis. In such cases the MCNP user may specify surfaces by giving the R and Z coordinates of a few points. Two points specify a cylinder or cone. Three points specify spheres, and ellipsoids, hyperboloids, and paraboloids of circular cross section.

MCNP may be used to rotate and translate surfaces from one coordinate system to another. Sometimes it is convenient to specify some of the surfaces in one coordinate system, such as by the point definition scheme described in the preceding paragraph. Then the code can be used to generate the coefficients that describe the surfaces in the main coordinate system of the problem.

Volumes of cells and areas of the portions of surfaces that bound cells are needed for normalizing tallies. MCNP has long been able to calculate these for cells rotationally symmetric about any axis. For other cells the user must enter the volumes and areas by hand. The code can, of course, be used in a separate run to calculate volumes by Monte Carlo in cases where it is hard to do it by hand. Recently the ability to calculate directly the volumes of polyhedral cells has been added to the code.

The code may also be used to plot pictures of the geometry on various computer graphics devices. The pictures are naturally very valuable to the users who are trying to check out their setups.

FUTURE IMPROVEMENTS

We intend to build a lattice capability into MCNP for better representation of geometries with repeated features.

We want to improve the plotting capability to show lines that are beyond the view plane, perhaps with perspective, instead of just pure cross sections of the geometry which is what we have now.

FLUX AT A POINT IN MCNP

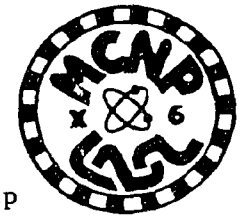

E. D. Cashwell and R. G. Schrandt
Group X-6
Monte Carlo, Applications and Transport Data Group
Theoretical Applications Division
Los Alamos Scientific Laboratory
Los Alamos, New Mexico

ABSTRACT

The current state of the art of calculating flux at a point with MCNP is discussed. Various techniques are touched upon, but the main emphasis is on the fast improved version of the once-more-collided flux estimator, which has been modified to treat neutrons thermalized by the free gas model. The method is tested on several problems of interest and the results are presented.

INTRODUCTION

The next-event estimator (NEE) used in a normal Monte Carlo game for the flux at a detector embedded in a scattering medium suffers from a $(1/r^2)$-singularity. Consequently, the variance of the estimator is infinite even though the mean is finite.

In 1977, Kalli and Cashwell[1] proposed and evaluated three estimation schemes for flux at a point. A new, once-more-collided flux estimator (OMCFE) was proposed, which differed from those proposed by Kalos in his original paper.[2] The scheme has a $(1/r)$-singularity, leading to finite variance and $(1/\sqrt{N})$-convergence. It is based on a very simple p.d.f. of the path lengths in the sampling of the intermediate collision points. In addition, this simple p.d.f. for the path length was used in two schemes with bounded estimators similar to those proposed by Steinberg and Kalos[3] and by Steinberg.[4] The three schemes were evaluated in a realistic problem using the continuous energy Los Alamos Monte Carlo code MCNG, the forerunner of MCNP.[5]

Once-More Collided Flux Estimator (OMCFE)

In the present discussion we wish to focus on the OMCFE referred to above. This scheme has been incorporated into MCNP and, although some work still remains to be done, we wish to discuss this method in conjunction with other techniques available in MCNP.

The details of the OMCFE as it exists in MCNP are, for the most part, given in Ref. (1). Without repeating the treatment given there, we wish to touch on the main points of the method, as well as mention generalizations of the method to a wider class of problems. The OMCFE is superimposed on the particle history without affecting it. At each collision (or source point), a nonanalog game is played whereby a next collision point A is chosen, from which a contribution to the detector is made. That is, from every real collision point of the particle history, a once-more-collided contribution is made to the detector.

The two main features in determining the intermediate point A of the once-more-collided scheme are:

1. A directional reselection procedure based on the reselection technique of Steinberg and Kalos;[3] and

2. A nonanalog p.d.f. $p^*(s)$ which was used by Kalli[6] in 1972.

In Fig. 1, consider a collision at S with the resulting scattered direction $\vec{\Omega}_0$ in the cone described. Suppose that a new direction $\vec{\Omega}_1$ is chosen by sampling a new angle β_1 uniformly in $(0,\beta_m)$ and a ϕ_1 uniformly in $(0,2\pi)$. The result is a concentration of scattered directions closer to the line from S to the detector D than would normally occur. Of course, an adjustment factor must be applied to the weight of the particle due to the reselection.

Once the direction $\vec{\Omega}_1$ is chosen, suppose the intermediate point A is selected along this direction from the p.d.f. $p^*(s)$, where

$$p^*(s) = \frac{b}{(\pi/2 - \alpha_1)r^2} \quad \text{(Cf. Fig. 2).} \tag{1}$$

This density function corresponds to α being chosen uniformly in $(\alpha_1,\pi/2)$. Use of $p^*(s)$ leads to another weight adjustment $p(s)/p^*(s)$, where $p(s)$ is the analog p.d.f. for sampling distance to collision.

In the normal OMCFE, the point A is not a real collision point of the particle history. When these calculations involve reselection of direction and the distance to A using $p^*(S)$, as well as the normal next-event estimator, they tend to be time-consuming. In order to speed up calculations using the OMCFE:

1. Draw an imaginary sphere around the detector;

2. If the collision point S_i is outside the sphere but the direction after the collision is within the cone defined by S_i and the sphere, calculate the once-more-collided flux contribution by performing the directional reselection in the cone and calculate the intermediate point A by using $p^*(s)$;

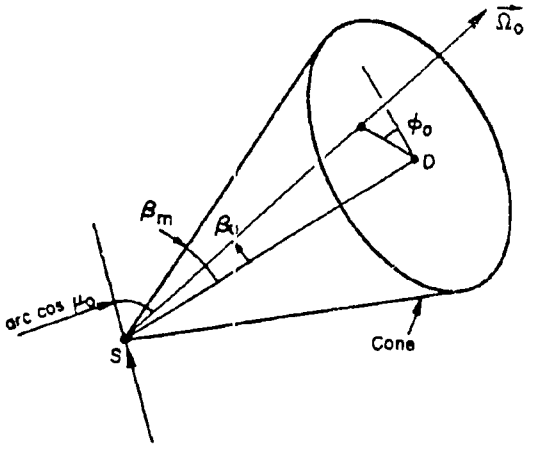

Fig. 1. Geometry in the reselection of a direction.

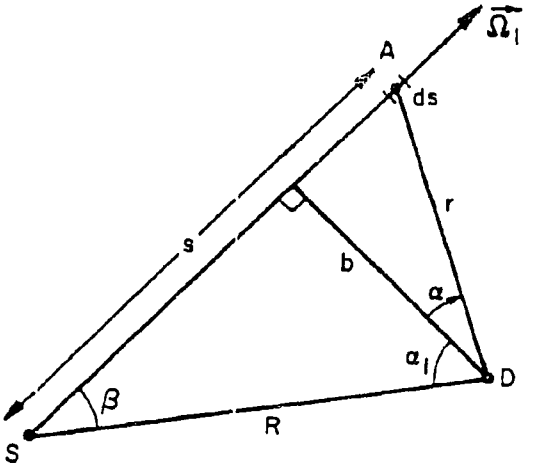

Fig. 2. Geometry in the selection of the intermediate collision point A.

3. If the collision point S_i is in the sphere and the direction $\vec{\Omega}_o$ after collision is in a 2π-cone (i.e., $\beta_o < \pi/2$) about the line from S_i to D, the once-more-collided point is calculated by reselection of $\vec{\Omega}_1$ and using p*(s) to determine the intermediate point A; if the direction $\vec{\Omega}_o$ after collision is such that $\beta_o > \pi/2$, no reselection is performed but the intermediate point A is chosen from p*(s); and

4. Otherwise, calculate the normal next-event contribution from the following collision point S_{i+1}.

The recipe as outlined above works very well in most problems containing ordinary materials. However, in non-thermal problems containing H, the forward scattering off H in the laboratory system of coordinates lead to some modification of the recipe because of the directional reselection procedure. Furthermore, the random motion of the target atoms combined with the motion of the neutron in the thermal routine using the free gas model in MCNP leads to rather extensive modifications for the same reason. The imaginary sphere around the detector may have to be reduced in size in the course of the calculation, as a result of using the reselection procedure.

With the necessary modifications, MCNP is able to treat problems of the types mentioned above, as illustrated by the sample calculations below. Several considerations led to the implementation of the OMCFE rather than one of the schemes leading to a bounded estimator in Ref. (1). First of all, the OMCFE was judged to be the simplest to insert into MCNP. Furthermore, the estimation of flux simultaneously at several points causes no problems in the OMCFE scheme. Finally, since the OMCFE does not alter the particle histories, its use has no effect on other tallies which may be required in a particular problem.

DXTRAN

Let us describe briefly a subroutine, DXTRAN, which has been used in Los Alamos for some years and is an option available in MCNP.[5] We shall indicate its usefulness in our examples below. DXTRAN is of value in sampling regions of a problem which may be insufficiently visited by particle histories to yield adequate statistical accuracy in a given tally. To explain how the scheme works, let us consider the neighborhood of interest to be a spherical region surrounding a designated point P_0 in space. In fact, we consider two spheres of arbitrary radii about the point $P_0(x_0,y_0,z_0)$. We assume that the particle having direction (u,v,w) collides at the point (x,y,z), as shown in Fig. 3. The quantities L, θ_I, θ_o, η_I, η_o, R_I, and R_o are clear from the figure. Let us somehow choose a point P_s on the outer sphere and assume that a scattered particle (let us call it a "pseudo-particle" for the moment) is placed there. We give this pseudo-particle a weight equal to the weight of the incoming particle at P_1 multiplied by the ratio of the p.d.f. for scattering from P_1 to P_s with no collision to the p.d.f. for choosing the point P_s in the first place.

If we sample directions isotropically in the cone defined by P_1 and the outer sphere, the number of directions falling inside the inner cone and the number falling in the outer cone will be proportional to $1-\eta_I$ and $\eta_I-\eta_o$, respectively. Let Q be a factor which measures the weight or importance which one assigns to scattering in the inner cone relative to scattering in the outer cone. We now proceed by the following steps:

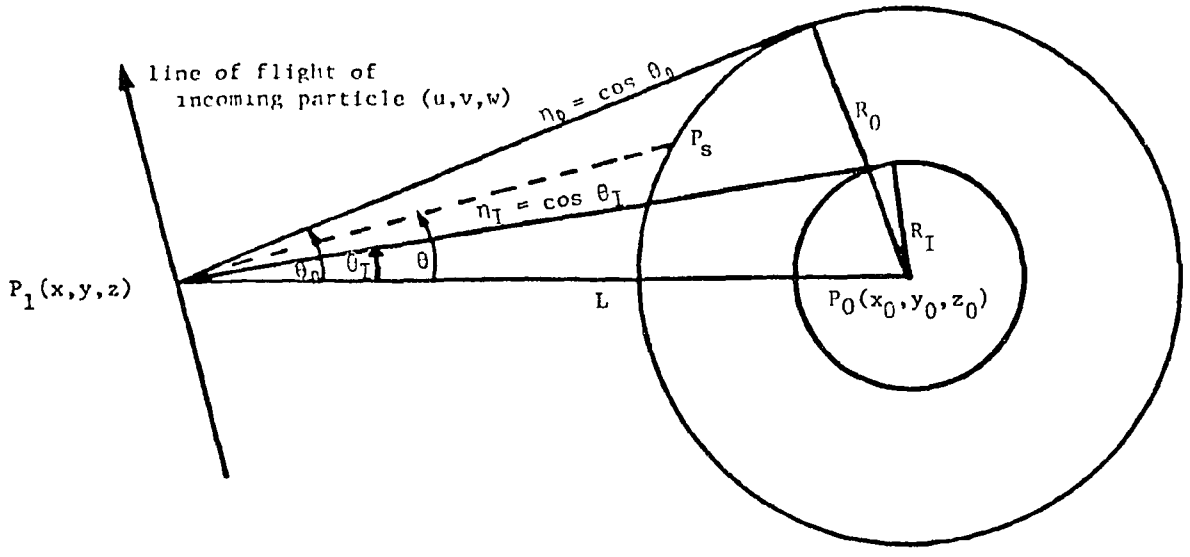

Fig. 3. The geometry of DXTRAN.

1. Sample η uniformly in $(\eta_I,1)$ with probability $Q(1-\eta_I)/[Q(1-\eta_I) + \eta_I-\eta_o]$; and with probability $(\eta_I-\eta_o)/[Q(1-\eta_I) + \eta_I-\eta_o]$ sample η uniformly in (η_o,η_I);

2. Having chosen θ from $\eta = \cos\theta$, we use the scattering formulas in the code to scatter through an angle θ (and an azimuthal angle ϕ chosen uniformly in $(0,2\pi)$) from the initial direction $\left(\frac{x_o-x}{L},\frac{y_o-y}{L},\frac{z_o-z}{L}\right)$, determining a new direction (u',v',w'). Advance the pseudo-particle in the direction (u',v',w') to the point P_s on the surface of the outer sphere. The new coordinates are saved;

3. The weight attached to the pseudo-particle is the weight of the particle at collision multiplied by

$$\nu \cdot \frac{P(\mu)\{Q(1-\eta_I) + \eta_I - \eta_0\} \exp\left\{-\int_{P_1}^{P_s} \Sigma_t(s)\,ds\right\}}{Q}, \quad \eta_I \le \eta \le 1$$

and

$$\nu \cdot P(\mu)\{Q(1-\eta_I) + \eta_I - \eta_0\} \exp\left\{-\int_{P_1}^{P_s} \Sigma_t(s)\,ds\right\}, \quad \eta_0 \le \eta < \eta_I ,$$

where

$\mu = uu' + vv' + ww'$

$P(\mu)$ = p.d.f. for scattering through the angle $\cos^{-1}\mu$ in the lab system for the event sampled at (x,y,z).

ν = number of neutrons emitted from the event.

Since a collision supplies a particle (let us now drop the term pseudo-particle - these particles are as real as any others) to the outer DXTRAN sphere, the particles from the collision at P_1 are picked up and followed further, but they are killed if they attempt to enter the sphere. It is apparent from the discussion above that this routine has certain features in common with a point detector routine.

This routine is used in a couple of the problems discussed below. In one problem, it is used to obtain the average flux in a small volume as a check against the result obtained from the OMCFE. In another, it is used to help get particles in the vicinity of a detector. While DXTRAN can be useful in many problems, it must be pointed out that the method is time-consuming, being similar in nature to a point detector routine. Further, attention must be paid to the problem of obtaining a sufficient number of histories in the vicinity of the DXTRAN sphere, not just inside the sphere.

CALCULATIONS

The problems discussed below were chosen to demonstrate the behavior of the OMCFE in a variety of settings, with some emphasis on the treatment of H and, in particular, its behavior in the presence of neutrons thermalized according to the free gas model. Illustrations of how DXTRAN can be useful, either as an aid to the OMCFE or as an aid in computing the average flux in a region with a track-length estimator, occur in two of the problems.

The geometries displayed in our problems are deliberately kept simple, partly so that we can display the so-called "exact flux", which is calculated very accurately (to a fraction of a percent) using a surface crossing estimator in the spherical geometry. In the schematics showing the geometry used, not every surface appears. Frequently, additional surfaces were added for the purposes of splitting and Russian roulette, or for the purpose of obtaining average flux in a region, but few surfaces were added in any one calculation.

In each problem, the source at the center of the sphere was chosen to be monoenergetic and isotropic in direction. As easily anticipated, it was found useful to use an exponential biasing to direct more particles toward the detectors. The latter were always placed on a radius of the sphere - say the positive x-axis. The initial flight of a neutron was chosen by sampling μ, the cosine of the angle the starting direction makes with the x-axis, from a p.d.f. $\sim e^{k\mu}$, with k a fixed parameter. The value of k used in each problem is listed on the schematic for that problem.

A feature of MCNP which was used in these calculations has to do with contributions to the detector D from collisions several free paths from the detector. E.g., when collisions occur more than x free paths from D, by playing Russian roulette one can permit, say, only one in ten collisions on the average to contribute to D, with weight enhanced by a factor of ten. The number x is set by the user and in these calculations was usually set to four. This feature of the code can save appreciable amounts of machine time in large systems.

Other information on the schematic which is of interest include the number density of atoms in the material used; the thermal temperature of the problem (if any); the average m.f.p. $\overline{\lambda}$, computed by MCNP over the course of the problem ; the source energy and energy cut-off (if any); the time on the CDC-7600 for a given sample of starting neutrons; and the imaginary sphere radii used in the OMCFE and in DXTRAN.

Figs. 4-12 display the geometries and graphs of the results for four problems. Table 1 gives a comparison of the final flux values at the end of each run with the "exact values". The errors in the final fluxes also appear.

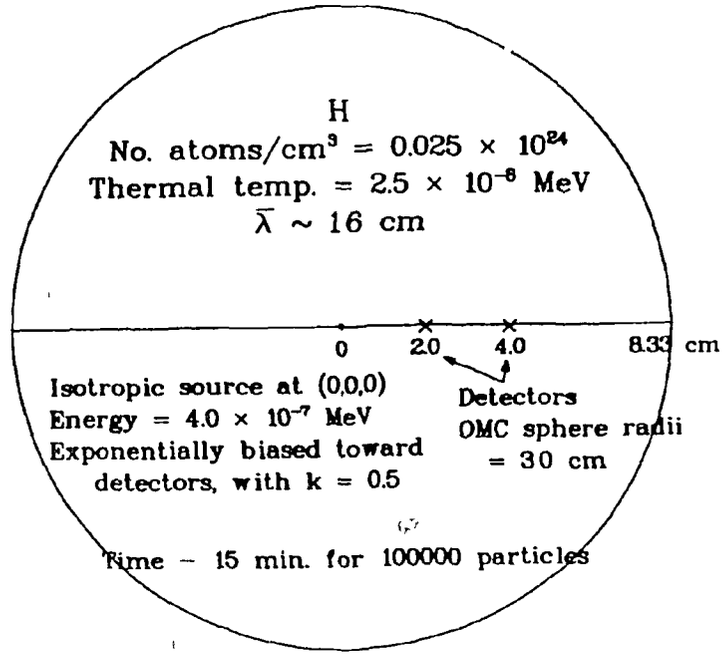

Fig 4 Geometry for Thermal Hydrogen Problem.

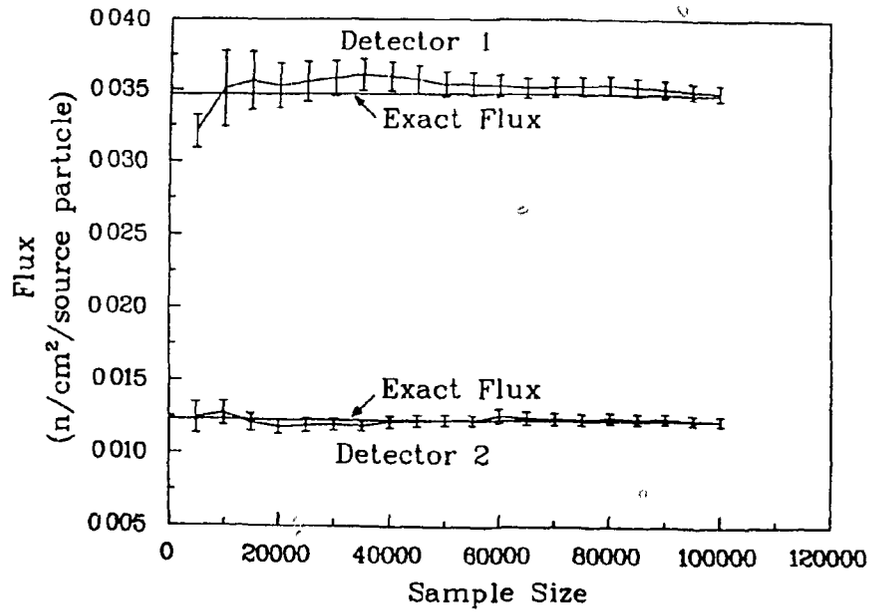

Fig. 5 Flux at Two Detectors in Thermal H with the OMCFE.

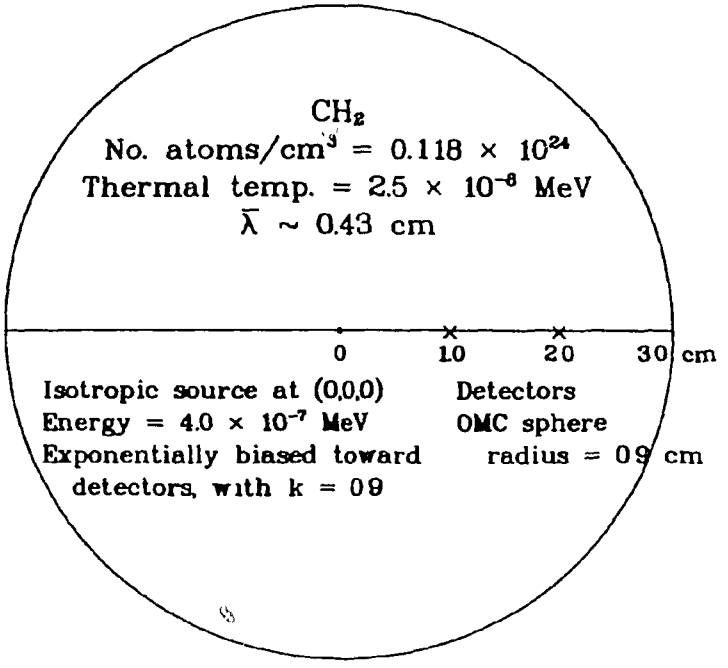

Fig. 6 Geometry for Thermal CH_2 Problem.

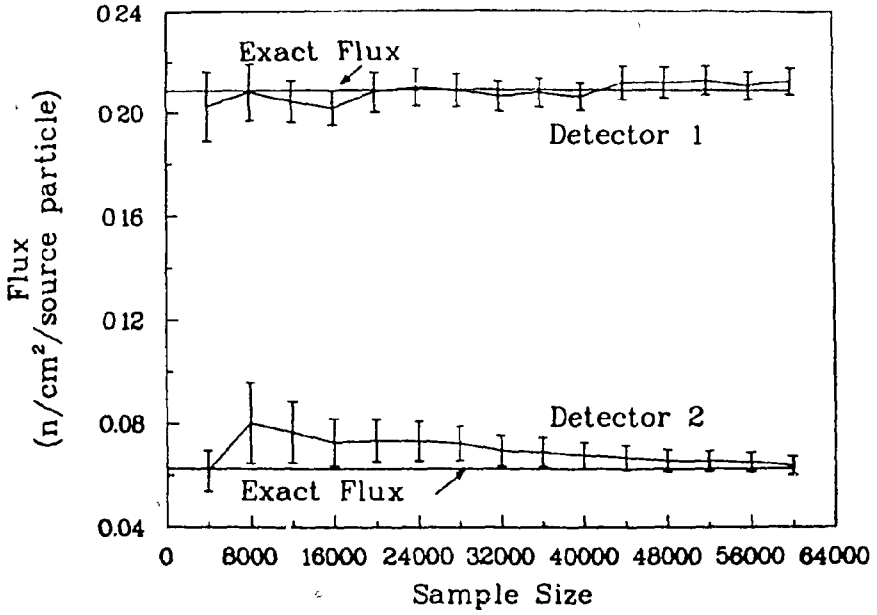

Fig. 7 Flux at Two Detectors in Thermal CH_2 with the OMCFE.

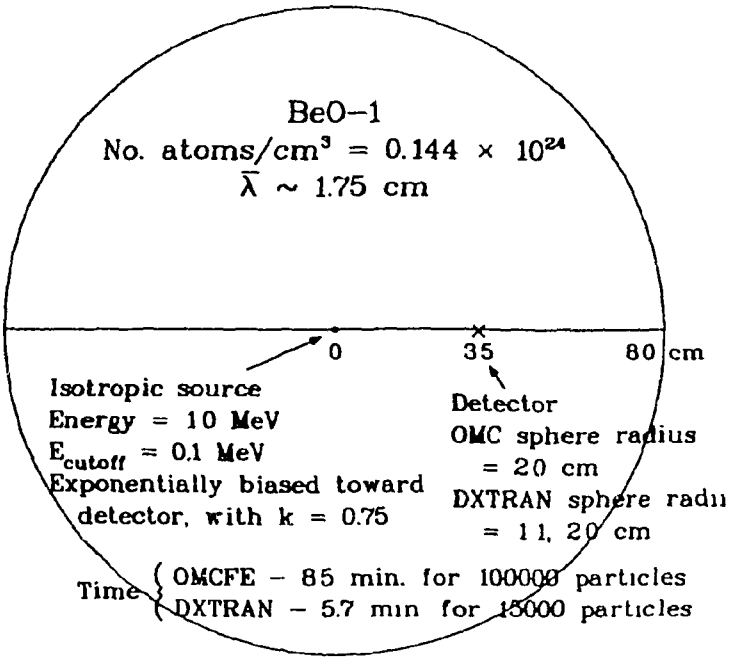

Fig. 8 Geometry for BeO–1 Problem

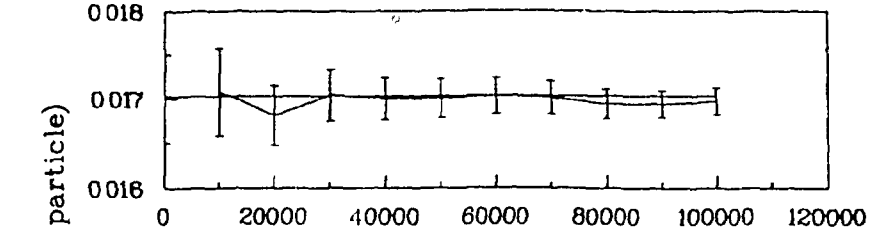

Fig 9 Flux at a Detector in BeO–1 with the OMCFE.

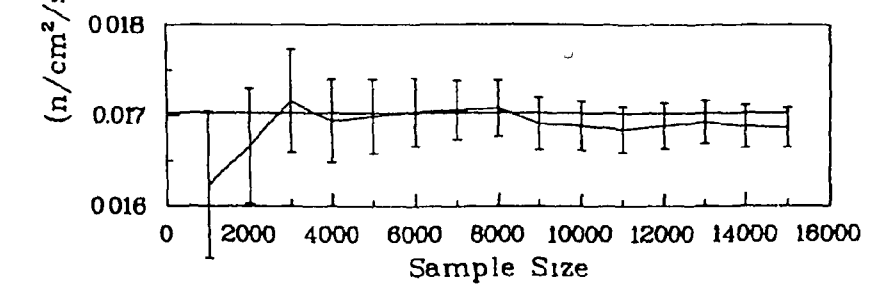

Fig. 10 Average Flux in the Vicinity of a Detector in BeO–1 Using DXTRAN.

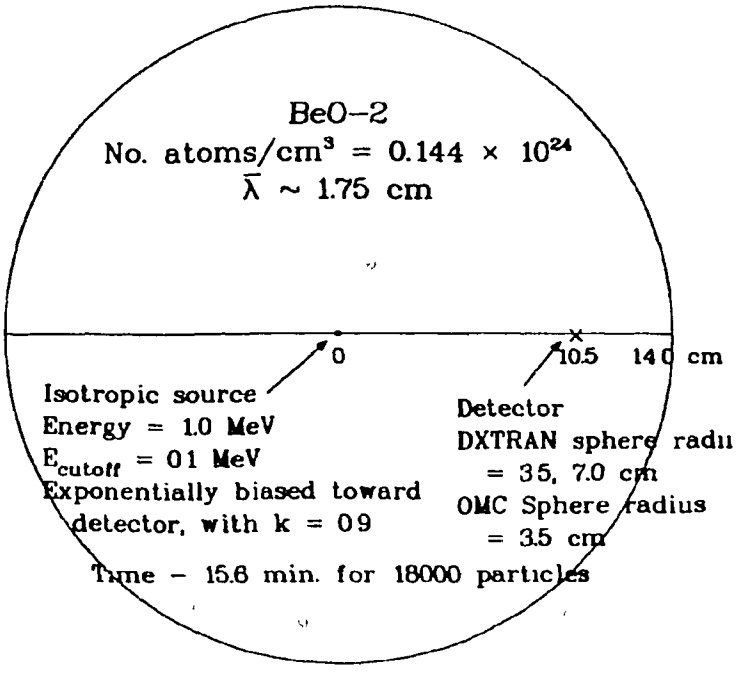

Fig. 11 Geometry for BeO–2 Problem

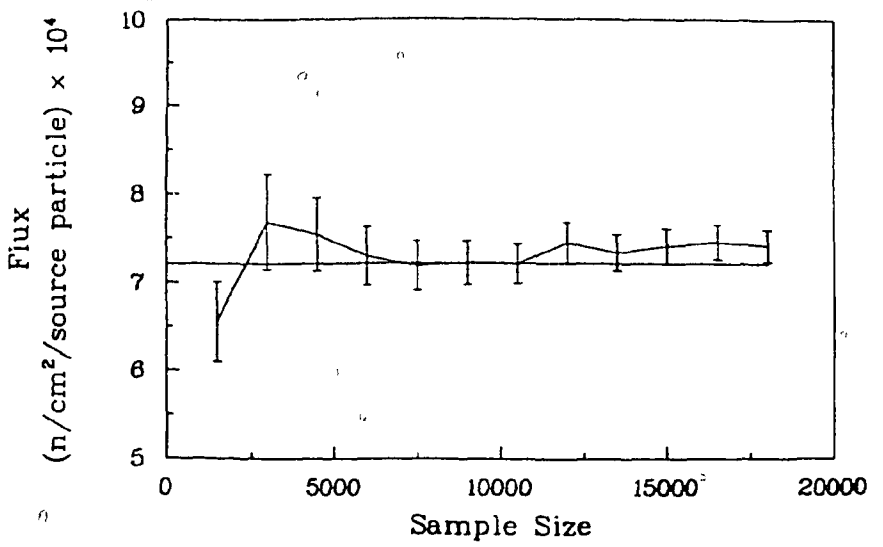

Fig. 12 Flux at a Detector in BeO–2 with the OMCFE and DXTRAN

TABLE I
Comparison of Calculated Flux with Exact Flux

		Flux (n/cm^2/source particle)			
		Exact (Surface Crossing Estimator)	OMCFE	Ave. Flux (Track Length Estimator)	Error (1 Standard Deviation)
Thermal H:	Detector 1	3.462×10^{-2}	3.486×10^{-2}		$.056 \times 10^{-2}$
	Detector 2	1.230×10^{-2}	1.231×10^{-2}		$.032 \times 10^{-2}$
Thermal CH_2:	Detector 1	2.086×10^{-1}	2.122×10^{-1}		$.053 \times 10^{-1}$
	Detector 2	6.259×10^{-2}	6.378×10^{-2}		$.357 \times 10^{-2}$
BeO - 1:	Detector 1	1.703×10^{-2}	1.697×10^{-2}		$.015 \times 10^{-2}$
	Detector 1	1.703×10^{-2}		1.687×10^{-2}	$.022 \times 10^{-2}$
BeO - 2:	Detector 1	7.207×10^{-4}	7.412×10^{-4}		$.185 \times 10^{-4}$

In Problem 1 the fluxes at two detector points in thermal H are calculated using the OMCFE. Problem 2 is a similar calculation in thermal CH_2. In Problem 3, the flux is calculated at a single detector in a sphere of BeO (non-thermal) for a source of 1 MeV neutrons at the center. The flux is first obtained using the OMCFE, and this is compared with an estimate of the average flux in a sphere about the detector of 1 cm radius. The latter estimate is obtained with the help of DXTRAN. Problem 4 finds the flux at a point in a BeO sphere situated approximately 6 free paths from the source using the OMCFE, but with the aid of a large DXTRAN sphere which encloses the detector. The error-bars (one standard deviation) on the points plotted indicate the statistical accuracy of the calculation in progress, as printed out by the code. The final results are, in every case, within a few percent of the value of the "exact flux" - in fact, the agreement appears somewhat better than expected in at least one case. For example, in the BeO-1 calculation the agreement between the exact flux and that obtained from the average flux in a sphere of 1-cm radius using DXTRAN is surprisingly good. Perhaps that is fortuitous - experience does not lead one to expect it in the average problem. The amount of computing time used could have been reduced in some cases without altering the results appreciably, but in dealing with estimates of flux at a point, it pays to be reasonably cautious. Quite frequently, the calculation is sensitive to the various parameters set in a problem - the size of the imaginary sphere in the OMCFE, the source bias, etc. Some care is essential in setting up a problem and a few short runs can be invaluable in making the necessary decisions, particularly in the case of a difficult problem.

Concluding Remarks

A very important method of estimating flux at a point in a problem with axial symmetry is through the use of a ring detector. MCNP contains a ring detector option and, although we did not use it in the present calculations, it should be mentioned as one of the tools available.

While the OMCFE in MCNP can deal with neutrons thermalized according to the free gas model, there remains the task of modifying the flux estimator to be compatible with neutrons thermalized with the $S(\alpha,\beta)$ treatment. It is hoped that this defect can be rectified in the not too distant future.

REFERENCES

1. H. J. Kalli and E. D. Cashwell, "Evaluation of Three Monte Carlo Estimation Schemes for Flux at a Point," Trans. Am. Nucl. Soc. 27, 370-371 (Nov. 27-Dec. 2, 1977). Also, Los Alamos Scientific Laboratory Report LA-6865-MS (September, 1977).

2. M. H. Kalos, "On the Estimation of Flux at a Point by Monte Carlo," Nucl. Sci. Eng. 16, 111-117 (1963).

3. H. A. Steinberg and M. H. Kalos, "Bounded Estimators for Flux at a Point in Monte Carlo," Nucl. Sci. Eng. 44, 406-412 (1971).

4. H. A. Steinberg, "Bounded Estimation of Flux-at-a-Point for One or More Detectors," Proc. NEACRP Meeting of a Monte Carlo Study Group, Argonne National Laboratory, July 1-3, 1974.

5. LASL Group X-6, "MCNP - A General Monte Carlo Code for Neutron and Photon Transport," Los Alamos Scientific Laboratory Report LA-7396-M, Revised Manual (November, 1979).

Blank

DEEP-PENETRATION CALCULATIONS

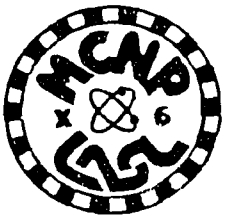

W. L. Thompson
O. L. Deutsch
T. E. Booth
Group X-6
Monte Carlo, Applications and Transport Data Group
Theoretical Applications Division
Los Alamos Scientific Laboratory
Los Alamos, New Mexico 87545

ABSTRACT

Several Monte Carlo techniques are compared in the transport of neutrons of different source energies through two different deep-penetration problems each with two parts. The first problem involves transmission through a 200-cm concrete slab. The second problem is a 90° bent pipe jacketed by concrete. In one case the pipe is void, and in the other it is filled with liquid sodium.

Calculations are made with two different Los Alamos Monte Carlo codes: the continuous-energy code MCNP and the multigroup code MCMG. With MCNP, several techniques and combinations are evaluated: analog Monte Carlo, geometry splitting with Russian roulette, the exponential transformation, a weight window (constraining the upper and lower particle weights to be within certain limits), and using a combination of random walk/deterministic schemes. With MCMG, a comparison is made between continuous-energy and multigroup Monte Carlo and also between different multigroup scattering models (including the one used by the MORSE code).

Several unexpected results were found in the comparisons of the various calculations. For example, compared to continuous-energy calculations, multigroup calculations with standard cross-section weighting (for both Monte Carlo and S_n) underpredict the neutron leakage transmitted through the 200-cm concrete slab by a factor of four.

When considering different techniques for reducing the product of variance and computing time with regard to ease of use, reliability, and effectiveness, we find geometric splitting with Russian roulette to be a superior technique. The weight window, however, appears to be more effective than originally anticipated.

INTRODUCTION

Several Monte Carlo techniques are compared in the transport of neutrons of different source energies in two different deep-penetration problems. The first problem involves transmission through a 200-cm-thick concrete slab. The second problem is a 90° bent pipe jacketed by concrete. In one case the pipe is filled with liquid sodium, and in another case it is void.

In actual shielding applications, one might need to account for photon production and transport, streaming paths, the exact compositions of the shielding material including rebar, and other factors depending on the problem. For example, for 14-MeV neutrons incident on 200 cm of concrete, Oak Ridge concrete reduces the transmitted dose by a factor of ten better than does Los Alamos concrete. All the above considerations, however, are beyond the scope of this paper.

Rather than addressing particular and detailed shielding problems, the purpose of this paper is to apply different Monte Carlo techniques to problems of general interest to the shielding community and to compare the merits of the techniques. The problems considered here have nontrivial attenuations, and an attempt has been made to select representative features of real shielding problems without incorporating arbitrary or extraneous detail. In addition to a comparison of methods, results such as leakage, flux, and dose rate are presented, and we believe these results to be reliable. Doses throughout this paper refer to biological dose and were obtained with the ANSI[1] flux-to-dose conversion factors. By providing these benchmark-type results, others may wish to compare results from the same problems using different calculational tools. Interesting comparisons could be then made in terms of accuracy and efficiency between MCNP and other Monte Carlo codes (such as MORSE, TRIPOLI, or SAM-CE) and other calculational techniques such as S_n or hand calculations using buildup factors.

Basically, several techniques such as the exponential transformation and geometrical splitting with Russian roulette will be compared using the continuous-energy code MCNP[2] with virtually no approximations, MCNP with a pseudo-multigroup set of cross sections, and a true multigroup version of MCNP called MCMG.[3] All calculations done with MCMG are with 30 neutron energy groups. MCMG has the option to represent the distribution of scattering angles for group-to-group transfers by equiprobable cosine bins or by MORSE-type discrete scattering angles.[4] The pseudo-multigroup cross-section set in which the reaction cross sections have been collapsed into 240 energy groups for use with MCNP is referred to as the discrete-reaction data (DRXS). More details can be obtained about MCNP and MCMG in another paper by Thompson and Cashwell given at this seminar.

The amount of computer memory required for cross-section data for the ten constituents of ordinary Portland concrete is given in Table 1 as a function of calculational method, data set, and energy range.

About six hours of CDC-7600 computer time were used for the calculations reported in this paper. The multigroup calculations were done by Deutsch, Booth did the calculations with the exponential transformation and the weight window, and the rest of the calculations were done by Thompson.

Table 1. Neutron Cross-Section Storage for Portland Concrete

Mode	$Words_{10}$
MCNP, ENDF/B-V 20 MeV < E < 0.00912 MeV	297462
MCNP, ENDF/B-IV 20 MeV < E < 0.00912 MeV	133091
MCNP, DRXS (ENDF/B-IV) 20 MeV < E < 0.00912 MeV	42952
MCMG, 30 group 20 MeV < E < 10^{-4} eV	23000
MCNP, ENDF/B-V 20 MeV < E < 10^{-5} eV	310621
MCNP, ENDF/B-IV 20 MeV < E < 10^{-5} eV	139316
MCNP, DRXS (ENDF/B-IV) 20 MeV < E < 10^{-5} eV	45852
MCNP, ENDF/B-V 184 keV < E < 8.32 eV	56161

All calculations for this paper were done with ordinary Portland concrete as found in Schaeffer's book.[5] One calculation (the pencil-beam fission spectrum incident on a 100-cm-radius, 200-cm-thick concrete disk) was also done with the 04 concrete from the ANSI standard.[6] The compositions of these two concretes are listed in Table 2. The transmitted dose through the 04 concrete is 4.7 times higher than through the ordinary Portland concrete, while the transmitted leakage and flux are each about 5.2 times higher (these results are within 5%). All following reported results will be with ordinary Portland concrete.

Table 2. Concrete Compositions

Element	04 Wt.%	Portland Wt.%
H	0.56	1.00
O	49.81	52.9
Si	31.51	33.7
Ca	8.29	4.4
C	--	0.1
Na	1.71	1.6
Mg	0.26	0.2
Al	4.57	3.4
S	0.13	--
K	1.92	1.3
Fe	1.24	1.4
	ρ=2.339 g/cc	ρ=2.30 g/cc

All continuous-energy calculations were done with ENDF/B-V cross sections. However, the first problem that will be discussed, the pencil-beam fission spectrum incident on 100-cm-radius by 200-cm-thick concrete, wasalso done with ENDF/B-IV cross sections. There were no perceivable differences in any of the results. The Monte Carlo multigroup calculations were done with ENDF-IV cross sections. If calculations had been made involving heating or photon production, this conclusion of equality between IV and V may not have been true. Again, it is not the purpose of this paper to compare cross sections; this has been extensively done at Los Alamos[7,8] and elsewhere by others.

With regard to the use of different Monte Carlo techniques on a variety of applications, there are no universally valid prescriptions. The only truly effective rule of thumb is to always make two or three short, experimental runs (say of half a minute each) to help discover the characteristics of the particular problem and the effect of varying a parameter or two in a particular variance-reduction technique. There is no substitute for practical experience to guide the approach to a particular problem. What works in one situation in no way guarantees success in another situation and may even be harmful. A good Monte Carlo code should provide a variety of standard summary and diagnostic information to help understand what is happening in a given problem. In doing the calculations for this paper, we encountered some surprises to our intuition. However, short, preliminary runs provided the necessary insight for the final runs.

Finally, before getting down to business, comparisons between the various techniques will be done on the basis of a relative figure of merit, FOM = $1/(\sigma^2 t)$ where σ is the standard error associated with a result of the

calculation and t is the computer time required. For example, if it took 30 minutes to get a 4% error, 20.8 is the figure of merit. Note that to compare your FOM to the ones reported in this paper, you will also need to factor in the speed of your computer system relative to ours. All calculations reported by us were done on a CDC-7600 computer. All reported errors represent one standard deviation. Note that there is also an error associated with the figure of merit, a variance of the variance. In the following calculations, we attach no significance to small differences in the FOM such as between 62 and 55.

The factor $\sigma^2 t$ is directly related to the dollar cost of running a job. It is important to note that the cost depends both on σ^2 and t; for example, you may reduce σ^2 but only at a greater expense in t or vice versa; the product of the two must be reduced to be beneficial. Not explicit in this relation for the total cost of a job is the cost in human time to set a job up and the cost of the preliminary experimental runs to set the parameters. If you spend three days with an elaborate setup and five hours of computer time refining and optimizing the parameters in the best possible way so that your job runs in 10 minutes rather than 20, you have lost. In all the following calculations, we usually made two or three preliminary runs for about a half minute each. We make no claim that our setups and figures of merit are the best, but they are acceptable as being cost-effective. Undoubtedly, someone can make improvements but probably not without diminishing returns.

VARIANCE-REDUCTION TECHNIQUES

The successful application of the Monte Carlo method to any deep-penetration problem generally requires the use of one or more variance-reduction techniques. In general, one can expect that some techniques or combinations of techniques will be more effective than others in terms of range of applicability, ease of use, reliability, and performance. We measure performance in terms of the figure of merit $1/(\sigma^2 t)$. By reliability, we refer to the possibility of injudicious selection of the parameters of a technique resulting in erroneous answers because an important part of phase space may not have been sampled adequately, if at all. Finally, ease of use refers to the degree of difficulty in determining the parameters of a technique and to the sensitivity of performance to precise selection of the optimal parameters.

Based on many years of experience and observations of users at Los Alamos, the most frequently-used techniques at Los Alamos are geometry splitting with Russian roulette, directional source biasing, survival biasing, and a weight-cutoff game incorporating Russian roulette. These techniques are frequently used in combination. It is assumed that if nenrgy and/or time cutoffs are appropriate for a problem, then they have been used also. The exponential transformation is infrequently used, and in fact, we have discouraged its use. We note all too frequently that the less experience a user has, the more any of the variance reduction

techniques are abused by using the techniques inappropriately, or with several techniques in conjunctionleading to conflicts, or most commonly by biasing too heavily. Any of these problems can result in a wrong answer. It cannot be overemphasized that any variance-reduction technique must be used with caution and understanding.

In the following calculations, several different techniques are tried and compared. For all problems, we compare geometry splitting with Russian roulette, the exponential transformation, a weight window, and DXTRAN. The effect of running the problems in a purely analog fashion will also be illustrated. Other techniques will also be tried but not for all cases. A short description will be given for the main techniques used in these calculations.

A more detailed description can be found in Ref. 2.

Geometry Splitting with Russian Roulette

MCNP does not split particle tracks upon collision but as a function of spatial location. The geometry is subdivided into several cells, and each cell is assigned an importance. When a track of weight W passes from a cell of importance I to a cell of higher importance I', the track is split into I'/I tracks, each of weight WI/I'. (Non-integer splitting is allowed, but we will consider only integral importance ratios for simplicity.) If a track passes from a cell of importance I' to a cell of lower importance I, Russian roulette is played; a track survives with frequency I/I' and is assigned a new weight of WI'/I if it survives. Generally, the source cell has importance of unity, and the importances increase in the direction of the tally. The importances are chosen to keep the track population roughly constant between the source and the tally.

Weight Cutoff with Russian Roulette

The weight cutoff is made relative to the ratio of the importance of the source cell to the importance of the cell where weight-cutoff is about to take place. This keeps the geometry-splitting and weight-cutoff games from interfering. If a track's weight falls below quantity WC2 (usually from survival biasing), Russian roulette is played. A track survives with frequency WC2/WC1 and is assigned the weight WC1 if it survives. WC1 and WC2 are generally chosen to be 0.5 and 0.25, respectively, for a starting weight of unity but are problem-dependent.

Exponential Transformation

This technique allows a track to move in a preferred direction by artificially reducing the macroscopic total cross section in the preferred direction and increasing the cross section in the opposite direction according to

$$\Sigma_{ex} = \Sigma_t(1 - p\mu) \quad , \tag{1}$$

where

Σ_{ex} = transformed total cross section,
Σ_t = true total cross section,
p = parameter used to vary degree, of biasing, $0 \leq p < 1$, and
μ = cosine of angle between preferred direction and track's velocity.

Upon collision, the track weight is multiplied by

$$w_c = \frac{e^{-p\Sigma_t \mu s}}{1 - p\mu} ,$$

where s is the distance to collision. Note this can lead to a dispersion of weight, and that it is possible for some weights to become very large if the tracks are traveling opposite to the preferred direction.

We have found the exponential transformation by itself to be of limited use. The dispersion of weights that it creates can result in an unreliable sample mean while the sample variance may erroneously indicate an acceptable precision. Furthermore, it is not clear how to choose the biasing parameter p, but we note that it is generally chosen too high - especially by novice users. For the calculations of this paper, the parameter was selected by observing the sample variance as a function of the parameter on a few short runs.

When combined with a weight window to place a bound on the upper and lower weights of tracks, we have found that the exponential transformation can be useful. However, choosing parameters for the weight window can further complicate the problem setup, especially for the inexperienced user.

Weight Window

A weight window consists of an upper and a lower bound for a particle's weight. If the track weight is less than the lower weight bound, Russian roulette is played and the weight is increased to lie inside the window or the track is killed. If the track weight is above the upper bound then the track is split so that the resulting tracks have their weights within the window. The bounds of the window can be set as a function of energy and spatial position.

This weight-window capability is presently not a permanent feature of MCNP. It is available as a modification and is under evaluation by Group X-6. Among other things, we are trying to learn how to use it. It appears that this technique has merit not only when used with the exponential transformation but in conjunction with other techniques. The bane of any variance-reduction technique is creating a dispersion of weights and especially creating a few tracks with very large weights. The weight window appears to reduce these problems effectively.

DXTRAN

In a geometry region which is difficult to sample adequately, the DXTRAN scheme of MCNP can be of value. At each collision, contributions of scattered particles are deterministically transported to a spherical neighborhood of interest. These contributions, or pseudo-particles, are placed on a sphere surrounding the neighborhood of interest and then transported in the ordinary random-walk manner. The parent particle giving rise to the pseudo-particle at a collision continues its random walk, but it is killed if it tries to enter the neighborhood during its random walk.

There are actually two DXTRAN spheres. The pseudo-particles are placed on an outer sphere. An inner sphere concentric to the outer one is used to bias the placement of pseudo-particles within the cone defined by the inner sphere and the point of collision.

DXTRAN has certain features in common with a point detector. It also has the disadvantages of a detector: it can significantly increase computation time, and it is susceptible to large-weighted contributions. For these and other reasons, success is not guaranteed when using DXTRAN, and it (like a detector) should be used selectively and carefully.

A useful feature of MCNP is the DD input card. This provides diagnostics pertaining to DXTRAN or point detectors such as the accumulative fraction of the number of contributions, the fractional contribution, and the accumulative fraction of the total contribution - all as a function of mean free path away from the DXTRAN sphere or detector. Having this information from a short run, Russian roulette can be played on contributions a selected number of mean free paths away. This can save substantial computer time.

Angle Biasing

Angle biasing for the problems of this paper was not applied for two reasons: (1) our experience with angle-biasing techniques is both limited and discouraging, and (2) angle biasing is not a standard MCNP option. We have experience with sampling two different (fictitious) exit densities, namely

$$p_1(\Omega) = \frac{1 + bv}{4\pi} = \text{probability of sampling a unit solid angle about } u,v,w \quad |b| \leq 1 \tag{3}$$

and

$$p_2(\Omega) = \frac{be^{bv}}{e^{b} - e^{-b}} \frac{1}{2\pi} = \text{probability of sampling a unit solid angle about } u,v,w \quad b > 0. \tag{4}$$

Both of these schemes seem to introduce a large variation in particle weights which is reflected in a poor variance of the sample mean. Use of weight window improves the variance, but only to the point where the variance matches that of the weight window alone.

It is entirely possible that other angle-biasing schemes may perform much better. In particular, angle-biasing schemes in discrete-angle Monte Carlo codes (such as TRIPOLI) can be easily fabricated to avoid large variations in particle weights. This does not appear to be the case in continuous-angle Monte Carlo codes (such as MCNP).

CONCRETE-SLAB PROBLEMS

A major advantage of Monte Carlo is the ability to calculate with no compromise in geometrical reality. Since the purpose of this paper is to illustrate some variance-reduction techniques, this advantage plays no role in this particular problem. S_n is more appropriate for this problem - but at the possible expense of getting the wrong answer because of the multigroup approximation (as will be seen later in this paper).

This problem consists of two parts. Both parts consist of a 200-cm-long homogeneous cylinder of ordinary Portland concrete with a pencil-beam source of fission-spectrum neutrons incident along the axis. In one case the radius of the cylinder is 100 cm, and in the other the radius of the cylinder is 20 cm. The object is to tally the net neutron leakage (or current) across the face opposite the source for comparison of all the methods. However, the transmitted flux and biological dose were also calculated by MCNP. The geometry of both cases is illustrated in Fig. 1.

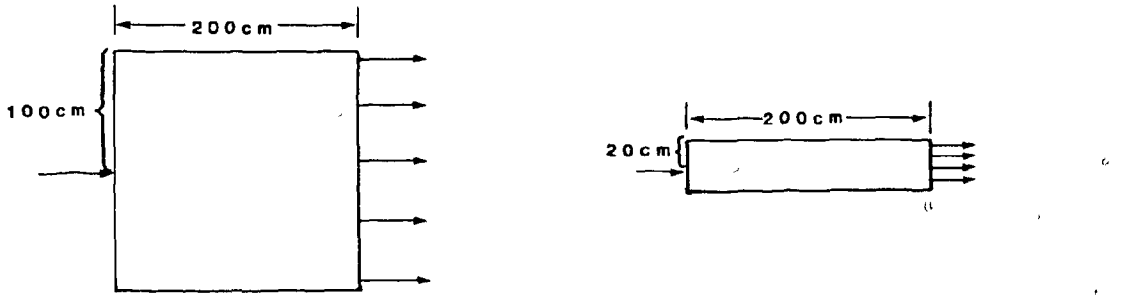

Figure 1. Concrete Slab Problems.

The source energy spectrum is defined according to the Maxwellian representation of the fission spectrum:

$$f(E) = \frac{2}{\sqrt{\pi}T}\sqrt{\frac{E}{T}}\, e^{-E/T} \quad , \tag{5}$$

where we have chosen the parameter T = 1.30 MeV that produces an average source energy of 1.95 MeV. A prescription that was used to sample from

this spectrum for MCNP is in the Appendix. For the multigroup calculations with MCMG, the spectrum was analytically integrated to determine the group sources:

$$\int_{E_{g+1}}^{E_g} f(E)\,dE = \frac{2}{\sqrt{\pi}}\left[\sqrt{\frac{E_{g+1}}{T}}\,e^{-E_{g+1}/T} - \sqrt{\frac{E_g}{T}}\,e^{-E_g/T}\right] + \left[\operatorname{erf}\left(\sqrt{\frac{E_g}{T}}\right) - \operatorname{erf}\left(\sqrt{\frac{E_{g+1}}{T}}\right)\right] \quad . \tag{6}$$

The group sources are listed in the Appendix.

A short adjoint run with MCMG plus an S_n calculation indicated that source particles below 3.68 MeV (this corresponds to one of the multigroup boundaries) made few tally contributions. More precisely, about 10% of the transmitted leakage results from source neutrons below 3.68 MeV. Therefore, the source spectrum was sampled for energies only above 3.68 MeV. These high-energy-source particles account for 12.929% of the total source particles in the unaltered spectrum. Therefore, all results were multiplied by 0.12929 to normalize to one total source neutron. By biasing the source in this manner, the figure of merit for MCNP calculations increased by a factor of two.

For the 3.68-MeV truncated fission spectrum, 200 cm of concrete is about 25 mean free paths thick; for the full, unaltered spectrum, the 200-cm-slab is about 28 mean free paths. In the first 10 cm, the average mean free path is about 6 cm. After only a few more centimeters into the concrete though, the average mean free path becomes about 4.5 cm and remains very close to this throughout the 200-cm thickness. The energy cutoff for the calculations was set at 0.00912 MeV (again this corresponds to one of the group boundaries) because only a couple of percent of the transmitted neutron dose comes from transmitted neutrons with an energy less than this. Using this cutoff increases the figure of merit by a factor of about three. There are 18 groups in the multigroup data above 0.00912 MeV. Furthermore, this energy cutoff requires a smaller computer-memory requirement.

To illustrate the effect of the above energy cutoffs and photon production and that the simplification for this academic paper may not be valid for actual shielding problems, MCNP was used for a 10-minute calculation with none of the above cutoffs and also accounted for photon production for a 100-cm radius by only a 100-cm-thick concrete slab. The figure of merit for the total neutron dose is 8.6 using splitting, and the total neutron dose is $8.1 \times 10^{-13} \pm 8.5\%$ mrem/source neutron. The dose from transmitted neutrons above 0.01 MeV is 7.5×10^{-13}, and the total photon dose is $1.7 \times 10^{-13} \pm 8.5\%$ mrem per source neutron. About 49% of the photons were started in the energy range 2-5 MeV, 2.7 MeV of photon energy were started on the average per neutron, and the average weight of photons started was 0.87 per neutron. Another run was made but with the neutron energy cutoff at 0.01 MeV. The figure of merit increased to about 56, the total neutron dose became $7.2 \times 10^{-13} \pm 6\%$, and the photon dose dropped to $2.6 \times 10^{-15} \pm 18\%$. Now about 14% of the photons start between 2 and 5 MeV,

0.24 MeV of photon energy were started per neutron, and the average weight of photons started was 0.14 per neutron. For 14-MeV neutrons incident on 100 cm of concrete and using no cutoffs or approximations, about 8% of the total dose comes from photons.

100-cm-Radius Problem

With the pencil-beam source, the axially penetrating leakage is $8.2 \times 10^{-9} \pm 4.4\%$, the transverse leakage is 1.9×10^{-5}, and the backscatter leakage is about 35%. Because of the negligible transverse leakage, the problem geometry is equivalent to a homogeneous, semi-infinite slab. About 9.5% of the neutron weight is lost to capture.

In a purely analog case (no splitting, survival biasing, or anything else), except for source energies greater than 3.68 MeV, 21484 source neutrons were started in two minutes of computer time. At 50 cm there were 5409 (25%) neutrons, 83 were at 100 cm, and none were at 150 cm. This is a very clear example of why variance-reduction techniques are necessary.

Adding survival biasing and weight cutoff with WC1 = 0.5 and WC2 = 0.25 to the above example, a slight improvement is noticed in the same two minutes of time: 19336 source particles were reduced to 5477 (28%) at 50 cm, to 102 at 100 cm, and to none at 150 cm. Only three tracks were lost to the Russian roulette part of the weight cutoff game. With WC1 and WC2 increased to 1.0 and 0.5 respectively, 19432 source particles were reduced to 5461 (28%) at 50 cm, to 106 at 100 cm, and to none at 180 cm. Only 121 tracks were lost to Russian roulette. In this problem survival biasing and weight cutoff help a little but not a significant amount. It is a generally accepted practice, however, to use these two techniques routinely (naturally there are exceptions).

To add geometry splitting with Russian roulette, the concrete cylinder was subdivided axially into cells 10-cm-thick by adding plane splitting surfaces; 10 cm was chosen because it is a convenient number and because it allows a couple of mean free paths between splitting surfaces (based on an average of 4.5 cm for a mean free path averaged over collisions). Cell thicknesses of 15 cm worked equally well. The problem was run for half a minute with the importances of all cells set to unity. Part of the standard summary output of MCNP is the track population in each cell, and wherever the population dropped by a factor of two, the importance of that cell was doubled relative to the adjacent cell in the direction of the source. In some places the two-for-one splitting was not enough, so four-for-one splitting was occasionally used. If an incremental cell thickness less than 10 cm had been chosen, two-for-one splitting could have been used throughout. Conversely, greater than 10-cm increments would have led to a more consistent use of four-for-one splitting. A goal is to try to keep the population roughly constant, say within 50%.

For this particular problem, there appears to be little difference in computer efficiency between two-for-one and four-for-one splitting. Other ratios can also be used as necessary. Two-for-one splitting makes it

easier to level the population, but it requires the user to add more cells and surfaces to the problem setup. Four-for-one splitting requires less input from the user and less arithmetic for the computer, but it is harder to level out the population. Going beyond four-for-one splitting introduces greater risk because that implies a fairly large reduction in the population before it is built back up. The danger is that once a sample population deteriorates to a small size, source information associated with the sample can be lost. Once information is lost, it can never be regained. For example, in the analog problem mentioned earlier, at 170 cm we could have introduced the first splitting surface and split 21484-for-one. The track population would be back to its original size, but then the true energy spectrum would be represented by one discrete energy. The old saying about squeezing blood out of a turnip is very appropriate here.

Three iterations of half a minute each were used to set the importances. The ratio of importances between cells, the actual importance assigned to a cell, and the track population in each cell are shown in Table 3 for 91440 source neutrons. In this final run, weight cutoff was played with WC1 = 0.5 and WC2 = 0.25 (both times the starting weight of the neutrons), resulting in 4233 tracks lost to Russian roulette. In the splitting game, 1118990 tracks were created, but 460729 were lost to Russian roulette. Note that in cell 18 the population is too high.

Table 3. Splitting in the 100-cm-Radius by 200-cm-Thick Concrete Problem

Cell		Importance Ratio	Importance	Track Population
(Source)	1	1	1	94215
	2	1	1	69498
	3	2	2	86168
	4	2	4	86972
	5	2	8	82441
	6	2	16	78332
	7	4	64	140593
	8	2	128	118175
	9	2	256	101254
	10	2	512	86628
	11	2	1024	75750
	12	4	4096	127292
	13	2	8192	102290
	14	2	16384	89215
	15	4	65536	151848
	16	2	131072	123118
	17	2	262144	107322
	18	4	1048576	180848
	19	2	2097152	142741
(Tally)	20	2	4194304	109876

For this problem the transmitted leakage is $8.21 \times 10^{-9} \pm 4.4\%$ for neutron leakage, the transmitted dose is $1.22 \times 10^{-17} \pm 4.5\%$ mrem per source neutron, the transmitted flux is $4.10 \times 10^{-13} \pm 4.3\%$ neutrons/cm^2, the leakage escaping through the curved cylindrical surface is $1.91 \times 10^{-5} \pm 16\%$ neutrons, the backscattered leakage is $4.51 \times 10^{-2} \pm 0.4\%$, and 6.7 is the figure of merit.

Other splitting games can also be played. The most obvious is a combination of axial and radial splitting. With radial splitting, one could set up a cone as a splitting surface with its vertex at the source point and then intersecting the edge of the exit face. Secondly, rather than a cone, a concentric cylinder could be used with its radius half that of the outer cylinder. It turns out that neither of these approaches results in much (if any) gain in this problem. What small amount is gained in reducing σ^2 is lost by an increase in t because of the added arithmetic for the computer.

There is a frequently-heard rule of thumb for geometry splitting that says split two-for-one every mean free path, but you do not hear if this means a mean free path based on source energy or average energy of the particles in the geometry. In this problem, a mean free path based on a source energy is about 8 cm and about 4.5 cm averaged over collisions. Splitting two-for-one every 4.5 cm in only a 100-cm-thick slab of concrete, 1 source neutron had been split into a population of 440 at 50 cm and 12740 at 100 cm and required 0.96 minutes of computer time. Splitting two-for-one every 8 cm in a similar 100-cm-thick slab of concrete was better; 335 source neutrons required 0.52 minutes of computer time and were split into a population of 1597 at 50 cm and 1904 at 75 cm. Obviously, this rule of thumb applied by either method leads to oversplitting.

Using the weight window with only survival biasing and nothing else, the transmitted leakage is $8.26 \times 10^{-9} \pm 9.3\%$ with 6.3 for a figure of merit. The lower weight bound in the source cell was chosen to be 50% lower than the particles' source weight. The lower weight bound for the rest of the cells was chosen to be a factor α less than the previous cell's lower weight bound where α for cell i was chosen as

$$(\text{starting weight})\alpha^i = \text{transmission obtained by previous short run.} \qquad (7)$$

The upper weight bound was chosen to be five times the lower weight bound.

Using the exponential transform with survival biasing, no weight-cutoff game, and a transform-biasing parameter of 0.7, only a very short run was required to see a poor performance. The figure of merit was 1.5, and the transmitted leakage was $4.86 \times 10^{-8} \pm 39\%$ which is too high by a factor of six - in other words, completely unreliable.

Adding to the exponential transformation a weight-cutoff game (but not the weight window) that is dependent on cell importances had the result that after 4.6 minutes of computer time the transmitted leakage was

$5.22 \times 10^{-9} \pm 19.2\%$ with a figure of merit of 4.2; after 10 minutes, $8.22 \times 10^{-9} \pm 26.7\%$; and after 17.6 minutes the leakage was $8.06 \times 10^{-9} \pm 18.4$ with 1.7 as the figure of merit. This example demonstrates the value in watching the behavior of a sample mean and its variance during the progress of a calculation. If either is unstable, the sample mean is unreliable. By not watching this behavior, a result (such as the leakage of 5.22×10^{-9}) may be incorrectly accepted as satisfactory based on an apparently low variance.

Applying the weight window and exponential transformation together produced the best of all results with a figure of merit of 22.6 and a transmitted leakage of $8.49 \times 10^{-9} \pm 3.0\%$.

The multigroup code MCMG using 30 groups and geometry splitting determined in the same manner as for MCNP was used on this problem. The figure of merit was 11.9, but the transmitted leakage was $2.17 \times 10^{-9} \pm 5.6\%$ which is low by a factor of four. Both the continuous-scattering angle and MORSE discrete-scattering angle treatments were used. No difference between the two was observed. For optically thin transmissions, however, the continuous treatment is superior.

MCNP itself can be used in a pseudo-multigroup fashion by using our discrete reaction cross-section set DRXS. These cross sections are equivalent to the regular continuous-energy cross sections used by MCNP except that the reaction cross sections have been collapsed into 240 energy groups. Using MCNP and these discrete cross sections along with geometry splitting on this problem, the transmitted leakage is $5.08 \times 10^{-9} \pm 6.8\%$ with 8.0 for the figure of merit.

All of these results are summarized in Table 4.

To our surprise, the performance of the weight window may be relatively insensitive to the size of the window. This problem was tried with the ratio of the upper to lower bound set at 400 to compare with the ratio of 5 used throughout this paper. The factor of 400 is consistent with a similar scheme used in MORSE. The results were virtually unchanged; the figure of merit was 19.5 and the leakage was $7.89 \times 10^{-9} \pm 10.6\%$. This implies that it is a very few tracks with very large weights that cause tallying problems. The problems caused by a weight dispersion have long been recognized, but the true nature of the dispersion may not have been fully appreciated.

The dramatic improvement in the performance of the exponential transform when it is used in conjunction with splitting at an upper weight limit seems to indicate that a substantial fraction of the tally variance is associated with very high-weight particles. Particles can accumulate a high weight by traveling against the transform vector for part of their trajectory. With splitting at the upper weight limit, the distribution of tally scores per source particle for each high-weight particle is shifted from a binary distribution of scoring or not scoring in one lump to a superposition of binary distributions with smaller components. The net

result is to reduce the variance while leaving the tally mean unchanged. The computational time involved is relatively small because the high-weight particles are relatively infrequent, and so a net gain is achieved in the figure of merit.

The biggest surprise we had in doing the calculations for this paper was the disagreement between the continuous-energy and multigroup results. We see from Table 4 that the MCMG multigroup results underpredict the continuous-energy results by a factor of almost 4. The group cross sections consist of 30 neutron groups from the ENDF/B-IV evaluation with a weighting spectrum which is a fission spectrum matching a 1/E spectrum for the energy range of interest.[9] In Table 5 we compare the partial leakage J^+ in the direction of penetration at 15-cm intervals through the concrete for continuous-energy and multigroup-collision treatments. It can be seen that the discrepancy appears to grow systematically. The column labeled "DRXS" is a calculation with the 240-group discrete-reaction cross sections using MCNP. The results of the DRXS calculations fall in between the continuous-energy and the 30-group MCMG results. One may conclude that an energy self-shielding effect introduces a discrepancy into the multigroup results and that the magnitude of the discrepancy may be quite significant for deep-penetration applications using standard cross-section sets. Although this effect has been reported in transport through pure materials (most notably in thick iron shields), it might not be expected in mixtures such as concrete with significant masking of cross-section windows and the presence of hydrogen to lessen the importance of windows.

Table 4. Summary of Results for 100-cm-Radius by 200-cm-Thick Concrete Cylinder

Method	Transmitted Leakage	% Error	FOM	Computer Minutes
MCNP, splitting	8.21×10^{-9}	4.4	6.7	77
MCNP, weight window	8.26×10^{-9}	9.3	6.3	18.4
MCNP, exponential transformation	4.86×10^{-8}	39	1.5	4.4
MCNP, exponential transformation and weight cutoff	8.06×10^{-9}	18	1.7	17.6
MCNP, exponential transformation and weight window	8.49×10^{-9}	3.0	22.6	49.2
MCMG, splitting	2.17×10^{-9}	5.6	11.9	26.8
MCNP, discrete reactions, splitting	5.08×10^{-9}	6.8	8.0	27.0

Given the discrepancy between continuous-energy and multigroup Monte Carlo, an obvious question becomes what is the result of an S_n calculation. Therefore, we made an S_n calculation with the one-dimensional S_n code ONETRAN.[10] The geometry was assumed to be a 200-cm Portland concrete slab of infinite lateral extent. An infinite extent is a very good approximation since the Monte Carlo calculations indicated the transverse leakage to be about 2×10^{-5}. Using the truncated fission spectrum (i.e., source energies greater than 3.68 MeV) and the same 30 group ENDF/B-IV cross-section set as used with MCMG, good convergence was achieved with ONETRAN using Δr of 1.66 cm and an S-8 Lobatto quadrature; the leakage was 2.45×10^{-9}. Using the full fission spectrum source, the leakage was 2.71×10^{-9}. Good convergence with a Gauss quadrature was not achieved until an S-16 or greater quadrature was used. There are a couple of conclusions: (1) S_n agrees with the MCMG result of $2.17 \times 10^{-9} \pm 5.6\%$ within two standard deviations, and (2) S_n requires a Lobatto or high-order Gauss quadrature for good convergence in deep-penetration problems.

To verify that the transverse leakage was truly negligible and that the one-dimensional S_n and MCMG results were comparable, an MCMG calculation was performed with infinite radial extent for the 200-cm-long concrete cylinder. The results were essentially identical to those with the 100-cm radius.

To further complete the picture (but not belabor the point), ONETRAN was also used with a 30-group ENDF/B-V multigroup cross-section set. The transmitted leakage was virtually identical with the ENDF/B-IV results from ONETRAN and MCMG. Finally, MCNP calculations were made with modified 240-group discrete-reaction cross sections based on ENDF/B-V. The cross sections for both silicon and oxygen were modified to accurately represent the large window in the total cross section for each nuclide, at 0.145 MeV for silicon and 2.35 MeV for oxygen. The result was the same as with the regular discrete cross sections in which the windows are averaged out. This indicates the difference between continuous energy and multigroup treatments is due to a self-shielding effect.

Another potential method to improve the results at the exit surface is to surround the surface with a DXTRAN sphere. DXTRAN, however, is generally only useful in situations where it is difficult to get tracks by a random walk to a particular place in the geometry in order to make a tally. This is not the case here since by geometric splitting an abundance of tracks gets to the surface tallies. In this case DXTRAN makes the problem more inefficient by adding additional arithmetic complexity for the computer to handle. However, if one is interested in calculating the flux at a point in the center of the exit surface, relatively few tracks are in the vicinity of any given point on the surface. A surface tally therefore is useless, and a point detector is required. Placing a DXTRAN sphere around a detector can improve the efficiency of a detector calculation significantly.

Table 5. Comparison of Partial Leakage as a Function of Method and Thickness

Surface	J^{+}MCNP	J^{+}DRXS	J^{+}MCMG	MCNP/DRXS	MCNP/MCMG
15 cm	7.44E-2 (.68%)	7.38E-2 (.62%)	7.35E-2 (.46%)	1.01	1.01
30	2.66E-2 (6.6%)	2.58E-2 (1.0%)	2.48E-2 (.74%)	1.03	1.07
45	8.07E-3 (1.5%)	7.65E-3 (1.4%)	7.00E-3 (1.0%)	1.05	1.15
60	2.26E-3 (1.9%)	2.14E-3 (1.8%)	1.79E-3 (1.3%)	1.06	1.26
75	6.14E-4 (2.4%)	5.69E-4 (2.2%)	4.40E-4 (1.7%)	1.08	1.40
90	1.61E-4 (2.9%)	1.48E-4 (2.7%)	1.06E-4 (2.1%)	1.09	1.52
105	4.25E-5 (3.5%)	3.81E-5 3.2%)	2.55E-5 (2.5%)	1.12	1.67
120	1.14E-5 (4.1%)	9.62E-6 (3.7%)	5.89E-6 (3.0%)	1.19	1.94
135	3.09E-6 (4.7%)	2.41E-6 (4.4%)	1.40E-6 (3.4%)	1.28	2.21
150	7.99E-7 (5.3%)	6.18E-7 (5.0%	3.31E-7 (3.9%)	1.29	2.41
165	2.13E-7 (6.0%)	1.59E-7 (5.7%)	7.77E-8 (4.4%)	1.34	2.74
180	5.63E-8 (6.8%)	3.91E-8 (6.1%)	1.81E-8 (4.9%)	1.44	3.11
200	8.20E-9 (7.9%)	5.08E-9 (6.8%)	2.17E-9 (5.6%)	1.61	3.78

20-cm-Radius Problem

This problem is identical to the 100-cm-radius problem in every aspect except for the radius. The smaller radius now makes the transverse and backscattered leakages almost identical, $3.84 \times 10^{-2} \pm 0.4\%$. This problem

runs only slightly less efficiently than the 100-cm-radius problem. The reason is that although it is harder to get particles through the cylinder, less time is spent on particles wandering around radially. They are killed by escaping.

This problem was done in only two modes: splitting with MCNP and MCNP with a combination of the weight window and exponential transformation. The exponential transformation by itself on this problem performs very poorly. The importances for splitting were set using the same technique as before, and another (but different) combination of two-for-one and four-for-one splitting resulted. The importance in the last cell was 21233664 as compared to 4194304 for the 100-cm-radius problem. For the case of splitting, the transmitted leakage is $7.50 \times 10^{-10} \pm 5\%$ with 6.0 as a figure of merit. The weight window and transformation (biasing parameter is again 0.7) result is $8.17 \times 10^{-10} \pm 4.9\%$ with 21.5 as a figure of merit.

From the calculation with splitting, the transmitted neutron dose is $2.74 \times 10^{-17} \pm 7.0\%$ mrem/per neutron, and the transmitted flux is $8.06 \times 10^{-13} \pm 6.9\%$ neutron/cm^2.

DXTRAN is also inappropriate for this case as it was for the 100-cm-radius case; the figure of merit is reduced by its use.

BENT-PIPE PROBLEM

This problem is also divided into two parts, both of which are much less demanding than the previous 200-cm-concrete problem. In both cases a 20-cm-radius pipe that is 240-cm long along the axis has a 90° bend in the center and is jacketed concentrically by a 20-cm-thick region of ordinary Portland concrete. In the first case, the pipe is filled with liquid sodium, and in the second case the pipe is void. The geometry is shown in Figure 2. With the sodium, the attenuation from one end to the other is about 10^6 and with the void about 10^3.

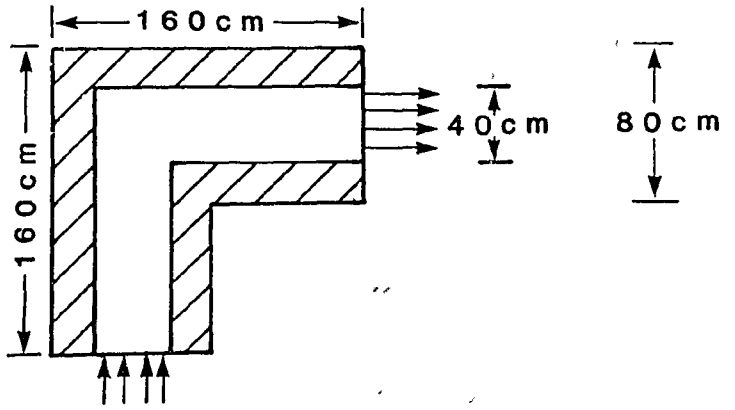

Figure 2. Bent Pipe Jacketed by Concrete.

The source for both cases is the same. It is an area source incident on one end of the pipe (but not including the jacket) with the energy and angular distribution given by

$$S(E,\mu) = \frac{\text{const.}}{E} \qquad \text{(1/E spectrum)} \tag{8}$$

$$= 0 \text{ otherwise} ,$$

where $\mu = +1$ is the cosine of the coaxial direction at the entrance plane. The procedure used to sample this distribution is given in the Appendix at the end of this paper. Constraints on the source are $8.32 \text{ eV} < E < 184 \text{ keV}$ and $0.8 < \mu < 1$.

The tally used to compare the various methods is the leakage transmitted out the opposite end of the pipe (pipe only and not including the jacket) within the direction $0.8 < \mu < 1.0$ where $\mu = +1$ is the cosine of the coaxial direction at the exit plane. Results of other tallies will be reported, however. The energy cutoff in all cases is 8.32 eV.

Sodium-Pipe Problem

The sodium density used is 0.705 g/cm^3 which is appropriate for sodium temperatures of approximately 1000°C. This problem is representative of design features in fast breeder coolant loops and possibly in fusion reactor coolant loops.

With only survival-biasing and a weight-cutoff game, in two minutes of computer time, no tallies were made. In fact, out of 33878 source neutrons, only nine had made it around the 90° bend. No particle got within 40 cm of the pipe exit.

In this problem, the mean free path averaged over collisions for sodium is about 16 cm and about 2 cm in the concrete. Therefore, plane splitting surfaces were placed across the axis of the pipe at 20-cm intervals. A 45° plane was also added where the two legs of the pipe intersect. Radial splitting was used in this problem by adding two concentric cylinders within the concrete jacket to be used as splitting surfaces. The first cylindrical splitting surface was placed 2 cm inside the concrete jacket, and the second was placed outward in the radial direction another 2 cm.

To set the importances, two runs of half a minute each were made to level the track population in the pipe between the source plane and the tally plane. Relative to the corresponding axial importance in the pipe, the radial importances were decreased by a factor of two for each of the first two sleeves and then a factor of four for the outer sleeve. To show that this elaborate radial setup is really not necessary, another run was made with only one radial-splitting surface in the middle of the concrete jacket. The importances of the inner radial cells were reduced by

a factor of two and by another factor of four for the outer radial cells. The figure of merit was 62 with the two concentric splitting surfaces and 58 with only one in the center of the jacket. The two surfaces are more effective in killing outward-bound tracks and maximizing backscattered tracks, but the extra cells and surfaces required more computation time.

In applying the weight window to the sodium pipe, the lower weight bound was derived from the set of importances used in the run with splitting. The lower bound was taken to be $3/I_i$, where I_i is the importance for cell i. The factor three was chosen so that the source particles would start within the weight window. The upper weight bound was taken to be five times the lower weight bound based on previous with the weight window, it was used with the biasing parameter p set to 0.4 in one case and to 0.7 in another.

A multigroup run was made with MCMG using geometry splitting with different axial-splitting planes and with one concentric splitting surface midway between the inner and outer surface of the concrete jacket.

Results of the above cases are summarized in Table 6.

Table 6. Results of Bent Sodium Pipe

Method	Transmitted Leakage ($.8 < \mu < 1$)	% Error	FOM	Computer Minutes
MCNP, splitting	5.83×10^{-7}	4.1	62	9.6
MCNP, weight window	6.38×10^{-7}	6.4	54	4.6
MCNP, weight window, expo. trans.(.4)	5.70×10^{-7}	5.7	67	4.6
MCNP weight window, expo. trans.(.7)	5.93×10^{-7}	6.3	55	4.6
MCMG, splitting	5.19×10^{-7}	5.0	46	8.7
MCNP, splitting, DXTRAN	5.92×10^{-7}	9.9	22	4.6

DXTRAN in conjunction with geometry splitting was tried for a couple of runs with MCNP. The DXTRAN sphere was placed around the sodium at the exit tally plane. A game was played with DXTRAN such that all contributions to the DXTRAN sphere were accepted within four mean free paths, and a Russian roulette game was played with contributions beyond four (a short run indicated about 90% of the contributions were being made within four mean free paths). In one case DXTRAN was tried with the setup with axial-splitting surfaces every 20 cm and with two concentric-splitting

surfaces in the concrete jacket; the figure of merit dropped from 62 to 22. Secondly, DXTRAN was tried with a very simple setup using one axial-splitting surface (four-for-one) at the 45° intersection of the cylinders and a second splitting surface (one-for-two) at the sodium-concrete interface; 0.7 was the figure of merit.

Results other than the transmitted leakage may be of interest. Using MCNP with geometry splitting, 56.5% of the starting weight was lost to energy cutoff, 0.8% to escape through the curved jacket, 0.9% to capture, and 41.2% to backscatter from the source plane. The transmitted leakage out of the sodium was $3.11 \times 10^{-7} \pm 4.3\%$ between 37° and 90° relative to the axis of the pipe at the exit and $5.83 \times 10^{-7} \pm 4.1\%$ between 0° and 37°. The leakage transmitted through the exit plane bounding the concrete jacket (an annular disk excluding the sodium in the center) was $6.27 \times 10^{-8} \pm 7.5\%$ between 37° and 90° and $5.05 \times 10^{-8} \pm 8.3\%$ between 0° and 37°. The neutron dose transmitted through the sodium exit plane was $1.28 \times 10^{-15} \pm 4.4\%$ mrem per neutron, and the dose transmitted through only the concrete at the exit plane was $6.39 \times 10^{-17} \pm 8.6\%$ mrem per neutron. The flux transmitted through the sodium exit plane was $1.01 \times 10^{-9} \pm 4.1\%$ neutrons/cm^2 and $5.02 \times 10^{-11} \pm 7.3\%$ neutrons/cm^2 through the concrete exit plane.

Void-Pipe Problem

This problem is identical to the sodium-pipe problem except that the sodium is replaced by a void. Two surprises came from this problem: (1) intuition led to preliminary problems with geometry splitting, and (2) DXTRAN performed very impressively.

Trying this problem without any variance-reduction techniques, in two minutes of computer time 31448 neutrons started but only 358 got past the 90° bend, and 20 actually got to the exit tally plane.

The splitting surfaces were very similar to the sodium-pipe setup: axial planes every 20 cm and two interior concentric cylinders (one 4 cm into the concrete jacket from the void and the other another 4 cm into the jacket). The final axial importance before the exit was 4096 where it was 2519424 with the sodium. The attenuation from the source to the exit is on the order of 10^3.

Initially the radial importances were set as with the sodium: relative to a given axial cell in the void, the first radial cell had an importance a factor of two less, the middle radial cell importance another factor of two less, and the outer radial cell a factor of four less than the middle cell. This setup led to a figure of merit of 16 which was surprising since the attentuation is three orders of magnitude less than with sodium where the figure of merit was 62.

Looking at the MCNP summary information, it was noted that each neutron created about 7 tracks, and each neutron had about 6.6 collisions. This says that on the average every time a track had a collision, it was

split. This was the clue to the problem: the importance of the inner sleeve of the concrete jacket was a factor of two less than the adjacent void region which meant that a track entering the concrete from the void underwent Russian roulette with 50% survival. If the track backscattered into the void, it was split two-for-one but then immediately went to the other side of the void where Russian roulette was played again, etc. Obviously this is very inefficient.

The next step was to set the importance of the inner sleeve equal to the importance of the adjacent void. The middle-sleeve importance was then reduced by a factor of two relative to the inner sleeve, and the outer-sleeve importance was reduced by a factor of four relative to the middle sleeve.

Playing other splitting games such as changing the thickness of the concrete sleeves and reducing the number of radial sleeves from three to two had relatively little effect.

The weight window by itself was used successfully in the problem; the exponential transformation is not applicable. The bounds of the windows were set based on experience and by experimenting with a couple of short runs and watching the behavior of the sample variance.

MCMG was used with geometry splitting incorporating one concentric splitting surface in the center of the concrete jacket. Furthermore, two scattering kernels were tried: (1) with a continuous-scattering angle and (2) with the MORSE discrete-scattering angle.

Results of these runs are summarized in Table 7.

Table 7. Results of Bent-Void Pipe

Method	Transmitted Leakage ($.8 < \mu < 1$)	% Error	FOM	Computer Minutes
MCNP, splitting	1.08×10^{-3}	5.6	33	9.6
MCNP, weight window	1.10×10^{-3}	4.2	53	10.7
MCMG, splitting, cont. angle	1.11×10^{-3}	3.7	60	12.2
MCMG, splitting, discrete angle	1.07×10^{-3}	3.8	57	12.1

The MCNP-with-splitting figure of merit is less than the others by about a factor of two and less than the sodium-pipe figure of merit also by

a factor of two. The reason for both of these observations is unclear at this point. It can be argued that the void pipe should take longer than the sodium pipe because with the void all scores at the tally come from time-consuming backscattering. With the sodium, a large number of tracks can get to the tally plane without having to backscatter.

DXTRAN with MCNP was tried on this problem in four cases: (1) with the above splitting setup that gave the 33 figure of merit, (2) with the same geometrical setup (all the cells and surfaces set up for splitting) but with importances set to unity, (3) no splitting and all internal cells and surfaces removed that were required for the earlier splitting, and (4) all the extra cells and surfaces still removed but split two-for-one axially where the two legs of the geometry intersect at 45° and reduce the importance of the adjacent concrete jacket by a factor of two relative to the void. The impressive results are shown in Table 8. The weight window was not used for any of these calculations, and there is a potential for further DXTRAN improvements by using it. All runs were for 4.6 minutes of computer time. Russian roulette was played for all contributions to the DXTRAN sphere beyond four mean free paths. In all cases the radius of the outer sphere was 30 cm, and the radius of the inner sphere was 20 cm.

Table 8. DXTRAN Results

Case	Transmitted Leakage ($.8 < \mu < 1$)	% Error	FOM
1 splitting, complex geometry	1.07×10^{-3}	3.8	148
2 no splitting, complex geometry	1.06×10^{-3}	4.0	134
3 no splitting, simple geometry	1.08×10^{-3}	3.3	195
4 mild splitting, simple geometry	1.04×10^{-3}	3.0	243

Some conclusions may be drawn from these DXTRAN calculations. The improvement from case 2 to case 3 points out the obvious: more cells and surfaces require more arithmetic by the computer; they don't come free. Comparing case 1 and case 2 suggests that when you are already doing a pretty good job by one other technique, an additional technique adds little more and may even hurt (this was observed in the other problems). Comparing cases 3 and 4 suggests that there is usually profit in adding a little obvious help to the random walk. Cases 1 and 4 suggest that a very complex, elaborate setup may be overkill; not only does it take a person longer to set up and debug a complicated geometry, it takes the computer a long time to get through it too.

Other results associated with this bent-void pipe include about 1% of the starting weight lost to escape through the curved jacket, 8% lost to backscatter, about 92% lost to energy cutoff, and 0.4% lost to capture. The leakage transmitted from the void at the exit plane between 37° and 90° is $1.65 \times 10^{-4} \pm 5.7\%$, the leakage transmitted from the concrete at the exit plane between 0° and 37° is $7.67 \times 10^{-5} \pm 12\%$ and $5.46 \times 10^{-5} \pm 7.7\%$ between 37° and 90°. The neutron dose through the void at the exit is $1.65 \times 10^{-12} \pm 5.8\%$ mrem per neutron and $6.64 \times 10^{-14} \pm 9.0\%$ through the concrete. The flux through the void at the exit is $1.16 \times 10^{-6} \pm 4.7\%$ neutrons/cm^2 and $5.25 \times 10^{-8} \pm 8.4\%$ neutrons/cm^2 through the concrete.

CONCLUSIONS

It is virtually impossible to be able to say when to use one variance-reduction technique or another. One needs to have many techniques at his disposal. Furthermore, it is also virtually impossible to be able to prescribe how to use a particular technique. Experience in these matters has no substitute.

Despite the above disclaimer, we will attempt some general conclusions.

It appears the weight-window concept has merit when used in conjunction with other techniques that produce a large weight dispersion. It keeps from wasting time on low-weighted particles and keeps a tally and its variance from being overpowered by a few large-weighted scores. However, we at Los Alamos have not had enough experience with this tool to put it into MCNP permanently. We know relatively little about how to set the bounds of the window - especially if energy dependence is required.

The exponential transformation has very limited use by itself. It should not be used alone but in conjunction with something like the weight window. The performance and especially the reliability of the transformation are sensitive to the biasing parameter which, in our opinion, makes this technique dangerous to use except for the experienced Monte Carlo practitioner. We sometimes refer to the exponential transformation as the "dial-an-answer" technique, because the result of a calculation frequently appears to be a function of the biasing parameter.

Geometry splitting with Russian roulette is our most frequently-used technique. Although other schemes may buy more in particular situations, geometry splitting will virtually always give good returns. Furthermore, it is easy to understand and reliable. An important aspect that is apparent from the calculations in this paper is that performance is fairly insensitive within a broad range to how the splitting is implemented (two-for-one, four-for-one, where the surfaces are located, etc.)

Furthermore, it is not just enough to look at a figure of merit and a final sample error. You must also look at the sample mean and its error at

frequent intervals to make sure they have settled down and converged on a reliable result. In other words, look at the variance of the variance. For example, after a relatively few histories, a point-detector flux may have an indicated error of 10% but be in actual error by several factors. After a few more histories, both the flux and its error could be perturbed significantly. This procedure was not emphasized earlier in the paper, but it was used. It is simply wise practice - because it may give the only clue of an unreliable result.

Group X-6 is experimenting with analytically calculating the variance of the variance (or error of the error) and most of the MCNP calculations for this paper were done with a modification to MCNP for this purpose.[11] We recognize that there is very little quantitative information in the fourth moment, but qualitatively it appears that whenever the error of the error is of the same order as the error (both about 5 or 10%, for example) then the sample mean is reliable. But if the error is about 10% and the error of the error is 50%, the mean is unreliable.

One valid rule of thumb is to always make a few short, experimental runs to get a feel for the problem and to see the effect for different techniques and parameters. The code you are using should automatically provide you with enough basic information to allow you to evaluate and understand the run and its attributes. It has been our observation that the more experience a person has, the more reliance is put on preliminary runs. The less experience a person has, the more likely a job will be set up as quickly as possible, a long run attempted, and whatever comes out believed.

Finally, this paper has probably generated more questions than it has answered - especially in the area of multigroup calculations. Also, as applications become increasingly more complicated, there are other important and interesting topics such as the effect of representing a complex three-dimensional geometry by a lower-dimensional model. We look forward to addressing these and other questions in the future.

Acknowledgement

We wish to acknowledge P.D. Soran of X-6 for the ONETRAN calculation using ENDF/B-V data and for modifying the silicon and oxygen data in the discrete-reaction cross-section set.

REFERENCES

1. "Neutron and Gamma-Ray Flux-to-Dose Rate Factors," ANSI/ANS-6.1.1-1977 (N666), American Nuclear Standards Neutron and Gamma-Ray Flux-to-Dose-Rate Factors, Am. Nuc. Soc. (Illinois, 1977).

2. LASL Group X-6, "MCNP - A General Monte Carlo Code for Neutron and Photon Transport," LA-7396-M, Revised (November, 1979).

3. O. L. Deutsch, "MCMG User's Guide," Internal X-6 Document (March, 1979).

4. L. L. Carter and C. A. Forest, "Transfer Matrix Treatments for Multigroup Monte Carlo Calculations - The Elimination of Ray Effects," Nuclear Science and Engineering, 59, 27 (1976).

5. N. M. Schaeffer, Editor, "Reactor Shielding for Nuclear Engineers," Published by U.S. A.E.C. Office of Information Services, p.451 (1973).

6. "The Analysis and Design of Concrete Radiation Shielding for Nuclear Power Plants," ANSI/ANS-6.4-1977 (N403), American Nuclear Standards Guidelines on the Nuclear Analysis and Design of Concrete Radiation Shielding for Nuclear Power Plants, Am. Nuc. Soc. (Illinois, 1977).

7. G. P. Estes and J. S. Hendricks, "Integral Testing of Some ENDF/B-V Cross Sections," Transactions of the ANS, 33, 679 (November, 1979).

8. R. E. MacFarlane, "Energy Balance of ENDF/B-V," Transactions of the ANS, 33, 681 (November, 1979).

9. R. J. Barrett and R. E. MacFarlane, "Coupled Neutron and Photon Cross Sections for Transport Calculations," LA-7808-MS (April, 1979).

10. T. R. Hill, "ONETRAN, A Discrete Ordinates Finite Element Code for the Solution of the One-Dimensional Multigroup Transport Equation," LA-5990-MS (June 1975).

11. G.P. Estes and E.D. Cashwell, "MCNP Variance Error Estimator," X-6 Activity Report, LA-8232-PR, p. 19 (July-December, 1979).

Appendix

1. Fission-Spectrum Groups for MCMG

The source fraction per group, S_g, is determined from

$$S_g = \int_{E_{g+1}}^{E_g} \left(\frac{2}{\sqrt{\pi}T}\right)\sqrt{\frac{E}{T}}\, e^{-E/T}\, dE, \quad T = 1.30 \text{ MeV} \quad .$$

Group	Lower Bound, MeV	S_g
1	15.0	3.0380E-5
2	13.5	7.8639E-5
3	12.0	2.3568E-4
4	10.0	1.1626E-3
5	7.79	5.9203E-3
6	6.07	1.7678E-2
7	3.68	1.0418E-1
8	2.865	9.1383E-2
9	2.232	1.0877E-1
10	1.738	1.1525E-1
11	1.353	1.1097E-1
12	0.823	1.8153E-1
13	0.50	1.1963E-1
14	0.303	6.9450E-2
15	0.184	3.6918E-2
16	0.0676	2.8169E-2
17	0.0248	6.6880E-3
18	0.00912	1.5188E-3
		0.99955

2. Sample Energy E from Fission Spectrum

$$f(E) = \frac{2}{\sqrt{\pi}\,T}\sqrt{\frac{E}{T}}\, e^{-E/T}$$

$$T = 1.30 \text{ MeV}$$
$$\overline{E} = 3T/2 = 1.95 \text{ MeV}$$

Let ξ be a random number (0,1),

$$a = (-\ell n\ \xi_o)\cos^2\left(\frac{\pi}{2}\,\xi_1\right) \text{ and}$$
$$E = T(-\ell n\ \xi_3 + a) \quad .$$

3. Sample 1/E Energy Distribution, Angular Distribution, and Spatial Distribution

Let ξ be a random number (0,1),

(a) Energy: $f(E) = (.10)/E$ $\quad 8.32 \text{ eV} < E < 184 \text{ keV}$

$$E = 0.184e^{-10\xi}$$

(b) Angular: $f(\mu) = \text{const.}$ $\quad 0.8 < \mu < 1$

$= 0$ $\quad$ otherwise

$$\mu = 0.8 + 0.2\xi$$

$\mu = +1$ is along y-axis

The direction cosines (u,v,w) = (0,1,0) must be rotated through the polar angle $\cos^{-1}\mu$ and through an azimuthal angle sampled uniformly from $(0,2\pi)$.

(c) Spatial: $y = 0$

$$x^2 + z^2 < 20^2 \quad .$$

EXPERIENCE WITH TRIPOLI AT ORNL

S. N. Cramer and R. W. Roussin
Oak Ridge National Laboratory
Oak Ridge, Tennessee 37830

ABSTRACT

Initial use of the TRIPOLI code at Oak Ridge National Laboratory (ORNL) involves calculation of sample problems for both neutron and gamma-rays. Comparison with existing MORSE results indicates that the computing efficiency of TRIPOLI is somewhat better for the problems studied. Calculation of a thick (90cm) concrete and steel integral experiment with TRIPOLI gives good agreement with the experimental results. This calculation involved the neutron count rate and unfolded energy spectra as measured in an NE213 detector behind the sample. It was necessary to expand the standard TRIPOLI cross section energy structure near the 2.3 MeV minimum in the total cross section of oxygen (a major constitutent of concrete) to correctly calculate the count rate near this energy. A drawback of the TRIPOLI code is the lack of an automated method of performing coupled neutron and gamma-ray production calculations.

INTRODUCTION

As a part of the preparation for the Monte Carlo seminar-workshop the Radiation Shielding Information Center (RSIC) has sponsored a limited calculational program involving the TRIPOLI code. This code has been in use at ORNL for the past year following the visit to RSIC of personnel from the CEA/CEN SERMA Shielding Laboratory, Saclay, France for the purpose of connecting ENDF/B to TRIPOLI. The TRIPOLI code is a very large and versatile Monte Carlo code system undergoing continuous development on an IBM computer system similar to that used at ORNL.

During the past year various problems of interest were analyzed using TRIPOLI, and results of three types of calculations are reported in this paper.

PROBLEMS CALCULATED WITH TRIPOLI

Three different problems were run to test some of the capabilities of TRIPOLI. These include a point fission neutron source in air, a point monoenergetic gamma-ray source in air, and an integral experiment measuring the time and energy spectra of neutrons penetrating through a reinforced concrete shield.

Neutron Fission Source in Air

Calculation of a neutron sample problem as described in the MORSE report are given in Table 1. These are flux calculations at various radii from a point fission source in infinite air. Two types of TRIPOLI results are given: those for no biasing and those with adjustments to the spatial, energy, and angular biasing input parameters in order to obtain comparable statistics at all radii. The values in the table are the standard deviation, given in per cent, and the figure of merit, the square of fractional standard deviation times the IBM 360/91 computation time (T) in seconds. No attempt was made to improve the efficiency for the reported MORSE results. Ten TRIPOLI calculations were made for this problem with different combinations of biasing input parameters. An average value of the flux was obtained for each radii, and it was observed that for the seventy fluxes 68.6% were within $\pm \sigma$, 94.3% were within $\pm 2\sigma$, and 100% were within $\pm 3\sigma$ of their respective average values.

Table 1 Results of the Neutron Source in Air Sample Problem

R (h in km)	MORSE $4\pi R^2\phi$	MORSE σ(%)	MORSE σ^2T	TRIPOLI (no biasing) $4\pi R^2\phi$	TRIPOLI (no biasing) σ(%)	TRIPOLI (no biasing) σ^2T	TRIPOLI (biasing) $4\pi R^2\phi$	TRIPOLI (biasing) σ(%)	TRIPOLI (biasing) σ^2T
0 1	1 720	16 0	0 77	1 870	8 7	0 26	1 811	5.0	0 12
0 2	1 979	9 5	0 27	1 941	7 2	0 19	2 023	5 4	0 15
0 3	1 681	7 9	0 19	1 723	9 1	0 30	1 833	3 7	0 07
0 6	0 604	7 4	0 20	0 680	12 8	0 57	0 651	5.3	0 14
0 7	0 451	8 6	0 22	0 452	14 9	0 78	0 419	4.7	0 11
0 9	0 147	9 1	0 25	0 196	19 0	1 26	0 154	4 4	0 09
1 2	0 042	21 8	1 43	0 041	29 9	3 13	0 036	5 9	0 17

Monoenergetic Gamma-Ray Source in Air

The results of a sample gamma-ray problem are given in Fig. 1. The flux spectrum at 1000 meters is shown resulting from a point 10 MeV gamma-ray source in air. The TRIPOLI boundary crossing estimator and the newly implemented MORSE[1] Klein-Nishina next event estimator were used. The differences in the calculation can be attributed to differences in the basic data (TRIPOLI library *vs.* ENDF/B) and also differences in the cross section processing (continuous energy *vs.* multigroup). The σ^2T for the MORSE total flux was a factor of 4 greater than that for TRIPOLI; however, MORSE boundary crossing estimator results gave a figure of merit comparable to that for TRIPOLI.

Concrete Integral Experiment

A final calculation with TRIPOLI involves a large scale integral experiment performed at IRT.[2] Figure 2 shows a schematic of the entire experimental set-up, and Fig. 3 shows the details of the sample problem geometry used to simulate a reinforced concrete shield. The incident neutron energy range is from 20 MeV to 10 eV.

At the time these calculations were performed, several TRIPOLI modules had not yet been fully implemented at ORNL. These features include the generation of secondary gamma rays from neutron interactions, the next event estimator, and the ENDF/B library. As a result, the calculations presented here are for neutrons only using a detector boundary crossing estimator and the standard TRIPOLI library based on UK data

evaluations. A simple one-dimensional two-medium (shield and air) spatial and angular biasing procedure centered at the detector position was utilized. Energy biasing was not used.

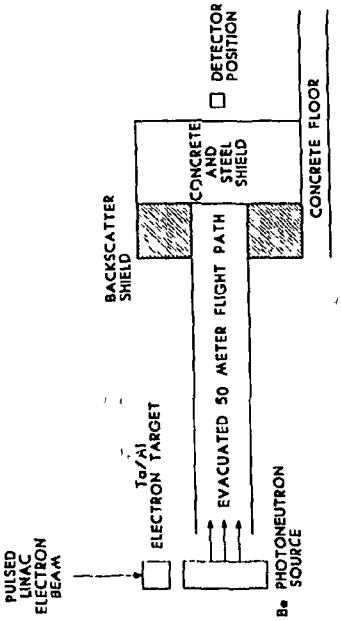

Fig. 2. Experimental set-up for the Concrete Integral Experiment.

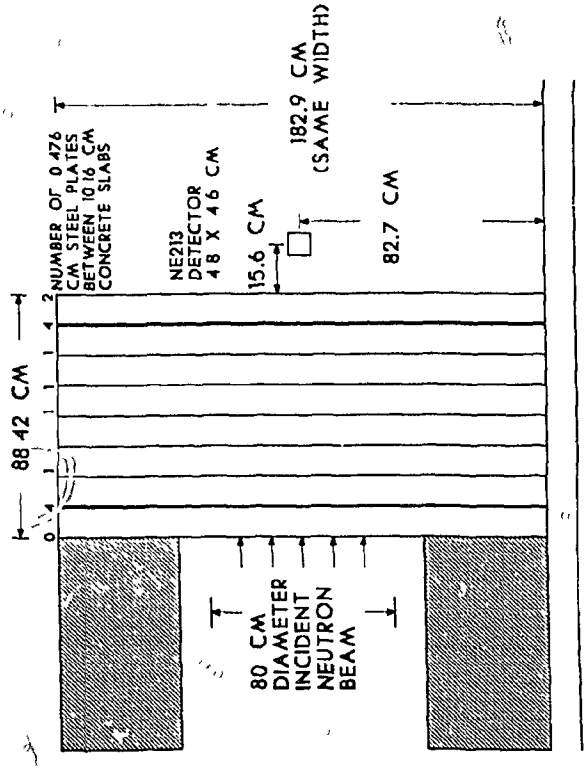

Fig. 3. Details of the Concrete and Steel Shield.

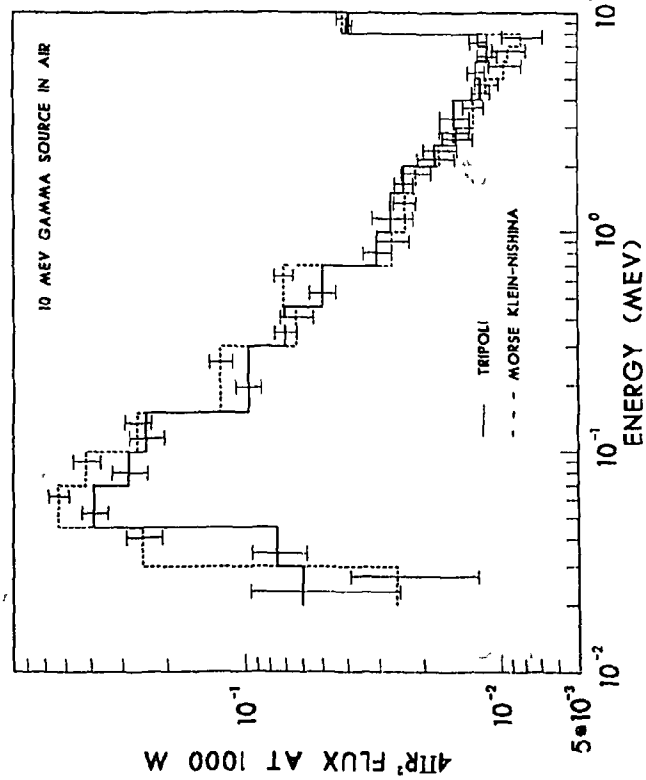

Fig. 1. Flux Versus Distance for the Infinite Air Gamma-Ray Sample Problem.

Time Dependent Count Rate Results

The calculated and experimental count rates are shown in Fig. 4. The incident source energy ranges corresponding to the time taken for the neutrons to traverse the 50 meter flight path are indicated on the figure. These count rate comparisons are absolute, each being normalized to the number of neutrons incident on the leading edge of the sample for the individual time (energy) intervals. In order to calculate the 2.5 μsec peak, due to the 2.3 MeV minimum in the oxygen cross section in the concrete, about 20 narrow energy intervals were used in the cross section structure in the vicinity of this minimum. With only two intervals to describe this minimum, the calculated count rate was about half that shown in Fig. 4. For penetration studies, the TRIPOLI cross section structure is continuous in energy but with constant values over specified energy intervals.

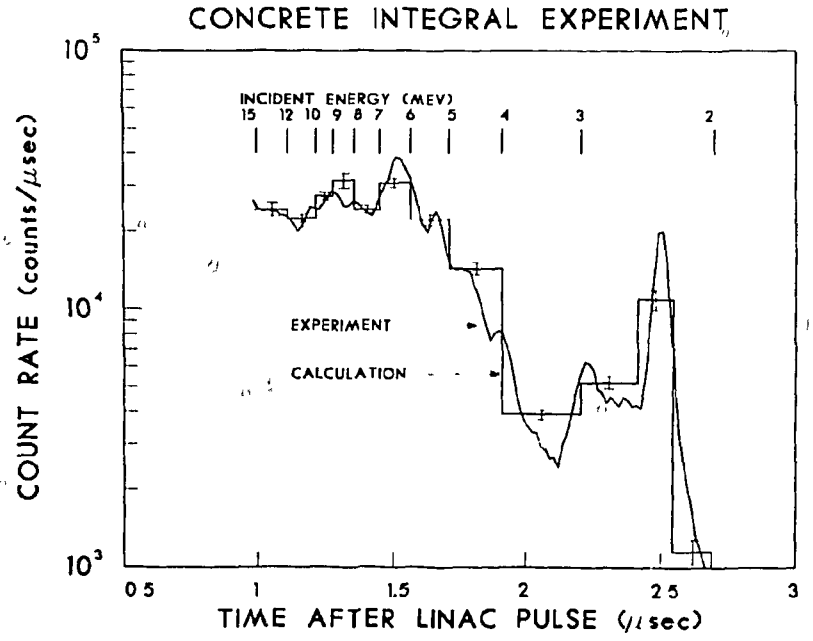

Fig. 4. Count Rate Comparisons for the Concrete Integral Experiment.

Neutron Energy Spectral Results

The secondary energy flux spectra, averaged over the incident energy intervals from Fig. 4 are given in Figs. 5 through 14. The spread between the experimental curves represents two standard deviations in the unfolded data. The same quantity is represented by the error bars on the calculated histograms. The flux spectra comparisons are generally in good agreement, the only consistent discrepancy being in the lowest (1-2 MeV) interval for which experimental data were reported. The histograms represent values which have been smeared with a Gaussian resolution function provided in the experimental results following the TRIPOLI calculation.

For a variety of reasons, this smearing is the probable cause of the low energy discrepancy, and it is still under investigation. The detector resolution below 1 MeV was not provided and was extrapolated in order to smear the very large fluxes below 1 MeV into the higher energy intervals. The coarseness of the smearing grid or any error or inconsistency in the low energy extrapolation or smearing procedure could easily cause the differences in the 1-2 MeV interval.

Comments on the Spectral Results

It was found necessary to modify the calculated spectra by an unexplained normalization factor, due to an inconsistency in the experimentally reported data, in order to obtain the comparisons shown. This factor of 15.7 was determined by comparing the total experimental counts integrated between 2 and 15 MeV from Fig. 4 (Fig. 22 in Ref. 2) with that obtained by folding the detector efficiency (Fig. 13, Ref. 2) into and integrating the experimental spectra between 2 and 15 MeV (Fig. 25, Ref. 2). This anomaly is also still under investigation in consultation with the experimentors.

CONCLUSIONS

The neutron fission source in air problem allowed a limited, but successful, application of some of the biasing techniques available in TRIPOLI. The spectral results calculated for the monoenergetic gamma-ray source problem were encouraging in that good precision was obtained for the entire energy range in a small amount of computer time.

The calculation of the integral experiment did not test many of the features of the TRIPOLI code, especially the intricate biasing procedures, next event estimator, gamma-ray production, etc.; however, it did demonstrate the capability to accurately analyze an experimental benchmark problem of significant importance for shielding applications.

REFERENCES

1. M. B. Emmett and J. T. West, III, "MORSE: Current Status of the Two Oak Ridge Versions," ORNL/RSIC-44, "A Review of the Theory and Application of Monte Carlo Methods: Proceedings of a Seminar-Workshop Oak Ridge, Tennessee, April 21-23, 1980," (to be published).

2. J. C. Young, L. Harris, et al., Time-Dependent Measurements of Fast-Neutron and Secondary Gamma-Ray Transport Through a Thick Concrete and Steel Shield," IRT 8025-723, April 1975.

ACKNOWLEDGEMENT

The authors thank J. Gonnord and his colleagues of CEA/CEN SERMA Shielding Laboratory, Saclay, France, for advice and guidance in using TRIPOLI at ORNL. We also thank Mildred Landay for preparing this manuscript.

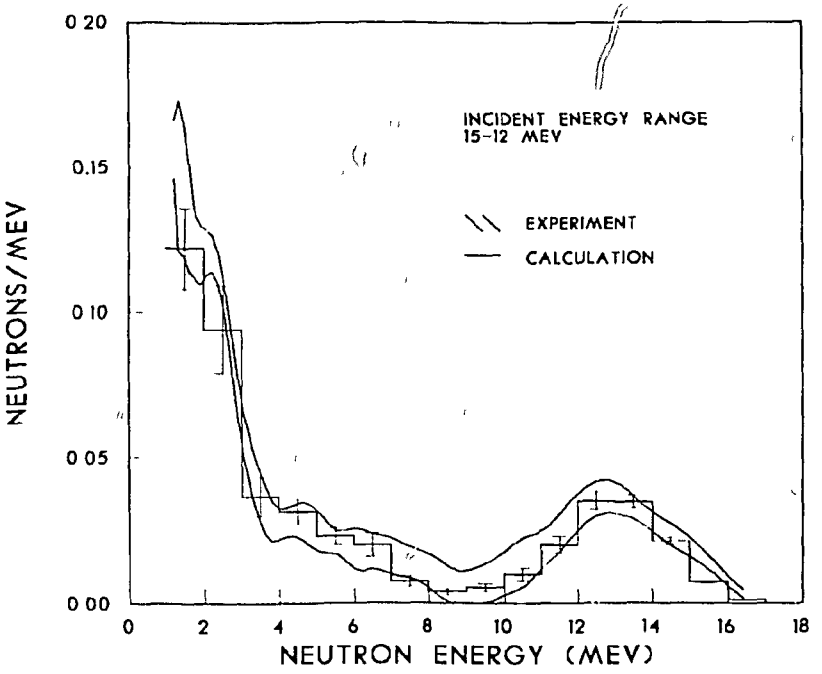

Fig. 5. Flux Spectra Comparisons for the Concrete Integral Experiment for the 15-12 MeV Incident Energy Interval.

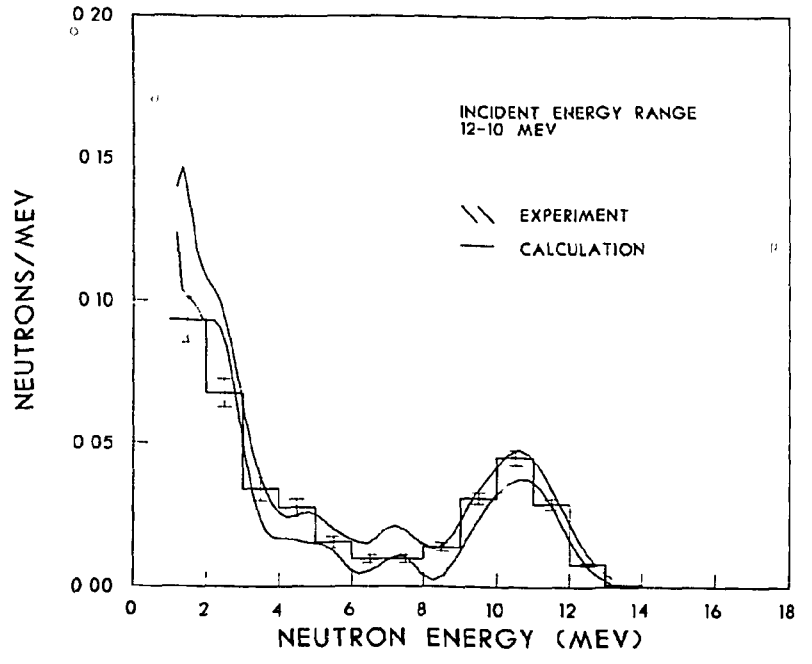

Fig. 6. Flux Spectra Comparisons for the Concrete Integral Experiment for the 12-10 MeV Incident Energy Interval.

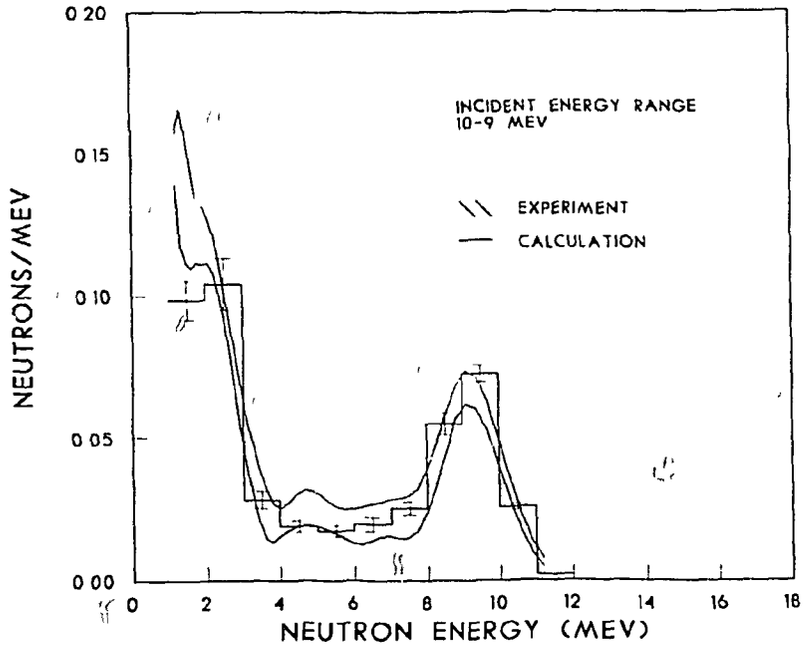

Fig. 7. Flux Spectra Comparisons for the Concrete Integral Experiment for the 10-9 MeV Incident Energy Interval.

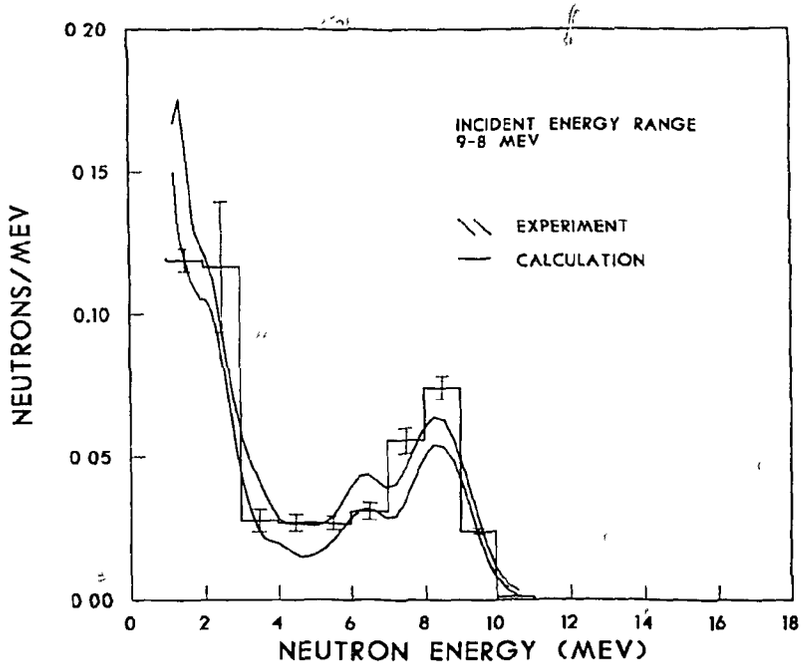

Fig. 8. Flux Spectra Comparisons for the Concrete Integral Experiment for the 9-8 MeV Incident Energy Interval.

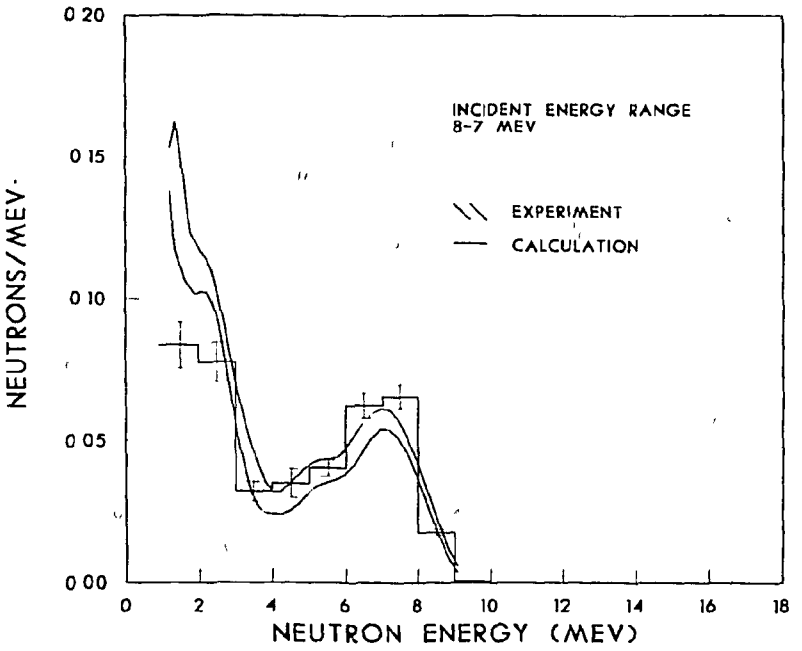

Fig. 9. Flux Spectra Comparisons for the Concrete Integral Experiment for the 8-7 MeV Incident Energy Interval.

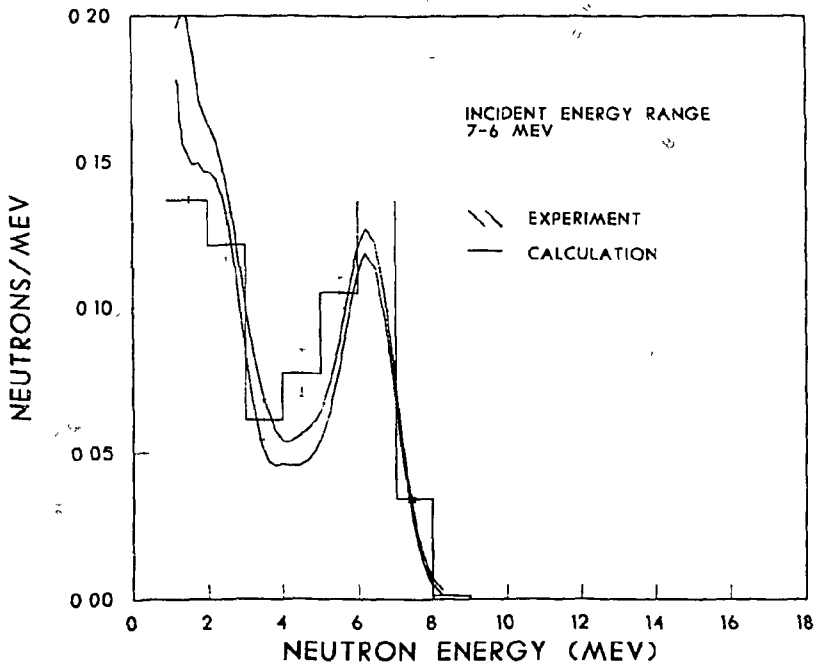

Fig. 10. Flux Spectra Comparisons for the Concrete Integral Experiment for the 7-6 MeV Incident Energy Interval.

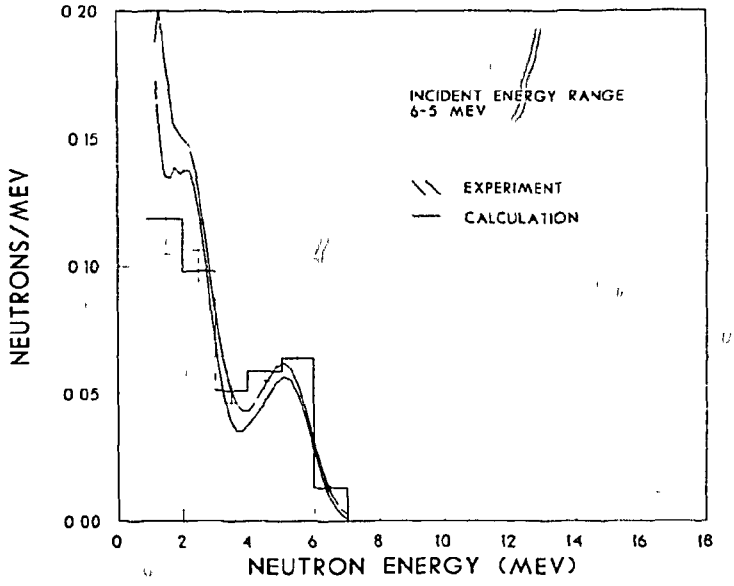

Fig. 11. Flux Spectra Comparisons for the Concrete Integral Experiment for the 6-5 MeV Incident Energy Interval.

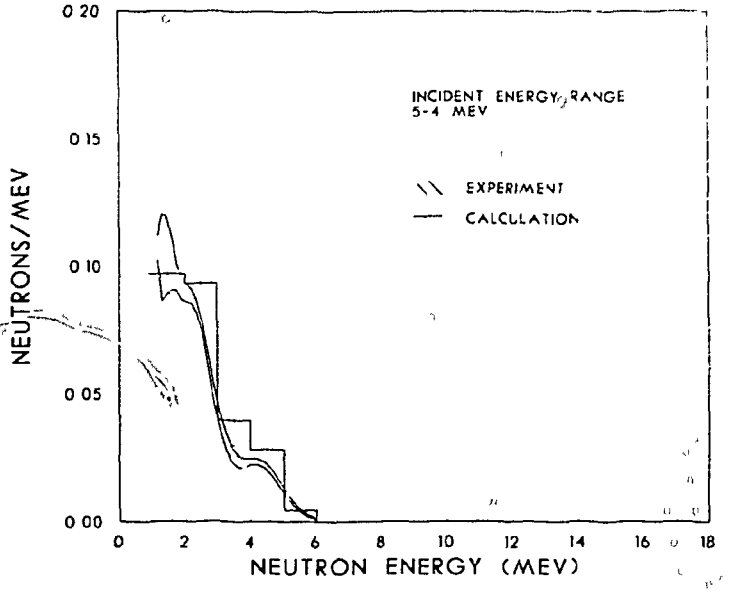

Fig. 12. Flux Spectra Comparisons for the Concrete Integral Experiment for the 5-4 MeV Incident Energy Interval.

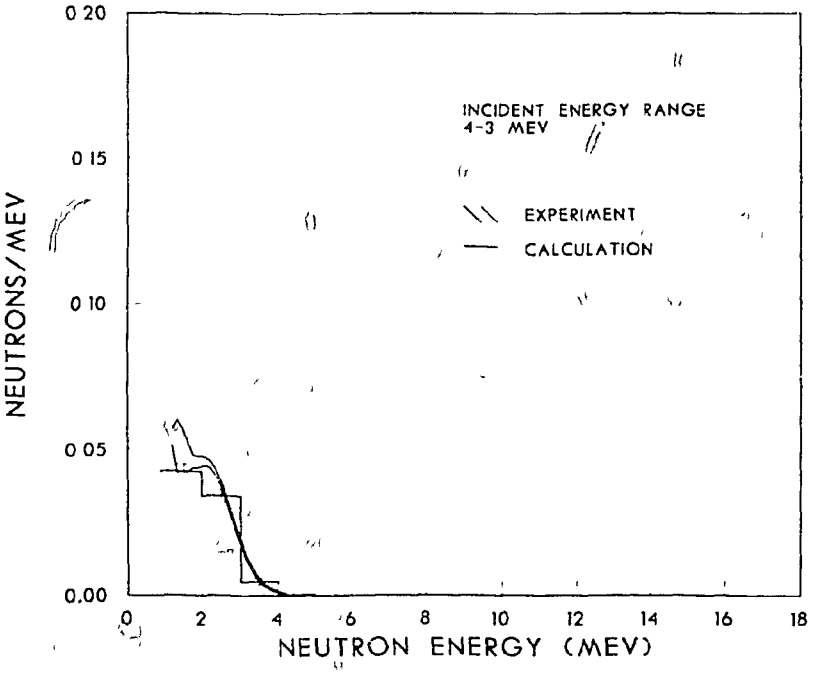

Fig. 13. Flux Spectra Comparisons for the Concrete Integral Experiment for the 4-3 MeV Incident Energy Interval.

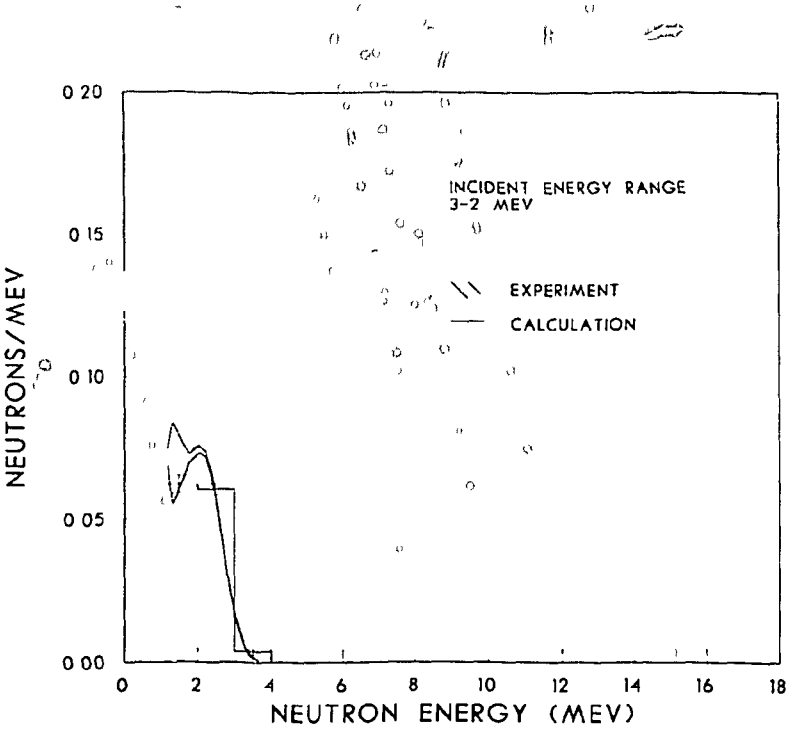

Fig. 14. Flux Spectra Comparisons for the Concrete Integral Experiment for the 3-2 MeV Incident Energy Interval.

MORSE: CURRENT STATUS OF THE TWO OAK RIDGE VERSIONS

M. B. Emmett and J. T. West, III
Computer Sciences Division
at Oak Ridge National Laboratory
Oak Ridge, Tennessee, USA

ABSTRACT

There are two versions of the MORSE Monte Carlo radiation transport computer code system at Oak Ridge National Laboratory. MORSE-CG is the most well-known and has undergone extensive use for many years. Development of MORSE-SGC was originally begun in order to restructure the cross section handling and thereby save storage, but the more recent goal has been to incorporate some of the KENO[9] ability to handle multiple arrays in the geometry and to improve on 3-D plotting capabilities. New capabilities recently added to MORSE-CG include a generalized form for a Klein Nishina estimator, a new version of BREESE, the albedo package, which now allows multiple albedo materials and a revised DOMINO which handles DOT-IV tapes.

MORSE-CG

MORSE-CG[1] is almost continuously undergoing development. Among the recent changes or additions are a more generalized Klein Nishina estimator, a new version of the BREESE[2,3] albedo package, a version of DOMINO[4] that handles DOT-IV type tapes and free-form input for the SAMBO analysis data.

The Klein Nishina estimator that is now being used takes pair production and Compton scattering cross sections directly from ENDF cross section libraries. The cross section routines have been altered to allow processing of these cross sections. The estimator itself is built into a version of RELCOL which uses the Klein Nishina estimator for gamma ray groups and the 'standard' point detector next-flight estimator for neutron groups. Several tests of this have been made. One such test was a comparison with DOT runs both with and without the standard source fixup which deletes negative fluxes and removes enough small positive values to restore particle conservation. MORSE was run both with and without the Klein Nishina estimator. A comparison of these results is shown in Figure 1 and a more detailed description of the test was given at the 1979 Winter ANS meeting[5].

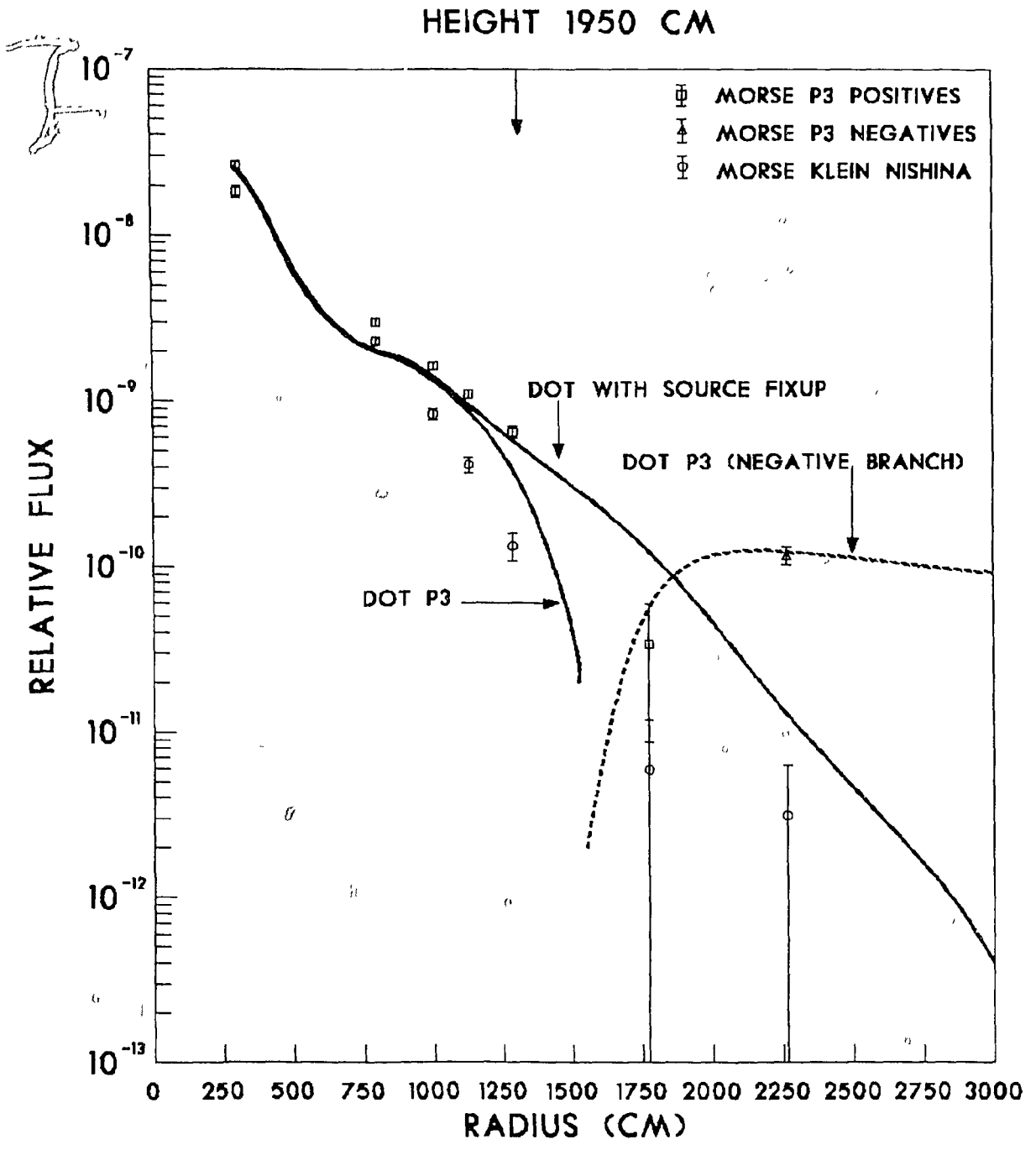

Figure 1. Comparison of MORSE and DOT Results

BREESE-II allows multiple albedo materials in a single MORSE run. It also allows the number of outgoing polar angles to be dependent on the value of the incoming polar angle and the number of outgoing azimuthal angles to be a function of the value of both the incoming and outgoing polar angles. The CARP code which prepares albedo tapes for BREESE usually collapses the group structure of the albedo data so that a reasonable amount of core is used. One method used to test this BREESE was to run the same problem in three ways: with materials only, with albedo only and with some material adjacent to albedo. Satisfactory results were obtained in this way. At present, albedo data is available for four materials: 12-inch water, 12-inch ordinary concrete, 9-inch carbon steel and 1/2-inch steel over concrete. Both the data and the two computer codes are available from RSIC.

DOMINO, the interface code between discrete ordinates (DOT) and Monte Carlo calculations has been modified to allow use of DOT-IV[8] boundary source tapes since most DOT users now run DOT-IV.

Another change to MORSE-CG allows use of both specular reflection media and actual albedo media in a run. This is done by using a media number greater than 1000 for the specular reflection media.

The use of free-form input data in the SAMBO analysis package has been implemented in subroutine SCORIN through a call to a new routine, RFRE. Old input decks are compatible only if there are no spaces within a number and no blanks used for zeroes and if a card containing either a $$ or an ** in Columns 2 and 3 is placed in front of the array to indicate integer or floating point.

The above is a brief summary of the current status of MORSE-CG at Oak Ridge. Now the status of MORSE-SGC will be presented.

MORSE-SGC

MORSE-SGC[6] is a supergroup version of the MORSE family of Monte Carlo codes. It has the ability to supergroup the cross section storage and particle tracking to allow fine group problems to be run on medium to small computer systems. This technique is especially beneficial on CDC computers. The combinatorial geometry system in MORSE-SGC has undergone extensive revision. The new geometry system, based on combinatorial geometry, is called MARS, an acronym for a Multiple ArRay System. This is a powerful tool for modeling either lattice geometry or complex geometry having repetitive features.

The MARS geometry system allows the user to describe many rectangular cells of arbitrary content, called "universes". These universes can be arbitrarily combined to describe arrays. Arrays may contain sub-arrays, universes, and vacancies. There exist three methods of nesting arrays inside of arrays in the MARS geometry system. There is no limit to the depth of geometric nesting. Geometry may be optionally

modeled around an array or arrays and repeated in its entirety. Furthermore, the position of an array is arbitrary, thereby allowing rotation as well as translation, when an array is repeated. Vacancies in an array may occur either on an array periphery or internal to an array. MARS allows the user to exit or enter an array from any cell in the array, providing the geometry surrounding the array is well defined. This feature was demonstrated recently in modeling the Three Mile Island Core for the Kemeny Commission. The core was modeled first as it was designed and then later modeled in a hypothetical disrupted configuration. This work was reported in ORNL-TM-106[7]. In both models no material homogenization was needed. The proper material composition and geometry description was achieved for the entire core taking into account three different fuel enrichments, two types of control rods, three types of burnable poison rods, orifice rods, and instrument channels. The design core required 6000 words of memory and the disrupted core required 9000 words of memory. The design core modeled about 40,000 pins and the disrupted core modeled about 241,000 pins. In both models the core periphery shape was described and in the disrupted core model a three step conical hole was modeled in the top center of the core. Inside this hole other material regions were modeled. Criticality studies were performed on both models. The work was performed in three weeks.

The development of the MARS system in MORSE-SGC was sponsored by the NRC Transportation Division. It is operational in the SCALE system (Standard Computer Analysis for Licensing Evaluation) in the SAS3 and SAS3X sequences. This system uses simple input and automatic cross section processing for quick efficient problem setup and execution. MORSE-SGC has been used in this system for both shielding and criticality analysis of several different shipping casks. A typical PWR Shipping Cask is shown with 7 PWR assemblies in Figure 2. This drawing was generated with the JUNEBUG Graphics code which was developed to allow three-dimensional display of the MORSE/MARS geometry. The geometry for this model required 1805 words of memory, and 74 cards of input. Figure 3 shows the array nesting for this model. Notice most of the arrays are very small arrays, such as 3 by 1 by 1, 2 by 6 by 1, 5 by 1 by 1, etc. By modeling small arrays, nesting other arrays inside these arrays, and repeating arrays, very efficient memory utilization is achieved. Figure 4 shows the different "Levels" of geometry nesting used in this model.

The MORSE-SGC code will be available from RSIC during the summer of 1980, along with the JUNEBUG graphics code, and the CDC version of SCALE.[10] It is hoped that the features of MORSE-SGC will complement the existing MORSE-CG capability and aid the criticality and shielding analyst in providing quick and efficient computer analysis.

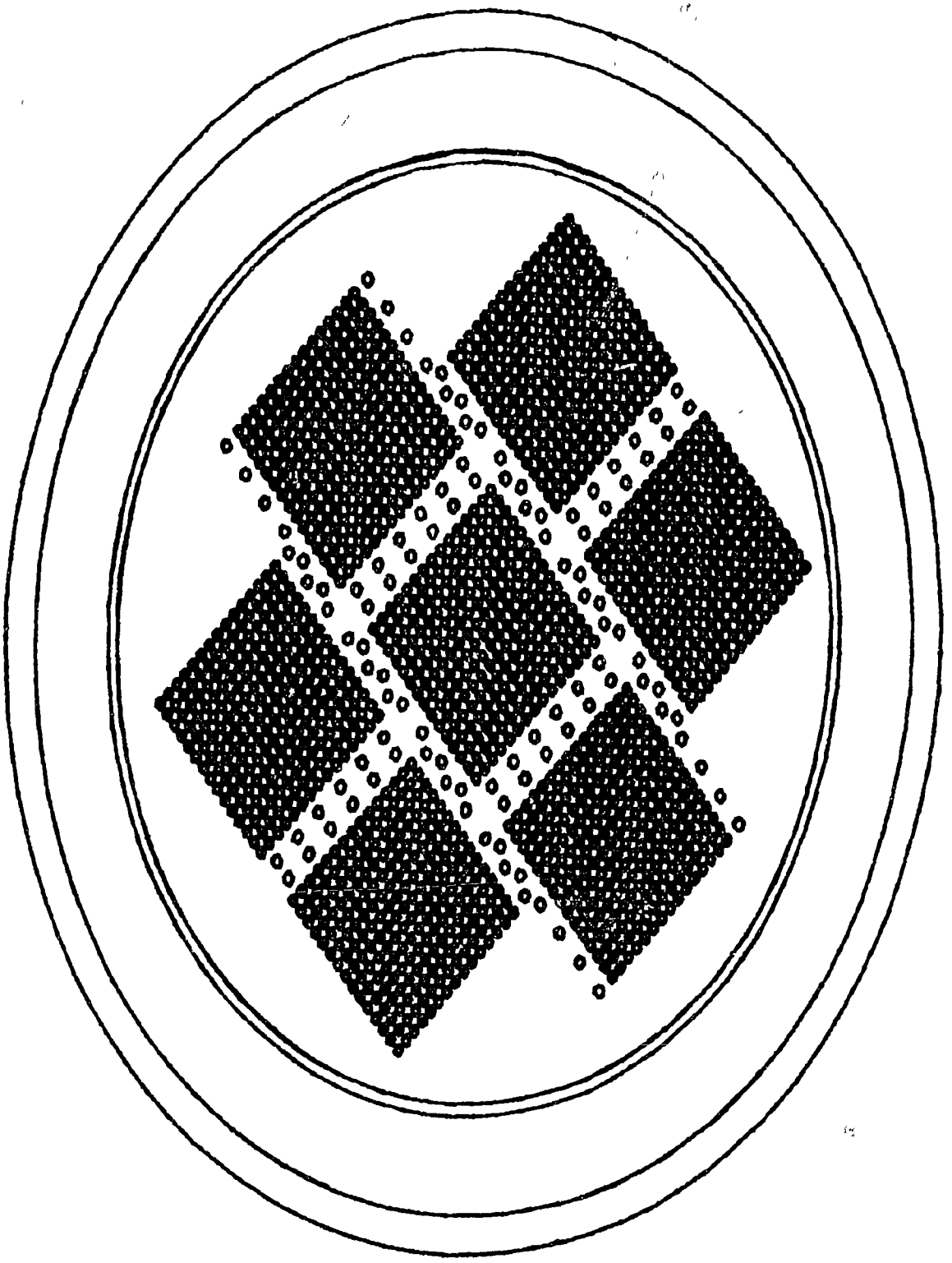

Figure 2. Typical PWR Shipping Cask

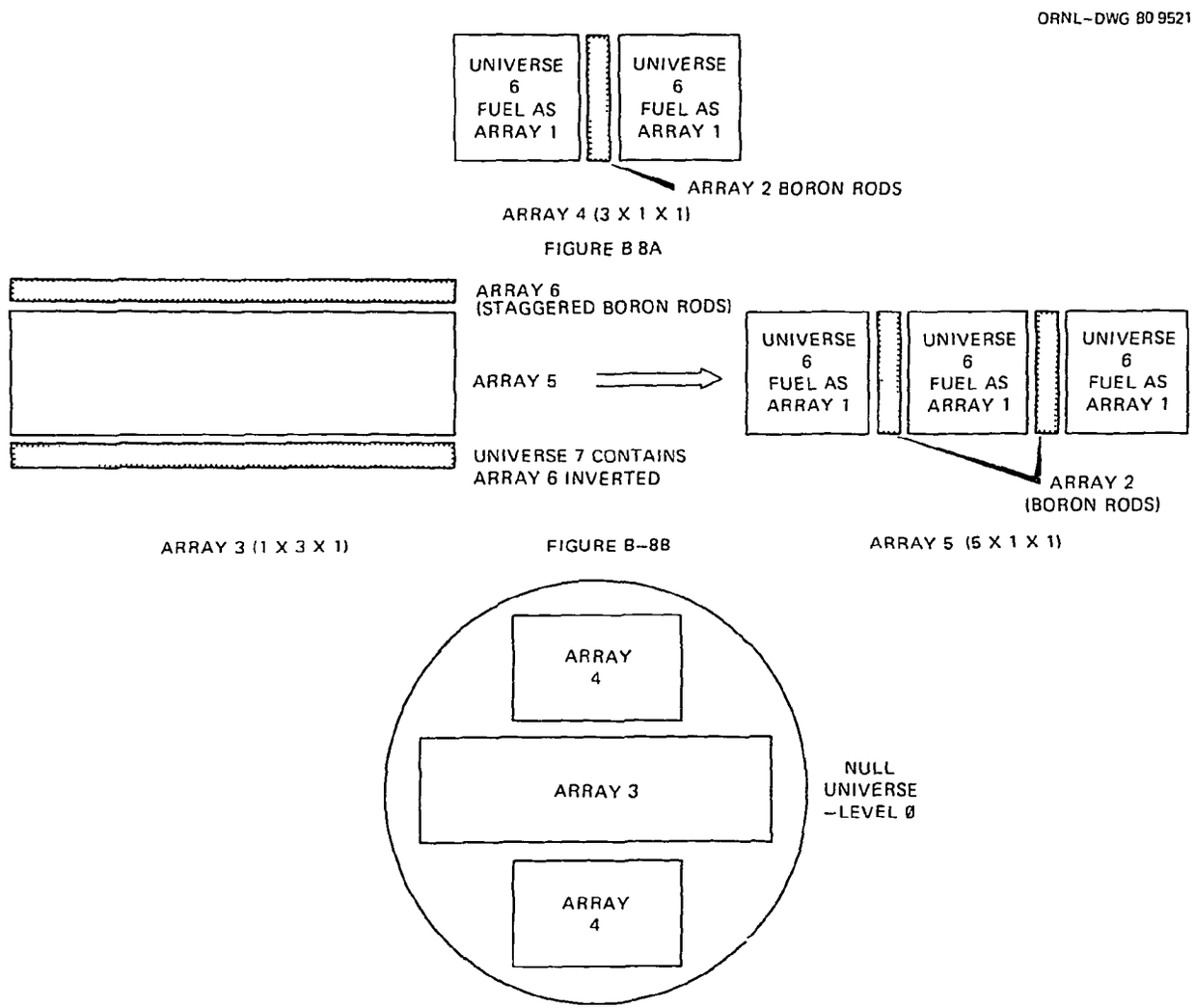

Figure 3. Array Nesting for Shipping Cask

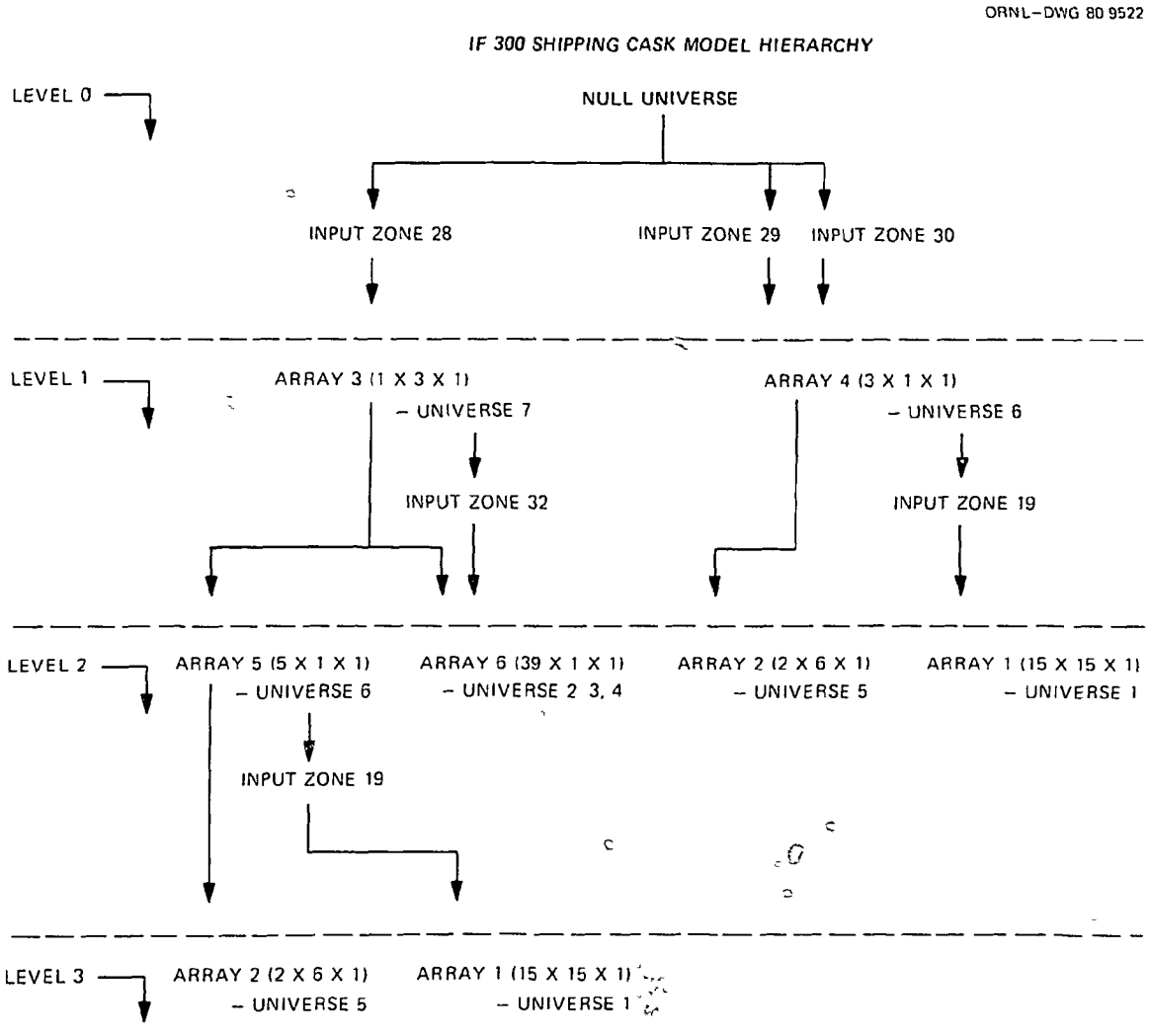

Figure 4. Levels of Geometry Nesting

REFERENCES

1. M. B. Emmett, The MORSE Monte Carlo Radiation Transport System, ORNL-4972 (February 1975).

2. M. B. Emmett and W. A. Rhoades, CARP, A Computer Code and Albedo Data Library for Use by BREESE, the MORSE Albedo Package, ORNL-TM-6503 (October 1978).

3. V. R. Cain and M. B. Emmett, BREESE-II: Auxiliary Routines for Implementing the Albedo Option in the MORSE Monte Carlo Code, ORNL-TM-6807 (July 1979).

4. M. B. Emmett, C. E. Burgart, and T. J. Hoffman, DOMINO, A General Purpose Code for Coupling Discrete Ordinates and Monte Carlo Radiation Transport Calculations, ORNL-4853 (July 1973).

5. M. B. Emmett, R. L. Childs, and W. A. Rhoades, "A Repair for Scattering Angle Truncation Errors in Transport Calculations," Trans. Am. Nucl. Soc., 33, 719 (1979).

6. S. K. Fraley, User's Guide to MORSE-SGC, ORNL-CSD-7 (March 1976).

7. R. M. Westfall, J. T. West, G. E. Whitesides, and J. T. Thomas, Criticality Analyses of Disrupted Core Models of Three Mile Island Unit 2, ORNL-CSD TM-106 (December 1979).

8. W. A. Rhoades, D. B. Simpson, R. L. Childs and W. W. Engle, Jr., "The DOT-IV Two-Dimensional Discrete Ordinates Transport Code with Space-Dependent Mesh and Quadrature," ORNL/TM-6529 (January 1979).

9. J. T. West, III, L. M. Petrie, S. K. Fraley, "KENO-IV/CG, The Combinatorial Geometry Version of the KENO Monte Carlo Criticality Safety Program," ORNL/NUREG/CSD-7, NUREG/CR-0200, (September 1979).

10. J. A. Bucholz, "SCALE: A Modular Code System For Performing Standardized Computer Analyses For Licensing Evaluation," ORNL/NUREG/CSD-2, NUREG/CR-0200, Volume 1 (January 1980).

OVERVIEW ON TRIPOLI 2

A. BAUR - L. BOURDET - G. DEJONGHE - J. GONNORD
A. MONNIER - J.C. NIMAL - T. VERGNAUD
COMMISSARIAT A L'ENERGIE ATOMIQUE - Service S.E.R.M.A.
Laboratoire de Protection - SACLAY B.P. N° 2 - 91190 GIF SUR YVETTE
FRANCE

ABSTRACT

We present in this paper the tridimensional Mcnte Carlo code TRIPOLI 2 wich solve transport problems for neutrons or gamma rays. This code is used either for shielding calculations with deep penetration or for core calculations with fixed sources or for critical or subcritical problems. The principal block diagram of the system is given.
We discribe successively the geometry characteristics, the cross sections utilization, the weighting, the source distribution and the results obtained by the code.

INTRODUCTION

TRIPOLI solves the transport equation for neutrons or gamma rays in tridimensional geometrical configurations. TRIPOLI uses the Monte Carlo method. This method allows to treat exactly the geometrical configurations, the energy losses and the scattering laws.

TRIPOLI 2 allows to treat the following problems :

- gamma transport problems
- neutron transport problems with fixed source, the problems can be time dependent or not
- critical problems without fixed source and research of multiplication factor due to fissions
- subcritical problems with fixed source and with multiplication by fission.

These problems can be separate in two types :

- first type, shielding problems essentially with deep penetration and streaming through voids. Biasing technics are used to reduce the computing time
- second type, core problems for cell calculations or for small core calculations. In this case, it is necessary to have a fine representation of the cross sections. The thermalization is also treated exactly.

In Saclay both types of application are used.

The starting of the conception of TRIPOLI[1] was in nineteen sixty five and the first version of the code was operational in sixty eight. The code was written for IBM 360.50 and used 270 kilo bytes only. It was essentialy devoted to shielding applications. The first applications we made, concerned fast breeder reactor and irradiation loops. We studied in particular the fast neutron facility HARMONIE and the fast breeder reactor PHENIX : flux on ionisation chambers and activation of the secondary sodium. We calculated also spectra and dammage rates for irradiation reactors such as PEGASE, RAPSODIE, OSIRIS, DIDO. Some shield design were made using TRIPOLI calculations.

In seventy four we added to TRIPOLI the thermalization and the fine treatment of the resonances between 6 keV and 5 eV. This addition allowed to treat cell calculations and small core calculations. The self shielding of the cross sections is now treated exactly. The cross sections were coming from UKNDL.

In seventy five we added the time to the particle parameters. We treat now time dependent problems essentialy for physical applications. The biasing was developped and we make still improvements in the biasing field.

In seventy six we added the fission and we treated the first critical problems. We made essentially benchmark for cell calculations and for instance we calculated the control rods efficiency for the reactor ORPHEE. In seventy six also, we modified TRIPOLI and its cross section file to treat gamma problems.

Finally in seventy nine, the code used ENDF/B cross sections and it was allowed to treat subcritical problems i.e. problems with external sources and multiplication per fission.

Actually we are still developping biasing technics and differential effect calculations by correlated sampling method.

It is planned to put in TRIPOLI a combinatory geometry with several level of heterogeneity. This will simplify the input data essentialy for core calculations.

TRIPOLI 2 system contains now sixty four thousand cards and forty five thousand cards for the cross section processing from ENDF/B.

THE TRIPOLI SYSTEM

Let us examine now the TRIPOLI system. The TRIPOLI system contains the code TRIPOLI itself, which solves the transport problem completely and some auxiliary codes. These auxiliary codes are facilities given to the user, but are not essential to solve a transport problem.

It has been made possible to divide the total job into separate stages. Thus the user has the option of either executing all or only a portion of the total calculation. The transfer of information from one stage to the following one is done by file such as magnetic tape or disk. This capability gives greater flexibility and security to the programm.

There are two types of stages in the TRIPOLI system : the task and the phase.

The task consists to execute TRIPOLI itself or one auxiliary code. Some very important tasks, as LINDA and TRIPOLI are divided in phases. For example, TRIPOLI is divided in six phases :

SECTA or MACROS, SECTP, GEOM, TEST GEOM, SOURCE, MONTEC. These phases are written in the lower part of the picture 1.

Let us examine now the tasks. There are in the upper part of the picture 1.

COLLFI uses one or several collision tapes produced by TRIPOLI. These tapes contain the characteristics of all events occured in the history of each particle. From this information COLLFI computes fluxes, spectra, reaction rates in several energy groups or time intervals and for several volumes in space.

MIXER carries out the management of the results from several TRIPOLI calculations (linear combination or addition of several results, concatenation of results).

ANALYSE prints and plots on a BENSON or on listing the total cross sections of the materials and the response functions used in calculating the activities. In option, ANALYSE print out the details of the table of nuclear interactions.

SPECTRE makes the plotting on a BENSON of the spectra calculated by TRIPOLI with optionally any reduction in the number of energy groups.

VISPAR visualizes histories or collisions undergone by certain particles selected from the population in accordance with certain criteria. The collision points of the particles of interest are projected on to any plane given by the user.

Among the selection criteria let us cite :

1) identification of particles which contribute to a given result in one portion of the geometry. Thus it is possible to retrace the history of these particles which makes possible to visualize the preferred passage ways of the particles contributing to the result.

2) detection of the assembly of points in phase space which correspond to a bad choice of the importance function.

VISPAR helps to choose the weighting. VISPAR uses a collision tape.

LINDA makes the management and the production of cross sections from ENDF/B. Jean GONNORD will talk to you about this program.

BIBLIO this program combines or reduces several LINDA libraries and products, if necessary, partial LINDA libraries for a given category of problems. BIBLIO prepares also the gamma rays production cross sections.

TRIPOLI makes the preparation of all data (cross section, weighting, geometry, source) used for the calculation. TRIPOLI realizes the simulation of the particle histories and prints the results : fluxes, spectra, reaction rates with their standard deviation.

FLUXPT computes the uncollided flux after each collision using the collision tape as COLLFI. From this flux, FLUXPT calculates spectra and reaction rates in several energy groups or several time intervals. FLUXPT can be use only for shielding problems.

RETRAITEMENT RETRAITEMENT is a program whose constants are analytic instructions involving results, spectra, reaction rates, from one or several TRIPOLI calculations. It makes it possible to avoid all manual calculations when the results are used. The language used in RETRAITEMENT is called FORTRI for FORMULATION TRIPOLI.

We return now to the task TRIPOLI. As we have said, this task is divided in six phases.

1) *SECTA, MACROS* the purpose of the phases SECTA and MACROS is to create a file of the nuclear constants required for the problem to be treated.

2) *SECTP* the phase SECTP has as its purpose the storage on a file of all the constants which provide for the description of the weighting.

3) *GEOM* the purpose of the phase GEOM consists in creating a file which contains the geometric input with a maximum of precalculation in the same format as the fast memory.

4) *TEST GEOM* this phase testes the geometry.

5) *SOURCE* the purpose of the phase SOURCE is to generate the characteristics of a collection of particles.

6) *MONTEC* this phase carries out the simulation of the particle histories and calculates the corresponding scores. MONTEC edits the output : fluxes, currents, reaction rates and spectra.

In option, the phase MONTEC gives : (see picture 2)

- some informations concerning the choice of the weighting
- a file containing all results used by RETRAITEMENT and SPECTRE
- a file containing all collision characteristics necessary for the programs COLLFI, FLUXPT, VISPAR. It is the collision tape. I recall you that COLLFI computes reaction rates and spectra, in volumes or on surfaces, FLUXPT calculates reaction rates and spectra at any point and VISPAR visualizes histories of particles.

Let us examine now the most important characteristics of the TRIPOLI task itself.

GEOMETRY

First the geometry. The geometry is tridimensional, it is composed by an assembly of volumes. These volumes are bounded by first and second degree surfaces. The arrangement in space is quite arbitrary.

We have nine types of boundary surfaces for a volume :

- the general planes
- the three planes perpendicular to the axis x, y, z
- the general quadratic for instance cone or ellipsoid
- the sphere
- the three cylinders with axis parallel to the axis x, y, z.

The volume consists of a single, chemically homogeneous substance and has the same weighting characteristics at every point.

We make a special treatment of geometry containing parallelipipeds whose faces are perpendicular to the principal directions Ox, Oy, Oz.

Some boundary conditions are available. These conditions are given on the external surfaces of the geometry. A particle which reaches such a surface may undergo :

- optical reflexion
- albedo
- rotation about the z axis
- translation of given components
- escape with or without recording of the characteristics of the particle.

These special conditions make it possible to treat repetitive geometries by symmetry, rotation and translation.

The picture n° 3 shows an example of geometry discribed in TRIPOLI. It is the PEGASE reactor. A special phase, called TEST GEOM, allows to test the geometry. The purpose of this phase is :

- first, to test the logic of the geometry
- second, to give the distances traversed in each region along a straight line. This possibility allows to verify the equation
- third to give a graphic print out for one cut through the geometry.

NUCLEAR DATA

Let us examine now how TRIPOLI use the nuclear data.

Two types of cross section representation are available :

- the fine multigroup representation
- the pointwise representation.

We have said in introduction that there are two types of problems: the shielding calculations and the core calculations.

For the core calculations we use pointwise cross section below 6 keV and above 5 eV with forty five thousand points in this range. Above 6 keV or below 5 eV, we use a fine multigroup representation. This allows to treat exactly the self shielding of the cross section.

For shielding calculations, we use only a fine multigroup representation of the cross sections with, for neutrons, two hundred seventy groups from fifteen MeV to the thermal region. For gamma rays we use sixty groups from 10 MeV to 10 keV.

For neutron, the data are coming from UKNDL or ENDF/B ; for gamma rays they are coming from UKNDL or from Los Alamos Laboratory (Storm et Israël LA 3753).

For neutrons the following interactions are treated :

- elastic scattering with exact anisotropy discribed by equal probability
- inelastic reaction with discrete levels
- inelastic reaction and (n, 2 n) isotropic in the center of mass system
- absorption
- fission
- thermalization with free gas model or using the frequency spectra of the molecule.

For shielding problems we can also use one group of thermal neutrons with isotropic scattering in the laboratory system. A transport correction is available.

The following interactions are treated for gamma rays :

- photoelectric effect
- pair production
- compton scattering.

The picture n° 4 shows the total neutron cross section for iron used in TRIPOLI.

The picture n° 5 shows the multigroup gamma ray production also for iron and for neutron.

WEIGHTING

I present you now the weighting in TRIPOLI. For deep penetration it is necessary to bias the game. If we consider a reactor core surrounded by a shield, the attenuation of the flux between the core and the outside boundary of the shield can be 10^{13}. If we want only thousand particles at this boundary we should have to simulate 10^{16} histories of particles. This is not possible : the computation time would be too expensive. These considerations introduce the biased game for the deep penetration For core problems, there is no difficulty : we don't need any biasing.

In TRIPOLI 2 a weight is assigned at each point X of the phase space. This weight is given by the relation (1) for one volume of the geometry :

(1) $$\Pi(X) = \Pi_{1_i}(\vec{r})\ \Pi_{2_i}(\vec{\Omega})\ \Pi_{3_i}(E)$$

for a given volume i

$\Pi_1(\vec{r})$ is the spatial component of the weight

$\Pi_2(\vec{\Omega})$ depends on the direction $\vec{\Omega}$

$\Pi_3(E)$ depends on the energy E

We define in TRIPOLI equiweight surfaces : there are surfaces where the spatial weight $\Pi_1(\vec{r})$ is constant. It is the relation (2) :

(2) equiweight surfaces S_λ : $\Pi_1(\vec{r}) = \lambda$ if $\vec{r} \in S_\lambda$

The equiweight surfaces are composed by an assembly of portions of planes, spheres, cylinders and cones. These equiweight surfaces are continuous or almost continuous.

According to this assigned weight, biasing are made to reduce the variance. The following biasing are used in TRIPOLI 2 :

- path biasing using the exponential transformation
- collision biasing for homogeneous or heterogeneous media.

The reduction of the variance is obtained by the following way : each particle has about the same contribution to the result.

SOURCE DISTRIBUTION

Let us examine now the source distribution. The source density in space energy and direction is given by the relation (3) where :

$$(3) \quad S(\vec{r}, E, \vec{\Omega}) = \sum_J \frac{H_J(E)}{\int_0^\infty H_J(E)} C_J S_J(\vec{r}) \frac{G_J(\vec{\Omega})}{\iint G_J(\vec{\Omega}) d\vec{\Omega}}$$

$\vec{r}$ position

E energy

$\vec{\Omega}$ direction

H_J is a spectrum, G_J an angular distribution and the product C_J S_J is a spatial density. This expression (3) allows to treat any distribution of sources.

The particles are emitted according to the assigned weight.

THE RESULTS

To conclude this short presentation, I give you some explanations concerning the results. The user defines some regions. Each region contains one or several volumes defined in the geometry phase. The results are averaged values or integrated values on regions or on boundary surfaces of region. The results are spectra, fluxes and reaction rates with their standard deviation.

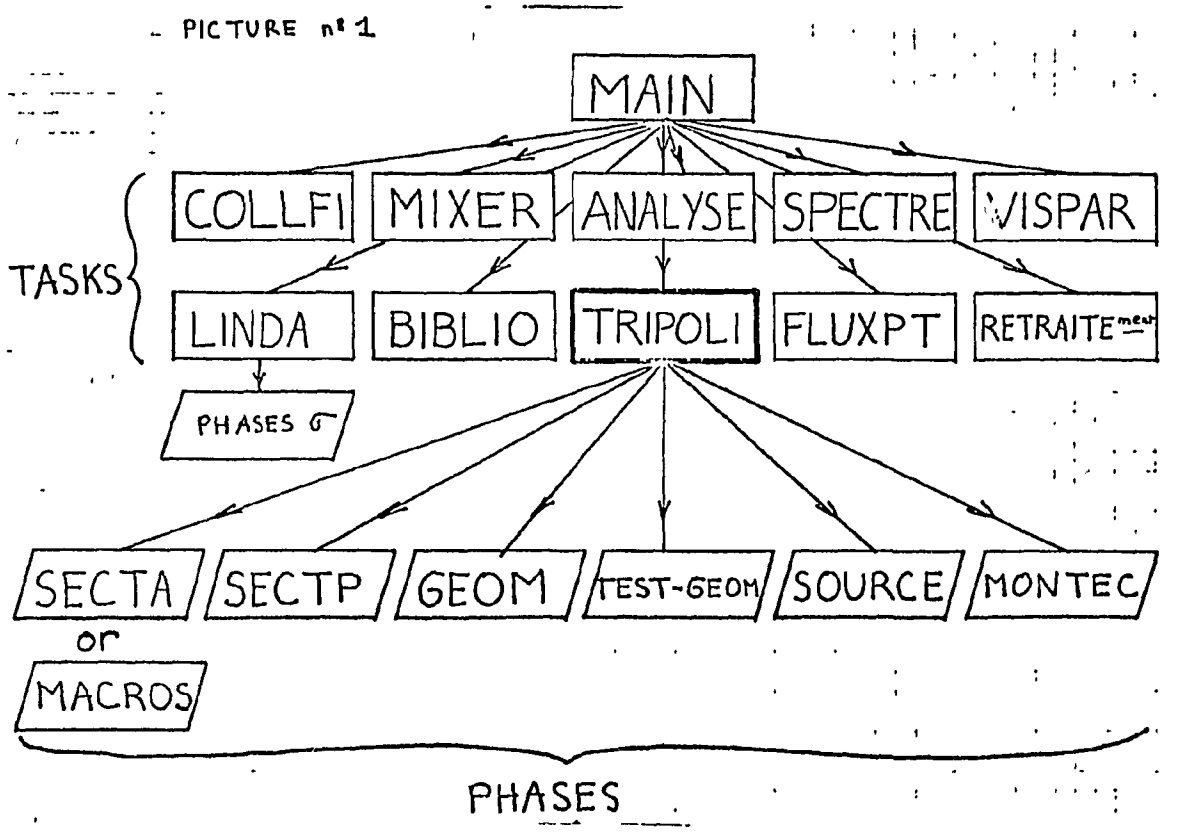

Fig. 1 - PRINCIPAL BLOCK DIAGRAM -

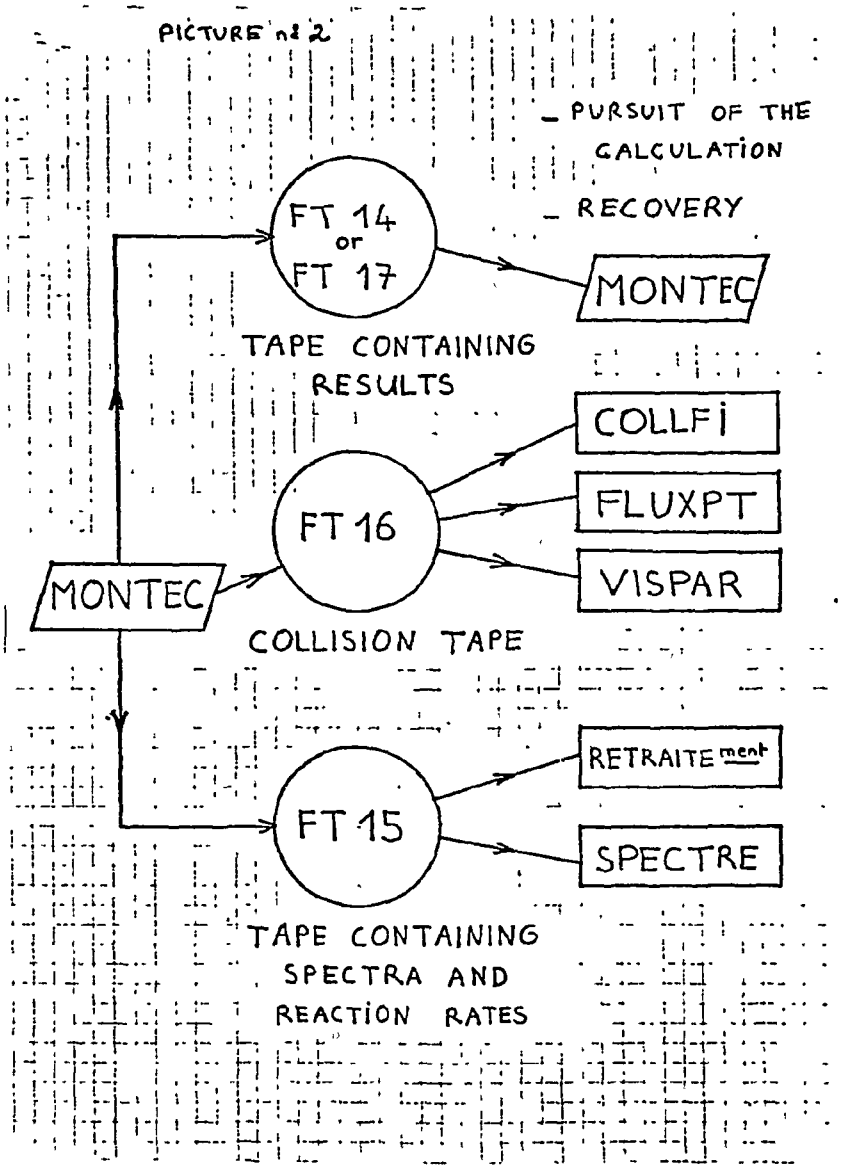

Fig 2 - CONNECTION OF THE PHASE MONTEC WITH THE AUXILIARY CODES -

Figure 3

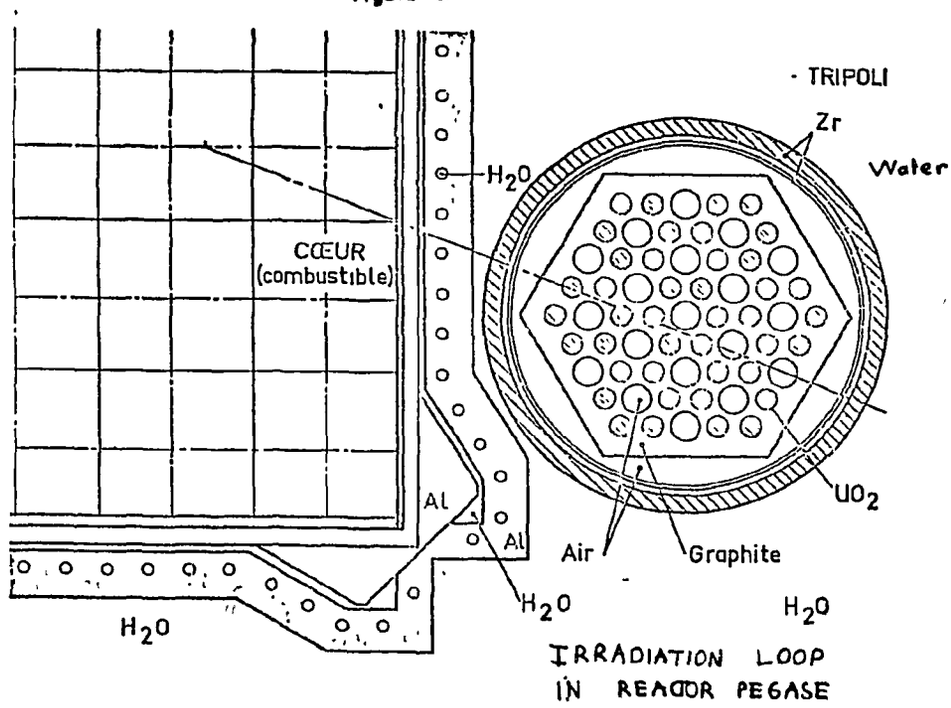

Fig 3 - AN EXAMPLE OF GEOMETRY DESCRIBED IN TRIPOLI :

AN IRRADIATION LOOP IN PEGASE REACTOR -

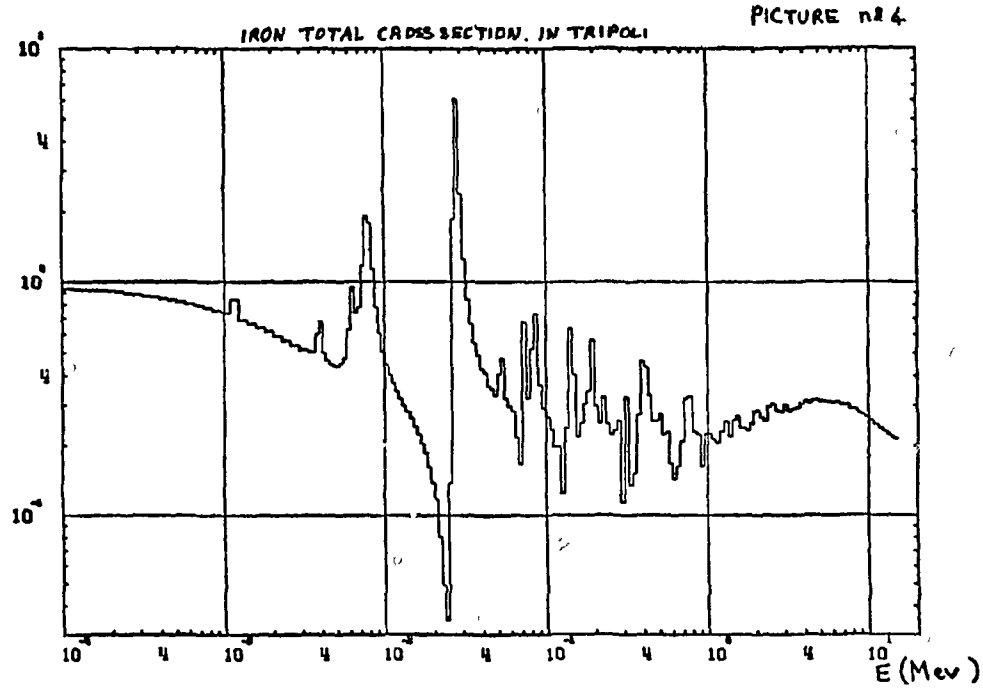

Fig 4 - MULTIGROUP CROSS SECTION IN TRIPOLI -

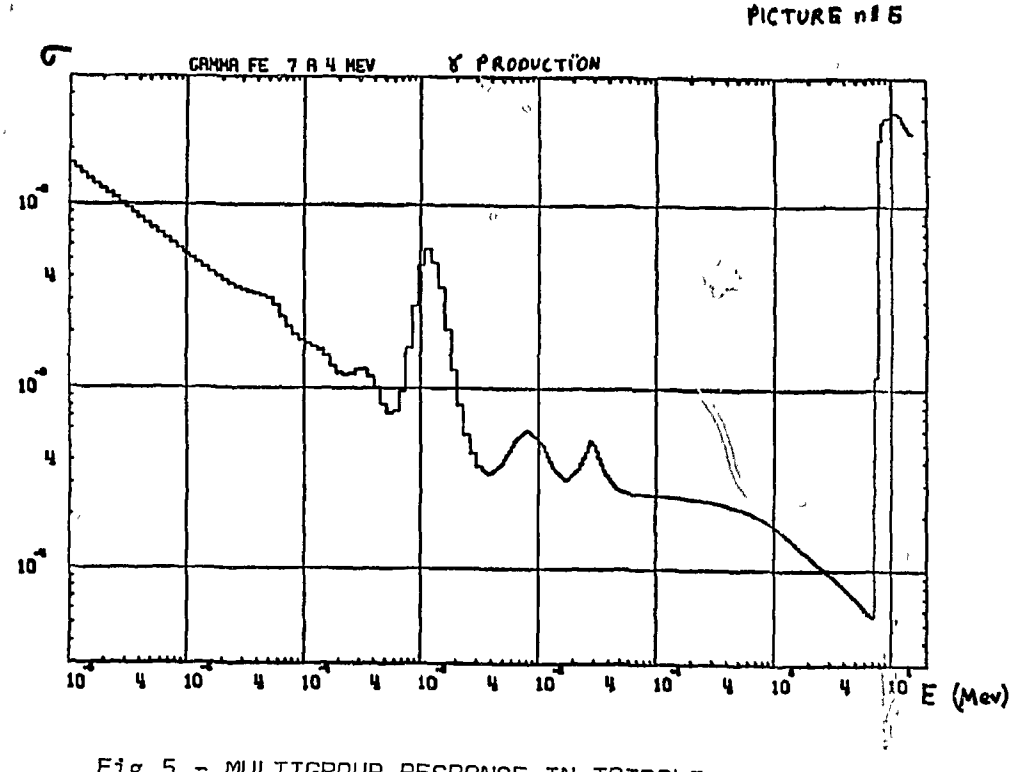

Fig 5 - MULTIGROUP RESPONSE IN TRIPOLI

REFERENCES

1 J.C. NIMAL and all.
Programme de Monte Carlo polycinétique a trois dimensions
TRIPOLI 01
Tomes 1 à 7 - Note CEA.N.1919 (September 1976)

VARIANCE REDUCTION TECHNIQES USING ADJOINT MONTE CARLO METHOD AND MONTE CARLO-MONTE CARLO COUPLING IN DEEP PENETRARION PROBLEM

Kohtaro UEKI
Ship Research Institute
Mitaca, Tokyo 181, JAPAN

ABSTRACT

The event value $W_g(\bar{r}, \hat{\Omega})$ has been derived in a form which can be obtained directry from existing adjoint Monte Carlo computer codes. It is demonstrated that the event value and the point value functions obtained from the adjoint Monte Carlo can be used as the path-length biasing and the angular biasing in the forward Monte Carlo calculation, respectively. The iterative forward-adjoint Monte Carlo method using the source biasing is employed to reduce the standard deviation. In addition, the Monte Carlo-Monte Carlo coupling technique is investigated to calculate effectively neutron streaming through the two-legged duct. Significant improvements are obtained on the collision density and on the efficiency in the duct problem.

INTRODUCTION

The Monte Carlo method is a very useful tool for solving a large class of radiation transport problem. In contrast with determistic method, geometric complexity is a much less significant problem for Monte Carlo calculations. The accuracy of Monte Carlo calculations is of course, limited by the statistical deviation of the quantity to be estimated. Especially, for the deep penetration problem where probability of contribution from a particle to the quantity of interest is small, importance sampling is indispensable to reduce the standard deviation.

It has been pointed out [1] that the adjoint solution is central to the problem of variance reduction, and the value function is always a good choice as the importance function for density biasing in the Monte Carlo caluculation. The event value and the point value functions obtained from the discrete ordinates code DOT were used as importance functions for biasing the path length and the scattering angle, respectively, of forward Monte Carlo calculations in the deep penetration problem [2,3,8]. The iterative forward-adjoint Monte Carlo was applied as a way of variance reduction for a geometrically simple problem of the air cylinder [4]. The iterative calculations produced an improvement in

the variance reduction.

In this study, an adjoint function -event value- is derived in a form which can be obtained from existing adjoint Monte Carlo codes by a minor modification. It is demonstrated that the adjoint functions - the event value and the point value functions- can be used as the path-length biasing and the angular biasing, respectively in the forward Monte Carlo calculation. The iterative forward-adjoint Monte Carlo method is employed to reduce the standard deviation in the duct problem. In addition, the Monte Carlo-Monte Carlo coupling technique is investigated to calculate neutron streaming through the two-legged annular duct installed in the JRR-4 swimming pool reactor. These calculations are performed with the Monte Carlo code MORSE, therefor the coupling technique can be entitlled as the MORSE-MORSE coupling tequnique.

MULTIGROUP BOLTZMAN TRANSPORT EQUATION

Multigroup Transport Equation for Forward Monte Carlo Method

The time-independent integral emergent particle density equation is written as :

$$\chi_g(\bar{r},\bar{\Omega}) = S_g(\bar{r},\bar{\Omega}) + \sum_{g'=g}^{I} \int_{4\pi} d\bar{\Omega}' \frac{\Sigma_s^{g'\to g}(\bar{r},\bar{\Omega}'\to\bar{\Omega})}{\Sigma_t^{g'}(\bar{r})} \int_0^\infty dR\, \Sigma_t^{g'} e^{-\beta_{g'}(\bar{r},R,\bar{\Omega}')} \chi_{g'}(\bar{r}',\bar{\Omega}'), \quad (1)$$

where $S_g(\bar{r},\bar{\Omega})$ = distribution of source particles for g-th group,
$\beta_g(\bar{r},R,\bar{\Omega})$ = optical thickness,
$\Sigma_t^g(\bar{r})$ = energy averaged total cross section for g-th group
$\Sigma_s^{g'\to g}(\bar{r},\bar{\Omega}'\to\bar{\Omega})$ = group g to group g scattering cross section ($cm^{-1}\,st^{-1}$).
$\chi_g(\bar{r},\bar{\Omega})$ = density of particles leaving a source or emerging from a real collision with phase space coordinates (group g, $\bar{r}$, $\bar{\Omega}$).

The integral equation can be expressed in a kernel form. To do this, introduce the transport operator

$$T_g(\bar{r}'\to\bar{r},\bar{\Omega}) = \int_0^\infty dR\, \Sigma_t^g(\bar{r})\, e^{-\beta_g(\bar{r},R,\bar{\Omega})} \quad (2)$$

and the collision operator

$$C_{g'\to g}(\bar{r},\bar{\Omega}'\to\bar{\Omega}) = \sum_{g'=g}^{I} \int d\bar{\Omega}' \frac{\Sigma_s^{g'\to g}(\bar{r},\bar{\Omega}'\to\bar{\Omega})}{\Sigma_t^{g'}(\bar{r})}, \quad (3)$$

$$= \sum_{g'=g}^{I} \int d\bar{\Omega}' \frac{\Sigma_s^{g'}(\bar{r})}{\Sigma_t^{g'}(\bar{r})} \cdot \frac{\Sigma_s^{g'\to g}(\bar{r},\bar{\Omega}'\to\bar{\Omega})}{\Sigma_s^{g'}(\bar{r})}, \quad (4)$$

where $\Sigma_s^{g'}(\bar{r}) = \sum_g \int d\bar{\Omega}\, \Sigma_s^{g'\to g}(\bar{r}, \bar{\Omega}' \to \bar{\Omega})$,

$\Sigma_s^{g'\to g}(\bar{r}, \bar{\Omega}' \to \bar{\Omega}) = \frac{1}{4\pi} \sum_{\ell=0}^{n} f_\ell^{g'\to g}(\bar{r}) P_\ell(\mu)$,

$f_\ell^{g'\to g}(\bar{r})$ = ℓ-th Legendre coefficient for group g to g transfer;
n = maximum order of truncation,
$\mu = \bar{\Omega}' \cdot \bar{\Omega}$, cosine of scattering angle.

Using the transport operator and the collision operator, the integral event density equation can be written as:

$$\psi_g(\bar{r}, \bar{\Omega}) = S_c^g(\bar{r}, \bar{\Omega}) + T_g(\bar{r}' \to \bar{r}, \bar{\Omega}) C_{g'\to g}(\bar{r}, \bar{\Omega}' \to \bar{\Omega}) \psi_{g'}(\bar{r}', \bar{\Omega}'), \tag{5}$$

where $S_c^g(\bar{r}, \bar{\Omega}) = T_g(\bar{r}' \to \bar{r}, \bar{\Omega}) S_g(\bar{r}', \bar{\Omega})$

$\psi_g(\bar{r}, \bar{\Omega})$ = number of collision events per unit volume at space point $\bar{r}$ experienced by particles having energies with g-th group and direction $\bar{\Omega}$.

Using the relationship $\psi_g(\bar{r}, \bar{\Omega}) = \Sigma_t^g(\bar{r}) \phi_g(\bar{r}, \bar{\Omega})$, Eq.(5) can be transformed into the integral flux density equation:

$$\phi_g(\bar{r}, \bar{\Omega}) = \frac{S_c^g(\bar{r}, \bar{\Omega})}{\Sigma_t^g(\bar{r})} + T_g(\bar{r}' \to \bar{r}, \bar{\Omega}) C_{g'\to g}(\bar{r}', \bar{\Omega}' \to \bar{\Omega}) \frac{\Sigma_t^{g'}(\bar{r}')}{\Sigma_t^g(\bar{r})} \phi_{g'}(\bar{r}', \bar{\Omega}'), \tag{6}$$

where $\phi_g(\bar{r}, \bar{\Omega})$ = time-independent group angular flux ($n/cm^2 st$).

Also, the integral emergent particle density equation is obtained with the transport and the collision operator:

$$\chi_g(\bar{r}, \bar{\Omega}) = S_g(\bar{r}, \bar{\Omega}) + C_{g'\to g}(\bar{r}, \bar{\Omega}' \to \bar{\Omega}) T_{g'}(\bar{r}' \to \bar{r}, \bar{\Omega}') \chi_{g'}(\bar{r}', \bar{\Omega}'). \tag{7}$$

Equation (7) is actually employed for the forward mode random walk in the MORSE code.

Multigroup Transport Equation for Adjoint Monte Carlo Method

It has been pointed out[4] that the derivation of the emergent adjuncton density equation described in Ref. (5) has several obscurities in terminology. Although the derivation in Ref. (4) is different from Ref. (5), it has still complexity. An easily understable procedure for the emergent adjuncton density equation is proposed in this chapter.

The point value $\chi_g^*(\bar{r}, \hat{\Omega})$ is defind[2,7,8] to be the contribution to the effect of interest of a particle that emerges from a collision or from a source at point $\bar{r}$ with energy group g and direction $\hat{\Omega}$, and the event value $W_g(\bar{r}, \hat{\Omega})$ is defined[2,7,8] to be the present and future contribution to the effect of interest of a particle that enters into a collision at point $\bar{r}$ with energy group g and direction $\hat{\Omega}$.

The integral point-value equation[5] modified by defining the direction $\hat{\Omega} = -\bar{\Omega}$ and considering the change in phase space coordinates to

occur in the reverse sense can be written as:

$$\chi_g^*(\bar{r},\hat{\Omega}) = P_g^{\chi}(\bar{r},\hat{\Omega}) + \int dR \Sigma_t^g(\bar{r}) e^{-\beta_g(\bar{r},R,\hat{\Omega})} \left[\frac{\Sigma_t^g(\bar{r}')}{\Sigma_t^g(\bar{r})}\right] \left[\sum_{g'} \int d\bar{\Omega}' \frac{\Sigma_s^{g\to g'}(\bar{r}',\hat{\Omega}-\hat{\Omega}')}{\Sigma_t^g(\bar{r}')}\right] \chi_{g'}^*(\bar{r}',\hat{\Omega}'), \quad (8)$$

where $P_g^{\chi}(\bar{r},\hat{\Omega})$ = response function of effect of interest due to a particle which emerges from a collision having phase space coordinates (group g, $\bar{r}$, $\hat{\Omega}$).

Equation (8) is designated to describe the trajectory of adjoint perticles which are called adjunctons[5] from $\bar{r}'$ to $\bar{r}$ along the $\hat{\Omega}$ direction. The transport integral operator describing the $\bar{r}\to\bar{r}'$ transport is modified to produce the following simple relationship:

$$T_g(\bar{r}\to\bar{r}',\hat{\Omega}) = T_g(\bar{r}'\to\bar{r},\hat{\Omega})\,\Sigma_t^g(\bar{r}')/\Sigma_t^g(\bar{r}) . \quad (9)$$

The new transport operator $T_g(\bar{r}'\to\bar{r},\hat{\Omega})$ is identical to the integral transport operator $T_g(\bar{r}'\to\bar{r},\hat{\Omega})$ used in the forward integral equations. Further, the numerical value associated with the collision integral operator in Eq. (8)

$$\sum_{g'}\int d\bar{\Omega}' \frac{\Sigma_s^{g\to g'}(\bar{r}',\hat{\Omega}\to\hat{\Omega}')}{\Sigma_t^g(\bar{r}')}$$

cab be interpreted as describing the $(g'\to g, \hat{\Omega}'\to\hat{\Omega})$ phase space change experienced by the adjuncton. This term identified as a new collision operator $\hat{C}_{g'\to g}(\bar{r},\hat{\Omega}'\to\hat{\Omega})$ is identical to the collision integral operator used in the forward integral equation:

$$\hat{C}_{g'\to g}(\bar{r}',\hat{\Omega}'\to\hat{\Omega}) = \sum_{g'}\int d\bar{\Omega}' \frac{\Sigma_s^{g\to g'}(\bar{r}',\hat{\Omega}\to\hat{\Omega}')}{\Sigma_t^g(\bar{r}')} = C_{g'\to g}(\bar{r}',\bar{\Omega}'\to\bar{\Omega}).$$

The point-value defining equation modified for the Monte Carlo analysis of adjunctons can be written as:

$$\chi_g^*(\bar{r},\hat{\Omega}) = P_g^{\chi}(\bar{r},\hat{\Omega}) + T_g(\bar{r}'\to\bar{r},\hat{\Omega})\frac{\Sigma_t^g(\bar{r}')}{\Sigma_t^g(\bar{r})}\hat{C}_{g'\to g}(\bar{r}',\hat{\Omega}'\to\hat{\Omega})\chi_{g'}^*(\bar{r}',\hat{\Omega}'). \quad (10)$$

Equation (10) could provide a reasonable basis for a Monte Carlo analysis of the adjoint problem. However the adjoint random walk would require the additional weight correction $\Sigma_t^g(\bar{r})/\Sigma_t^g(\bar{r})$ which would be applied after selection of the next collision site. To avoid the additional weigth correction, the following quantities are defined:

$$H_g(\bar{r},\hat{\Omega}) \equiv \Sigma_t^g(\bar{r})\chi_g^*(\bar{r},\hat{\Omega}), \quad (11)$$

$$H_g(\bar{r},\hat{\Omega}) \equiv T_g(\bar{r}'\to r,\hat{\Omega})G_g(\bar{r}',\hat{\Omega}). \quad (12)$$

Equation (12) may be written in correspondence with the relation of the event value and the point value[5]:

$$\chi_g^*(\bar{r}, \bar{\Omega}) = T_g(\bar{r} \to \bar{r}', \bar{\Omega}) W_g(\bar{r}', \bar{\Omega}) .$$

Since $\chi_g^*(\bar{r}, \hat{\Omega})$ is a flux-like variable, the new variable $H_g(\bar{r}, \hat{\Omega})$ can be regarded as an event density and $G_g(\bar{r}, \hat{\Omega})$ likes an emergent particle density. The defining equation for the adjoint event density $H_g(\bar{r}, \hat{\Omega})$ is obtained by considering the following equation:

$$\chi_g^*(\bar{r}, \hat{\Omega}) = \int_0^\infty dR \Sigma_t^g(\bar{r}') e^{-\beta_g(\bar{r}, R, \hat{\Omega})} [P_g^\psi(\bar{r}', \hat{\Omega}) + \hat{C}(\bar{r}', \hat{\Omega}' \to \hat{\Omega}) \chi_{g'}^*(\bar{r}', \hat{\Omega}')], \quad (13)$$

where $P_g^\psi(\bar{r}, \hat{\Omega})$ = response function of effect of interest due to a particle which experiences an event at group g, $\bar{r}$ and $\hat{\Omega}$,
$= P_g^\phi(\bar{r}, \hat{\Omega}) / \Sigma_t^g(\bar{r})$,
$P_g^\phi(\bar{r}, \hat{\Omega})$ = responce function of effect of interest due to an unit angular group flux.

Multiply Eq. (13) by $\Sigma_t^g(\bar{r})$ and arrange as follows:

$$\Sigma_t^g(\bar{r}) \chi_g^*(\bar{r}, \hat{\Omega}) = \int dR \Sigma_t^g(\bar{r}) e^{-\beta_g(\bar{r}, R, \hat{\Omega})} \Big[\Sigma_t^g(\bar{r}') P_g^\psi(\bar{r}', \hat{\Omega}) + \hat{C}_{g' \to g}(\bar{r}', \hat{\Omega}' \to \hat{\Omega}) \frac{\Sigma_t^g(\bar{r}')}{\Sigma_t^{g'}(\bar{r}')} \Sigma_t^{g'}(\bar{r}') \chi_{g'}^*(\bar{r}', \hat{\Omega}') \Big] . \quad (14)$$

Since $H \equiv \Sigma_t \chi^*$ and $P^\phi = \Sigma_t P^\psi$, Eq. (14) can be rewitten as :

$$H_g(\bar{r}, \hat{\Omega}) = T_g(\bar{r}' \to \bar{r}, \hat{\Omega}) \Big[P_g^\phi(\bar{r}', \hat{\Omega}) + C_{g' \to g}(\bar{r}', \hat{\Omega}' \to \hat{\Omega}) H_g(\bar{r}', \hat{\Omega}') \Big], \quad (15)$$

where

$$C_{g' \to g}(\bar{r}', \hat{\Omega}' \to \hat{\Omega}) = \hat{C}_{g' \to g}(\bar{r}', \hat{\Omega}' \to \hat{\Omega}) \frac{\Sigma_t^g(\bar{r})}{\Sigma_t^{g'}(\bar{r}')} ,$$

$$= \sum_{g'} \int d\bar{\Omega}' \frac{\Sigma_s^{g \to g'}(\bar{r}', \hat{\Omega} \to \hat{\Omega}')}{\Sigma_t^{g'}(\bar{r}')} . \quad (16)$$

A comparision of Eq. (15) with Eq. (12) reveals that

$$G_g(\bar{r}, \hat{\Omega}) = P_g^\phi(\bar{r}, \hat{\Omega}) + C_{g' \to g}(\bar{r}, \hat{\Omega}' \to \hat{\Omega}) H_{g'}(\bar{r}, \hat{\Omega}') , \quad (17)$$

and subsequent substitution of Eq. (12) into Eq. (17) yields the following density equation for the emergent adjuncton density:

$$G_g(\bar{r}, \hat{\Omega}) = P_g^\phi(\bar{r}, \hat{\Omega}) + C_{g' \to g}(\bar{r}, \hat{\Omega}' \to \hat{\Omega}) T_{g'}(\bar{r}' \to \bar{r}, \hat{\Omega}') G_{g'}(\bar{r}', \hat{\Omega}') . \quad (18)$$

A comparision of Eq. (18) with Eq. (7)

$$\chi_g(\bar{r},\bar{\Omega}) = S_g(\bar{r},\bar{\Omega}) + C_{g'\to g}(\bar{r},\bar{\Omega}'\to\bar{\Omega})\,T_{g'}(\bar{r}'\to\bar{r},\bar{\Omega}')\chi_{g'}(\bar{r}',\bar{\Omega}'), \qquad (17)$$

reveals that the two equations are identical in all respects and that the Monte Carlo realization of Eq. (18) could be accomplished by the same procedures used to simulate the integral emergent particle density equation, Eq. (7). Equation (18) is actually employed for the adjoint random walk in the MORSE code.

Derivation of Event Value Function

Divide Eq. (17) by $\Sigma_t^g(\bar{r})$:

$$\frac{G_g(\bar{r},\hat{\Omega})}{\Sigma_t^g(\bar{r})} = \frac{P_g^{\phi}(\bar{r},\hat{\Omega})}{\Sigma_t^g(\bar{r})} + \frac{C_{g'\to g}(\bar{r},\hat{\Omega}'\to\hat{\Omega})}{\Sigma_t^g(\bar{r})} H_{g'}(\bar{r},\hat{\Omega}') \qquad (19)$$

According to Eqs. (11) and (16), and using the relationship $P_g^{\phi}(\bar{r},\hat{\Omega}) = \Sigma_t^g(\bar{r})P_g^{\psi}(\bar{r},\hat{\Omega})$,Eq. (19) can be rewitten as:

$$\frac{G_g(\bar{r},\hat{\Omega})}{\Sigma_t^g(\bar{r})} = P_g^{\psi}(\bar{r},\hat{\Omega}) + \frac{\Sigma_t^{g'}(\bar{r})}{\Sigma_t^g(r)} C_{g'\to g}(\bar{r},\hat{\Omega}'\to\hat{\Omega})\chi_{g'}^*(\bar{r},\hat{\Omega}'),$$

$$= P_g^{\psi}(\bar{r},\hat{\Omega}) + \hat{C}_{g'\to g}(\bar{r},\hat{\Omega}'\to\hat{\Omega})\chi_{g'}^*(\bar{r},\hat{\Omega}'). \qquad (20)$$

A comparision of Eq. (20) with the govering equation of the event value,[5]

$$W_g(\bar{r},\bar{\Omega}) = P_g^{\psi}(\bar{r},\bar{\Omega}) + C_{g\to g'}(\bar{r},\bar{\Omega}\to\bar{\Omega}')\chi_{g'}^*(\bar{r},\bar{\Omega}'),$$

it reveals that

$$W_g(\bar{r},\hat{\Omega}) = G_g(\bar{r},\hat{\Omega})/\Sigma_t^g(\bar{r}), \qquad (21)$$

or

$$G_g(\bar{r},\hat{\Omega}) = W_g(\bar{r},\bar{\Omega})\,\Sigma_t^g(\bar{r}), \qquad (22)$$

because the probabilities associated with $(g'\to g, \hat{\Omega}'\to\hat{\Omega})$ change in the phase space coordinates during the adjoint random walk correspond to the probabilities associated with the $(g\to g', \bar{\Omega}\to\bar{\Omega}')$ change in phase space coordinate that would have been experienced by the particle transportation in the forward mode. Equation (20) has a form which can be obtained directly from existing adjoint Monte Carlo computer codes by a minor modification.

DESCRIPTION OF STANDARD PROBLEM AND BIASING TECHNIQUES

Standard Problem

The standard problem is almost the same as the Tang's[8] except the height of the cylinder, which is shown in Fig. 1. The shield configulation consists of a right circular concrete cylinder with an axial duct (void) of 15.24 cm in diameter. An isotropic monoenergetic (the first energy group) neutron source is uniformly distributed over the bottom surface. One detector is located at a point just on the z-axis which is 50.0 cm beyond the top surface. The first 14 energy groups of the 22 group structure[8] are analized on the neutron transport. The cross section set for the concrete is taken from Ref. (8), in which the maximum order of the Legendre coefficient is truncated by P_3.

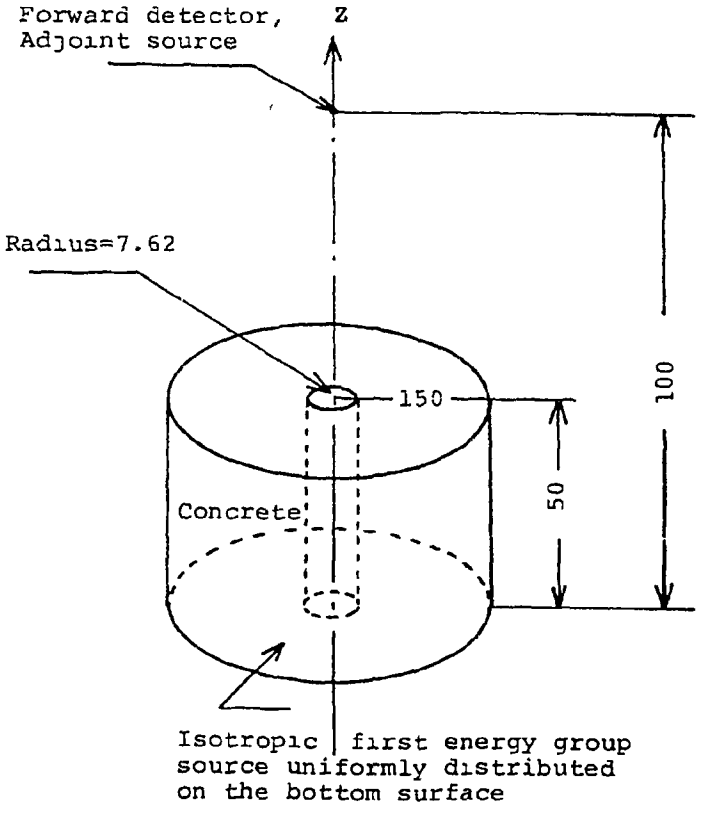

Fig. 1 Geometry of concrete cylinder with axial duct, source, detector, and adjoint source.

Source Location Biasing, Source Direction Biasing and Source Energy Biasing

It was observed by Coveyou et al.[1], that the source biasing using a reasonable a good estimate of the importance function would, in general, yield substaintial saving in variance with relatively low cost.

A particle random walk starts off with the selection of energy group, spatial position and direction from a source distribution function. The source energy is of the first group in the forward mode and the energies are from first to fourteenth group in the adjoint mode because the analysis on the neutron transport is performed only through the first 14 energy groups of the 22 group structure. Although the source is isotropic, only the upward source particles can contribute to the answer in the forward mode and only the source particles entered into the glaring angle spreded to the top of the cylinder can contribute to the answer in the adjoint mode. As for the source spatial location in the forward mode, particles which originate inside and around the duct may be more important and as for the source direction in the adjoint mode, particles which enter into inside and around the duct may be more important because they may penetrate deeper into the shield by streaming through the duct. Thus, the source location biasing and the source direction biasing were employed in this study. Since the energy flux at a detector depends on geometry and materials of the shield, the selection of energy group using the altered distribution function obtained from the forward mode calculation is more proper than the flat distribution in the adjoint mode. Russian roulette and splitting were employed routinely in all the calculations performed.

Angular Probability Biasing

The subroutine COLISN in the MORSE code is called at each collision site to determine the outgoing energy group and the outgoing direction. To carry out the angular probability biasing, the subroutine COLISN was modified to use the region averaged point value from the cards prepared by the adjoint mode calculation of the MORSE code. In the modified COLISN subroutine, the outgoing energy is still selected from the down scattering matrix, but the outgoing direction is selected from the biased angular distribution function given by the followings[3,8].

$$\gamma^{g\to g'}(\bar{r}, \hat{\Omega}\to\hat{\Omega}') = P_i \chi^*_{g'}(\bar{r}, \hat{\Omega}_i') \Big/ \sum_{i=1}^{N} P_i \chi^*_{g}(\bar{r}, \hat{\Omega}_i') \quad i = 1, \quad N, \qquad (23)$$

where $\gamma^{g\to g'}(\bar{r}, \hat{\Omega}\to\hat{\Omega}')$ = biased angular distribution function,

$$= \frac{\Sigma_s^{g\to g'}(\bar{r}, \hat{\Omega}\to\hat{\Omega}')}{\Sigma_s^{g\to g'}(\bar{r})} \chi^*_{g'}(\bar{r}, \hat{\Omega}') \Big/ \int_{4\pi} \frac{\Sigma_s^{g\to g'}(\bar{r}, \hat{\Omega}\to\hat{\Omega}')}{\Sigma_s^{g\to g'}(\bar{r})} \chi^*_{g}(\bar{r}, \hat{\Omega}') d\hat{\Omega}',$$

P_i = probability that polar angle $\cos\mu_i$ will selected.

Then the statistical weight of the emergent particles are corrected by the following :

$$WT_c = \sum_{i=1}^{N} P_i \chi^*_{g'}(\bar{r}, \hat{\Omega}'_i)/\chi^*_{g'}(\bar{r}, \hat{\Omega}'_j) , \tag{24}$$

where the direction j has been selected from the biased distribution function given by Eq. (23).

Path Length Biasing

The path length biasing technique utilizes the event value as an importance function to select particle flight paths. To implement the path length biasing in the MORSE code, the subroutine NXTCOL was rewritten. When a particle emerges from a collision site with a given energy group and direction, its flight trajectory is determined by the subroutine REGION which calculates the regions that this particle may go through and corresponding track lengths within the regions, then returns to NXTCOL. Then the event value corresponding to the direction closest to the particle's direction can be determined for each region. Now that the event values and these regions are known, the selection of the path length (or the next collision site) can be achieved from the biased path length distribution function by the followings[2,8]:

$$\begin{aligned} T^*_g(\bar{r} \to \bar{r} + R\hat{\Omega})dR &= (e^{-\eta} W_1/NF)d\eta \quad 0 \leqq \eta < \eta_1 , \\ &= (e^{-\eta} W_2/NF)d\eta \quad \eta_1 \leqq \eta < \eta_2 , \\ &\cdots\cdots\cdots \\ &= e^{-\eta} d\eta \quad \eta_n \leqq \eta < \infty . \end{aligned} \tag{25}$$

The statistical weights of the biased particles are corrected by the followings:

$$WT_c = \frac{e^{-\eta}}{\frac{W_i}{NF}\int_{\eta_{i-1}}^{\eta_i} e^{-\eta} d\eta \; \frac{e^{-\eta}}{\int_{\eta_{i-1}}^{\eta} e^{-\eta} d\eta}} = \frac{NF}{W_i} , \tag{26}$$

where NF = normalization factor: $\frac{1}{1-e^{-\eta_n}}\left[\int_0^{\eta_1} e^{-\eta} W_1 d\eta + \cdots + \int_{\eta_{n-1}}^{\eta} e^{-\eta} W_n d\eta\right]$,

W_i = event value of region i.

IMPLEMENTATION, RESULTS AND DISCUSSIONS

Application of Event-Value Path-Length Biasing and Point-Value Angular Biasing

The event value and the point value were calculated by summing all the particle's weight going into a collision and emerging from a collision, respectively, in the calculation of the standard shielding problem by the adjoint Monte Carlo method. These procedures were used in the modified subroutine named MORSE in the MORSE code. Actual forms of the event value and the point value which can be obtained from an adjoint Monte Carlo calculation are described in Ref. (10).

A comparision of three MORSE calculations is shown in Table 1. The first is with the exponential transform, the secound with the angular biasing and the exponential transform, and the last with the path-length biasing. It is noted that when employing the event-value path-length biasing or the point-value angular biasing, the fractional standard deviation (f.s.d.) of the total fast-neutron flux at the detector is reduced approximately 15% as compared with the f.s.d. using only the exponential transport, however the f.s.d. of the uncollided fast-neutron flux is reduced by a factor of 6.5 in comparision with the f.s.d. obtained from the calculation using only the exponential transform. The total fast-neutron flux obtained from the calculation using only the exponential transform is regarded as underestimate as compared with the results in Table 2. On the other hand, the total flux obtained from the calculation using the event-value path-length biasing or point-value angular biasing is recognized as reasonable in comparision with the results given in Table 2.

Table 1 Fast-neutron flux† of forward Monte Carlo calculations with event value and point value of duct problem

Biasing schemes	Detector		
	Uncollided flux	Total flux	$\sigma^2 T^{(b)}$
Exponential transform with PATH 0.5	1.0365 8 (0.59317)[a]	1.6800 7 (0.16669)	0.2058
Point-value angular biasing, source location biasing and PATH=0.5	2.3299 8 (0.09016)	2.3793 7 (0.14121)	0.1672
Event-value path-length biasing and source location biasing	2.5880 8 (0.09091)	2.4082-7 (0.13810)	0.2033

† Unit: n/cm² per source neutron
(a) Read as 1.0365×10^{-8}, with fractional standard deviation of 0.5917
(b) $\sigma^2 T$: Efficiency (σ: Fractional standard deviation in percents, T: Total computation time in minutes)
For each calculation, 1,000 source particles were generated

Iterative Forward-Adjoint Monte Carlo Calculation

The iterative forward-adjoint Monte Carlo calculations were started off with the 1F forward mode calculation. The forward obtained from the 1F calculation was used as the source energy distribution function of the 1A adjoint mode calculation, and then the adjoint flux obtained from the 1A adjoint mode calculation was likewise used as the source location

distribution function of the following 2F forward mode calculation. The source direction biasing was employed independently in the adjoint mode of the iterative adjoint-forward Monte Carlo calculations. These procedures were applied till the 5A adjoint mode calculations. The exponential transport. PATH=0.5 in the MORSE code was employed in all calculations. Table 2 shows the fluxes obtained from the iterative forward-adjoint Monte Carlo calculations at the detector.

Table 2 Fast-neutron fluxes of iterative forward-adjoint Monte Carlo calculations with adjoint flux and energy spectrum for source biasing of duct problem

Iterative mode	Biasing schemes	Detector		
		Uncollided flux	Total flux	σ^2T[b]
1F	Source location biasing with the Tang's[c] step function and exponential transform with PATH=0.5	2.5985-8 (0.03381)[a]	2.2546-7 (0.27271)	0.5662
1A	Source direction biasing, source energy biasing with energy spectrum of the 1F and PATH=0.5	2.1975-8 (0.17160)	2.3484-7 (0.18345)	0.2379
2F	Source location biasing with adjoint flux of the 1A and PATH=0.5	2.7038-8 (0.08945)	2.5014-7 (0.14960)	0.1829
2A	Source direction biasing, source energy biasing with energy spectrum of the 2F and PATH=0.5	2.8258-8 (0.16878)	1.9338-7 (0.12900)	0.1116
3F	Source location biasing with adjoint flux of the 2A and PATH=0.5	2.6684-8 (0.06731)	2.1498-7 (0.12716)	0.1274
3A	Source direction biasing, source energy biasing with energy spectrum of the 3F and PATH=0.5	2.5760-8 (0.12619)	2.4839-7 (0.11139)	0.0884
4F	Source location biasing with adjoint flux of the 3A and PATH=0.5	2.7737-8 (0.08407)	1.9947-7 (0.13785)	0.1550
4A	Source direction biasing, source energy biasing with energy spectrum of the 4F and PATH=0.5	2.7559-8 (0.13601)	2.4153-7 (0.11490)	0.0891
5F	Source location biasing with adjoint flux of the 4A and PATH=0.5	2.5591-8 (0.08577)	2.1499-7 (0.09640)	0.0788
5A	Source direction biasing, source energy biasing with energy spectrum of the 5F and PATH=0.5	2.2911-8 (0.18650)	2.3047-7 (0.12792)	0.1214

F Forward mode A Adjoint mode

† Unit=n cm^2 per source neutron

(a) Read as 2.5985×10^{-8}, with fractional standard deviation of 0.03381

(b) σ^2T Efficiency (σ Fractional standard deviation in percents, T Total computation time in minutes)

(c) *ORNL TM-3414*

1,000 source particles were generated for forward mode and 2,000 source particles were generated for adjoint mode.

The f.s.d.'s of the 5F and 5A calculations are a factor of 2.8 better than the 1F calculation and a factor of 1.7 better than the 1A calculation in Table 2, respectively. In addition, the efficiencies[9], σ^2T's of the 5F and 5A calculations are approximately a factor of 7 better than the 1F calculation and that of 3 better than the 1A calculation in Table 2, respectively. It is estimated that the iterative number of 3 (i.e. 3F or 3A) is proper to obtain the sufficiently improved distribution function and the f.s.d. because there is no remarkable improvement after the successive iteration in Table 2.

MONTE CARLO-MONTE CARLO COUPLING TECHNIQUE

Two-Legged Annular Duct Problem

The experiment on radiation streaming was performed with the two-legged annular duct installed in the JRR-4 swimming pool reactor.[6] Fig.2 shows the calculated configuration for the experiment. The dimensions of the two-legged annular duct are 180 cm height in the first-leg and 140 cm height in the second-leg, and 20 cm in outer-radius and 10 cm in inner-radius. The inside of the annular duct is filled with air in the Case-I experiment and with water in the Case-II experiment. The outside of the annular duct is filled with air in both the Case-I and the Case-II experiment. The distance from the center of the JRR-4 core to the entrance of the annular duct is 69 cm. The cross section set for the calculation is taken from the ENDF-B/IV libraly and corrupted to 15 groups with the ANISN code, in which the maximun order of the Legendre coefficient is truncated by P_5. The first 14 energy groups of the 15 group structure are analyzed on the neutron transport.

Monte Carlo-Monte Carlo Coupling Technique; MORSE-MORSE Coupling Technique

It is expected that the probability of contribution of neutrons originated in the JRR-4 core is small for the streaming through the annular duct shown in Fig. 2. Therefor, the Monte Carlo-Monte Carlo coupling technique is investigated to improve the standard deviation and the efficiency due to the increasing of collision density in and around the annular duct. In the first Monte Carlo calculation, a pseudo disk is placed as a disk detector at 5 cm distance in front of the entrance of the annular duct, as shown in Fig. 2. The disk serves as the source plane in the secound Monte Carlo calculation. The angular flux $\phi_g(\bar{r}, \bar{\Omega})$ at the pseudo disk is reserved in the first calculation, then the reserved flux is employed as the source distribution $S_g(\bar{r}, \bar{\Omega})$ of the source plane in the secound calculation. Therefor, this coupling technique may be called as Monte Carlo-Monte Carlo coupling technique. All the calculations were performed with the Monte Carlo code MORSE in this study, thus the technique can be entitlled as MORSE-MORSE coupling technique. The subroutine NESXE(N) is developed as a estimator of the disk detector in the first calculation and the subroutines SOURCE and SDATA are modified as the pseudo disk can be used as the source plane in the secound calculation.

Fig. 3 shows the comparision of measured[6] and calculated $Ni(n,p)$ reaction rates to the experiment shown in Fig. 2. Fairly good agreements are obtained over all the detector locations. Especially the standard deviations of the detectors located outside of the first-leg of the annular duct (filled with air) are less than approximately 0.1. Computation time to each detector is less than 5 minutes for 8000 histories by FACOM M-200 computer.

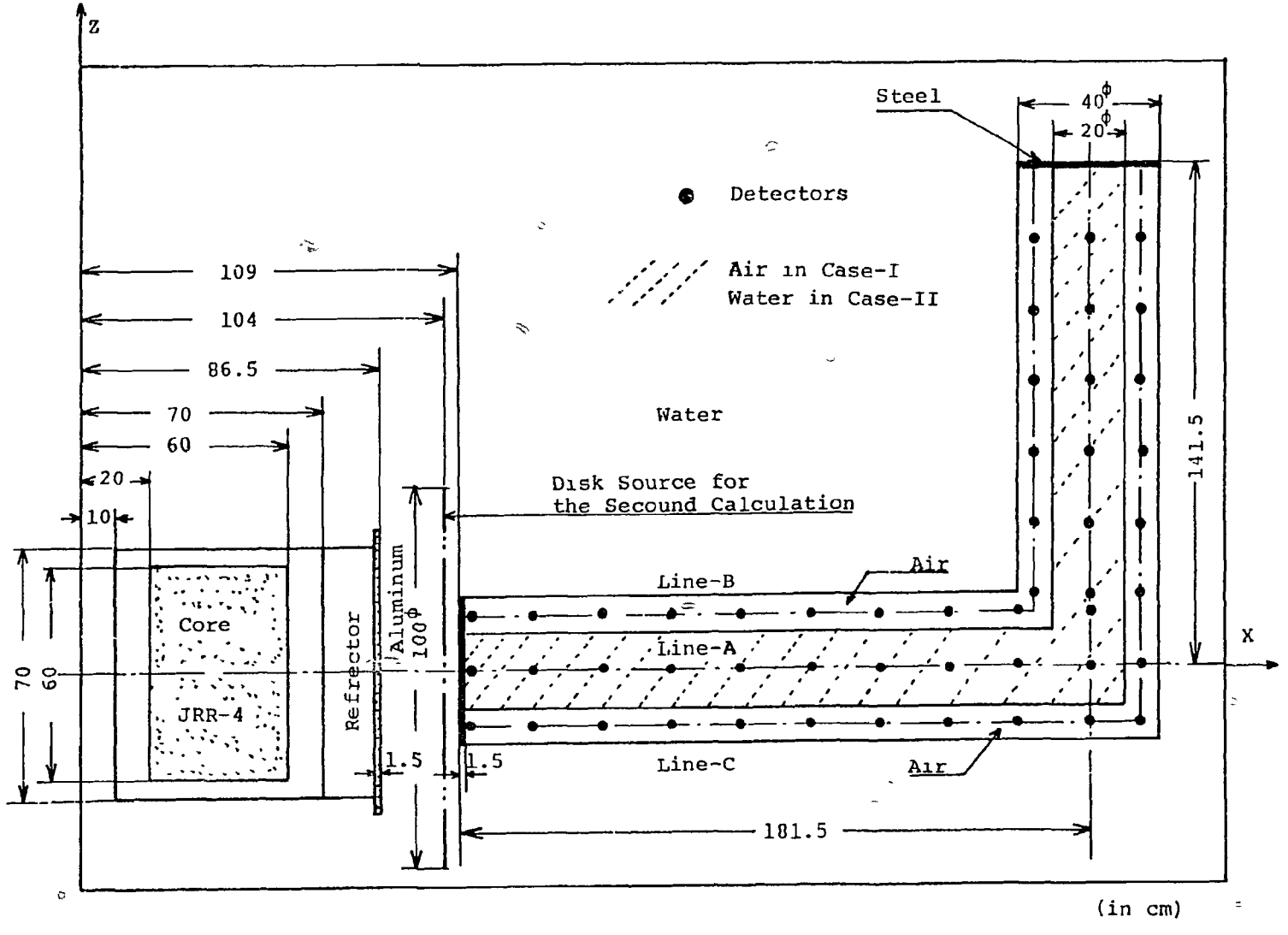

Fig. 2 Calculated model for the JRR-4 experiment.

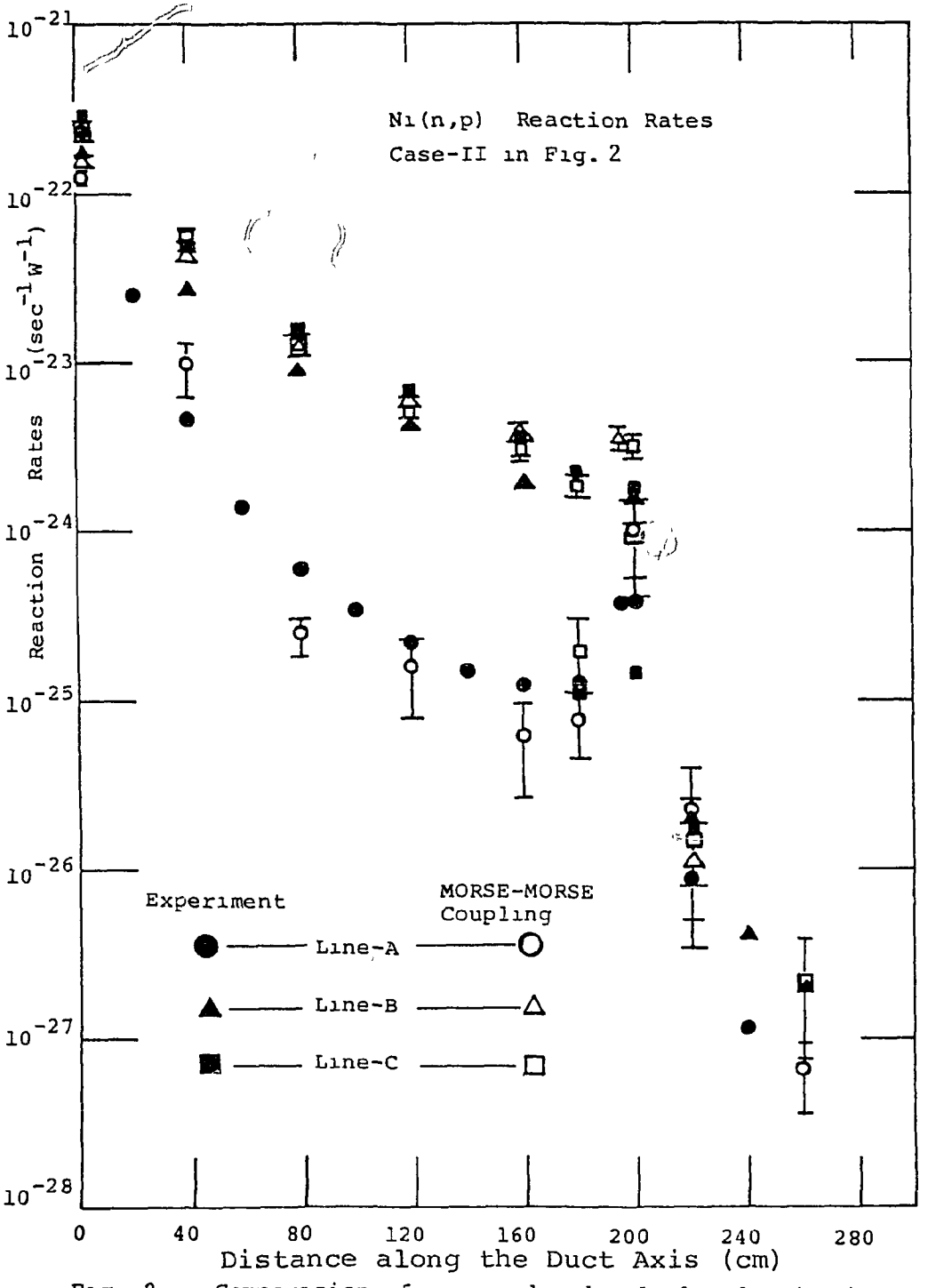

Fig. 3 Comparision of measured and calculated Ni(n,p) reaction rates. Present Monte Carlo calculation employs the MORSE-MCRSE coupling technique.

CONCLUSIONS

The event value $W_g(\vec{r}, \hat{\Omega})$ is derived in a form which can be obtained directly by a minor modification from existing adjoint Monte Carlo codes. It is demonstrated that the event value and the point value functions can be employed as importance functions for the path-length biasing and the angular biasing in the forward Monte Carlo calculation, respectively. These value functions obtained from the adjoint Monte Carlo calculation can be applied directly as importance functions in the forward Monte Carlo calculation.

The iterative forward-adjoint Monte Carlo method using the source biasing is effective to reduce the f.s.d. and to obtain the improved distribution functions by a relatively low cost. The source location biasing and the source direction biasing are substantially effective to reduce the f.s.d. in the standard problem.

It is revealed that the Monte Carlo-Monte Carlo coupling technique is effective to reduce the f.s.d. especially in a radiation streaming problem in which the entrance of the duct is apart from the source of particles.

REFERENCES

1. R. R. Coveyou, et al., Adjoint and Importance in Monte Carlo Application, Nucl, Sci. Eng., 27,219 (1967).

2. J. S. Tang, et al., Monte Carlo Shielding Calculation Using Event-Value Path-Length Biasing, idid., 62,617 (1977).

3. idem, Angular Biasing of the Collision Process in Multigroup Monte Carlo Calculations, idid., 64,837 (1977).

4. N. R. Byrn, Iterative Forward-Adjoint Monte Carlo Solutions of the Boltzman Transport Equation, Thesis, Georgia Inst. of Technol., (1976).

5. E. A. Straker, et al., The MORSE Code: A multigroup Neutron and Gamma-Ray Monte Carlo Transport Code, ORNL-4585, (1970).

6. T. Miura, et al., Measured and Calculated of Radiation Streaming through Annular Duct, Papers Ship Research Institute(in Japanese), Vol. 16, No. 6,(1979).

7. D. C. Irving, The Adjoint Boltzman Transport Equation and Its simulation by Monte Carlo, ORNL-TM-2879, (1970).

8. J. S. Tang, et al., Methods of Monte Carlo Biasing Using Two-Dimensional Discrete ordinates Adjoint Flux, ORNL-5414, (1976).

9. M. H. Kalos., Importance Sampling in Monte Carlo Shielding Calculation, I, Neutron Penetration through Thick Hydrogen Slabs, Nucl. Sci. Eng., 16, 227 (1963).

10. K. Ueki and P. N. Stevens, Variance Reduction Techniques Using Adjoint Monte Carlo Method in Shielding Problem, J. Nucl. Sci. Technol., 16, 41 (1979).

APPLICABILITY OF MONTE CARLO CODE KENO-IV

H. Yamakoshi
Ship Research Institute, Ministry of Transport of JAPAN
6-38-1. Shinkawa, Mitaka-Shi, Tokyo, JAPAN

ABSTRACT

Experimental data on criticality of a subcritical assembly was analyzed by Monte Carlo code KENO-IV for the purpose of verifying applicability of the code in the calculation of multiplication factor K_{eff} for hetorogeneous systems consisting of fuel rods about two hundreds.

Analysis was focused on studying influence of difference in adopted lattice constants upon calculated K_{eff}. Two sets of lattice constants were generated from group constants calculated by a transport code WIMS-D; One was generated with transport approximation. The other was , on the other hand, without the transport approximation, i.e. diffusion approximation.

Following conclusions are obtained. (1) The transport approximation is inevitable for generating lattice constants for KENO-IV calculation. (2) Applicability of KENO-IV is dependent much on lattice constants used.

INTRODUCTION

In general speaking, Monte Carlo code KENO-IV is thought to be powerful for criticality analysis of neutron multiplication systems with strong heterogeneity. In the case of system consisting of few numbers of fuel rods, detailed geometry of each fuel rod is described by input data fed to the code KENO-IV. However, as the number of fuel rods increases, one can not give detailed description of geometry for each fuel rod to the input data because of limited machine memory. In such case, one is obliged to homogenize the system by assigning lattice constants for fuel rods on each position of fuel rod as is usual procedure.

Aim of this report is to show influence of adopted lattice constants upon K_{eff} calculated by the code KENO-IV. As a result, applicability of this code will be discuused.

In what follows, experimental data[1] will be shown at first. Next will be explanation of procedure for genarating lattice constants. The procedure for performing transport approximation will also be shown. Calculated K_{eff} will be shown in the 3rd section with discussion on applicability of the code KENO-IV. Concluding remarks come at the last section.

EXPERIMENTAL DATA

Low enriched 225 fuel rods are soaked[1] in light water making squared array of 15x15. Table 1 shows lattice structure of effective unit cell.

Table 1. Lattice Structure

Lattice Pitch (cm)	Fuel Radius (cm)	Inner Radius of Cladding (cm)	Outer Radius of Cladding (cm)	Effective Radius (cm)	V_{water}/V_{fuel} [a]
2.293	0.625	0.6325	0.7085	1.2937	3.0

[a] Water to fuel volume ratio

Criticality is attained for water level of 90.65 cm at 15.6°C and of 90.56 cm at 16°C. Their avaraged value is 90.6 cm.

Reflector savings for axial direction z and horizontal direction r are 11.1 $\pm$ 0.5 (cm) and 14.0 $\pm$ 0.8 (cm), respectively. Buckling B_z for axial direction is given by:

$$B_z^2 = [\pi/(90.6 \pm 11.1)]^2 \quad (1)$$

Buckling B_r for horizontal direction is given by:

$$B_r^2 = [2.405/(R + 14.2/2)]^2 \quad (2)$$

where $R = (2.293 \times 15)^2/\pi$

LATTICE CONSTANTS

A transport code WIMS-D was used to calculate neutron flux for 69-group structures with attached cross section data library. Obtained neutron flux was used to calculate group constants for neutrons in 10-group structures. Finally, region averaged 3-group constants were obtained for each region. Table 2 shows meshing scheme for each region in an unit cell. Tables 3 and 4 show group structures for the 10- and 3- groups, respectively. Table 5 shows lattice constants as output from the code WIMS-D. Table 6 shows lattice constants in transport approximation.

In the transport approximation, transport cross section Σ_{tr} was defined as follows in terms of diffusion coefficient D

$$\Sigma_{tr} \equiv D/3 \quad (3)$$

As a result of definition of the transport cross section by equation 3, values of cross sections were slightly changed. These changes were compensated by a sort of scattering cross section Σ_s defined by following relations:

$$\left.\begin{aligned} \Sigma_{tr} &= \Sigma_a + \Sigma'_s \\ \Sigma_{tot} &= \Sigma_a + \Sigma_s \end{aligned}\right\} \qquad (4)$$

As a result, cross section $\Sigma_s^{i\to i}$ obtained by following substitution was adopted as scattering cross section from group i to group i itself.

$$\Sigma_s^{i\to i} - (\Sigma_{tot}^{i} - \Sigma_{tr}^{i}) \longrightarrow \Sigma_s^{i\to i} \qquad (5)$$

Where the leftest scattering cross section is just output from WIMS-D code.

Table 2. Meshing Scheme of Unit Cell

Region	Material	Radius(cm)	Meshes	Mesh Width(cm)	Temp.
1	Pellet	0.6250	5	0.125	20°C
2	Air Gap	0.6325	1	0.0075	20°C
3	Aluminum	0.7085	3	0.02533	20°C
4	L. Water	1.2937	6	0.09753	20°C

CALCULATED K_{eff}

Table 7 shows results of criticality analysis. In the present analysis, the quantity K_{eff} was also calculated by CITATION code, as well as KENO-IV code. Lattice constants without transport approximation was used for CITACION calculation. Hansen-Roach 16-group constants were used for calculation of K_{eff} by the KENO-IV code ,too.

It should be noticed that application of lattice constants in transport approximation gives very good explanation of experiment, while lattice constants in diffusion approximation, i.e. without transport approximation, fails in explanation of experiment by KENO-IV calculation.

CITAION code and KENO-IV code with Hansen-Roach 16-group library give fairly good result.

Conclusion

Transport approximation is inevitable for generation of lattice constants for KENO-IV code. Applicability of KENO-IV code depends much on lattice constants adopted.

Table 3

10-Energy Group Structure

GN	Lower Energy Limit
1	821.0 KeV
2	5.53 KeV
3	3.3 eV
4	0.625 eV
5	0.350 eV
6	0.220 eV
7	0.100 eV
8	0.050 eV
9	0.010 eV
10	0.0 eV

Table 4

3-Energy Group Structure

GN	Lower Energy Limit
1	5.53 KeV
2	0.625 eV
3	0.0 eV

Table 5

Lattice Constants Obtained by WIMS-D

(For Fuel Region)

GN	D	Σ_a	$\nu\Sigma_f$	Σ_t
1	1.3233+0	2.6007-3	3.8732-3	4.8815-1
2	6.8094-1	1.5921-2	8.3484-3	1.1585+0
3	2.3323-1	7.6489-2	1.1314-1	2.3565+0

GN	$\Sigma_s^{\rightarrow 1}$	$\Sigma_s^{\rightarrow 2}$	$\Sigma_s^{\rightarrow 3}$
1	4.3280-1	5.2746-2	5.0982-6
2	0.0	1.0460+0	9.6610-2
3	0.0	3.3365-4	2.2797+0

GN stands for Group Number

(For Water Reflector Region)

GN	D	Σ_a	$\nu\Sigma_f$	Σ_t
1	1.5904+0	2.5594-4	0.0	5.6588-1
2	6.0454-1	9.0793-4	0.0	1.4794+0
3	1.6042-1	1.8894-2	0.0	3.0756+0

GN	$\Sigma_s^{\rightarrow 1}$	$\Sigma_s^{\rightarrow 2}$	$\Sigma_s^{\rightarrow 3}$	
1	4.931 -1	7.246 -2	8.845 -6	
2	0.0	1.327 +0	1.516 -1	P_0
3	0.0	7.821 -5	3.0566+0	

GN	$\Sigma_s^{\rightarrow 1}$	$\Sigma_s^{\rightarrow 2}$	$\Sigma_s^{\rightarrow 3}$	
1	6.690 -1	4.411 -2	6.086 -8	
2	0.0	2.535 +0	1.881 -1	P_1
3	0.0	6.024 -4	3.057 +0	

Table 6.

Lattice Constants Used in KENO-VI

(For Fuel Region)

GN	D	Σ_a	$\nu\Sigma_f$	Σ_{tr}
1	1.3233+0	2.6007-3	3.8732-3	2.5190-1
2	6.8094-1	1.5921-2	8.3484-3	4.8952-1
3	2.3323-1	7.6489-2	1.1314-1	1.4292+0

GN	$\Sigma_s^{\rightarrow 1}$	$\Sigma_s^{\rightarrow 2}$	$\Sigma_s^{\rightarrow 3}$
1	1.9655-1	5.2746-2	5.0982-6
2	0.0	3.7697-1	9.6610-2
3	0.0	3.3365-4	1.3524+0

(For Water Reflector Region)

GN	D	Σ_a	$\nu\Sigma_f$	Σ_{tr}
1	1.5904+0	2.5594-4	0.0	2.0959-1
2	6.0454-1	9.0793-4	0.0	5.5139-1
3	1.6042-1	1.8894-2	0.0	2.0779+0

GN	$\Sigma_s^{\rightarrow 1}$	$\Sigma_s^{\rightarrow 2}$	$\Sigma_s^{\rightarrow 3}$
1	1.3681-1	7.246 -2	8.845 -6
2	0.0	3.990 -1	1.516 -1
3	0.0	7.821 -5	2.0590+0

Table 7. Calculated K_{eff}

Code Name	Group Constants	K_{eff}	Comments
KENO-IV	Hansen-Roach (16-Energy Groups)	1.03230 ± 0.006	
KENO-IV	Output from WIMS-D Code	1.13507 ± 0.007	Without Transport Approximation
KENO-IV	Output from WIMS-D Code	1.01686 ± 0.006	With Transport Approximation
CITATION	Output from WIMS-D Code	1.00448	

REFERENCES

1. H. Tsruta et al., Critiacl Sizes of Light Water Moderated UO_2 and PuO_2-UO_2 Lattice, JAERI Report 1254, 1977